Filtering Geometric Imperfection Patterns for Analysis and Design of Composite Shell Structures

Von der Fakultät für Bauingenieurwesen und Geodäsie

der Gottfried Wilhelm Leibniz Universität Hannover

zur Erlangung des Grades

Doktor-Ingenieur

Dr.-Ing.

genehmigte Dissertation

von

Dipl.-Ing. Alexander Dietmar Meurer

geboren am 06.06.1986 in Aachen

eingereicht im April 2017

Referent: Prof. Dr.-Ing. habil. Raimund Rolfes, Leibniz Universität Hannover
Korreferent: Prof. Chiara Bisagni, Delft University of Technology
Tag der Promotion: 14.06.2017

“The dinosaurs became extinct because they didn't have a space program.

And if we become extinct because we don't have a space program,

it'll serve us right!”

Larry Niven, as quoted by Arthur Clarke

"Meeting of the Minds: Buzz Aldrin visits Arthur C. Clarke" by Andrew Chaikin
(27 February 2001)

Abstract

When it comes to aerospace structures, the most prevalent components are conical and cylindrical shells. Subjected to axial loading, thin-walled shells are prone to buckling. Here, the critical load level is heavily influenced by deviations of a real specimen from the planned ideal structural geometry. While those so-called imperfections exhibit comparatively low amplitudes, adequatly taking into account their effect still poses a major task for designing these structures.

Hence, to ensure a safe design of shell components, expectable imperfection patterns have to be predicted by means of probabilistic methods or robust lower bounds have to be derived by applying deterministic procedures. Despite the rapid technological progess of the last decades concerning calculation, manufacturing and inspection, in industrial practice thin-walled shells are still designed using old and overly conservative design methods. As a result of the growing economic pressure, calls are growing louder to overcome these aging concepts.

To derive the aspired innovative design procedures, it is of vital importance to understand the specific influence of imperfections on the nonlinear and localized buckling behavior. While substantial progress was made in the field of modelling, numerical analysis and derivation of viable surrogate imperfections, the fundamental questions remain unanswered:

What exactly causes the local failure of a shell and why does one given imperfection pattern lead to a lower buckling load than another pattern?

In the framework of this dissertation, a reduction method is proposed. This procedure filters given imperfection patterns down to the inherent parts which are essential to trigger buckling of a shell with that particular pattern. In this way, a direct relation between the imperfection state of a real, measured and unloaded shell and its physical behavior right before buckling is established. The gained knowledge is used to explain why different measured imperfection patterns lead to different buckling load reductions.

Based on this, in the second part of this work, a new design procedure for cylindrical and conical shells is proposed. By combining the advantages of determinstic approaches and probabilistic methods, safe and economic design loads are derived. Merging both concepts, the design procedure is able to account for the influence of generally any type of imperfection while at the same time being independent from costly measurements of geometric imperfections.

Kurzfassung

Die tragendenden Komponenten von Strukturen der Luft- und Raumfahrt bestehen zum großen Teil aus konischen oder Kreiszylinderschalen. Unter axialer Last versagen diese meist dünnwandigen Tragwerke schlagartig durch Beulen. Das dazugehörige Lastniveau wird stark von durch den Fertigungsprozess bedingten Abweichungen der realen von der ursprünglich geplanten Geometrie beeinflusst. Trotz der sehr geringen Amplituden dieser sogenannten Imperfektionen stellt deren adequate Berücksichtigung bis heute eine große Hürde für den Bemessungsprozess solcher Strukturen dar.

So müssen für die sichere Auslegung von dünnwandigen Schalen entweder erwartbare Imperfektionsmuster im Rahmen von probabilistischen Methoden vorausgesagt oder aber mithilfe von deterministischen Verfahren sichere untere Grenzen für deren Einfluss auf die Beullast gefunden werden. Trotz des rasanten technischen Fortschritts der letzten Dekaden in den Gebieten Berechnung, Fertigung und Inspektion werden Schalenstrukturen in der industriellen Praxis noch immer mit alten und unwirtschaftlichen Bemessungsverfahren entworfen. Durch den steigenden ökonomischen Druck wird der Wunsch, diese Konzepte abzulösen, immer größer.

Für die Herleitung neuer, innovativer Bemessungsverfahren ist es zunächst nötig, den konkreten Einfluss von Imperfektionen auf das nichtlineare und lokalisierte Beulverhalten zu verstehen. Während die Forschung deutliche Fortschritte bezüglich der mathematischen Modellierung, der numerischen Analyse sowie der Bestimmung möglicher Ersatzimperfektionen verzeichnen konnte, bleibt doch die grundsätzliche Frage ungeklärt:

Was genau verursacht das lokale Versagen der Schale und warum führt ein gemessenes Imperfektionsmuster zu einer geringeren Beullast als ein anderes?

Im Rahmen der vorliegenden Dissertation wird ein Verfahren entwickelt, dass gegebene Imperfektionsmuster auf die darin enthaltenen Teile reduziert, die für das Beulversagen der Schalen mit jenen Imperfektionsmustern maßgeblich ist. Hiermit kann zum ersten Mal eine direkte Verbindung zwischen dem Imperfektionsmuster einer realen, vermessenen und unbelasteten Schale und deren physikalischem Verhalten kurz vor dem Beulversagen hergestellt werden. Aus den gewonnen Erkentnissen werden Schlüsse darauf abgeleitet, warum genau unterschiedliche gemessene Imperfektionsmuster unterschiedliche Beullastreduktionen hervorrufen.

Im zweiten Teil der Arbeit wird das erlangte Wissen angewendet, um einen Vorschlag für ein neues, innovatives Bemesssungsverfahren zu unterbreiten. Hierbei werden die Vorteile von deterministischen Konzepten und probabilistischen Methoden kombiniert, um sichere und ökonomisch attraktive Bemessungslasten zu berechnen. Durch die Integration beider grundsätzlicher Betrachtungsweisen entsteht ein Verfahren, welches grundsätzlich jede Art von Imperfektionen abbilden kann, gleichzeitig aber keine konstenintensiven Messungen von geometrischen Imperfektionsmustern erfordert.

Table of Contents

1 Introduction 1

1.1 Motivation and aim of this work 1

1.2 Structure of this work 3

2 State of the art 4

2.1 Buckling behavior of cylindrical and conical shells 4

2.1.1 Solving the stability problem of isotropic shells 4

2.1.2 From traditionally stiffened to composite shells 6

2.2 Design of cylindrical and conical shells 7

2.2.1 Bypassing the unpredictable: the Knock-Down-Factor design 7

2.2.2 Assumption of the worst case: design using „stimulating“ imperfections 8

2.2.3 From measurements to models: design using „realistic“ imperfections 11

2.2.4 Incorporating the unpredictable: probabilistic design 13

3 Methods for buckling prediction and design of shells 15

3.1 Stability problems: classification and calculation methods 15

3.1.1 Classification of bifurcation points and limit points 18

3.1.2 Linear buckling analysis 19

3.1.3 Nonlinear buckling analysis 19

3.2 Universal characteristics of the nonlinear buckling process 23

3.2.1 Global nonlinear prebuckling deformations 25

3.2.2 Local nonlinear prebuckling deformations 26

3.2.3 The beginning of the end: the initial dimple 27

3.2.4 Propagation of local failure: postbuckling deformations 29

3.3 Single Perturbation Load Approach (SPLA) 31

3.3.1 Basic Scheme 31

3.3.2 Understanding the constancy of the buckling load after P_1 32

3.3.3 Enhancing the numerical efficiency of the SPLA 34

3.3.4 The SPLA as a design procedure 35

3.4 Semi-analytical, probabilistic method (SAP) 37

3.4.1 From deterministic to probabilistic design 37

3.4.2 Approximation of the objective function by a quadratic Tailor series 37

3.4.3 Decorrelating input parameters: the Mahalanobis-Transformation 41

4 Reduction of imperfection patterns to the components essential for buckling 43
4.1 Fourier-representation of geometric imperfections 43
4.1.1 From a measured cloud of points to the phase-shift representation 43
4.1.2 Practical advantages of Fourier series for geometric imperfection patterns 47
4.1.3 On the required fidelity of the Fourier representation 47
4.1.4 On the coupling of imperfection modes 51
4.2 The stepwise imperfection filtering method (SIFM): main idea and discussion of parameters 53
4.2.1 Basic scheme 54
4.2.2 Exemplary application case: shell Z25 56
4.2.3 Variation of the mode evaluation order 57
4.2.4 Variation of the threshold value 62
4.2.5 Dynamic adaptation of the reference load level 69
4.2.6 On the numerical costs 72
4.3 Application of the SIFM to multiple shell specimen 74
4.3.1 Application to shells with coinciding geometry and laminate setup 74
4.3.2 Application to shells with varying geometry and laminate setup 78
4.3.3 Application to conical shells 83
4.3.4 Interpretation of the reduced imperfection shapes 84
4.4 What makes the essential imperfection shapes essential? 85
4.4.1 On the exclusivity of the reduced pattern within the original imperfection shape 85
4.4.2 Putting the essential patterns into context: comparison to other characteristic imperfection shapes 87
4.4.3 From essential parts of meaured patterns to a single perturbation load 93
4.4.4 Comparison of prebuckling equilibrium states 98
4.4.5 Explanation for the buckling load discrepancy of given imperfection patterns 103
4.4.6 Practical examples: patterns with divergent and matching buckling loads 110
4.5 Summarizing gain of knowledge 112
5 New design method for thin-walled composite shells 113
5.1 Necessities and demands for shell design methods 113
5.1.1 Shortcomings of currently prevailing design methods 113
5.1.2 What are the features of an ideal design procedure? 114
5.1.3 Classification of design procedures regarding their required amount of information about anticipated imperfections 115

5.2 Probabilistic Perturbation Load Approach (PPLA) 118
5.2.1 Basic scheme 118
5.2.2 Interpreting reliability of design loads 119
5.2.3 Application guideline 121
6 Application examples for the new design procedures 122
6.1 Numerical modelling of cylindrical and conical shells 122
6.1.1 Nominal geometries and laminate setups of considered shells 122
6.1.2 Numerical models for buckling analysis 124
6.1.3 Conical shells: peculiarities in manufacturing and modeling 125
6.2 Scatter of input parameters 128
6.2.1 Application of design procedures in practice: necessities and compromises 128
6.2.2 Overview of scattering imperfections 129
6.2.3 Geometric imperfections 130
6.2.4 Wall thickness and material properties 131
6.2.5 Loading imperfections 132
6.3 Results 134
6.3.1 Cylindrical Shells 134
6.3.2 Conical Shells 138
7 Summary and Conclusions 140
7.1 Summary 140
7.2 Conclusions 141
7.3 Outlook 142
List of figures 145
List of tables 150
Appendix A 152
Appendix B 157
References 159

1 Introduction

1.1 Motivation and aim of this work

The supporting structure of most aerospace vehicles is heavily dominated by cylindrical and conical shells. Due to their rotationally symmetric shape, these structures feature very high load carrying capacities at comparatively low structural weights. Therefore, cylinders and cones are used to realize numerous parts of the launcher, including tanks, interstage skirts and payload adapters (compare Figure 1-1).

Figure 1-1: Exploded view of Ariane 5 ECA, compare [1]

Under axial loading, cylindrical and conical shells are prone to buckling. Here, the load level at which a shell abruptly fails is heavily influenced by small deviations from the specimen's nominal surface, so called geometric imperfections. Among others, these discrepancies between planned and built specimen cannot be reliably predicted before manufacturing. Nevertheless, their impact on the load carrying capacity has to be accounted for when determining design parameters like for example a shell's thickness.

During the early days of human space flight in the 1960s, guidelines like the commonly applied NASA-SP 8007 were developed to derive primarily save design load levels. These lower-bound curves were based on experimental experience and enabled engineers to robustly account for the, at that time, mostly unexplored effects of imperfections on the buckling load. During the space race, economic reflections played a more subordinate role compared to the wish to "safely" put men on the moon.

Over the decades, circumstances shifted notably. Due to the enormous economic pressure prevailing in today's aerospace industry, the urge to minimize structural weight became one of the main drivers in launcher design. When it comes to thin-walled shells, the structural weight can be decreased in different ways. Here, the most promising ones might be the use of modern lightweight composite materials as well as the elimination of unnecessarily conservative safety margins within the design phase.

Since the pioneering days of space exploration, manufacturing techniques, measurement equipment and calculation capabilities substantially improved. Today, it is possible to precisely portray the exact prebuckling and buckling behavior of a real cylinder. Here, not only the general nonlinear behavior can be accounted for, but also the concrete and detailed inhomogeneous stress states initiating buckling can be simulated and correlated to experimental behavior. Consequently,

calls for safe but more economic design guidelines were growing louder to exploit these technical advances and their implied potentials for weight saving.

However, to perform highly detailed calculations, exact and extensive information about the real state of a shell structure is needed, be it laser scans of geometric imperfections, detailed measurements of load introduction irregularities and other variations from the nominal state of the specimen.

This poses a significant challenge when deriving innovative and less conservative design procedures. Obviously, detailed information about for example geometric imperfections is not available within the design phase, as the respective specimen is not yet build and thus cannot be measured. Therefore, the aforementioned high-fidelity calculations cannot be performed when designing the structure. This constitutes the quite paradoxical demand for new design procedures to robustly account for the influence of various imperfections without actually requiring information about their concrete manifestation.

Consequently, to nonetheless derive those innovative procedures, it is indispensable to precisely understand how exactly these imperfections with their anticipated manifestations influence the stability of a shell. Despite half a century of research and quite substantial progress, this knowledge is unfortunately not established yet.

As described above, the buckling loads corresponding to for example two measured geometric imperfection patterns can very well be calculated with high precision. However, an explanation for one particular measured imperfection pattern leading to a lower buckling load than another given pattern is still not found. Besides vague general claims (high imperfection amplitudes lead to low buckling loads), over the years researchers gained more detailed insight by investigating on the effect of superpositions of limited amounts of wave shapes within analytical and semi-analytical schemes. Others tried to circumvent the problem by establishing worst-case methods, assuming that lower-bound values can be found which cannot be undershot in reality. By treating imperfections as random variables, knowledge from measurements of existing shells could be transferred and extrapolated to new specimens to predict their most probable buckling loads.

Nevertheless, by visually or mathematically inspecting measured patterns, it still cannot be explained which shapes have a higher or lower detrimental effect on buckling loads and, just as importantly, why.

The main aim of this work is to tackle this persisting lack of knowledge.

In this thesis, a connection between detailed measured imperfection patterns and the precise nonlinear buckling states is established. By filtering measured patterns down to their inherent parts which are essential for triggering buckling of the shell, the coherences between the features of measured imperfection patterns and the buckling conditions caused by them can be revealed. The proposed filtering method is meant to serve as a tool for purposefully evaluating imperfection patterns to contribute to finally understanding their detrimental effect on the local loss of stability.

1.2 Structure of this work

This thesis is divided into seven chapters.

After this introduction, chapter 2 gives a detailed overview of the state of the art. Here, first the history of general buckling analysis of thin-walled shells is presented, followed by a discussion of the various attempts that were undertaken to tackle the aforementioned paradoxical situation of shell design and derive robust design loads.

In chapter 3, existing methods for buckling prediction and design of composite shells are discussed in greater detail. After introducing the basics of general stability analysis, the distinct characteristics of the nonlinear buckling behavior are depicted as a basis for subsequent analyses and reflections. Then, two recent design procedures which are frequently discussed in the scientific community are presented: the single perturbation load approach (SPLA) and the semi-analytical probabilistic method (SAP).

Chapter 4 can be considered as the core of this thesis. Here, the stepwise imperfection filtering method (SIFM) is proposed and discussed. After an overview of how to utilize Fourier series to describe geometric imperfection patterns, the main idea of the SIFM is presented, its influential parameters are discussed and the results of its application to various shell specimens are presented. By applying the SIFM, a given measured imperfection pattern can be reduced to its inherent parts which show to be essential for the highly nonlinear localized buckling initiation caused by the given measured pattern. Based on these essential shapes, a physical interpretation and tangible explanation for the varying criticality of different measured imperfection patterns is found.

In the fifth chapter of the work, a new proposal for designing thin-walled shell structures is given, transferring the gained knowledge in buckling analysis to the derivation of design methodologies. By combining the deterministic treatment of geometric imperfections (SPLA) and the probabilistic handling of various other kinds of imperfections (SAP), the probabilistic perturbation load approach (PPLA) is derived. The application of the PPLA to numerous cylindrical and conical composite shells in chapter 6 leads robust design loads that are substantially less conservatives than the ones of well-established design procedures.

Chapter 7 closes the work by summarizing major findings and conclusions, followed by a discussion of open questions to provide a basis for future research.

2 State of the art

2.1 Buckling behavior of cylindrical and conical shells

2.1.1 Solving the stability problem of isotropic shells

The awareness of the general characteristic difference between bending and stability problems arose as early as in the 18th century. In 1757, EULER was the first to describe the geometrically driven buckling failure of columns. Many researchers like BERNOULLI, LAGRANGE and KIRCHHOFF followed his work and derived theories to cover the buckling behavior of flat plates. However, not until the beginning of the 20th century, first ideas for describing the buckling behavior of cylindrical shells were found. LORENZ [2], TIMOSHENKO [3] and SOUTHWELL [4] independently postulated the equation for the buckling load of an isotropic cylindrical shell:

$$\sigma_{cr} = \frac{E}{\sqrt{3(1-\nu^2)}} \frac{t}{R}$$

Based on the assumption of a perfect initial shape with radius R and thickness t, the purely membrane stress state would become unstable at the load level σ_{cr} and bifurcation would occur.

When in the 1930s LUNDQUIST [5] and DONNELL [6] conducted experiments on thin cylindrical shells, it figured that the experimental buckling loads were significantly lower than the theoretical values. Despite approaches by DONNELL [6], incorporating large deflections, as well as by VON KÁRMÁN and TSIEN [7], who chose a parameterized pattern for the radial buckling deflections of the solution assumption, the origin of this significant discrepancy could not be explained.

With the start of the cold war and the birth of space exploration, methods for predicting the real buckling load of very thin walled cylinders became indispensable. In 1965, WEINGARTEN et al. [8] published a review of numerous experimental results of axially compressed thin cylindrical shells (cf. Figure 2-1).

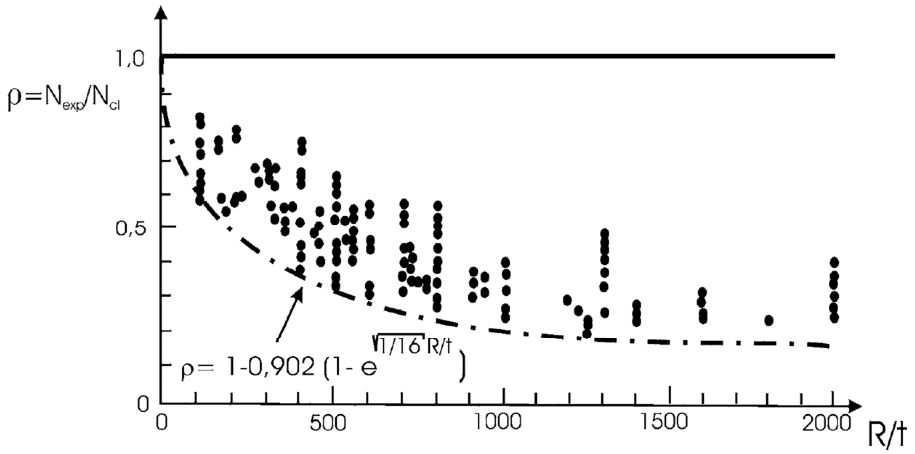

Figure 2-1: Normalized experimental buckling loads over the slenderness of the shell [8], [9]

It was observed that the buckling loads obtained from experiments significantly differ from the theoretical predictions even for comparatively thick shells. For an increasing slenderness R/t this discrepancy gets bigger and approaches a value of no more than 20% of the analytical buckling

load. To appropriately account for this significant difference between the theoretical prediction and the buckling load of real cylindrical shells poses a challenging task to a large number of researchers up to the present day.

After the problem became known to the research community, first explanations were sought after in the assumptions inherent in the original buckling load equation: the assumed linearity of the prebuckling state as well as the assumption of perfect boundary conditions. Thus, SEIDE [10] and HOFF et al. [11] investigated the influence of the boundary conditions on the stability behavior of shells. They concluded that due to the significant clamping forces, friction would prohibit notable deflections of the shell's edges and thus experimental boundary conditions could be compared to theoretically perfect ones. ALMROTH [12] also investigated the influence of different combinations of boundary conditions on the stability behavior of cylindrical shells. While he indeed showed that different boundary conditions had a notable influence on the buckling load, it also became apparent that the nonlinear prebuckling behavior is of great importance for the analysis as opposed to assuming a purely membrane stress state.

Meanwhile KOITER published his Ph.D. thesis [13] in the Netherlands in 1945. Not until a translation to English [14] was established in 1965, his findings became apparent to the scientific community. KOITER asymptotically described the initial postbuckling behavior of the shell. In his series expansion of the load factor λ in the regime of the lowest eigenvalue λ_c, the slope of the secondary equilibrium path plays a decisive role:

$$\lambda/\lambda_c = 1 + a\xi + b\xi^2 + \ldots$$

For symmetric buckling problems, the factor a becomes zero. The factor b however gives a direct indication of the slope of the load-deflection curve at the bifurcation point. Based on that, KOITER adjudged the factor b to be an indicator for the general sensitivity of a shell to initial deflections in its surface. He showed that when b becomes negative, and thereby the secondary path has a negative slope, buckling will cause a significant drop in load carrying capacity while the associated critical load heavily depends on the degrading influence of initial geometric imperfections. BUDIANSKY and HUTCHINSON [15] gave a condensed overview of KOITER's theory and thereby contributed to its dissemination and acceptance.

Based on KOITER's findings, numerous authors investigated the influence of various initial imperfection shapes on the buckling load of cylindrical shells. While TENNYSON and MUGGERIDGE [16] applied local axisymmetric imperfection shapes, YAMAKI [17] assumed geometric disturbances affine to the characteristic postbuckling pattern and JÜRCKE [18] chose imperfection shapes affine to the periodic eigenforms. As many authors of that time were limited by the amount of necessary calculations, HERZLINGER [19] chose a simplified approach for the buckling problem. He described the buckling behavior by a pseudo bifurcation of a beam with elastic boundaries with results well comparable to existing methods.

In 1970, ESSLINGER [20], [21] was able to visually capture the dynamic buckling behavior of cylindrical shells using high speed cameras. In these short films, the transition from the stable prebuckling state to the unstable postbuckling state became visible for the first time. It was

observed that buckling starts with a single initial dimple which abruptly grows in magnitude. This initial dimple causes a local loss of stability leading to a propagating pattern of uniform dimples, spreading around the shell's circumference. After the propagation of this unstable postbuckling pattern, the well-known, long-waved stable postbuckling pattern emerges. These post-buckling patterns are thoroughly depicted and analyzed, both experimentally and numerically, by for example BISAGNI [22].

2.1.2 From traditionally stiffened to composite shells

To counter the at that time unpredictable influence of geometric imperfections on the buckling load and to rise load carrying capacities in general, longitudinally and circumferentially stiffened shells became popular in launcher design. Stiffened shells can be characterized by their separation of local buckling phenomena within the stringer pockets and global buckling indicating structural failure. This separation leads to a reduction of imperfection sensitivity as local geometric imperfections mostly trigger pocket buckling and not global failure [23].

Obviously, the effect of different stringer geometries had to be investigated. While VAN DER NEUT [24] showed that outward stiffeners lead to higher buckling loads in comparison to inward stringers, HUTCHINSON, BUDIANSKY and AMAZIGO [25], also revealed a higher imperfection sensitivity of shells with outward stiffeners. WELLER and SINGER [26] showed that also the stringer geometry and density have a significant influence on the load carrying capacities. Furthermore, in an experimental campaign by BISAGNI and CORDISCO [27] the possibility to exploit load carrying capacities of stiffened structures which are beyond buckling but in the post-buckling regime was demonstrated.

Besides the shell and stringer design, again the question of the effect of different boundary conditions on the buckling load arose. SINGER and ARBOCZ [28] produced and tested several stringer stiffened shells to investigate the influence of varying edge conditions on their buckling loads. In compliance with other authors like ARBOCZ et al. [29] and WELLER [30], they found that the boundary conditions of stiffened shells have a much more substantial influence on the buckling load as in the case of unstiffened isotropic shells.

The introduction of modern fiber composite materials to aerospace structures in the late 1970s promised high weight savings and thus a significant reduction in operational costs – be it in commercial airplanes or in space launcher structures. The general structure of composite shells can be compared to the structure of stiffened isotropic shells as the laminate stacking sequence has a significant influence on the structural behavior, similar to the one of traditional stringers. In analytic calculations, ZIMMERMANN [31] showed that the buckling load of geometrically perfect composite shells is heavily influenced by fiber orientations and stacking sequence. This behavior can be compared to the varying effect of inward and outward stringers mentioned above [32].

HILBURGER and STARNES [33] showed that apart from the perfect shell's buckling load also the imperfection sensitivity of composite shells is highly dependent on the laminate setup. The question arose, whether the findings and design guidelines based on isotropic or stiffened shells could be applied to composite shells. ALMROTH [24] pondered if the knock-down factors derived

from isotropic shells would be on the safe side once the imperfection sensitivity of a specific laminate setup is determined.

Apart from the influence of imperfections on the buckling load it was also discussed whether composite shells show different general imperfection signatures as shells made from isotropic material or not. While CHRYSSANTHOPULUS and POGGI [34] postulated that for an investigated set of shells the fiber orientation did not influence the amplitude or distribution of geometric imperfections, ESONG et al. [35] and SINGER et al. [28] showed that for composite shells characteristic imperfection signatures can be linked to certain manufacturing techniques.

Besides the general strive for answers on how to handle geometric imperfections, the research on composite structures evoked entirely new questions. ALMORTH [24] remarks that in case of composite shells also so called non-traditional imperfections like delamination, fiber waviness and voids and their influence on buckling loads should be studied. HILBURGER and STARNES [33] investigated the influence of ply-gaps, thickness imperfections and uneven shell edges on the buckling loads and showed their importance in analysis of composite cylindrical shells.

2.2 Design of cylindrical and conical shells

2.2.1 Bypassing the unpredictable: the Knock-Down-Factor design

As shown above, researchers intensively investigated the buckling behavior of shells and pursued insight on the influence of imperfections on the buckling loads. However, at the same time they had to derive criteria and approaches to account for these unknown and at that time unpredictable reductions in load carrying capacities during design phase.

The first thorough measurements of geometric imperfections were conducted by ARBOCZ and BABCOCK [36] in 1969. Before that, the knowledge of imperfection types and distributions was rather vague, so robust design procedures had to be developed without proper means of incorporating imperfections in the analyses. The solution at that time was to bypass dealing with imperfections numerically but using statistical knowledge from measured specimen. Beginning in 1957, HARRIS et al. [37] started to predict load carrying capacities using experimental results which finally lead to the collection of test results by WEINGARTEN et al. [8], as already shown above in Figure 2-1.

WEINGARTEN proposed the dashed lower bound curve as a design guideline, yielding a so called Knock-Down-Factor (KDF) γ which is given by:

$$\gamma = 1 - 0.901(1 - e^{-\phi}) \qquad \text{with} \quad \phi = \frac{1}{16}\sqrt{\frac{R}{t}}$$

This KDF γ, which only depends on the shell's slenderness, would then be multiplied with the analytically determined buckling load of the perfect shell to obtain a robust design load for the structure. NASA adopted the idea in 1968 and established the guideline NASA SP-8007 [38] which is broadly used for the design of cylindrical shells up to the present day. For conical shells, design load recommendations are be found in NASA SP-8019 [39].

Having in mind the need for design criteria also for stiffened shells, NASA SP-8007 also offered a way to incorporate orthotropic structural behavior by modifying the exponent ϕ:

$$\phi = \frac{1}{29.8}\sqrt{\frac{R}{t^*}} \quad \text{with} \quad t^* = \sqrt[4]{\frac{D_x D_y}{E_x E_y}}$$

Here, the mechanical similarity between stiffened shells and unstiffened composite shells can again be noticed. By inserting the entries of the ABD matrix, a KDF for composite shells is obtained:

$$\phi = \frac{1}{29.8}\sqrt{\frac{R}{t^+}} \quad \text{with} \quad t^+ = \sqrt[4]{\frac{D_{11} D_{22}}{A_{11} A_{22}}}$$

While this formulation allows to account for the highly anisotropic behavior of laminated composites, it should be noted that the possible coupling of bending and membrane stresses are neglected by disregarding the entries of the B matrix. DE VRIES [40] unified the formulation and considered the isotropic shell as a special case of the anisotropic one:

$$\phi = \frac{1}{16}\sqrt{\frac{R}{\tilde{t}}} \quad \text{with} \quad \tilde{t} = \sqrt{12}\sqrt[4]{\frac{D_{11} D_{22}}{A_{11} A_{22}}}$$

A widespread overview on different isotropic and anisotropic shells and their KDF by NASA SP-8007 was given by TAKANO [41].

The great advantage of the NASA SP-8007 guideline was to give a robust design load which accounts for the increasing imperfection sensitivity for shells with high slenderness. However, over the years it figured that the obtained design loads were in most cases considerably exceeded by the real structures and test specimens. As over the time doubts about the manufacturing and testing quality of some of the data in Figure 2-1 arose [42], the Caltech group around ARBOCZ et al. [43] carefully produced and tested a group of new specimen which lead to KDFs of twice the values by NASA SP-8007, showing its distinct overly-conservativeness.

With the aim to cover the increasing imperfection sensitivity with increasing slenderness, numerous other guidelines were published over the years. In contrast to the statistically driven background of the NASA SP-8007, those guidelines are based on judging the expectable or acceptable manufacturing accuracy by means of the deepest initial imperfection dimple. Published in 1988, the ECCS 56 [44] gives KDFs dependent on the R/t ratio, its use however is limited to steel shells. The German norm DIN 18800-4 [45] and the more recent general European guideline Eurocode 3 [46] also account for the shells slenderness but – in contrast to all preceding guidelines – subdivide shells into groups by taking into account their lengths.

2.2.2 Assumption of the worst case: design using „stimulating" imperfections

Besides the convenient but purely statistically based design of cylindrical shells, researchers tried to find numerical ways to predict the expected drop in buckling loads due to geometric imperfections. As mentioned earlier, KOITER [14] was the first to include initial deflections of the shell's surface into the solution of the stability problem. Based on that, all investigators at that time used basically similar approaches to computationally obtain reduced buckling loads. The

general scheme was to choose a combination of single imperfection modes and then solve the equations assuming stable eigenmode shapes for the postbuckling deflections. As there obviously are numerous ways to assume an initial superposition of imperfection modes, the designers' question arose which kind of imperfection pattern was the worst one by the means of stimulating the shells' behavior and thus leading to the highest reduction in buckling loads.

As the analytic equations were solved for buckling mode shapes, consequently the eigenmode-affine imperfection patterns soon were assumed to have the highest impact on the buckling behavior [47]. While already commonly used in the field of civil engineering, significant reductions in buckling loads could be achieved, depending on the amplitude of these eigenmode shapes [48]. Based on findings by IMBERT [49] and SINGER et al. [50], ARBOCZ [51] stated that for an imperfection shape to be critical for the buckling load, the eigenvalue of the imperfection mode has to be near the critical eigenvalue of the perfect shell.

However, despite the advantage of being easily obtained by a linear buckling analysis, eigenmode imperfections sporadically lead to a significant reduction in axial stiffness which is generally not witnessed in experiments. Thus, HAYNIE and HILBURGER [52] concluded that eigenmode imperfections and the associated buckling load reductions are to be considered as rather unrealistic.

When KOITER [14] established a relation between the number of waves of the assumed buckling mode and the number of waves of the imperfection mode, the attention was directed to axisymmetric imperfection patterns. These patterns yielded significant disturbances of the stability of the shells as described by many authors like ALMROTH [53], TENNYSON and MUGGERIDGE [16] and HUTCHINSON et al. [54]. However, depending on the chosen wavelength and amplitude, they show a similar disagreeable reduction of axial stiffness.

An entirely different approach to find a stimulating imperfection shape for cylindrical shells was first stumbled upon by RICARDO [55] in 1961. He investigated the influence of small constant lateral perturbation loads on the buckling behavior of a cylinder (Figure 2-2, left). While RICARDO concentrated on evaluating the occurring buckling shapes connected to the perturbation load, in 1970 OKUBO [56] realized the fact that starting from a certain level of perturbation loads, the critical loading of the cylinder (in his case the bending moment) does not decrease any further (Figure 2-2, right).

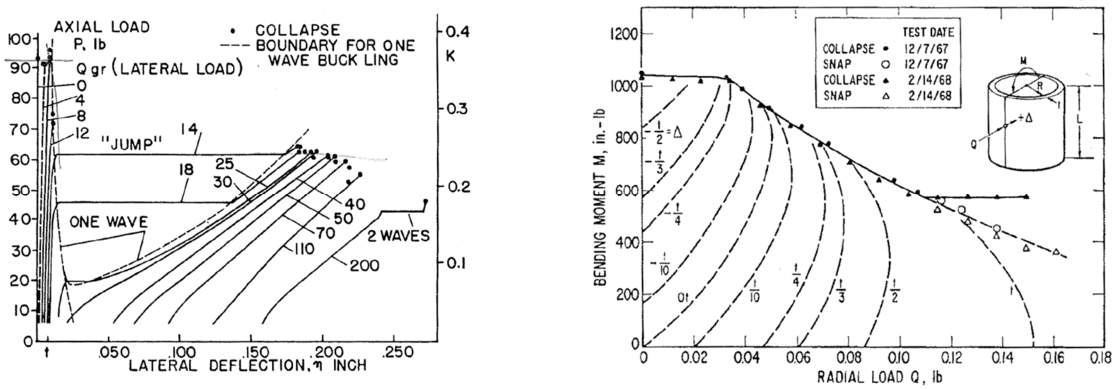

Figure 2-2: Axial load over lateral deflection caused by a constant perturbation load by RICARDO [55] (left) and critical bending moment over lateral perturbation load by Okubo [56] (right)

However, as both authors focused on explaining the danger of lateral perturbations for the stability behavior of cylinders and did not align their findings to the relatively new problem of unknown imperfections in the design phase, their contribution did not receive much attention.

Thus, it was not until 2005 when HÜHNE [42], [57] independently discovered the high potential of lateral perturbation loads as a measure for deriving design loads for cylindrical shells. In an extensive experimental and numerical campaign, he described in detail the phenomena laterally perturbed shells undergo under axial loading and derived the Single Perturbation Load Approach (SPLA). This approach is at the present heavily investigated as a possible way to obtain robust but not overly conservative design loads. Figure 2-3 shows the experimental results obtained by HÜHNE, which were matched within the framework of a numerical analysis.

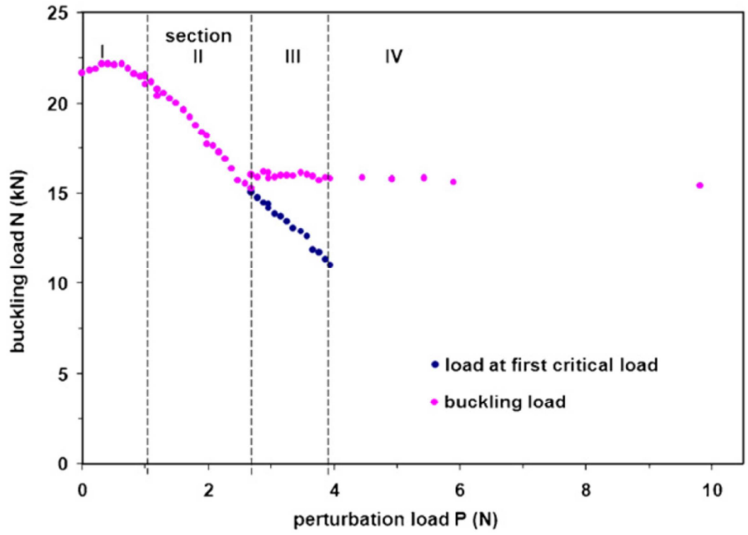

Figure 2-3: Experimental results of axially compressed cylinders with a constant lateral perturbation load P [57]

It is noticed that in the regime of low perturbation loads, the buckling loads show a steady decrease (section II). When reaching a critical perturbation load P_1, the buckling load does not decrease any further (sections III and IV). This constancy of the buckling load is interpreted as a lower bound and thus serves as a design value for the load carrying capacity of the cylinder. The outstanding advantages of this approach lie in its simplicity, applicability to isotropic and composite shells and its independence from measurement data.

Since 2006, many authors contributed to the further understanding and applicability of the SPLA. WANG et al. [58] and STEINMÜLLER et al. [59] found a way derive P_1 by an empiric formula to avoid performing the otherwise required multiple nonlinear analyses. When it comes to the application of P to the cylinder, ARBELO et al. [60] investigated the influence of multiple perturbation loads at different positions of the cylinder and found a steady decrease of design loads with an increasing number of lateral forces. WANG et al. [61] showed that the angle of the perturbation load has a negligible influence on the SPLA results. WULLSCHLEGER [62] represented the deformation shape of the cylinder under a lateral perturbation load by a stress free single dimple and obtained comparable results. Finally, in a comprehensive investigation, CASTRO et al. [63] precisely described the characteristic physical behavior of shells under lateral perturbation loads and revealed the reason for the observed constancy of the buckling load.

However, despite the notable progress over the last years, the SPLA has proven to be not conservative in certain cases [64] and thus unfortunately does not give a final answer to the design of cylindrical shells in its current state.

2.2.3 From measurements to models: design using „realistic" imperfections

In parallel to the strive for a theoretically critical and stimulating imperfection shape in order to numerically obtain conservative design loads, researchers continuously tried to also cover and predict the real manufacturing signatures and shell behaviors.

In the 1960s and 1970s, computational power was limited and many researchers were bound to analytical or semi-analytical procedures. Thus, when in the late 1960s ARBOCZ and BABCOCK [36] and SINGER et al. [28] conducted the first complex and rigorous measurements of geometric imperfections (cf. Figure 2-4), the scientific community was faced with a barrier.

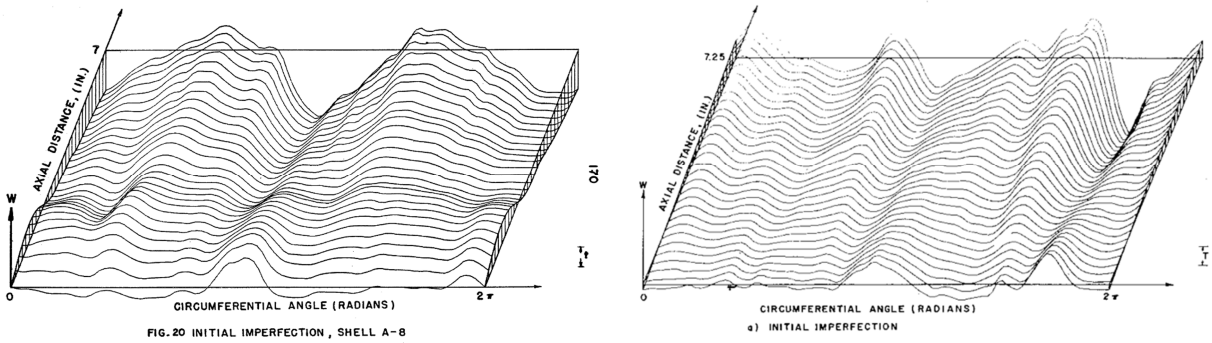

Figure 2-4: Early geometric imperfection measurements by Arbocz et al. [36] (left) and by Singer et al. [28] (right)

While the measured imperfection signatures could be conveniently represented by Fourier series to reduce the amount of data [65], the numerical application of those real geometric imperfections to the existing analytical methods was not possible [66]. The reason for this is that with growing fidelity of the assumed initial deflection shape, the solution of the nonlinear differential equation models drastically grows in complexity. Thus, many authors applied single mode shapes, a limited combination of imperfection modes or other modest assumptions to reflect the actual measured imperfections and used the first basic numerical models to describe the buckling behavior of the imperfect cylindrical shells.

In 1968, REED [67] was the first to approximate geometric imperfections by multiple diamond-shaped flat spots in the shell's surface. He derived a connection between the number of those flat spots and the associated buckling loads. Later, GILLIE [68] approximated a cylinder by a flat n-gon and used energy formulations to obtain the number of edges leading to the lowest buckling loads.

Coming closer to an adequate description of the measured imperfection pattern, ARBOCZ [69] represented geometric imperfections by a superposition of seven imperfection mode shapes and compared the results for various different shell types like panel composed and monolithic ones.

In contrast to that ELISHAKOFF [66] used a DONNEL-IMBERT type approach [49] to cover the geometric imperfection pattern, taking into account a much higher number of axial and circumferential waves. Similar to the typical Fourier Spectrum of a measured pattern where imperfection modes of higher wave numbers in axial direction (k) and circumferential

direction (l) show decreasing Fourier coefficients, he chose the amplitudes ξ_{kl} of his imperfection modes to satisfy $\xi_{kl} = \frac{\xi}{kl}$.

After an extensive study on different assumptions on geometric imperfections, ARBOCZ [51] gave an overview on the application of different more and more complex approaches for geometric imperfections in a semi-analytical analysis framework. First, he showed the validity of KOITER's general theory while applying axisymmetric and asymmetric imperfection shapes. After that, when it came to the combination of axisymmetric and asymmetric imperfections, the formulations became much more extensive. ARBOCZ [51] stated that for the subsequent step – the application of real measured geometric imperfection patterns – very costly iterative processes became necessary.

When in the 1980s and 1990s computational power tremendously increased due to the rise of micro- processor technology and parallel processing, the analysis of shell buckling largely shifted from the original semi-analytical approaches to finite element based models. With the increasing computing power, the application of as measured distributions of various types of imperfections became possible.

Numerous authors like DEGENHARDT et al. [70], BROGGI et al. [71], HILBURGER [33], KRIEGESMANN [64] and many more now incorporated detailed measured geometric imperfections in their semi-analytical as well as finite element models and succeeded in simulating the geometric imperfections' actual share of the buckling load reduction. Figure 2-5 shows a highly detailed state of the art imperfection laser scan of a composite shell and the equivalent detailed imperfection pattern included in the numerical analysis.

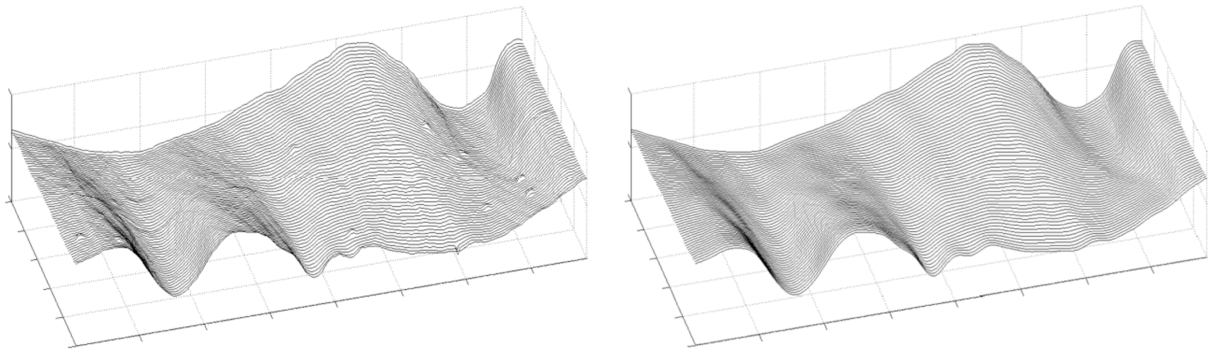

Figure 2-5: State of the art imperfection measurements by Hühne [57], [64] (left) and imperfection pattern included in the numerical analysis by Kriegesmann [64] (right)

However, with the new methods of analysis, it also became apparent that many other types of imperfections, referred to as non-traditional imperfections, significantly contribute to the structural failure of shells. ARBOCZ and STARNES [43] measured and calculated the influence of edge unevenness and thickness imperfections while HILBURGER and STARNES [33] also incorporated ply-gaps and elastic boundary conditions. As numerous cylindrical aerospace structures are composed from single curved panels, EL DAMATTY et al. [72], NEMETH et al. [73] and WINTERSTETTER and SCHMIDT [74] investigated the influence of realistic welding-induced imperfections.

The combination of all those efforts to incorporate traditional and non-traditional imperfections within a numerical analysis framework was the necessary basis for the next step in cylindrical

shell design. Thus, aside from the approaches based on abstract but critically stimulating imperfections described in chapter 2.2.2, current research just as well focuses on obtaining design procedures which are based on using realistic imperfections to accurately predict the sensitivities and the real buckling behavior of cylindrical shells.

2.2.4 Incorporating the unpredictable: probabilistic design

Besides the evident question of how to model imperfections in shell analysis and design, researchers since the beginning were faced with an additional crucial problem. As in the manufacturing process the appearance of imperfections can only be influenced to a certain degree, their actual final shape has to be considered as rather random. Thus, BOLOTIN [75] concluded that imperfections have to be treated probabilistically in analysis. His imperfection sensitivity concept was one of the first attempts to account for the scatter of geometric imperfections in cylindrical shells.

Starting in 1979, ELISHAKOFF [76], [77] used space-random fields for describing the stochastic scatter of input parameters within a Monte Carlo analysis. Monte Carlo analyses in general are based on creating numerous samples depending on the scatter of the input parameters and then evaluating the objective function, namely the buckling load as a function of the imperfections. The discrete distribution of obtained buckling loads can then be used to derive a reliability function and, with a chosen level of reliability, robust design loads. This technique was further utilized and refined by many authors like VELDS et al. [78], CHAMIS and ABUMERI [79] as well as BROGGI et al. [71] to obtain buckling load distributions and compare them to experimental data.

A different approach was first presented by ELISHAKOFF et al. [66] and ARBOCZ and HOL [69]. The first-order second-moment (FOSM) method is based on approximating the unknown objective function by a Taylor series and using standard estimators to numerically obtain a continuous buckling load distribution. The computational costs of the FOSM method directly depend on the number of input parameters, therefore both authors used simplified models to account for the scattering imperfections. To compare the method's results with experiments, TU Delft conducted an exceptional study when carefully measuring and testing thirty beer cans under axial compression [80]. As not all types of imperfections were included in the analysis, the results could not be matched to the experimental buckling load distributions [81].

In all those early works of probabilistic analysis, the methods generally focused on the effect of scattering geometric imperfections without accounting for non-traditional imperfections. With the beginning of the digital age however, whole new possibilities for probabilistic analysis emerged. In 1991, CHRYSSANTHOPOULOS et al. [82] were the first to incorporate finite element calculations of the buckling load within a probabilistic framework. This paved the way for many authors like ARBOCZ and STARNES [43], DEGENHARDT et al. [70] and KRIEGESMANN et al. [64] to additionally investigate the scatter of numerous non-traditional imperfections (cf. chapter 2.2.3) and thus to approach the real probability distribution of buckling loads obtained by test results.

In a detailed study in 2005, ARBOCZ and HILBURGER [83] investigated a set of shells and compared the results of Monte Carlo and FOSM analyses. They found that FOSM yields slightly more

conservative but also generally robust design loads. KRIEGESMANN et al. [84] also compared Monte Carlo, FOSM and incomplete second-order (ISOA) analyses taking into account numerous kinds of imperfections. While obtaining similar results for all applied methods, he finally was able to closely match the distribution of experimental results conducted by DEGENHARDT et al. [85].

Regardless of the chosen probabilistic methods, insight on the expected scatter of the input parameters, namely the various imperfections, is evident for accurately predicting the buckling load distribution of a shell. ARBOCZ and BABCOCK [36] showed that certain manufacturing processes are directly linked to certain characteristic distributions of imperfections. KRIEGESMANN et al. [86] investigated the critical influence of the sample size on the results of probabilistic design procedures. After all, it became apparent that to obtain realistic buckling load distributions with probabilistic design procedures a sufficiently large set of shells had to be produced and the various kinds of imperfections had to be thoroughly measured.

The fundamental caveat of probabilistic design up to the present day is to obtain this required data base.

A first collection of imperfection measurements was compiled by TU Delft, Netherlands and Technion, Israel in the 1970s [87]. In smaller projects, research establishments like Deutsches Zentrum für Luft und Raumfahrt (DLR), Germany were able to produce and measure small series of specimen [70], [83]. Nevertheless, the extensive production of test articles of different geometries, materials and manufacturing techniques seems to be as unrealistic from a financial point of view as the large scale measurement of real launcher structures within the running production chain. Therefore, researchers and designers still lack sufficient knowledge for the proper application of the probabilistic methods in practice.

Hence, sophisticated design procedures have to be developed which incorporate the advantage of probabilistic methods, namely the known bucking load distributions and chosen reliability levels, as wells as the advantages of deterministic approaches, namely the independence from imperfection measurements.

3 Methods for buckling prediction and design of shells

3.1 Stability problems: classification and calculation methods

The mechanical behavior of structures under loading can generally be divided into so-called stress problems and stability problems.

In the case of stress problems, to every load level one particular deflection state can be ascribed (compare Figure 3-1, a)). Stress problems mostly occur in structures where tension or bending is predominant or which are designed with comparatively high thicknesses. In these cases, design and failure loads are mainly derived based on material behavior and properties.

However, if a comparatively slender structure is predominantly subjected to a compression state, a fundamentally different type of failure has to be analyzed, the so called stability problems. In contrast to stress problems, the load deflection curve of such structures is not always continuous but shows distinct singularities, called singular points or instability points. In a stability problem, for a particular load level, multiple equilibrium states of different deflections can exist (compare Figure 3-1, b)). Therefore, stability problems can also be referred to as ambiguity problems.

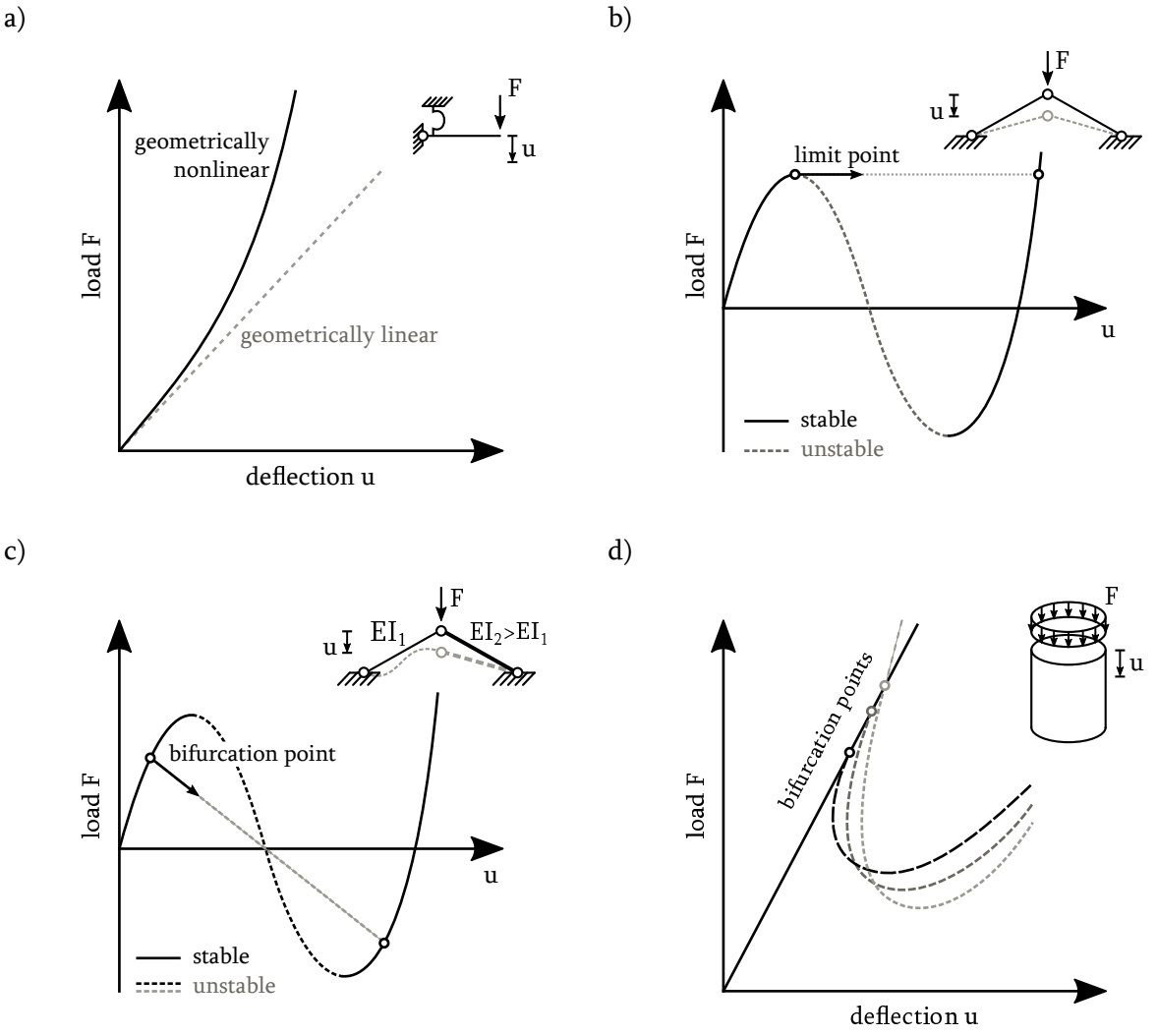

Figure 3-1: Schematic overview of stress problems and stability problems, compare [42] and [88]

Stability problems can generally be divided into snap-through and bifurcation problems. The most common example to illustrate their different behavior is the von Mises truss, depicted in Figure 3-1, b). When investigating on the load-deflection-curve, local minima and maxima with horizontal tangents are noticed. These points, between which the equilibrium is instable, are called limit points. If a limit point is reached and the load level P is increased any further, the structure suddenly snaps through into the neighboring stable equilibrium state (compare Figure 3-1, b), arrow). This promptly releases a significant amount of energy which, depending on the type of structure, can lead to structural failure.

In the case of bifurcation problems, the ambiguity of the system state is not necessarily caused by local maxima and minima but by intersection of primary and secondary equilibrium paths. When again looking at the von Mises truss, the structural behavior changes if for example the individual stiffness of a beam is low enough or a certain geometric imperfection is introduced. Then, the structural response branches to a secondary and unstable equilibrium path before the limit point is reached (compare Figure 3-1, c)). This intersection of two equilibrium paths is called a bifurcation point.

In more complicated structures, bifurcation, snap-through and snap-back problems can occur collectively. For example cylindrical shells as well as conical shells show multiple bifurcation points, which lead to different unstable secondary branches (compare Figure 3-1, d)). After the bifurcation points, the load deflection curve then shows the characteristics of a snap back problem which finally leads to the equilibrium path being stable again.

The buckling load of a shell is defined by the maximum load level before the stable postbuckling deflection occurs. In the case of a geometrically perfect shell, this concurs with the first bifurcation point. When looking at realistic structures with geometric imperfections, the behavior changes fundamentally. In these cases, the buckling load levels significantly decrease while bifurcation points transition into limit points with comparatively small radii (compare Figure 3-2).

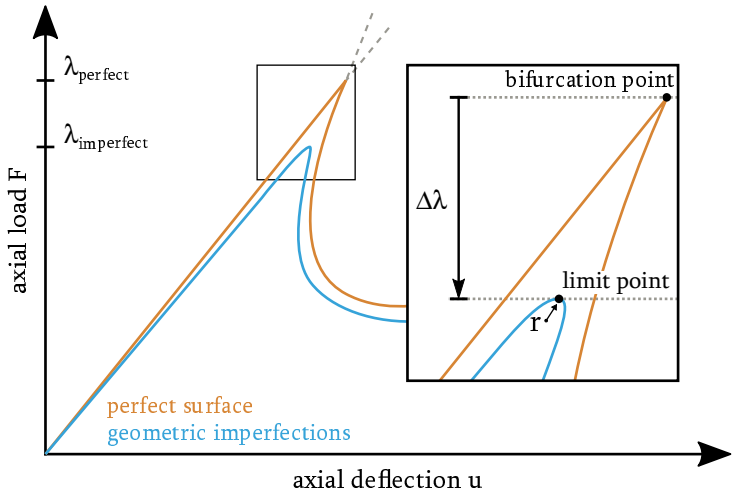

Figure 3-2: Perfect and imperfect shell: buckling load reduction and transition from bifurcation point to limit point

As indicated in Figure 3-2, the difference between the buckling load of an imperfect shell and the one of the equivalent perfect shell is referred to as $\Delta\lambda$ in the following. On the one hand, the

buckling load reduction $\Delta\lambda$ serves as an important measure to compare the effects of different particular imperfection patterns on the buckling load in the subsequent chapters.

On the other hand, it is used to judge on the imperfection sensitivity of a shell specimen to geometric imperfections in general. While in traditional works related to KOITER's b-factor method (compare chapter 2), the term imperfection sensitivity is mathematically related to the slope of the load deflection curve after buckling, in this thesis a more practical definition is chosen. As the main focus of cylindrical shell design is to accurately predict or robustly account for real life buckling load levels, in the following imperfection sensitivity is interpreted as the susceptibility of a given shell configuration (measures, laminate setup, etc.) to a reduction of its buckling load level due to geometric imperfections. In this way, a shell specimen exhibiting large buckling load reductions $\Delta\lambda$ will be judged as highly imperfection sensitive (e.g. shell Z25, see chapter 4.2.2) while others, showing only marginal differences between perfect and imperfect buckling loads will be classified as not imperfection sensitive (e.g. shell Z09, see chapter 4.3.2).

Coming back to the fundamental mechanical differences between perfect and imperfect shells, it should be noted that the transition from bifurcation points to limit points with small radii applies only for realistic and somewhat inhomogeneous imperfection patterns which are similar to the shell surfaces measured in reality. In the case of certain artificial and academically assumed imperfection patterns, the behavior can change. When for example applying axially symmetric imperfection shapes within a numerical analysis, the radius of the limit point can significantly increase, so that the structural behavior can even transition from a bifurcation or snap-through problem into a bending dominated stress problem with nearly horizontal tangents.

In the following, an overview of the most commonly applied procedures to detect stability points and predict structural stability failure is given. As these basics are frequently discussed in literature, this synopsis is based on the work of numerous authors. Thus, for additional and more detailed information it is particularly referred to the summaries of HÜHNE [42], KRIEGESMANN [89] and JÄPPELT [90] as well as the works of PFLÜGER [91], WRIGGERS [92], EL NASCHIE [93] and NASDALA [94].

3.1.1 Classification of bifurcation points and limit points

From a mathematical point of view, singular points, which are the aforementioned limit points and bifurcation points, can be classified based on three main approaches:

- Variation of the total potential energy
- Investigation of the dynamic response of the perturbed system
- Inspection of the nontrivial equilibrium states

In the following, a short summary of the commonly applied definition of the nontrivial equilibrium states shall be given.

A state of equilibrium $\boldsymbol{G}(\boldsymbol{u},\lambda)$ is defined as the sum of the vector of internal nodal forces $\boldsymbol{I}(\boldsymbol{u})$ at a given deflection state $\boldsymbol{u}$ and the vector of external forces $\boldsymbol{P}(\boldsymbol{u})$, scaled by a load factor λ:

$$\boldsymbol{G}(\boldsymbol{u},\lambda) = \underbrace{\boldsymbol{I}(\boldsymbol{u})}_{inner\ nodal\ forces} - \underbrace{\lambda\,\boldsymbol{P}(\boldsymbol{u})}_{external\ forces} = 0 \tag{3-1}$$

Around instability points, for a given base equilibrium state ${}^{B}\boldsymbol{G}$ a neighboring equilibrium state ${}^{N}\boldsymbol{G}$ exists at the same critical load level λ_{cr}.

$${}^{B}\boldsymbol{G}(\boldsymbol{u}_{cr},\lambda_{cr}) = 0 \quad \text{and} \quad {}^{N}\boldsymbol{G}\left({}^{N}\boldsymbol{u},\lambda_{cr}\right) = 0 \tag{3-2}$$

By performing a Taylor series expansion and linearization, the neighboring equilibrium state can be expressed by the status variables of the base state.

$${}^{N}\boldsymbol{G}\left({}^{N}\boldsymbol{u},\lambda_{cr}\right) = {}^{N}\boldsymbol{G}(\boldsymbol{u}_{cr}+\Delta\boldsymbol{u},\lambda_{cr}) = 0 \tag{3-3}$$

By defining $(\cdot)_{,\boldsymbol{u}} = \left.\frac{\partial(\cdot)}{\partial\boldsymbol{u}}\right|_{\boldsymbol{u}=\boldsymbol{u}_{cr}}$, the tangential stiffness matrix $\boldsymbol{K}_T$ can be isolated:

$$\begin{aligned} {}^{N}\boldsymbol{G}(\boldsymbol{u}_{cr}+\Delta\boldsymbol{u},\lambda_{cr}) &= {}^{B}\boldsymbol{G}(\boldsymbol{u}_{cr},\lambda_{cr}) + \boldsymbol{G}(\boldsymbol{u}_{cr},\lambda_{cr})_{,\boldsymbol{u}}\,\Delta\boldsymbol{u} = 0 \\ &\rightarrow \boldsymbol{K}_T(\boldsymbol{u}_{cr},\lambda_{cr})\,\Delta\boldsymbol{u} = 0 \end{aligned} \tag{3-4}$$

To obtain a nontrivial solution, the determinant of the stiffness matrix has to be zero. From a physical point of view, this can be interpreted as the system being able to switch to the neighboring equilibrium state without requiring additional energy [90]. Thus, the indifference criterion or buckling condition is:

$$\det \boldsymbol{K}_T = 0 \tag{3-5}$$

From (3-4) it follows that the stiffness matrix $\boldsymbol{K}_T$ is singular and not positive definite. This is the case in the direction $\boldsymbol{\phi}$, which is the so called eigenmode or buckling mode:

$$\boldsymbol{K}_T\,\boldsymbol{\phi} = 0 \tag{3-6}$$

The singularity of $\boldsymbol{K}_T$ at the singular point applies to all kinds of instability points. By varying equation (3-1) in load and displacement and multiplying by $\boldsymbol{\phi}$, the criterion to differentiate between bifurcation points and limit points is derived:

$$\boldsymbol{\phi}^T\boldsymbol{P} = \begin{cases} = 0 & \rightarrow bifurcation\ point \\ \neq 0 & \rightarrow limit\ point \end{cases} \tag{3-7}$$

3.1.2 Linear buckling analysis

Apart from only indirectly assessing the stability state of the structure, the buckling load can directly be calculated by evaluating the indifference criterion (3-5) as a function of the load parameter λ. For this, the tangential stiffness matrix $\boldsymbol{K}_T$ is split up into its basic and deflection dependent parts.

$$\boldsymbol{K}_T = \boldsymbol{K}_L + \boldsymbol{K}_U(\boldsymbol{u}) + \boldsymbol{K}_\sigma(\boldsymbol{u}) \tag{3-8}$$

Here, $\boldsymbol{K}_L$ represents the initial stiffness matrix in unloaded state, $\boldsymbol{K}_U$ accounts for the change of the structural stiffness due to the change in geometry under loading and $\boldsymbol{K}_\sigma$ gives the influence of the internal stresses under loading.

When assuming that the deflection grows linearly with the load parameter λ, the indifference criterion (3-5) leads to an eigenvalue problem which includes the load factor λ:

$$\left[\boldsymbol{K}_L + \lambda\left(\boldsymbol{K}_U^l + \boldsymbol{K}_\sigma^l\right) + \lambda^2\left(\boldsymbol{K}_U^{nl} + \boldsymbol{K}_\sigma^{nl}\right)\right]\boldsymbol{\phi} = 0 \tag{3-9}$$

By dismissing terms of higher order which include the nonlinear parts of the stiffness matrix, the general eigenvalue problem is obtained:

$$[\boldsymbol{K}_L + \lambda(\boldsymbol{K}_U + \boldsymbol{K}_\sigma)]\,\boldsymbol{\phi} = 0 \tag{3-10}$$

By calculating the lowest eigenvalue and thus the critical load parameter λ_{cr}, the buckling load can be determined with the original load vector:

$$\boldsymbol{P}_{cr} = \lambda_{cr}\,\boldsymbol{P} \tag{3-11}$$

To appraise the buckling load of cylindrical and conical shells, in most cases the so called classical buckling analysis is applied. Here, a purely linear prebuckling behavior is assumed and thus the influence of nonlinear deformations is neglected:

$$[\boldsymbol{K}_L + \lambda\,\boldsymbol{K}_\sigma]\,\boldsymbol{\phi} = 0 \tag{3-12}$$

In doing so, it is possible to quickly and easily assess the buckling load of a given structure. However, this can lead to noticeable deviations from the actual buckling load. This is due to the fact that in the case of cylindrical and conical shells, nonlinear deformations have a significant influence on the prebuckling behavior and the buckling load levels.

3.1.3 Nonlinear buckling analysis

Apart from the general linear buckling analysis, in many cases more sophisticated procedures are applied, so called nonlinear buckling analyses. While different procedures to iteratively obtain the equilibrium state at a given nonlinear deflection state exist, they can also be coupled with accompanying linear analyses. In this way, the influence of traditional and non-traditional imperfections as well as the nonlinear prebuckling deformations can accurately and realistically be accounted for within a numerical framework.

3.1.3.1 Newton-Raphson method

The general equilibrium (3-1) is in most cases solved using an iterative nonlinear analysis. Here, the most common procedure is the Newton-Raphson method. The basic notion is to perform a Taylor series expansion and linearization of the general system of equations (3-1). Then, the solution can be found iteratively:

$$\boldsymbol{K}_T(\boldsymbol{u}_i)\,\Delta\boldsymbol{u}_{i+1} = -\boldsymbol{R}(\boldsymbol{u}_i, \bar{\lambda}) \tag{3-13}$$

Here, $\boldsymbol{R}(\boldsymbol{u}, \lambda) = \boldsymbol{I}(\boldsymbol{u}) - \lambda\,\boldsymbol{P}(\boldsymbol{u})$ is the residual vector which emerges in consequence of the linearization. Starting from an initial state, the deflections are then stepwise increased by $\boldsymbol{u}_{i+1} = \boldsymbol{u}_i + \Delta\boldsymbol{u}_{i+1}$ and the nonlinear stiffness matrices $\boldsymbol{K}_T(\boldsymbol{u}_i)$ calculated. By iteratively minimizing the residual $\boldsymbol{R}(\boldsymbol{u}_i, \bar{\lambda})$, the equilibrium state of the system can be approximated at each load step $\bar{\lambda}$ (compare Figure 3-3, left).

The Newton-Raphson method can be performed load driven as well as displacement driven which makes it suitable for a broad range of applications in structural mechanics.

3.1.3.2 Arc length methods

To properly depict the postbuckling snap-back behavior of cylindrical shells (compare Figure 3-1, d)), it would be necessary to perform displacement driven and at the same time load driven analyses. To realize this, arc length methods can be applied. Here, numerous approaches are available which all originate from the same basic idea.

In a first step, the load factor λ is no longer just a modifier for the vector of external forces but now introduced as an additional degree of freedom of the system. Therefore, the general equilibrium state (3-1) has to be extended by an additional constraint function $f(\boldsymbol{u}, \lambda) = 0$:

$$\begin{pmatrix} \boldsymbol{G}(\boldsymbol{u}, \lambda) \\ f(\boldsymbol{u}, \lambda) \end{pmatrix} = \boldsymbol{0} \tag{3-14}$$

Then, linearization gives:

$$\begin{bmatrix} \boldsymbol{K}_T & -\boldsymbol{P} \\ f_{,\boldsymbol{u}}^T & f_{,\lambda} \end{bmatrix}_i \begin{bmatrix} \Delta\boldsymbol{u} \\ \Delta\lambda \end{bmatrix}_{i+1} = -\begin{bmatrix} \boldsymbol{R} \\ f \end{bmatrix}_i \tag{3-15}$$

The displacement increments and load increments for the iteration are then determined to:

$$\begin{aligned} \Delta\boldsymbol{u}_{i+1} &= \Delta\boldsymbol{\lambda}_{i+1}\left(\boldsymbol{K}_{T_i}\right)^{-1}\boldsymbol{P} - \left(\boldsymbol{K}_{T_i}\right)^{-1}\boldsymbol{R}_i \\ \Delta\lambda_{i+1} &= -\frac{f_i - f_{,\boldsymbol{u}_i}^T\left(\boldsymbol{K}_{T_i}\right)^{-1}\boldsymbol{R}_i}{f_{,\lambda_i} + f_{,\boldsymbol{u}_i}^T\left(\boldsymbol{K}_{T_i}\right)^{-1}\boldsymbol{P}} \end{aligned} \tag{3-16}$$

The difference between all arc length methods is the choice of the constraint function f. The most wide-spread approach is the one proposed by RIKS [95]:

$$f = (\boldsymbol{u}_i - \overline{\boldsymbol{u}})^T(\boldsymbol{u}_{i+1} - \boldsymbol{u}_i) + (\lambda_i - \bar{\lambda})(\lambda_{i+1} - \lambda_i) \tag{3-17}$$

This linear constraint function represents the scalar product of the prediction vector and the correction vector. Together with $f(\boldsymbol{u},\lambda) = 0$ (compare (3-14)), it implies that the correction vector is perpendicular to the prediction step (compare Figure 3-3, right).

The big advantages of arc length methods lie in their ability to cover snap-through as well as snap-back problems. However, the computational effort is much higher as the band structure of the stiffness matrix is lost when introducing the constraint function (compare equation (3-1)). Furthermore, when simulating pure bifurcation problems (like for example a perfect cylindrical shell) difficulties can arise to properly hit the correct secondary path.

Aside from these drawbacks, in this thesis the influence of geometric imperfections on the prebuckling behavior and most importantly the buckling load is investigated upon. For this, a precise calculation of the snap-back behavior in the postbuckling regime is not necessary. Therefore, all nonlinear simulations presented in this thesis were performed using the Newton-Raphson method.

Figure 3-3 graphically gives the general ideas of the classical Newton-Raphson method and the arc length method with RIKS constraint.

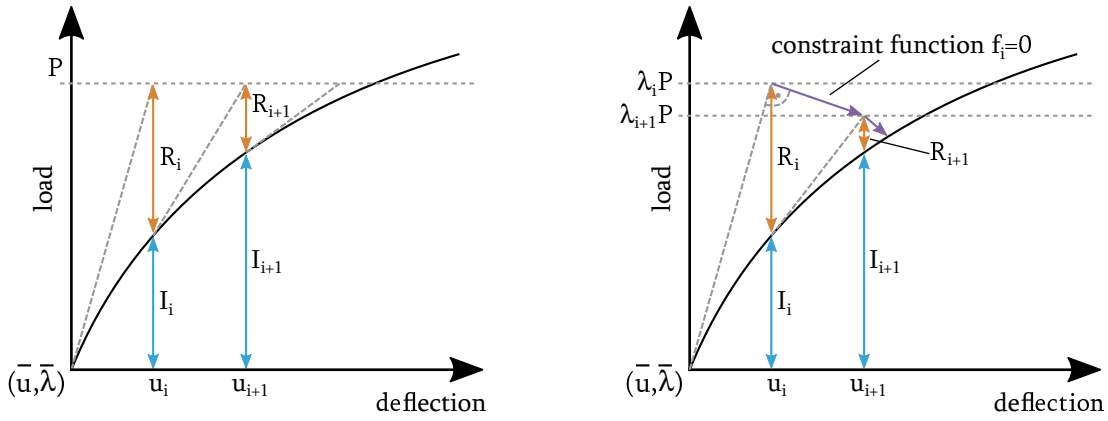

Figure 3-3: Schematic overview of Newton-Raphson method (left) and arc length method with Riks constraint (right), compare [94]

3.1.3.3 Accompanying eigenvalue analysis

Independent from the choice of the numerical procedure to solve the nonlinear equilibrium, the tangential stiffness matrix has to be calculated in every load increment. Thus, without any further numerical costs, the indifference criterion (3-5) can be evaluated. This is due to the fact that the LDU decomposition of the tangential stiffness matrix $\boldsymbol{K}_T = \boldsymbol{L}^T \boldsymbol{D} \boldsymbol{L}$ leads to a simplification of the indifference criterion:

$$\det \boldsymbol{K}_T = \prod D_{ii} \tag{3-18}$$

Now, only by evaluating the diagonal elements D_{ii} of the tangential stiffness matrix, conclusions about the current equilibrium state can be drawn. If all diagonal elements D_{ii} are positive, also $\det \boldsymbol{K}_T > 0$ and $\boldsymbol{K}_T$ is positive definite and thus the equilibrium state is stable. If one diagonal element becomes equal to zero, the indifference criterion is fulfilled and thus an instability point is found with the equilibrium being indifferent. Finally, in the case of at least one negative diagonal element, $\det \boldsymbol{K}_T < 0$ and the equilibrium is unstable.

In this way, the equilibrium state itself can be monitored during the simulation. However, if an indifference point is detected, no information about the type of this point is obtained. To do so, by using the byproducts of the nonlinear analysis $\boldsymbol{K}_U$ and $\boldsymbol{K}_\sigma$, the linear eigenvalue problem (3-10) can be solved to determine the eigenvectors and eigenvalues at the current load step.

Using (3-7), the eigenvectors help in determining whether a bifurcation point or a limit point is present.

By inspecting the eigenvalues during the nonlinear simulation, the instability points can not only be indirectly detected (as shown above) but can also actively be anticipated during the course of the incremental loading. When the lowest eigenvalue (and load factor) λ_{cr} decreases during loading and finally approaches zero, the indifference criterion is fulfilled. This procedure is commonly referred to as an accompanying eigenvalue analysis and provides a valuable tool to make sure that no singular points are missed.

3.1.3.4 On the relevance of dynamic effects

Buckling of a cylindrical or conical shell in general is a highly geometrically nonlinear and highly dynamic process. Firstly, the nonlinear deflections the shell structure undergoes during loading have a high influence on the deflection state and load level at the limit point, where loss of stability occurs. After reaching the limit point and after the onset of buckling is initiated, dynamic load redistributions occurring at very high speeds define the deformations the shell undergoes on its way to a stable postbuckling pattern.

All investigations and methods applied in this thesis are centered around identifying and predicting the crucial influence of prescribed perturbances of the shell surface on its initial loss of stability. While these imperfections do have a crucial geometrically nonlinear effect on the buckling load level, the dynamic effects play a subordinate role. Thus, in this thesis, geometrically nonlinear quasi-static analyses are performed, neglecting the influence of dynamic effects (for details on simulation parameters confer chapter 6.1.2). However, if the postbuckling behavior or the in-situ behavior of the shells is in the center of investigations, analysis methods have to be adjusted to properly capture dynamic load redistributions in the postbuckling regime.

3.2 Universal characteristics of the nonlinear buckling process

Before being able to investigate on the influence of particular geometric imperfections shapes on the structural response under failure load, the general effects and phenomena witnessed in a cylindrical or conical shell under axial loading have to be discussed. Thus, in the following, a detailed overview on the general characteristics of the loading phase of a shell is given.

Figure 3-4 again schematically depicts the buckling curve of an imperfect shell. Additionally, information on the different characteristic phases of buckling is given.

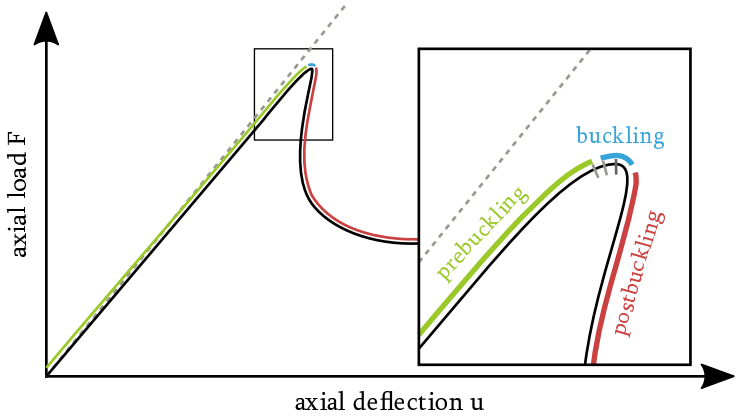

Figure 3-4: Schematic load deflection curve of an imperfect cylindrical shell: prebuckling, buckling and postbuckling phases

As the distinction of these phases varies heavily within the scientific community (depending on the subject of investigations), they are redefined as follows. The prebuckling phase spans from early loading until the second last calculation increment before the limit point is reached. In the last calculation increment before the limit point, a single initial dimple starts to snap-in, marking the beginning of the buckling phase. Once the initial dimple reaches a certain amplitude, subsequent dimples snap in, initiating the postbuckling phase.

During these three phases, characteristic radial deflection fields of the shell surface can be isolated and identified. These main deflections patterns are noticed in shells of any geometry and material in experiments and numerical analyses:

a) the global nonlinear prebuckling deformations,
b) the local nonlinear prebuckling deformations,
c) the snap-in of a local initial dimple which initiates the sudden loss of stability and
d) the subsequent postbuckling dimples propagating around the shell's circumference

For reasons of cross reference in chapters 3.2.1 to 3.2.4, Figure 3-5 again gives a schematic load deflection curve of an imperfect cylindrical shell. The regions in which the aforementioned characteristic radial deflection patterns occur are marked in colors.

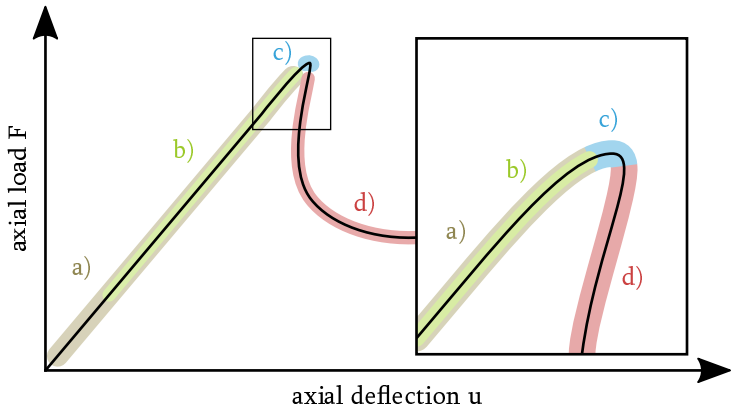

Figure 3-5: Schematic load deflection curve of an imperfect cylindrical shell: area of appearance of a) global nonlinear prebuckling deformations, b) local nonlinear prebuckling deformations, c) snap-in of initial dimple, d) postbuckling deformations

All cylindrical and conical shell surfaces shown in this thesis are depicted in their unwrapped state to simplify visual evaluation of the imperfection patterns, deflection fields and stress states. Figure 3-6 schematically gives the transformation from original to unwrapped surface.

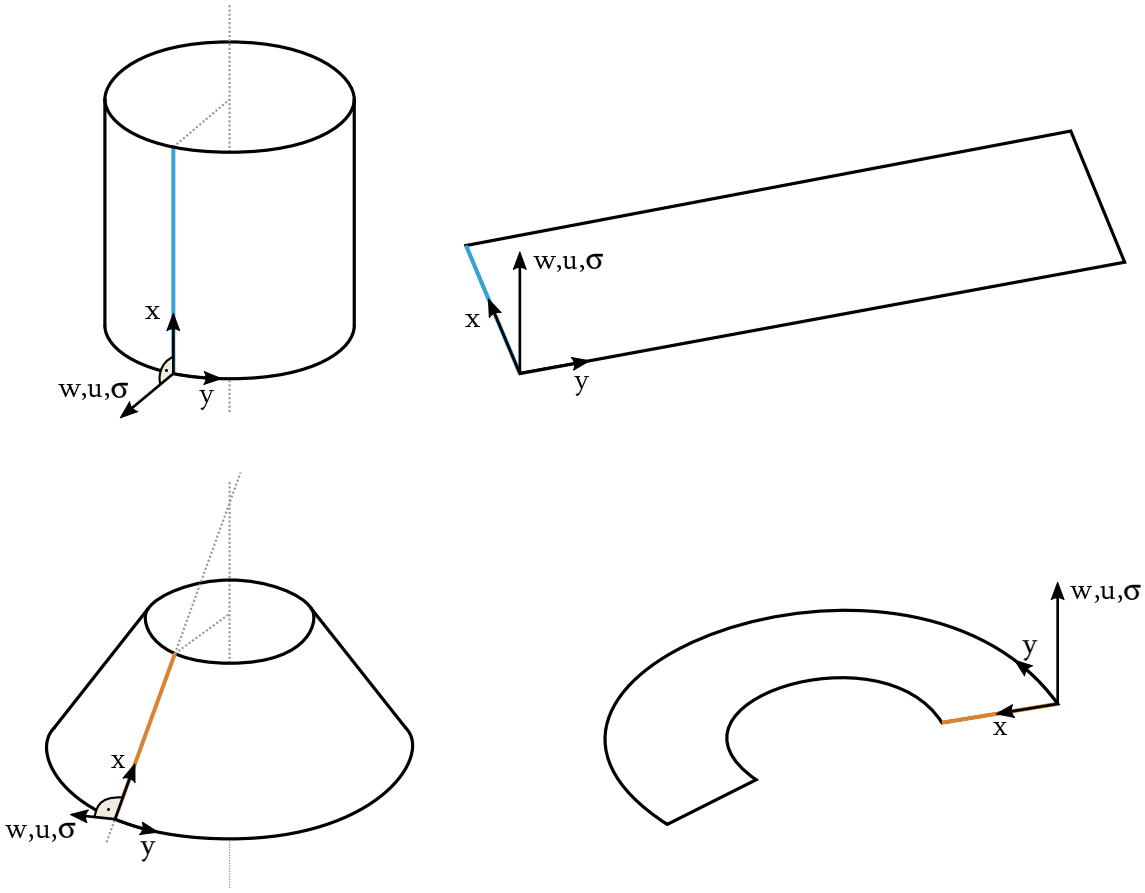

Figure 3-6: Schematic transformation from three dimensional cylinder and cone to unwrapped shell surfaces

3.2.1 Global nonlinear prebuckling deformations

The global nonlinear prebuckling deformations, often colloquially referred to as the elephant's foot, can best be depicted at the example of a cylindrical shell with an ideal, so-called perfect surface. Figure 3-7 exemplarily shows the calculated radial deflection state of a composite shell with perfect surface, at an axial load level below limit load (compare Figure 3-5, a)). The nominal shell properties correspond to a specimen labeled "Z25" which was produced and tested by Deutsches Zentrum für Luft und Raumfahrt (DLR), Braunschweig. However, the specific design parameters of the shell do not qualitatively impact the general results shown herein. Therefore, for reasons of clarity and to prevent distraction of focus from the basic phenomena, details on the shell's length, radii and laminate stacking sequences are given no earlier than chapter 6.1.1.

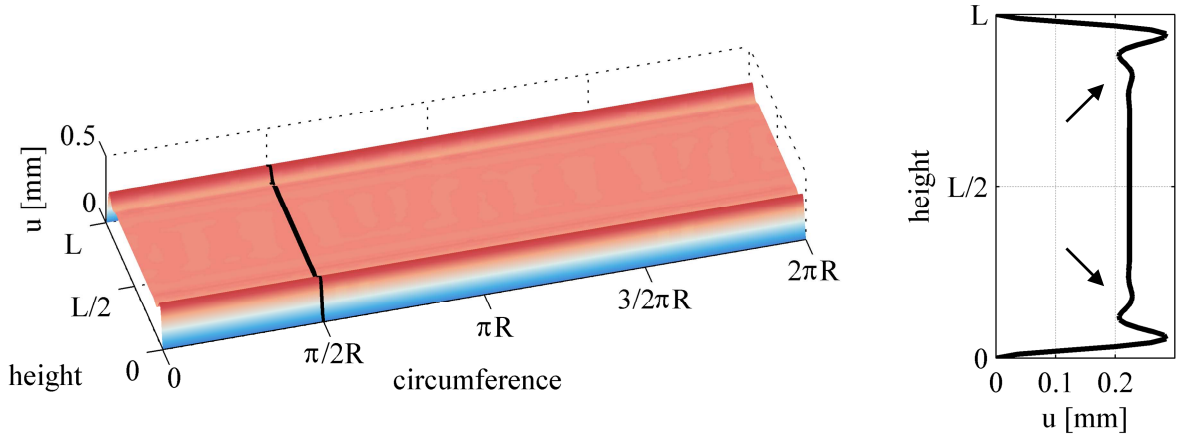

Figure 3-7: Global nonlinear radial deformations of shell Z25 with perfect shell geometry (left) and axial cut (right), indicated by black line

When looking at the cut surface on the right of Figure 3-7, the distinct deformations at the shell's upper and lower edge are noticed. After a maximum at around 5% of the shell's height, these oscillations quickly decay when approaching the center line.

These characteristic deformations can be traced back to the restrained widening of the shell. To mimic the boundary conditions of real shells in aerospace applications, in most laboratory experiments, shell specimen are clamped at their upper and lower edges to prevent any radial and bending deformations. In order to be able to validate numerical procedures with these experiments, the shell's edges are frequently also assumed to be clamped in simulation. Under axial compression, the Poisson effect causes the cylinder to widen. As the radial deflections of the edges are restrained, a bending deformation occurs between the freely widening center and the restrained edges.

These global bending deformations impose a considerable distortion of the load vector around the shell's edges. Thus, especially for shells of comparatively short lengths, they can be of high significance for the limit point load level. In addition to that, if a locally critical imperfection shape happens to occur in the same area, both overlay and cause even more severe distortions of the load flow. This in turn leads to a snap-in of the initial dimple near the shell's edge as opposed to the shell's center, which in other respects is generally more prone to bending deformations. In the case of conical shells, this effect is even more pronounced. Here, the axial compression of the

shell is not in line with its surface, causing a more significant bending of the shell's edge. This can lead to a reduction of sensitivity to geometric imperfections in general, as the detrimental effect of the deformations near the edge may outweigh the detrimental effects of geometric imperfections in the shell's center.

3.2.2 Local nonlinear prebuckling deformations

Apart from the global deformations, also more localized deflections occur during the loading process. These local nonlinear deformations are primarily noticed in the case of shells with imperfect surfaces. Figure 3-8 exemplarily shows the calculated prebuckling deflection state of shell Z25 with the corresponding measured imperfection pattern, at an axial load level below the limit load (compare Figure 3-5, b)).

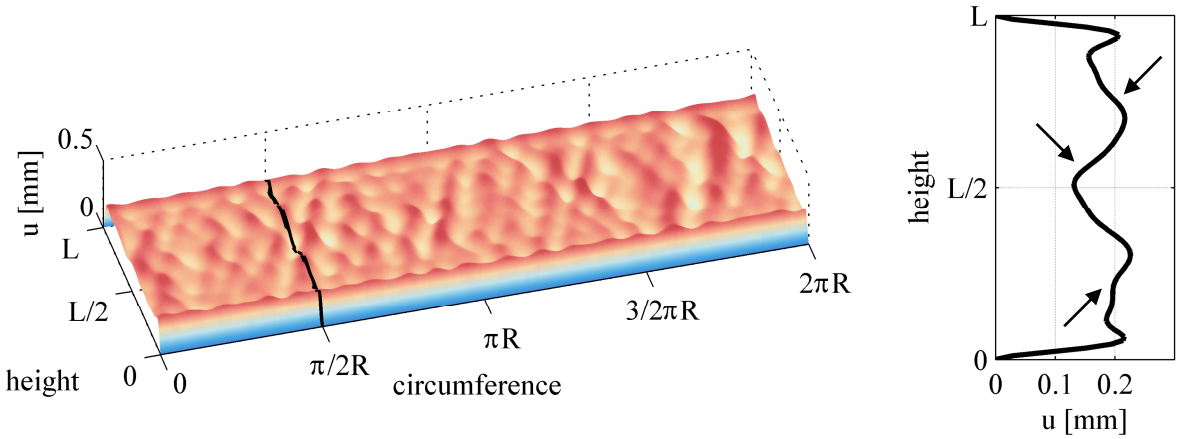

Figure 3-8: Local nonlinear radial deformations of shell Z25 with imperfect shell geometry (left) and axial cut (right), indicated by black line

Again, the previously described heavy global oscillations at the shell's edges are noticed (compare Figure 3-7 and Figure 3-8).

However, in addition to that, localized deformations are clearly visible. Caused by the axial loading, local surface irregularities are pronounced. Imperfection dimples which are directed outside of the nominal shell surface are pushed further outside while inward dimples are pushed inward. Accordingly, these deformations increase in magnitude when increasing the axial loading of the shell.

If the shell is made of anisotropic material, as it is the case in this thesis, this effect shows to be more intricate. For composite shells, the prebuckling deformations heavily depend on the laminate stacking sequence. As GEIER et al. [32] show, the allocation of axially stiff layers to the inside of the cylinder leads to dampened local nonlinear deformations. In turn, the allocation of axially stiff layers to the outside of the cylinder amplifies the effect described above.

As they heavily depend on the laminate setup, the local nonlinear prebuckling deformations do not simply represent a uniform amplification of the underlying imperfection pattern. They can rather be interpreted as an evolving pattern which represents the transition from an underlying imperfection field in the unloaded state to the critical deflection state which initiates buckling.

This can also be made clear by considering shells with an assumed perfect surface. In the course of the simulation, these shells do not show any of the local nonlinear deformations until very close to the limit load but still show a distinct initial dimple triggering the loss of stability.

3.2.3 The beginning of the end: the initial dimple

As described above, the local nonlinear prebuckling deformations become more and more pronounced from early loading to the prebuckling regime. While this deformation field gradually evolves during loading, at a certain load level very close to the buckling load, at one position on the surface area of the shell, a sudden single deflection dimple snaps in. This abruptly occurring singularity of high magnitude will be referred to as the initial dimple in the following. Similarly, when it is referred to the initiation or the onset of buckling, the state of the snap-in of the initial dimple is meant.

Figure 3-9 shows two frames of the film by ESSLINGER, shot with high speed cameras and described in chapter 2 [21]. The depicted specimen ($t_E = 0.25\,mm$, $R_E = 200\,mm$) was made from an isotropic plastic foil of dimensions roughly comparable to the composite shells treated within this thesis ($t_{Z25} = 0.5\,mm, R_{Z25} = 250\,mm$, compare chapter 6.1.1).

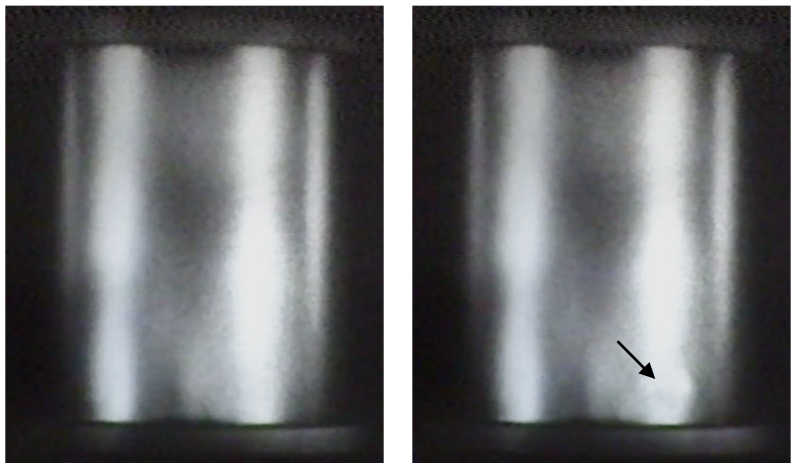

Figure 3-9: Snap-in of the initial dimple: high speed camera pictures by Esslinger [21] (enhanced in brightness and contrast), late prebuckling state (left) and initial dimple (right)

In the left frame, shot right before initiation of buckling at a very high load level, no radial deformations are apparent to the eye. When inspecting cylinders with modern visual inspection system, the global and local nonlinear prebuckling deformations discussed before can be made visible at this stage.

In the right frame, shot at an incrementally higher load level, the sudden snap-in of the initial dimple becomes visible near the lower edge of the cylinder (compare Figure 3-5, c)).

For better visual perceptibility, Figure 3-10 exemplarily shows the initial dimple occurring in the simulation of a composite shell with the according measured imperfection pattern. While shell Z25 is an unrelated shell specimen of different material and size than the one filmed by ESSLINGER, the general buckling characteristics still show to be very similar.

The circumferential position of the initial dimple is indicated with a black line. When viewed in axial direction, it is noticed that the initial dimple snaps in at the center of the shell. This is not

necessarily always the case but can be considered exemplary for the majority of shells investigated herein.

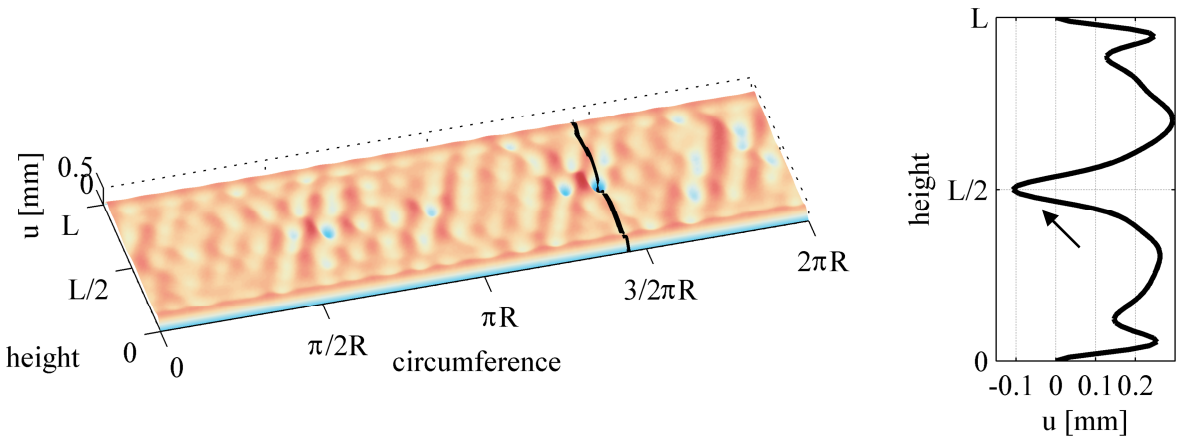

Figure 3-10: Buckling deformations at snap-in of the initial dimple of shell Z25 with imperfect shell geometry (left) and axial cut (right), indicated by black line

From a mechanical point of view, the initial dimple represents a severe local bending deformation which causes a drop in the local effective axial stiffness of the shell. Thus, the axial loads are redistributed around this critical area.

The example of shell Z25 is chosen in this context as in this shell, contrary to the majority of cases, not only one single distinct initial dimple forms. When looking at Figure 3-10 at a position of $y \approx 0.6\pi R$, a second local dimple of comparatively high amplitude is noticed. Throughout the late prebuckling phase, this second dimple matches closely the first one with regards to its size and amplitude. Bluntly speaking, both local prebuckling deformations compete to trigger the snap-in of the initial dimple. Eventually, right before buckling occurs, the prebuckling deformations at $y \approx 1.4\pi R$ show to be slightly more severe for the stability and thus the initial dimple snaps in at this position.

This ambiguous behavior is well suited to illustrate a fundamental finding when it comes to judging the influence of imperfections on the buckling state. It appears that in every imperfection pattern, certain local areas feature certain characteristics which are more detrimental to the load transfer than the characteristics of other local areas. In the case of the imperfection pattern of shell Z25, there seem to be two areas with characteristics of almost matching severity, explaining the competing local dimples. Eventually, the initial dimple snaps in at the position where the most detrimental characteristics are present.

However, what exactly these detrimental characteristics are is yet unknown. Therefore, by solely visually inspecting a given imperfection pattern, the position of the initial dimple and thus the failure state of the shell cannot be predicted. A discussion on possible candidates for the ominous characteristics mentioned above as well as a procedure to reveal the specific parts of an imperfection pattern which are essential for buckling is given in this thesis.

All in all it is concluded that the initial dimple is of great importance for investigating the buckling process of shells. It gives a hint to the specific location on the surface where the most detrimental imperfection characteristics are present.

3.2.4 Propagation of local failure: postbuckling deformations

As described above, the snap-in of the initial dimple leads to a sudden relocation of axial loads. However, the neighboring areas again can only bear a certain load level and subsequently fail by forming subsequent local dimples. This instable pattern of comparatively short waved dimples propagates around the shell's circumference (compare Figure 3-5, d)). Figure 3-11 depicts the high speed camera records of ESSLINGER on the left. The simulation results of shell Z25 for the corresponding buckling phase are depicted on the right.

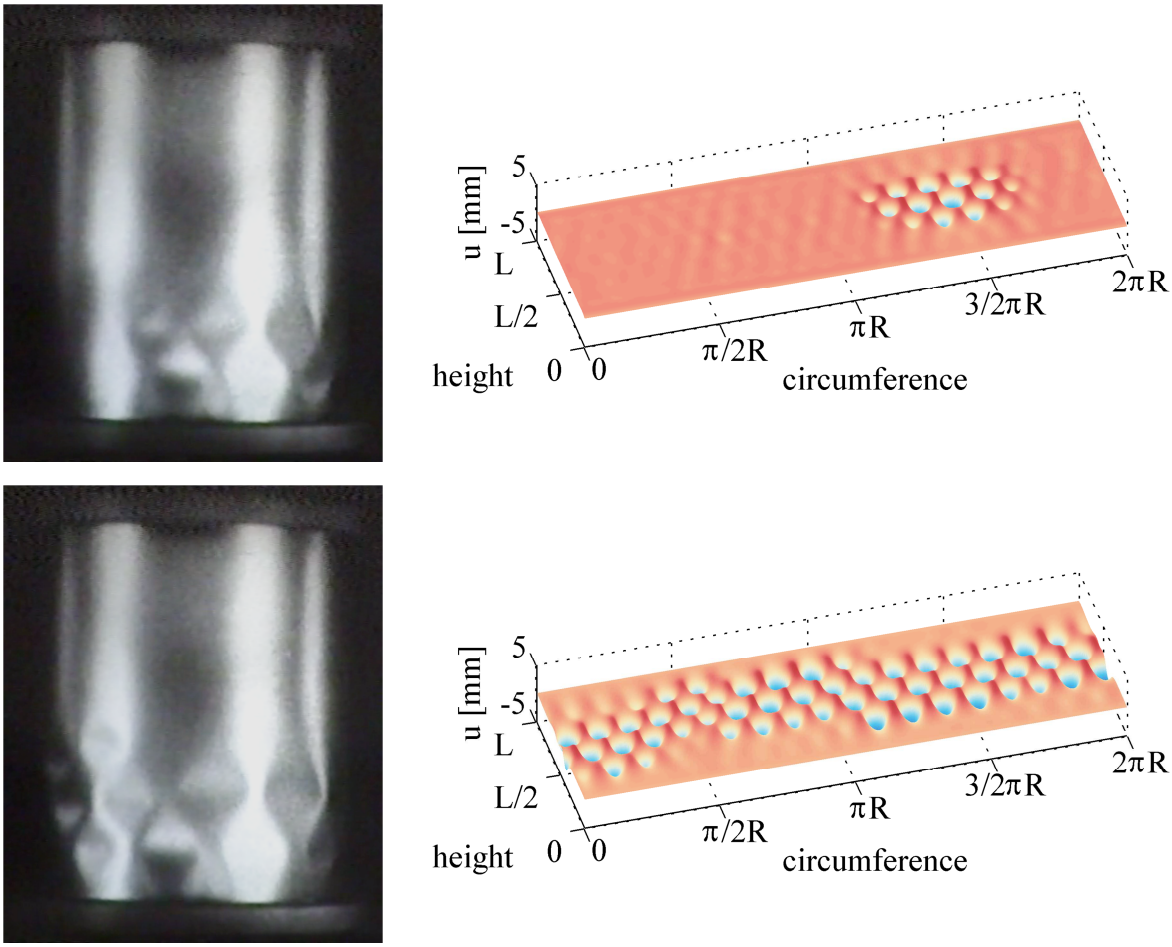

Figure 3-11: Postbuckling deformations: propagating pattern, high speed camera pictures by Esslinger [21] (enhanced in brightness and contrast) (left) and simulation of shell Z25 (right)

Due to the fact that the nonlinear quasi-static analysis neglects the strong dynamic part of the postbuckling behavior, these results have to be interpreted with special care (see chapter 3.1.3.4). While they can be used to better visualize the characteristic behavior, they are by no means usable for quantitative interpretation.

When further increasing the axial deflection, the short waved pattern of the instable early postbuckling phase transforms into a stable, uniform and long waved postbuckling pattern around the axial center of the shell.

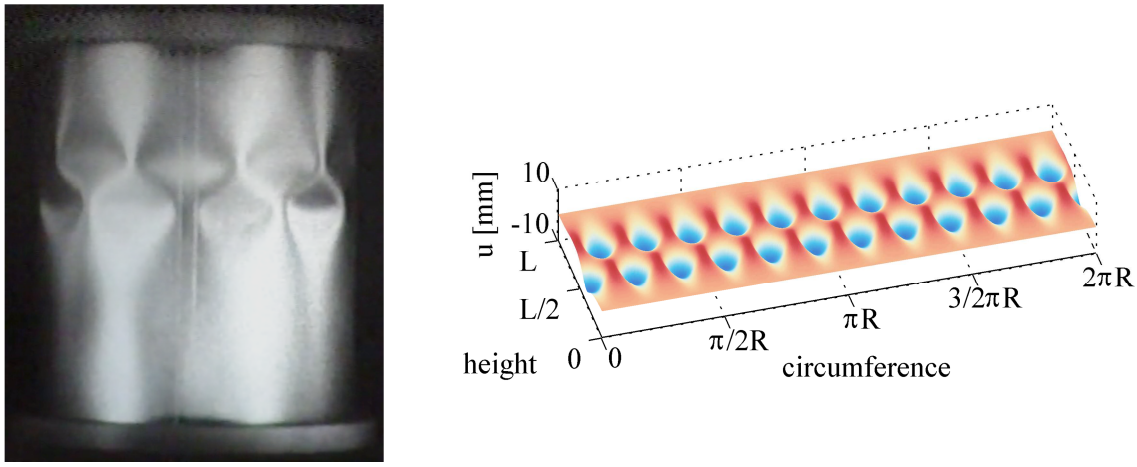

Figure 3-12: Postbuckling deformations: stable postbuckling pattern, high speed camera picture by Esslinger [21] (enhanced in brightness and contrast) (left) and simulation of shell Z25 (right)

It is interesting to emphasize that when witnessing a real buckling test, only the undisturbed surface depicted in Figure 3-9, left and immediately after that the stable postbuckling pattern depicted in Figure 3-12 are visible. As the unstable postbuckling region is traversed at such high speed, the various deformation states of the shell consequently can only be made visible by simulation or high speed capturing.

3.3 Single Perturbation Load Approach (SPLA)

3.3.1 Basic Scheme

Due to the fact that the Knock-Down-Factor design of the NASA-SP 8007 showed to be overly conservative in various cases and only partly applicable to composite shells, other deterministic design procedures for cylindrical shells were desired. As described in chapter 2.2.2, RICARDO [52] and OKUBO [53] where investigating the influence of lateral perturbations on the load carrying capacity of shells as early as the 1960s and 1970s. However, it was not until 2005 when HÜHNE [42] discovered the significant potential of lateral perturbations to help in finding lower bounds of buckling loads, which in turn could be used in the design phase of a cylindrical shell structure.

The basic idea of HÜHNE's approach is to numerically apply a lateral perturbation load in the middle of the perfect cylinder's height to deliberately trigger the stability failure of the shell. This lateral perturbation load is stepwise increased while monitoring the buckling load connected to every perturbation state. It is assumed that a lateral perturbation load of sufficiently high amplitude causes an imperfection dimple which critically stimulates the shell and thus leads to a lower bound of possible buckling loads.

Figure 3-13 gives a general scheme of the SPLA. In the regime of comparatively low perturbation loads, the imperfection dimple depth as a negligible influence on the buckling load. From a certain perturbation load level on, the buckling load steadily decreases with an increasing level of the perturbation load. From a certain perturbation load level P_1 on, the buckling load does not decrease any further.

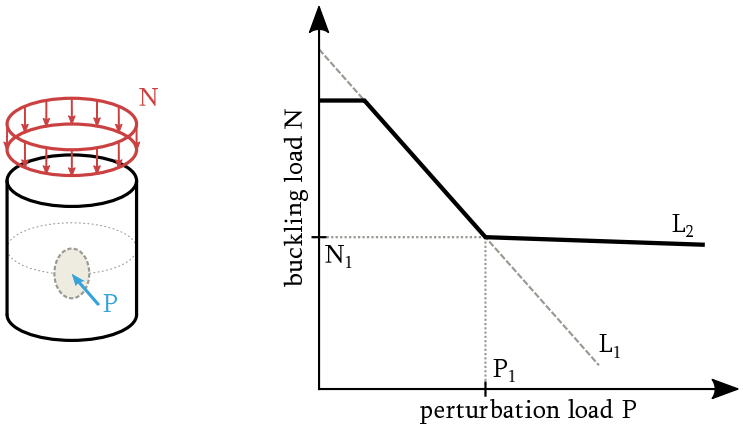

Figure 3-13: The Single Perturbation Load Approach; Schematic overview of the idealized numerical model (left) and buckling load over the applied perturbation load P (right)

This distinct behavior of a lower bound of buckling loads is then utilized to derive a design criterion. It is assumed that the buckling load level N_1 corresponds to a general lower bound of buckling loads, which will be exceeded by the buckling loads caused by any real life imperfection patterns.

The main advantages of the SPLA as a method for buckling load prediction lie in its simplicity and, most importantly, in its independency from detailed knowledge about geometric imperfection. This major hitch of numerous other approaches is caused by the very high costs for high-fidelity geometric imperfection measurements.

3.3.2 Understanding the constancy of the buckling load after P_1

Before establishing the SPLA as a procedure for the design of shells, the distinct constancy of the buckling load has to be investigated well understood. Various authors like HÜHNE et al. [57] or CASTRO et al. [63] contributed to a better understanding of the detailed effects.

The reason for the constancy in buckling load of the SPLA after P_1 can be explained in three steps:

1. $P < P_1$: The perturbation load causes a bending deflection of the cylinder wall which acts like a geometric imperfection. Increasing the perturbation load increases the depth of the single imperfection dimple and therefore causes an increasing need for load distribution around the perturbation position. This increasing weakening of the cylinder at the perturbation position leads to decreasing buckling loads.

   When looking at the load-displacement curve, two peaks are noticed. The first one is connected to the local snap-through of the cylinder wall due to the lateral perturbation (grey area) load and the subsequent drop in axial load carrying capacity. The second peak indicates the classical stability failure of the shell, where the initial local deflection spreads around the shell's circumference, causing global failure. Increasing the perturbation load leads to a decrease of the first peak's load level, while the second peak, leading to global failure, remains unaffected.

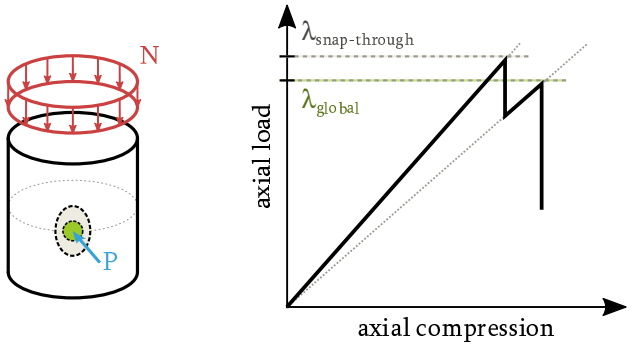

Figure 3-14: SPLA: shematic shell surface (left) with local snap-through (gray area) and initial dimple (green area) and load-deflection-curve (right) with snap-through load level and global buckling load level

2. $P = P_1$: From a specific perturbation load level on, the single imperfection dimple enforces a level of load distribution which is comparable to a factual cut-out in the shell's surface. Therefore, the initial dimple triggering stability failure can no longer occur at the position of the perturbation dimple, but at the stress peaks which neighbor the perturbation area.

   Investigating the load-displacement curve, it is noticed that both the local snap-through peak and the global failure peak occur at the very same load level.

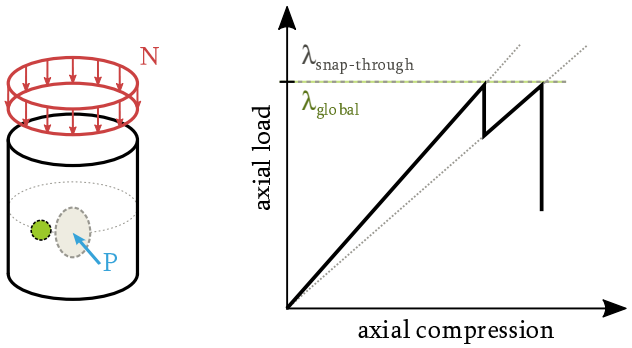

Figure 3-15: SPLA: shematic shell surface (left) with local snap-through (gray area) and initial dimple (green area) and load-deflection-curve (right) with snap-through load level and global buckling load level

3. $P > P_1$: A further increase in perturbation load only marginally increases the areal size of the imperfection dimple. In turn, the stress state around the factual cut-out remains unchanged and thus the position of the initial dimple causing local failure is hardly affected. This in turn causes the observed constancy of the buckling load.

   The load-displacement curve shows that for increasing perturbation loads the snap-through at the respective position occurs at lower axial load levels. Equivalent to the behavior of the initial dimple causing stability failure, the load level of the second peak is not influenced by the perturbation load level and local snap-through. Therefore, the global buckling load remains unchanged when further increasing perturbation loads.

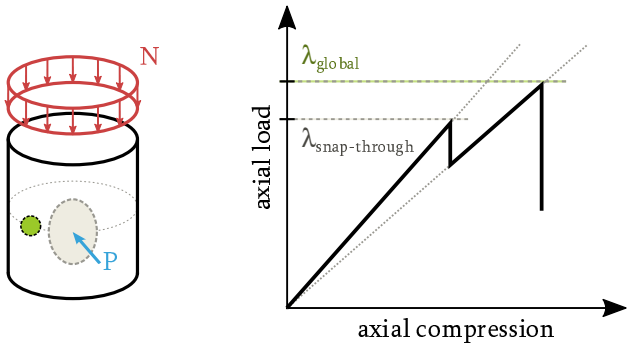

Figure 3-16: SPLA: shematic shell surface (left) with local snap-through (gray area) and initial dimple (green area) and load-deflection-curve (right) with snap-through load level and global buckling load level

3.3.3 Enhancing the numerical efficiency of the SPLA

While being a comparatively lightweight procedure on its own, still numerous nonlinear finite element calculations are needed to reliably depict the lower bound regime to obtain N_1. Therefore, many researchers tried to enhance the numerical efficiency of the SPLA.

CASTRO et al. [63] hinted at deriving a semi-analytical method which is based on evaluating the axial deflections corresponding to the prebuckling and global buckling states. WANG et al. [58] and STEINMÜLLER et al. [59] succeeded to derive empirical formulas to directly estimate the critical perturbation load level P_1. For composite shells however, no equivalent formula is published. It seems highly questionable whether a purely empirical formula for P_1 can accurately and universally predict the corresponding perturbation load level obtained from nonlinear finite element simulations. While a precise semi-analytical prediction of P_1 seems unfeasible, such formula could still serve as a first guess to evaluate the necessary perturbation load levels for highly nonlinear composite shells.

Once this analytical formula to roughly estimate P_1 is established, the SPLA could be enhanced in the following way. Based on initial remarks made by CASTRO et al. [63], the number of required calculations could be significantly reduced as follows:

1. When extrapolating the diagonal line defined by the prebuckling state L_1, the load level corresponding to a perturbation load of $P = 0$ can be obtained by a basic linear buckling analysis. (compare Figure 3-13, L_1)
    - $\lambda_{lin,perf,P=0}$
2. The approximate perturbation load level P_1 has to be established. This can be achieved by utilizing the future estimation formula mentioned above.
    - P_{est}
3. A single nonlinear buckling calculation is performed with a perturbation load P notably above the estimation P_{est} obtained before. The load level of the observed snap-through is used to define the prebuckling line L_1 of the SPLA-diagram. The load level of the observed global buckling serves as the first point of the lower bound line L_2.
    - $\lambda_{nonlin,P=1.2*P_{est,snap-through}}$
    - $\lambda_{nonlin,P=1.2*P_{est,global\ buckling}}$
4. A second nonlinear buckling calculation is performed with a perturbation load P signifac-ntly higher than the estimation P_{est} obtained before. The load level of the observed global buckling serves as the second point of the lower bound line L_2.
    - $\lambda_{nonlin,P=2.0*Pest,global\ buckling}$
5. By geometrical determination of the intersection of the lines L_1 and L_2, the design load N_1 is obtained.

To illustrate the procedure, the SPLA is exemplarily applied to shell Z15 (for design parameters see chapter 6.1.1). When performing the SPLA in the classical way, numerous nonlinear finite element calculations are necessary to precisely determine the load level N_1 (compare Figure 3-17, left).

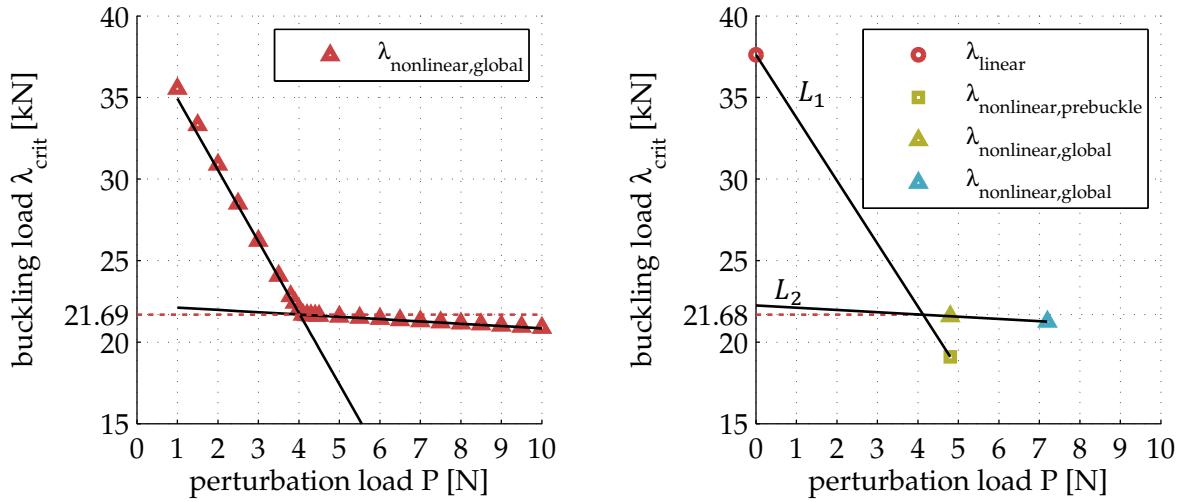

Figure 3-17: Single Perturbation Load Approach applied to shell Z15; classical scheme (left) and enhanced scheme (right)

Figure 3-17, right shows the derivation of N_1 with the enhanced scheme, described above. Thus, once an estimation formula for P_1 is available, the computational costs of the SPLA can be significantly reduced to:

- one analytical formula evaluation
- one linear buckling analysis
- two non-linear buckling analyses

3.3.4 The SPLA as a design procedure

After the introduction of the SPLA by HÜHNE, numerous researchers contributed to the understanding and exploitation of this promising approach. The main findings for detailed definition of the SPLA's methodology are the following:

1. The general lower bound behavior is detected for cylindrical [57] as well as conical [96] shells of isotropic [97] and composite [63] material.
2. The lateral perturbation load should be applied in the middle of the shell's length to reliable cause the distinct lower bound behavior [61] and obtain the lowest N_1 [98].
3. The angle of the lateral perturbation load has negligible influence on N_1 [61].
4. The application of not only one but multiple perturbation loads leads to a lowering of the lower bound load line L_2, branching from the same L_1 path [60].

Besides these comparatively detailed investigations on the specific features of the SPLA as a design procedure, its general robustness is heavily discussed within the scientific community. Thus, different authors argue whether the load level N_1 may be suitable as a final design load for the cylindrical shell [57], whether it may robustly account only for the influence of solely geometric imperfections on the buckling load [64], [99] or whether the displacement-driven SPLA may not be applicable at all [100].

By performing nonlinear buckling simulations using the shell data, material parameters and software specifications given in chapter 6.1, the buckling load and design load values given in Table 3-1 are obtained.

buckling loads [kN]	Z07-Z08	Z09	Z10-Z11	Z12	Z15-Z26	Z36-Z37
experiment *(minimum of corresp. set)*	21.8	15.7	15.7	18.6	21.3	58.3
measured geometric imperfections *(minimum of corresp. set)*	28.0	17.6	20.1	23.1	29.6	76.3
SPLA (N_1)	19.3	15.8	15.3	21.8	21.7	65.6

Table 3-1: SPLA results for different cylindrical shell configurations, experimental buckling loads given as minimum of the specific configuration set, experimental buckling load values taken from [42], [85] and [101]

The results compare well with the results obtained by other authors investigating the same sets of shells [99]. The minor deviations from the corresponding values given in [102] are ascribed to the slightly finer resolved FE-mesh employed for all calculations within this thesis to achieve consistency with the results presented in chapter 6.

It is noticed that in case of shells Z09, Z10-Z11 and Z15-Z26, the SPLA's design load N_1 is remarkably close or even higher than the experimentally obtained buckling loads of the respective cylinder sets. When comparing the different N_1 to the buckling loads with solely measured geometric imperfections included in the numerical analyses, it is noticed that in all investigated cases the SPLA leads to load carrying capacities which are lower than the ones of solely geometric imperfections.

Therefore, it is concluded that the SPLA is not suitable as a design procedure on its own, covering all types of anticipated imperfections. However, in all investigated cases, the application of a perturbation load larger than P_1 causes a deviation from the perfect shell's surface significant enough to robustly account for the influence of geometric imperfections on the buckling load.

It is important to note that this does not in any way mean that the SPLA-dimple was the worst geometric imperfection (compare chapter 4.4.2).

To avoid confusion of terms in the following, the load level N_1 obtained by performing the SPLA will not be referred to as a design load (as practice in literature) but rather as a so-called lower bound load.

3.4 Semi-analytical, probabilistic method (SAP)

3.4.1 From deterministic to probabilistic design

Most deterministic design methods, like the Knock-Down-Factor design or the SPLA described above, share a significant disadvantage. By applying these methods, design loads are obtained which may be declared robust if they show to be always lower than the experimentally obtained buckling loads of the respective shell setups. However, the actual level of safety of these designs is not known and thus possible overly-conservativeness cannot be excluded.

When applying probabilistic approaches like the Monte-Carlo method or more sophisticated semi-analytical approaches, the actual level of safety of the obtained load levels is not only known but chosen by the designer.

This opens various ways of design scheme alteration with respect to the various conditions of each specific structure. Thus, a component which is not crucial for the structural collapse of a whole assembly may be attributed with a lower level of safety than a component which is critical for an assembly's load carrying capacity.

On the flip side, probabilistic procedures usually come with very high numerical costs. For example, when using the Monte-Carlo simulation to obtain a design load for a given shell specimen, hundreds of non-linear buckling simulations are needed to achieve convergence of a chosen level of reliability (compare KRIEGESMANN, 2012 [89]).

The second catch of probabilistic approaches compared to deterministic procedures is their dependence on knowledge of the scatter of input parameters. While for deterministic procedures input parameters such as Young's moduli or thicknesses obviously affect the design load levels, the real life scatter of those parameters is not needed, as it is accounted for in the approaches basic justification of generally delivering robust design loads. In contrast to that, the advantage of known levels of reliability of probabilistic approaches itself is fueled by the imperatively required knowledge of the expectable scatter of input parameters.

The semi-analytical probabilistic procedure described below address both drawbacks raised above. While requiring very low numbers of simulations, the mean value and standard deviation of the scattering input parameters still have to be known. However, information about the type of distribution of those input parameters is not needed. In the case of for example scattering material properties, the type of distribution is obtained from experimental data, due to a large number of samples. In the case of geometric imperfections, distributions of input parameters are much harder and costlier to obtain.

3.4.2 Approximation of the objective function by a quadratic Tailor series

The general idea of the semi-analytical probabilistic procedure (SAP) is to approximate the objective function by a quadratic Taylor series at the mean values of input parameters:

$$g(\boldsymbol{x}) = g(\boldsymbol{\mu}) + \sum_{i=1}^{n} \frac{\partial g(\boldsymbol{\mu})}{\partial x_i}(x_i - \mu_i) + \frac{1}{2}\sum_{i=1}^{n}\sum_{j=1}^{n} \frac{\partial^2 g(\boldsymbol{\mu})}{\partial x_i \partial x_j}(x_i - \mu_i)(x_j - \mu_j) + \ldots \tag{3-19}$$

In the case of calculating buckling loads for cylindrical shells, the objective function $g(\boldsymbol{x})$ is the buckling load $\lambda(\boldsymbol{x})$ depending on the scatter of n input parameters $\boldsymbol{x}$, like for example Young's moduli or wall thicknesses. In the following, the random vector of input parameters is denoted as $\boldsymbol{X}$, while it's realizations are denoted as $\boldsymbol{x}$. The mean vector of the input parameters is expressed as $\boldsymbol{\mu}$.

3.4.2.1 Estimation of the stochastic moments of the objective function

The mean value μ_g of the objective function is obtained by neglecting the higher order terms of the objective function and inserting (3-19) into the standard mean value estimator:

$$\mu_g = E\big(g(\boldsymbol{X})\big) = \int_{-\infty}^{\infty} g(\boldsymbol{x}) f_{\boldsymbol{X}}(\boldsymbol{x})\, d\boldsymbol{x} \approx g(\boldsymbol{\mu}) + \frac{1}{2}\sum_{i=1}^{n}\sum_{j=1}^{n}\frac{\partial^2 g(\boldsymbol{\mu})}{\partial x_i \partial x_j} cov\big(X_i, X_j\big) \tag{3-20}$$

Here, $f_{\boldsymbol{X}}(\boldsymbol{x})$ is the probability density function of the input parameters $\boldsymbol{x}$. One of the major advantages of the SAP is that $f_{\boldsymbol{X}}(\boldsymbol{x})$ does not have to be known analytically, as the stochastic moments of input parameters can be estimated from measurements.

When assuming independence of the input parameters, the covariance of two given input parameters equals zero. Then, (3-20) simplifies to

$$\mu_g \approx g(\boldsymbol{\mu}) + \frac{1}{2}\sum_{i=1}^{n}\frac{\partial^2 g(\boldsymbol{\mu})}{\partial z_i^2} var(Z_i) \tag{3-21}$$

where $\boldsymbol{z}$ are the uncorrelated input parameters. If the input parameters are correlated, the transformation given in chapter 3.4.3 can be used to obtain the uncorrelated parameters $\boldsymbol{z}$.

The variance and skewness of the objective function σ_g^2 and ν_g, respectively, can be determined equivalently:

$$\begin{aligned}
\sigma_g^2 = \mu_{g,2} \quad &= \quad E\left(\left[g(\boldsymbol{X}) - \mu_g\right]^2\right) = \int_{-\infty}^{\infty}\big(g(\boldsymbol{z}) - \mu_g\big)^2 f_{\boldsymbol{Z}}(\boldsymbol{z}) d\boldsymbol{z} \\
\textit{(FOSM)} \quad &\approx \quad \sum_{i=1}^{n}\left[\frac{\partial g(\boldsymbol{\mu})}{\partial z_i}\right]^2 \mu_{i,2} \\
\textit{(SOTM)} \quad &\quad + g^2(\boldsymbol{\mu}) - \mu_g^2 + g(\boldsymbol{\mu})\sum_{i=1}^{n}\frac{\partial g^2(\boldsymbol{\mu})}{\partial z_i^2}\mu_{i,2} + \sum_{i=1}^{n}\frac{\partial g(\boldsymbol{\mu})}{\partial z_i}\frac{\partial g^2(\boldsymbol{\mu})}{\partial z_i^2}\mu_{i,3} \\
\textit{(ISOA)} \quad &\quad + \frac{1}{4}\sum_{i=1}^{n}\left[\frac{\partial g^2(\boldsymbol{\mu})}{\partial z_i^2}\right]^2 \mu_{i,4} + \frac{1}{2}\sum_{i=1}^{n}\sum_{j=i+1}^{n}\frac{\partial g^2(\boldsymbol{\mu})}{\partial z_i^2}\frac{\partial g^2(\boldsymbol{\mu})}{\partial z_j^2}\mu_{i,2}\mu_{j,2} \\
\textit{(FULL)} \quad &\quad + \sum_{i=1}^{n}\sum_{j=i+1}^{n}\left[\frac{\partial g^2(\boldsymbol{\mu})}{\partial z_i \partial z_j}\right]^2 \mu_{i,2}\mu_{j,2}
\end{aligned} \tag{3-22}$$

and

$$\nu_g = \frac{\mu_{g,3}}{\sigma_g^3} = E\left(\left[g(\boldsymbol{X}) - \mu_g\right]^3\right)/\sigma_g^3 = \int_{-\infty}^{\infty}\big(g(\boldsymbol{z}) - \mu_g\big)^3 f_{\boldsymbol{Z}}(\boldsymbol{z}) d\boldsymbol{z}\,/\sigma_g^3 = \ldots \tag{3-23}$$

For more details on the mathematical background of the semi-analytical probabilistic procedure, the reader should refer to KRIEGESMANN, 2012 [89].

As the mean value, standard deviation and skewness approximations of the objective function are independent from the probability density function $f_Z(\boldsymbol{z})$, knowledge of the distribution of input parameters is not necessary. The k-th central moments $\mu_{i,k}$ of the input parameters $\boldsymbol{z}$ can be determined numerically using discrete measurement data of the input parameters.

3.4.2.2 First and second order derivatives and required number of calculations

The first and second order derivatives of the objective function at the mean vector of input parameters, $\frac{\partial g(\boldsymbol{\mu})}{\partial z_i}$ and $\frac{\partial g^2(\boldsymbol{\mu})}{\partial z_i^2}$, respectively, are estimated numerically by central differences:

$$\frac{\partial g(\boldsymbol{\mu})}{\partial z_i} \approx \frac{g(\mu_1, \dots, \mu_i + \Delta z_i, \dots, \mu_n) - g(\mu_1, \dots, \mu_i - \Delta z_i, \dots, \mu_n)}{2\Delta z_i} \tag{3-24}$$

and

$$\frac{\partial g^2(\boldsymbol{\mu})}{\partial z_i^2} \approx \frac{g(\mu_1, \dots, \mu_i + \Delta z_i, \dots, \mu_n) - 2g(\mu) + g(\mu_1, \dots, \mu_i - \Delta z_i, \dots, \mu_n)}{2\Delta z_i} \tag{3-25}$$

To calculate these derivatives from evaluations of the objective function, the finite differences step size has to be chosen. This obviously is highly dependent on the problem treated with the semi-analytical probabilistic method. On the one hand, the step size has to be chosen preferably small to achieve precise numerical derivatives around the mean value of input parameters (compare equations (3-24) and (3-25)). On the other hand, the step size has to be chosen high enough so that the Taylor series gives a reasonable approximation of the objective function within the bounds of input parameter values (compare equation (3-19)). For investigating the influence of the traditional and non-traditional imperfections listed in chapter 6.2.2 on the buckling loads of cylindrical shells, KRIEGESMANN [89] showed that a step size of $\Delta z_i = 1.5\ \sigma_i$ is appropriate, which is adopted in this thesis.

Based on the number of terms included in the estimation of the stochastic moments, different approaches are defined. Neglecting all higher order terms and including only second moments in equations (3-21), (3-22) and (3-23), the so-called first-order second-moment method (FOSM) is obtained. Due to only first order derivatives of the objective function being active, a total of $n + 1$ evaluations of the objective function are needed, where n is the number of input parameters. As stated above, in the case of buckling analyses of cylindrical shells, this refers to $n + 1$ buckling load calculations. By increasing the amount of considered terms, the second-order third-moment method (SOTM) and the incomplete second-order approach (ISOA) are derived, increasing the amount of evaluations of the objective function to $2n + 1$.

The full approach would also include terms with derivatives with respect to different input parameters (for example the last term in equation (3-22)). This drastically increases the amount of required evaluations of the objective function to $2n + 1 + \frac{1}{2}n(n-1)$ while not improving the results when investigating the buckling loads cylindrical shells [84]. Therefore, in this thesis, the ISOA is applied.

3.4.2.3 Choosing a level of reliability to obtain design values

After calculating the mean value μ_g and standard deviation σ_g of the objective function, a probabilistic design value g_d can be obtained:

$$g_d = \mu_g - b\,\sigma_g \tag{3-26}$$

Here, b is a factor combining a chosen level of reliability and the assumed type of distribution of the objective function. The type of distribution can be determined with the help of the skewness ν_g as well as by optically judging discrete experimental distributions and performing fitting tests like the Kolmogorov-Smirnov-scheme [89], [103]. KRIEGESMANN proposed that a normal distribution is best suited to describe the scatter of buckling loads of the cylindrical shells investigated within this thesis (compare [89] and chapter 6.3). Therefore, in thesis, a normal distribution of the objective functions is assumed.

The factor b is based on the commonly applied concept of reliability index β. When assuming normal distribution, β can be interpreted as the number of standard deviations which separates a given design value from the mean value of the objective function:

$$\beta = \frac{g_d - \mu_g}{\sigma_g} = -b \quad \text{with} \quad \beta = -\Phi^{-1}(P_f) = -\Phi^{-1}(1-R) \tag{3-27}$$

Here, Φ^{-1} is the inverse cumulative distribution function of the standard normal distribution. Thus, when assuming normal distribution and choosing a reliability of $R = 90\%$, b is equal to 1.2816. For a reliability of $R = 99\%$, b is equal to 2.2362.

Figure 3-18 gives a schematic overview of the application of the semi-analytical probabilistic procedure to obtain design loads for cylindrical shells. The scattering traditional and non-traditional imperfections serve as input parameters for establishing the required shell realizations to determine the first and second order derivatives of the objective function at the mean values of the input parameters. In the case of design of cylindrical shells with respect to stability failure, the objective function is the buckling load of the shell. Thus, the necessary evaluations of the objective function comply with finite element buckling load calculations of the before mentioned realizations. By estimating the stochastic moments, the scatter of buckling loads is obtained. By classifying the expected distribution and choosing a level of reliability, a design load can be acquired.

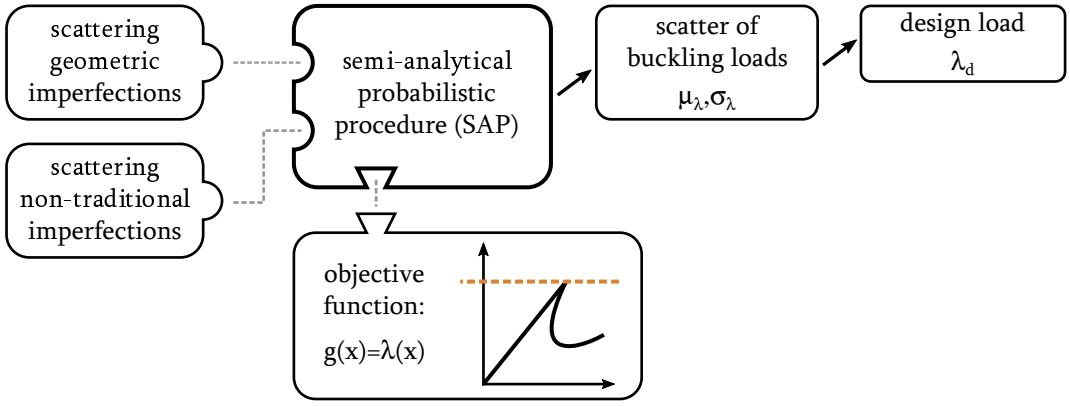

Figure 3-18: The semi-analytical probabilistic procedure (SAP): schematic overview

3.4.3 Decorrelating input parameters: the Mahalanobis-Transformation

In order to simplify the estimation of the stochastic moments of the objective function, independence of the input parameters has to be assumed (compare equations (3-20) and (3-21)). This assumption has to be justified in each application case of the semi-analytical probabilistic method. In the case of traditional and non-traditional imperfections of cylindrical shells it may, for example, seem acceptable to treat material property deviations and loading imperfections as stochastically uncorrelated. However, when looking at the numerous Fourier Coefficients describing the geometric imperfection patterns (compare chapter 4.1), it is not at all justified to assume independence.

Thus, to be able to still treat correlated input parameters within the SAP-framework, they have to be decorrelated. This is achieved by the Mahalanobis-Transformation [104] which is similar to the principle component analysis and given by

$$\boldsymbol{x} = \boldsymbol{\Sigma}^{\frac{1}{2}}\boldsymbol{z} + \boldsymbol{\mu_x} \quad \text{and accordingly} \quad \boldsymbol{z} = \boldsymbol{\Sigma}^{-\frac{1}{2}}(\boldsymbol{x} - \boldsymbol{\mu_x}) \tag{3-28}$$

Here, $\boldsymbol{x}$ is the realization vector of the correlated input parameters (for example all Fourier coefficients of the Fourier series describing the geometric imperfection shape) with its mean vector $\boldsymbol{\mu_x}$, $\boldsymbol{\Sigma}$ is the covariance matrix of the random vector $\boldsymbol{X}$ and $\boldsymbol{z}$ is the realization vector of the uncorrelated input parameters. The sample mean vector $\boldsymbol{\mu_x}$ and sample covariance matrix $\boldsymbol{\Sigma}$ can be determined from m measurements of the input parameters $\boldsymbol{x}$ by:

$$\boldsymbol{\mu_x} = E(\boldsymbol{X}) \approx \frac{1}{m}\sum_{i=1}^{m} \boldsymbol{x}_i \tag{3-29}$$

$$\boldsymbol{\Sigma} = \frac{1}{m-1}\sum_{i=1}^{m} (\boldsymbol{x}_i - \boldsymbol{\mu_x})(\boldsymbol{x}_i - \boldsymbol{\mu_x})^T \tag{3-30}$$

To perform the transformation given in equation (3-28), the root of the covariance matrix $\boldsymbol{\Sigma}$ has to be determined. In most practical cases (as in the case of geometric imperfections), the number of measurements m (manufactured shell specimens) is smaller than the number of input parameters n (Fourier coefficients to describe the imperfection pattern). In this case, when $m < n$, the covariance matrix $\boldsymbol{\Sigma} \in \mathbb{R}^{nxn}$ is singular, as proven in [89]. Then, $\boldsymbol{\Sigma}^{\frac{1}{2}}$ can be determined using spectral composition:

$$\boldsymbol{\Sigma}^{\frac{1}{2}} = \boldsymbol{Q}\,\boldsymbol{D}^{\frac{1}{2}} = \left(\boldsymbol{q}_{\boldsymbol{\Sigma},\boldsymbol{1}}, \dots, \boldsymbol{q}_{\boldsymbol{\Sigma},\boldsymbol{m-1}}\right) diag\left(\sqrt{\lambda_{\boldsymbol{\Sigma},1}}, \dots, \sqrt{\lambda_{\boldsymbol{\Sigma},m-1}}\right) \tag{3-31}$$

Here, $\boldsymbol{q}_{\boldsymbol{\Sigma},\mathrm{i}}$ denote the eigenvectors and $\lambda_{\boldsymbol{\Sigma},\mathrm{i}}$ the eigenvalues of $\boldsymbol{\Sigma}$.

With $m < n$, the rank of the covariance matrix is $rank(\Sigma) \leq m - 1$. An explanation for this can be derived based on the fact that the centralized realizations of the input parameters $(\boldsymbol{x}_i - \boldsymbol{\mu_x})$ in equation (3-30) are not independent (as multiple measured geometric imperfection shapes show common features). The sum of the centralized realizations of the input parameters equals zero:

$$\sum_{i=1}^{m}(\boldsymbol{x}_i - \boldsymbol{\mu}_{\boldsymbol{x}}) = \sum_{i=1}^{m}\boldsymbol{x}_i - m\boldsymbol{\mu}_{\boldsymbol{x}} = 0 \tag{3-32}$$

With (3-32), the m-th centralized realization $(\boldsymbol{x}_{\boldsymbol{m}} - \boldsymbol{\mu}_{\boldsymbol{x}})$ can be rewritten as

$$(\boldsymbol{x}_{\boldsymbol{m}} - \boldsymbol{\mu}_{\boldsymbol{x}}) = 0 - \sum_{i=1}^{m-1}(\boldsymbol{x}_i - \boldsymbol{\mu}_{\boldsymbol{x}}) = -\sum_{i=1}^{m-1}(\boldsymbol{x}_i - \boldsymbol{\mu}_{\boldsymbol{x}}) \tag{3-33}$$

By substituting $\boldsymbol{\chi}_{\boldsymbol{i}} = (\boldsymbol{x}_{\boldsymbol{i}} - \boldsymbol{\mu}_{\boldsymbol{x}})$ and inserting (3-33), (3-30) can be rewritten as

$$\boldsymbol{\Sigma} = \frac{1}{m-1}\sum_{i=1}^{m}\boldsymbol{\chi}_i\,\boldsymbol{\chi}_i^{\boldsymbol{T}} = \frac{1}{m-1}\left[\sum_{i=1}^{m-1}\boldsymbol{\chi}_i\,\boldsymbol{\chi}_i^{\boldsymbol{T}} + \left(-\sum_{i=1}^{m-1}\boldsymbol{\chi}_i\right)\boldsymbol{\chi}_m^{\boldsymbol{T}}\right] = \frac{1}{m-1}\sum_{i=1}^{m-1}\boldsymbol{\chi}_i\,(\boldsymbol{\chi}_i^{\boldsymbol{T}} - \boldsymbol{\chi}_m^{\boldsymbol{T}}) \tag{3-34}$$

Looking at equation (3-34) it is apparent that only $m-1$ matrices of $rank(\boldsymbol{\chi}_i\,\boldsymbol{\chi}_i^{\boldsymbol{T}}) = 1$ are summed up. Thus, the rank of the covariance matrix is $rank(\boldsymbol{\Sigma}) \leq m-1$, and therefore it only has a maximum of $m-1$ eigenvectors and eigenvalues (compare equation (3-31)). This in turn means that the realization vector of the uncorrelated input parameters $\boldsymbol{z}$ must be of length $m-1$ (compare equation (3-30)).

Apart from the intended decorrelation of the input parameters for the estimation of the characteristic moments, the great benefit of applying the Mahalanobis Transformation lies in this reduction of the input vector size. The $length(\boldsymbol{x}) = n$ Fourier coefficients describing the geometric imperfection shape are reduced to $length(\boldsymbol{z}) = m-1$ random numbers describing the geometric imperfection shape.

For more details on the mathematical background of the Mahalanobis Transformation, it is again referred to KRIEGESMANN, 2012 [89].

4 Reduction of imperfection patterns to the components essential for buckling

In this chapter, a new methodology for reducing geometric imperfection patterns to their inherent parts which are essential for buckling is presented.

First, an overview of the decomposition of geometric imperfection patterns into Fourier series is given. After that, the basic idea of the imperfection filtering methodology is given and the main parameters are discussed. In a subsequent step, the method is applied to multiple measured shell specimen of concurring and varying design parameters, followed by the derivation of a physical justification of the essential imperfection shapes as well as an explanation for the buckling load discrepancies noticed for any two given imperfection patterns.

While the shell design parameters like geometry, laminate setup and material properties certainly influence the concrete buckling loads and shell behavior, for the qualitative interpretation of the application and results of the reduction method itself they play subordinate roles. This is due to the fact that the reduction procedure is realized based on finite element analyses including the geometry, laminate setup and material properties of every particular shell specimen. Therefore, the effect of those properties on the essential imperfection shapes is automatically accounted for. As a consequence, details on the shell specimens will be given no earlier than chapter 5, when the structural properties play an important role in quantitatively discussing established design loads.

4.1 Fourier-representation of geometric imperfections

When performing buckling load calculations which include geometric imperfections, an efficient way to counter measurement noise and reduce data size is decomposing the imperfection pattern to Fourier series (compare for example [84], [87] and [105]). Furthermore, the description of imperfection patterns by Fourier series is not dependent on a fixed finite element mesh. Thus, the same set of information can be applied to multiple meshes of different fidelity, without the need of interpolation between discrete nodal imperfection values.

4.1.1 From a measured cloud of points to the phase-shift representation

The classical formulation of the approximation of the two-dimensional periodic function f by a discrete Fourier series is given by:

$$f(x,y) \approx \tilde{f}(x,y) = \sum_{k=0}^{n_x} \sum_{l=0}^{n_y} A_{kl} \cos\left(\frac{k\,\pi\,x}{a}\right) \cos\left(\frac{l\,\pi\,y}{b}\right) + B_{kl} \cos\left(\frac{k\,\pi\,x}{a}\right) \sin\left(\frac{l\,\pi\,y}{b}\right) + C_{kl} \sin\left(\frac{k\,\pi\,x}{a}\right) \cos\left(\frac{l\,\pi\,y}{b}\right) + D_{kl} \sin\left(\frac{k\,\pi\,x}{a}\right) \sin\left(\frac{l\,\pi\,y}{b}\right) \quad (4\text{-}1)$$

Where x and y are the spatial coordinates and a and b are the periods in x-direction and y-direction, respectively. A_{kl}, B_{kl}, C_{kl} and D_{kl} are the Fourier coefficients corresponding to k waves in x-direction and l waves in y-direction. The parameters n_x and n_y denote the maximum amount

of waves included in the series. For increasing n_x and n_y, the Fourier series delivers a more detailed description of the original function and thus $\tilde{f}(x,y)$ approaches $f(x,y)$ for $n_x, n_y \to \infty$.

Due to the orthogonality of trigonometric basis-functions, the integral over a single basis-function as well as the integral over the product over two differing basis-functions vanish on the interval $[0, 2\pi]$. Thus, the Fourier coefficients can be independently determined to:

$$A_{kl} = \frac{\alpha}{a\,b}\sum_{x=0}^{a}\sum_{y=0}^{b} w_{real}(x,y)\cos\left(\frac{k\,\pi\,x}{a}\right)\cos\left(\frac{l\,\pi\,y}{b}\right)\Delta x\Delta y$$

$$B_{kl} = \frac{\alpha}{a\,b}\sum_{x=0}^{a}\sum_{y=0}^{b} w_{real}(x,y)\cos\left(\frac{k\,\pi\,x}{a}\right)\sin\left(\frac{l\,\pi\,y}{b}\right)\Delta x\Delta y$$

$$C_{kl} = \frac{\alpha}{a\,b}\sum_{x=0}^{a}\sum_{y=0}^{b} w_{real}(x,y)\sin\left(\frac{k\,\pi\,x}{a}\right)\cos\left(\frac{l\,\pi\,y}{b}\right)\Delta x\Delta y$$

$$D_{kl} = \frac{\alpha}{a\,b}\sum_{x=0}^{a}\sum_{y=0}^{b} w_{real}(x,y)\sin\left(\frac{k\,\pi\,x}{a}\right)\sin\left(\frac{l\,\pi\,y}{b}\right)\Delta x\Delta y \qquad (4\text{-}2)$$

Here, α is numerical substitutor with $\alpha = 4$ for $k \wedge l > 0$, $\alpha = 2$ for $k \vee l > 0$ and $\alpha = 1$ for $k \wedge l = 0$. When interpreting equations (4-2), it is observed that discrete Fourier series are inclusive. This means that once the coefficients for a given fidelity n_x, n_y of the representation are established, the coefficients remain exactly the same when the fidelity of the representation is further increased (compare equation (4-1)). Thus, the increase in approximation quality with increasing n_x, n_y mentioned above is only contributed to by the additional wave shapes of increasingly shorter wavelengths.

Equation (4-1) assumes periodicity in x-direction and y-direction. This poses a problem when applying Fourier series to the geometric imperfection patterns of cylindrical shells. While an imperfection pattern is indeed periodic in circumferential direction, assumptions have to be made with regards to the periodicity in the axial direction. This is because real imperfection patterns not only show different gradients but most importantly different imperfection magnitudes at the shell's upper and lower edge. Figure 4-1 depicts an exemplary imperfection shape in axial direction in black. The red line gives the full Fourier approximation. It is noticed that due to the representation being periodic, significant deviations from the original function occur in the regime of the edges.

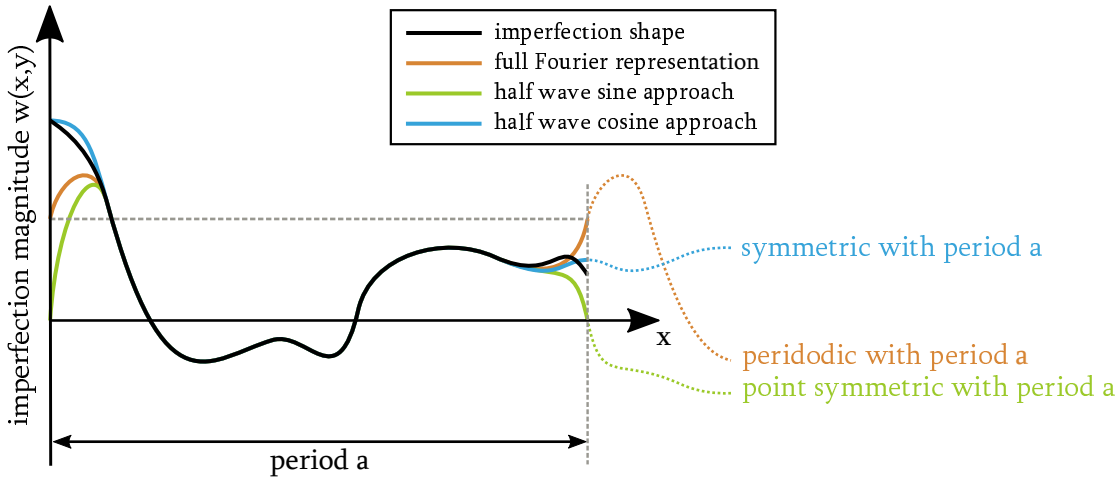

Figure 4-1: Schematic illustration of the effect of different symmetry conditions of the Fourier series on the aproximated imperfection shape

To reduce the discrepancies at the shell's edges, two assumptions can be made.

Firstly, the imperfection shape can be assumed to be point symmetric with a period of $2a$, forcing the function to be zero at the edges (compare Figure 4-1, green line). By modifying equation (4-1) in this way, the so-called half wave sine representation is obtained:

$$\tilde{f}(x,y) = \sum_{k=0}^{n_x} \sum_{l=0}^{n_y} \sin\left(\frac{k\,\pi\,x}{a}\right)\left(C_{kl}\cos\left(\frac{l\,\pi\,y}{b}\right) + D_{kl}\sin\left(\frac{l\,\pi\,y}{b}\right)\right) \tag{4-3}$$

Secondly, the imperfection shape can be assumed to be symmetric with a period of $2a$, forcing gradients at the edges to be zero but enabling the function to have different magnitudes at both edges (compare Figure 4-1, blue line). By modifying equation (4-1) in this way, the so-called half wave cosine representation is obtained:

$$\tilde{f}(x,y) = \sum_{k=0}^{n_x} \sum_{l=0}^{n_y} \cos\left(\frac{k\,\pi\,x}{a}\right)\left(A_{kl}\cos\left(\frac{l\,\pi\,y}{b}\right) + B_{kl}\sin\left(\frac{l\,\pi\,y}{b}\right)\right) \tag{4-4}$$

As mentioned above, the half wave sine representation does not allow deflection values at the shell's edges. However, measured geometric imperfection patterns generally show significant imperfection magnitudes at the shell's edges (compare for example Figure 4-2). This is due to the fact that the clamping rings of the shell specimen unavoidably force deflection states onto the shell edges. These deviations from the original geometry add to the original geometric imperfections and lead to the regularly encountered high imperfection values at the boundaries [89]. To account for these deflections, in most cases the half wave cosine representation is best suited to describe imperfection shapes.

By inserting the cylinder's length L and the circumference $2\pi R$ for a and b, respectively, into equation (4-4), the half wave cosine Fourier representation for geometric imperfections is obtained:

$$\tilde{w}(x,y) = 2t \sum_{k=0}^{n_x} \sum_{l=0}^{n_y} \cos\left(\frac{k\,\pi\,x}{L}\right)\left(A_{kl}\cos\left(\frac{l\,y}{R}\right) + B_{kl}\sin\left(\frac{l\,y}{R}\right)\right) \tag{4-5}$$

When using Fourier series to approximate measured imperfection patterns, the Fourier coefficients A_{kl} and B_{kl} can directly be determined from measurement data using equations (4-2). It should be noted that, due to convention in scientific community, the Fourier coefficients are normalized by the shell's wall thickness and thus the Fourier representation has to be multiplied with t (compare equations (4-4) and (4-5)).

Traditionally, the Fourier coefficients of multiple shell measurements were determined based on the full Fourier series with A_{kl}, B_{kl}, C_{kl} and D_{kl}, given in equation (4-1) (compare for example the TU Delft database [87]). In contrast to that, as described above, the half wave cosine representation with only A_{kl} and B_{kl} is very well suited to describe geometric imperfections and thus widely applied in modern applications (compare for example KRIEGESMANN et al. [84]).

Figuratively speaking, the coefficient A_{kl} is a measure for the symmetry of the pattern to its middle axis at $\frac{2\pi R}{2}$ and B_{kl} is a measure for the point symmetry of the pattern to this middle axis. However, when investigating the influence of different wave shapes on the buckling behavior (see chapter 4), this interpretation does not benefit perceivability. Thus, the so-called phase shift representation is introduced:

$$\widetilde{w}(x,y) = 2t \sum_{k=0}^{n_x} \sum_{l=0}^{n_y} \xi_{kl} \cos\left(\frac{k\,\pi\,x}{L}\right) \cos\left(\frac{l\,y}{R} - \varphi_{kl}\right) \tag{4-6}$$

with

$$\xi_{kl} = \sqrt{A_{kl}^2 + B_{kl}^2} \tag{4-7}$$

and

$$\varphi_{kl} = \begin{cases} \tan^{-1}\left(\frac{B_{kl}}{A_{kl}}\right) f\ddot{u}r\ A_{kl} > 0 \\ \tan^{-1}\left(\frac{B_{kl}}{A_{kl}}\right) + \pi\ f\ddot{u}r\ A_{kl} < 0 \\ sgn(B_{kl}) * \frac{\pi}{2}\ f\ddot{u}r\ A_{kl} = 0 \end{cases} \tag{4-8}$$

In the following, the three dimensional wave shape corresponding to a specific wave number in axial direction and in circumferential direction, k and l, respectively, is referred to as the Fourier mode (k, l). Due to the literal commonality it is particularly emphasized that the Fourier modes treated within the course of this thesis are in no way related to the well-known Eigenmodes of shells.

In equation (4-6), a single Fourier coefficient ξ_{kl} is used to define the amplitude of a specific Fourier mode (k, l) while the circumferential phase shift of this mode is given by φ_{kl}. For scientific purposes, this offers a much more straightforward interpretation and handling of Fourier modes.

When performing probabilistic analyses with scattering imperfection patterns (compare chapters 3.4 and 6.3), it is important to express the phase shift φ_{kl} of all modes relative to the phase shift of a particular chosen mode, for example $\varphi_{0,2}$ (compare [89]). In this way, possible smearing of mean

imperfection patterns can be excluded. As the probabilistic treatment of scattering geometric imperfections is only a minor part of this thesis, it is referred to KRIEGESMANN, 2012 [89] for more details.

4.1.2 Practical advantages of Fourier series for geometric imperfection patterns

The decomposition of a measured imperfection pattern into a set of Fourier modes has numerous advantages for practical buckling analysis. Firstly, the amount of data required for the preprocessing of numerical analyses is vastly reduced from the order of 10^6 measurement points to the order of 10^2 Fourier coefficients. More importantly, obtaining Fourier modes of a measured pattern makes the information on the geometric imperfection shape independent from the finite element mesh. This has numerous advantages for example in the case of convergence studies or the transformation of imperfection patterns to different shell geometries in academic studies.

For investigating the influence of geometric imperfections on the buckling behavior of shells from a scientific or engineering perspective, Fourier series also serve as a means to obtain a more practical or feasible description of the imperfection shape. Two dimensional fields of discrete nodal deflection values are inconvenient to handle and complex to manipulate in a meaningful way. In contrast to that, global wave shapes define the same spatial data with just two parameters and their superposition is in most cases more easily imaginable for the researcher or designer. In the subsequent chapters, sets of Fourier modes are assessed based on their corresponding contribution to the degradation of buckling loads. As a practical metaphor, in this context, the Fourier modes and their amplitudes can be interpreted as the valves and setscrews of a complex machine yielding buckling loads.

Apart from these practical advantages of Fourier series, expressing imperfection shapes as superpositions of waves also correlates with multiple aspects of the physical and mechanical behavior of cylindrical shells. From eigenmode shapes calculated in linear eigenvalue analyses to global prebuckling and postbuckling deformations observed in nonlinear buckling analyses and experiments to the shape of the initial dimple which initiates local failure: all can be reduced to a superposition of a sufficient amount of wave shapes.

4.1.3 On the required fidelity of the Fourier representation

When transforming measurement data by the use of Fourier series or when judging the influence of different Fourier modes on the buckling load, another important question arises, namely how many waves in axial and circumferential direction of which wavelength to include in the Fourier representation.

In the time of analytical or semi-analytical calculation of buckling loads, authors like ALMROTH [53], TENNYSON and MUGGERIDGE [16] and ARBOCZ [65] were practically limited to a comparatively low total amount of wave shapes included in their analyses. To somehow be able to still achieve an acceptable representation of real imperfection shapes or buckling modes, these few wave shapes were consequently chosen to be in the regime of high wavelength or lower wave numbers. The introduction of finite element calculation methods lead to practically unlimited fidelities of Fourier representations. Hence, the imperfection database established at TU Delft [87],

for example, gives Fourier coefficients for representations of higher fidelity for different shells, mostly of $n_{total} = n_1 x\, n_2 = 15\, x\, 15 = 225$.

Figure 4-2, left shows the imperfection shape of shell Z25, with a very fine Fourier representation of $n_{total} = 16\, x\, 31 = 496$ wave shapes (details on the shell geometry are given in chapter 6.1.1). Figure 4-2, right depicts the same shell surface using a Fourier representation with $n_{total} = n_1 x\, n_2 = 16\, x\, 16 = 256$ modes of increasing wave numbers, starting with $n = 0$.

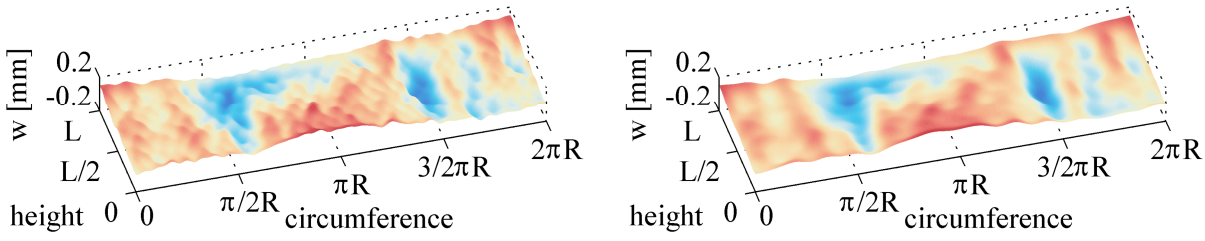

$\lambda_{0-15,0-30} = 32.95\ kN$ $\lambda_{0-15,0-15} = 36.06\ kN$

Figure 4-2: Imperfection shapes of shell Z25: Fourier representation with n_1 x n_2 = 496 modes (left) and with 256 modes (right)

It is noticed that the approximated pattern on the right generally represents the shape of the very fine Fourier representation. The regions of inward and outward deflection, the general waviness of the pattern as well as the minimum and maximum amplitudes roughly match.

When comparing the buckling loads, however, a significant discrepancy is noticed. While the fine Fourier series causes a buckling load reduction from the perfect shell's buckling load of $\Delta\lambda_{0-15,0-30} = 37.62 - 32.95 = 4.67\ kN$, the buckling load reduction of the coarser Fourier approximation is $\Delta\lambda_{0-15,0-15} = 37.62 - 36.06 = 1.56\ kN$ and thus only a fraction (~33 %) of the former.

Figure 4-3 shows the Fourier spectrum of the fine decomposition of with $n_{total} = n_1 x\, n_2 = 16\, x\, 31 = 496$ modes. It is noticed that the modes with the highest amplitude are in the regime of less than 15 circumferential full waves, consorting with the visual observations above, while modes in the regime of higher wave numbers show decreasingly small amplitudes.

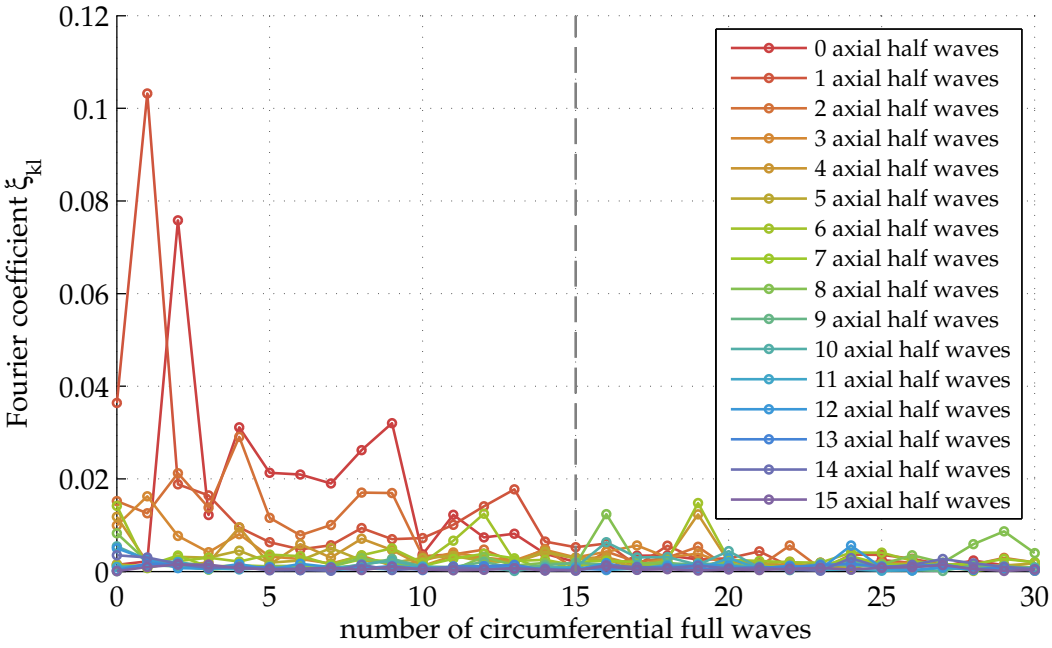

Figure 4-3: Fourier spectrum of shell Z25 with n_1 x n_2 = 496 modes

In the calculation example above, modes of $0 - 15$ axial half waves and $0 - 15$ circumferential full waves were taken into account, which corresponds to the left part of Figure 4-3 (left of dashed line), as Fourier representations of increasing wave numbers are inclusive (compare chapter 4.1.1). In a second calculation, the right hand part of the spectrum, containing modes of $0 - 15$ axial half waves and $16 - 30$ circumferential full waves, are taken as a basis to obtain the imperfection pattern depicted in Figure 4-4, right.

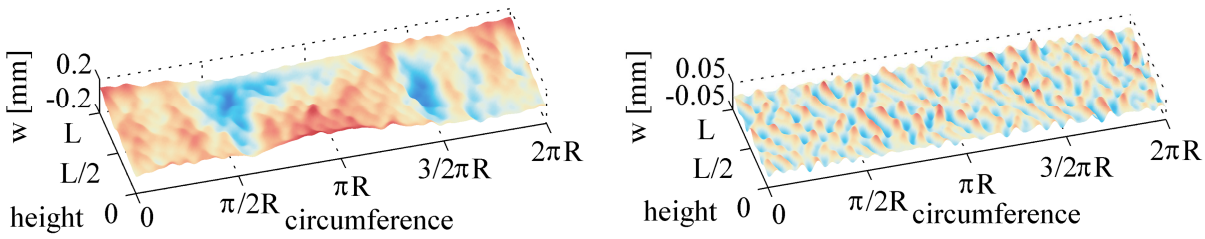

$\lambda_{0-15,0-30} = 32.95\ kN$ $\lambda_{0-15,16-30} = 33.92\ kN$

Figure 4-4: Imperfection shapes of shell Z25: Fourier representation with n_1 x n_2 = 496 modes (left) and with 256 short-waved modes (right)

It is noticed that the approximated pattern on the right does not show visual commonalties with the measured shape. The regions of inward and outward deflection, the general waviness of the pattern as well as the minimum and maximum amplitudes significantly differ.

When comparing the buckling loads, however, closely matching values are noticed. The buckling load reduction of the short-waved Fourier approximation is $\Delta\lambda_{0-15,16-30} = 37.62 - 33.92 = 3.7\ kN$. Compared to the long-waved Fourier approximation in Figure 4-2, right, this is much closer to the buckling load reduction of the complete Fourier representation of $\Delta\lambda_{0-15,0-30} = 4.67\ kN$ (see above). It seems that the set of modes of high wave numbers and low wavelengths is much better suited to reflect the buckling behavior of the original pattern than the set of modes of low to medium wave numbers.

This finding leads to two important conclusions for buckling analysis of shells in general.

Firstly, it has to be noted that modes of higher wavenumbers and short wavelengths have a significant influence on the buckling behavior of shells (compare also HILBURGER et al. [106]). The decomposition of measured imperfection patterns into Fourier series with low to medium wave numbers of traditionally around 10 to 20 (compare [84], [87], [106]) seems to be insufficient. However, it has to be noted that the number of waves required to match the buckling load of measured patterns depends on the nominal shell geometry, the laminate setup and the measured imperfection shape itself.

Secondly, when investigating the influence of particular mode sets on the buckling behavior and identifying the essential parts of the imperfection pattern driving stability failure (see chapter 4.2), an appropriate choice of the minimum wavelength of the Fourier series is crucial. The results obtained for a specific minimum wavelength of the Fourier representation have to be compared to the ones obtained for lower minimum wavelengths to make sure that no essential modes stay hidden in neglected wave number regimes.

For all shells given in the following, a representation of $n_{total} = n_1 x\, n_2 = 16\, x\, 31 = 496$ is chosen in this thesis as multiple sensitivity studies showed that modes of higher wave numbers have negligible influence on the buckling loads and, more importantly, prebuckling deformations and initial dimple positions.

4.1.4 On the coupling of imperfection modes

In chapter 4.1.3 it was shown that the choice of the fidelity of the Fourier series heavily impacts the obtained buckling loads. Furthermore, it was demonstrated that different sets of modes lead to different buckling loads. In addition to that, it is important to note that every single mode has a different detrimental effect on the buckling load within every given set of present modes. This means that the buckling load reduction caused by application of a particular mode is not only caused by the detrimental effect of its particular wave shape but also by its interaction with other wave shapes within a given spectrum.

The effect of imperfection wave shapes on the buckling load can be characterized by three main characteristics:

1. *The influence of imperfection modes on the buckling load varies*

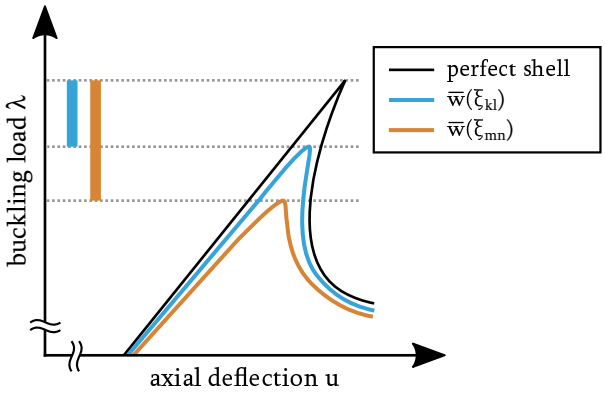

$$\frac{\partial\lambda\left(\bar{w}(\xi_{kl})\right)}{\partial\xi_{kl}} \neq \frac{\partial\lambda\left(\bar{w}(\xi_{mn})\right)}{\partial\xi_{mn}}$$

When applying two given Fourier modes to two otherwise perfect shell surfaces and normalizing their amplitudes, two different buckling loads are noticed.

2. *The influence of imperfection modes on the buckling load is coupled*

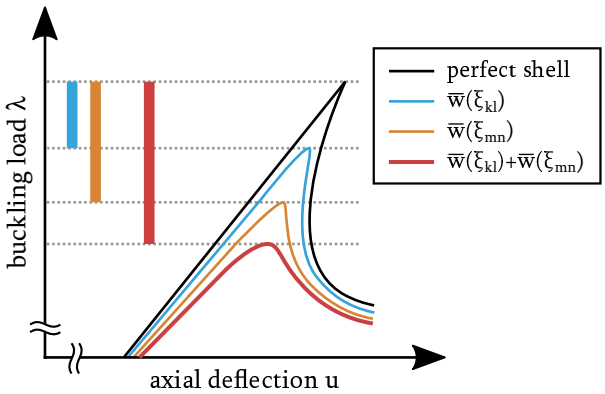

$$\Delta\lambda\left(\bar{w}(\xi_{kl}) + \bar{w}(\xi_{mn})\right) \neq \Delta\lambda\left(\bar{w}(\xi_{kl})\right) + \Delta\lambda\left(\bar{w}(\xi_{mn})\right)$$

The buckling load reduction of a pattern containing two given Fourier modes is not equal to the sum of buckling load reductions of two patterns with the respective single modes.

3. The influence of imperfection modes on the buckling load is not necessarily detrimental

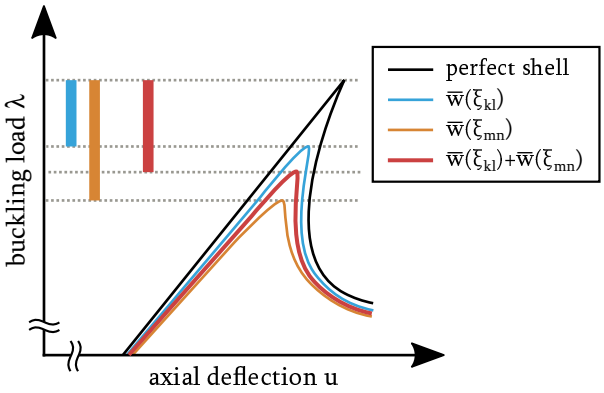

$$\Delta\lambda\left(\overline{w}(\xi_{kl}) + \overline{w}(\xi_{mn})\right) <^{?} \Delta\lambda\left(\overline{w}(\xi_{nm})\right)$$

When a given Fourier mode is added to a set of modes, the buckling load of the shell may very well increase. This is due to the fact that the interaction of that particular mode with the surrounding shape may cause a mitigation of the severity of the resulting imperfection pattern. Stabilizing modes can for example be found in the regime of zero axial waves and medium circumferential wave numbers. These can be geometrically interpreted as axial stringers, stiffening the shell.

The aim of the reduction method described in the following is to determine the inherent parts of a given imperfection pattern that is crucial for triggering buckling of the shell. Here, not a specific set of critical modes is sought for but the geometrical imperfection shape which is essential for buckling, regardless which amount of which modes it is composed of.

To achieve this, individual wave shapes are evaluated based on their particular detrimental effect on the buckling load. When doing so, due to the effects described above, it is of vital importance not only to examine every single mode but always account for the interaction of this mode with some or all of the other modes included in a given spectrum.

4.2 *The stepwise imperfection filtering method (SIFM): main idea and discussion of parameters*

As described above, the actual triggers and exact reasons for the local loss of stability a real shell experiences at a certain load level are not yet understood.

The snap-in of a local initial dimple in general can be traced back to a somewhat ominous local bending stress field which disrupts uniform axial loading. However, there is no explanation on how exactly a real geometric imperfection field influences the local stability states and why the local loss of stability occurs at one specific position instead of an arbitrary other one.

As briefly discussed in chapter 3.2.3, it appears that in every imperfection pattern, one specific part of the surface area features certain characteristics which are more detrimental to the load transfer than the ones of other parts and thus trigger the snap-in of the initial dimple. The most obvious candidates for these unknown characteristics seem to be preferably high local imperfection magnitudes or preferably localized imperfection shapes.

Figure 4-5 exemplarily gives the unloaded imperfection pattern of shell Z15 on the left and the radial buckling deflections with the initial dimple on the right.

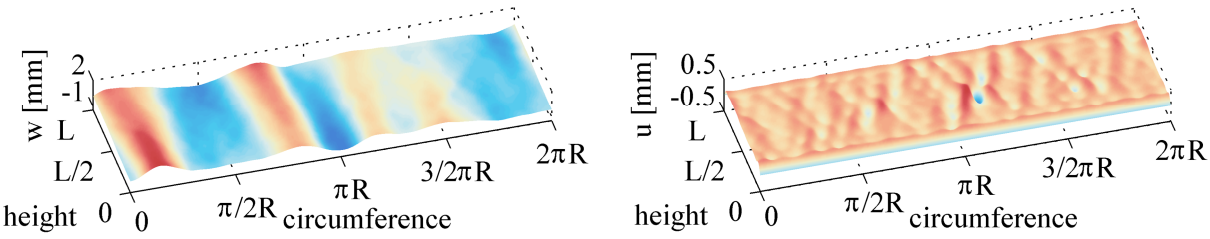

Figure 4-5: Imperfection pattern of shell Z15 (left) and radial prebuckling deformations with the initial dimple (right)

When looking at the imperfection shape on the left, the highest imperfection magnitudes occur at the shell's edges. No localized imperfection shapes can be found, as the surface is dominated by comparatively broad axial bands. When performing a nonlinear analysis and inspecting the deformation pattern at the onset of buckling, the initial dimple is identified in the very center of the shell. It is apparent that the modest guesses for visual inspection criteria made above are not applicable to predict the position of the initial dimple or the buckling state of the shell.

To tackle this lack of fundamental understanding of the specific impact of imperfection shapes on the buckling behavior, a new procedure is proposed in this thesis. It is based on filtering measured or arbitrarily assumed imperfection patterns down to their individual parts which are essential for establishing the buckling behavior observed for that particular original imperfection pattern. Based on the Fourier representation of the imperfection patterns, the reduction procedure does not only incorporate the individual modes' influence on the buckling load but also the effects of their interactions on the loss of stability.

In the following, evaluating buckling loads of given imperfection patterns refers to numerically determining the non-linear buckling load of a given shell geometry with the discussed

imperfection pattern. As the proposed procedure is an instrument to investigate on geometric imperfections and to analyze their detrimental influence on the shell's stability, no non-traditional imperfections are applied in this context. Thus, the buckling loads given in the following do not compare to experimentally obtained buckling loads, as real specimen inhibit not only geometric but numerous kinds of non-traditional imperfections. The influence of non-traditional imperfections on the buckling load is accounted for in the framework of the shell design procedures discussed and applied in chapters 5 and 6.

4.2.1 Basic scheme

The main idea of the stepwise imperfection filtering method (SIFM) is to successively assess each fraction of a given geometric imperfection representation (compare chapter 4.1) with respect to its influence on the buckling load. These ominous fractions of a given geometric imperfection pattern can be defined in various ways. In this thesis, fractions of imperfection patterns are understood as the individual wave shapes of a Fourier series decomposition of the respective pattern.

Then, by eliminating all modes which have negligible influence on the buckling load, only the characteristic parts of the imperfection pattern which are essential for the sudden stability failure of the shell are retained.

In a first step, the buckling load of a shell with the original measured geometric imperfection pattern λ_{orig} is established. This buckling load level is modified by a threshold value η_t, which is necessary for the reduction process. While in the following the threshold value is chosen to $\eta_t = 1.01$, chapter 4.2.4 gives a detailed discussion on the influence of η_t on the SIFM results. The reference load λ_{ref} for the reduction process is then defined as:

$$\lambda_{ref} = \eta_t \, \lambda_{orig} \tag{4-9}$$

The reduction procedure itself is based on firstly eliminating a single mode (i, j) from the original Fourier spectrum. This can be done by setting its amplitude to $\xi_{ij} = 0$. With this alteration of the Fourier spectrum, a new imperfection shape is established:

$$\widetilde{w}_{temp,ij} = 2t \sum_{k=0}^{n_x} \sum_{l=0}^{n_y} \left(1 - \delta_{ki}\delta_{lj}\right) \xi_{kl} \cos\left(\frac{k\,\pi\,x}{L}\right) \cos\left(\frac{l\,y}{R} - \varphi_{kl}\right) \tag{4-10}$$

Here, the KRONECKER deltas δ_{ki} and δ_{lj} are used to eliminate a single mode (i, j).

Using the modified imperfection shape $\widetilde{w}_{temp,ij}$, a temporary buckling load level $\lambda_{temp,ij}$ is calculated.

If $\lambda_{temp,ij} > \lambda_{ref}$, the elimination of the mode (i, j) leads to a substantial increase in load carrying capacity. This in turn means that the mode (i, j) or its interaction with any or all of the other modes has a significant influence on the buckling load. Then, the Fourier mode (i, j) is judged as essential, its amplitude is restored to the original value and the mode remains active in the spectrum to contribute to establishing λ_{ref}.

If $\lambda_{temp,ij} \leq \lambda_{ref}$, the elimination of the mode (i, j) causes no remarkable increase or even a reduction of the load carrying capacity. This in turn means that the mode (i, j) itself as well as its

interaction with any or all of the other modes has no significantly detrimental influence on the buckling load or even stabilizes the structure. Then, the Fourier mode (i, j) is judged as negligible, its amplitude stays zero and the mode remains deactivated.

This elimination and buckling load evaluation of the Fourier modes is conducted continually until all modes of the original Fourier spectrum are characterized as either essential or negligible for establishing the original pattern's buckling load.

As described in chapter 4.1.4, the influence of a single mode on the buckling load is not only driven by the sole effect of its particular wave shape on the stability behavior but also by the effects of the interaction with the wave shapes of other modes. This means that the change in buckling load caused by removing a particular mode (i, j) from the spectrum, $\Delta\lambda_{temp,ij} = \lambda_{ref} - \lambda_{temp,ij}$, may very well be different for different sets of modes the mode (i, j) is removed from. Thus, it is not known whether the classification of a mode (i, j) to be essential for the buckling process still holds true in a subsequent step of the procedure.

Therefore, after evaluating all modes of the original spectrum, the set of remaining modes has to be filtered again to ensure that every mode still shows detrimental influence on the buckling load in interaction with the rest of the reduced spectrum.

The procedure reaches its end when no further modes can be eliminated from the spectrum.

Figure 4-6 gives a schematic overview of the application of the stepwise imperfection filtering method to reduce an original imperfection pattern to its parts which are essential for buckling.

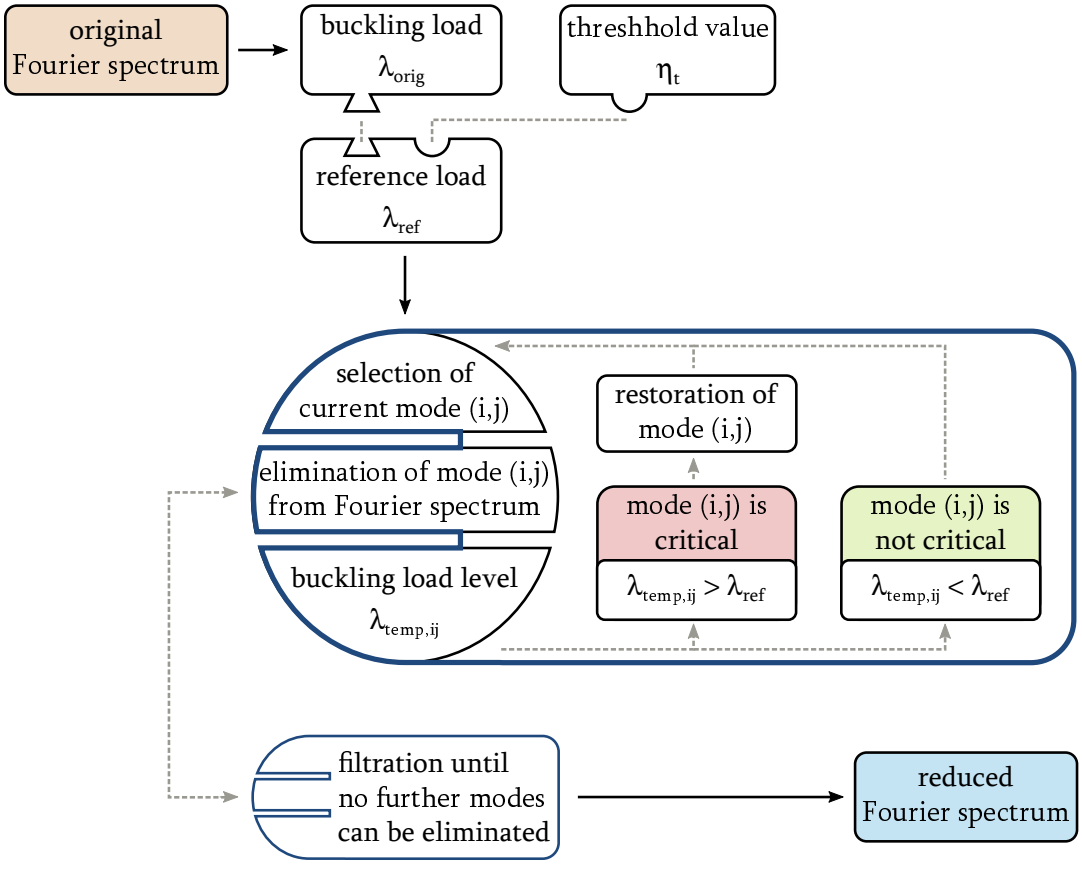

Figure 4-6: The stepwise imperfection filtering method (SIFM): schematic overview

4.2.2 Exemplary application case: shell Z25

When applying the procedure to a given shell imperfection measurement, the original Fourier spectrum is reduced to only the specific set of modes which is essential for the buckling processes of the original shell. Figure 4-7 exemplarily gives the original imperfection shape of shell Z25 with a fidelity of the Fourier representation of $n_{total} = n_1 x\, n_2 = 16\, x\, 31 = 496$ modes. The buckling load corresponding to this pattern is calculated to $\lambda_{orig} = 32.95\ kN$.

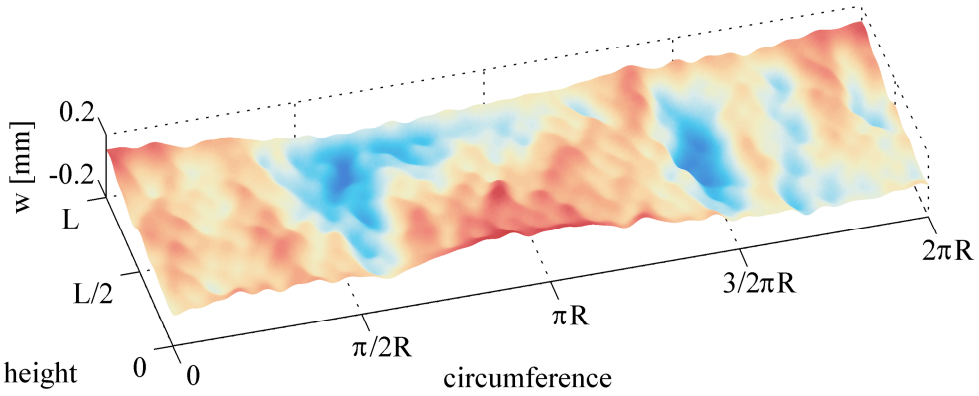

Figure 4-7: Imperfection shape of shell Z25,Fourier representation fidelity of $n_{total} = n_1 x\, n_2 = 16\, x\, 31 = 496$ *modes, non-linear buckling load* $\lambda_{orig} = 32.95\ kN$

By applying the SIFM to the original pattern depicted in Figure 4-7, a reduced set of $n_{total} = 14$ modes is obtained. The buckling load corresponding to the reduced set of modes is calculated to $\lambda_{red} = 33.27\ kN$ which is, by definition of the procedure given above, within one percent of the original buckling load λ_{orig}. Figure 4-8 depicts the reduced imperfection shape of only the essential modes.

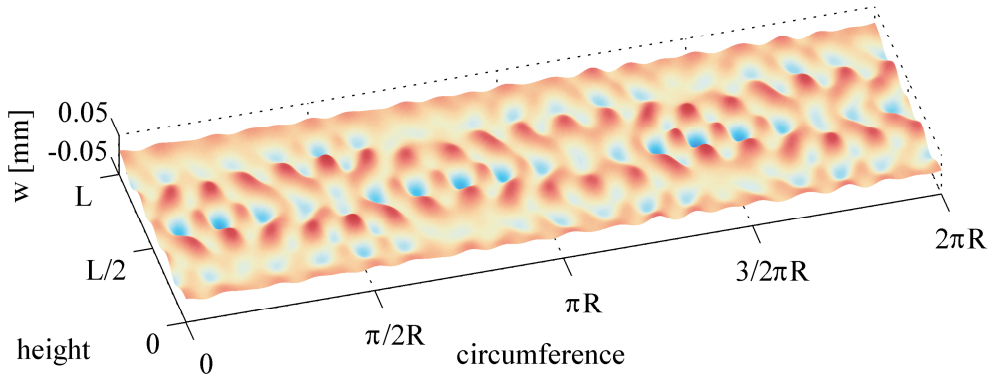

Figure 4-8: Essential imperfection shape of shell Z25, $n_{total} = 14$ *modes, non-linear buckling load* $\lambda_{red} = 33.27\ kN$

It is noticed that the reduced pattern shows maximum imperfection amplitudes which are around one order of magnitude smaller than the ones of the original pattern. This is due to the remaining modes retaining their original amplitude while at the same time a total of $496 - 14 = 482$ wave shapes and their contribution to the superposed imperfection pattern were eliminated. It should be noted that even though the imperfection amplitudes of the reduced patterns are very low (in this case $\bar{w}_{red} \approx 0.05\ mm$), they are still well above the accuracy tolerances of the ATOS measurement system used to scan the original patterns (compare [107], [108]).

While a more detailed discussion of the results of the SIFM is given in the following chapters, the distinct short-waved checker board pattern of the reduced imperfection shape shall be briefly mentioned. This characteristic shape of alternating local minima and maxima of comparatively short wavelengths heavily concurs with the basic observations in chapter 4.1.3 and is observed in a large amount of shells with varying geometry, laminate setup and measured imperfection patterns.

Figure 4-9, left gives the radial deflections of the shell with the original imperfection pattern right before buckling occurs. Figure 4-9, right accordingly gives the pre-buckling deformations of the shell with the reduced imperfection pattern. As in the case of all simulations in this thesis, both deflection surfaces were obtained with the simulation specifications given in chapter 6.1.2.

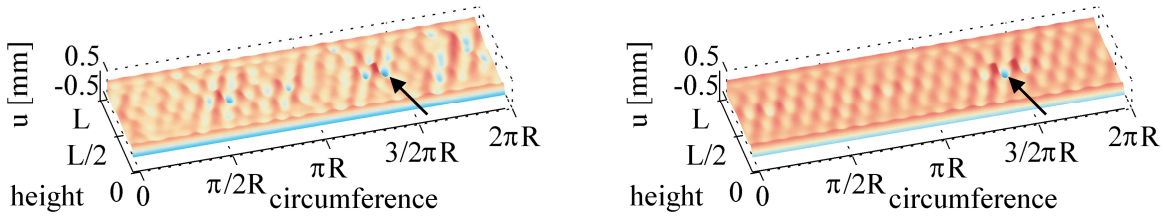

Figure 4-9: Pre-buckling deformations of the original shell Z25 (left) and the shell with the reduced imperfection pattern (right)

It is noticed that in both deflection surfaces, the distinct initial dimple occurs at the same position. This initial dimple causes local loss of stability and propagates around the shell's circumference in the early post-buckling phase. Despite slight inhomogeneities in the case of the original pattern, both deflection surfaces show the same characteristic wavelengths, especially in the vicinity of the initial dimple (compare Figure 4-9, arrows).

All in all, the essential imperfection shape shows a significantly lower imperfection amplitude, almost the same buckling load, the same characteristic pre-buckling deformations as well as the same position of the initial dimple which triggers the loss of stability in the first place.

Therefore, it is concluded that the reduced pattern is actually the (comparatively small) fraction of the original pattern which is essential for establishing the original pattern's buckling load. The following chapters aim at explaining the influence of input parameters like the threshold value η_t, proceed by broadening the application cases to numerous measured shells of varying geometry and laminate setup. Finally, the gained knowledge is used to deliver physical reasoning for the reduced patterns being the essential parts of original patterns.

4.2.3 Variation of the mode evaluation order

As described above, the SIFM is based on consecutively evaluating Fourier modes with respect to their influence on the buckling load. Here, the order in which the Fourier modes are evaluated has a significant effect on the set of remaining modes in the final reduced spectrum, due to the various mode interactions mentioned above. Thus, in the following the influence of various mode evaluation orders is investigated and recommendations are given.

When establishing an order in which the modes are evaluated, the most general case seems to be an arbitrary or random order. Thus, in a first step, a pseudo random mode evaluation order R1 is established. Figure 4-10, left shows a matrix of the Fourier modes, giving the axial half wave number and the circumferential full wave number on the x and y-axis, respectively. The colors of the squares indicate the position of the single modes in the vector defining the evaluation order. The arbitrariness of the mode evaluation order can easily be noticed. Figure 4-10, right gives the same matrix, indicating the set of remaining modes which have been characterized as essential for establishing the original shell's buckling load after completion of the SIFM routine.

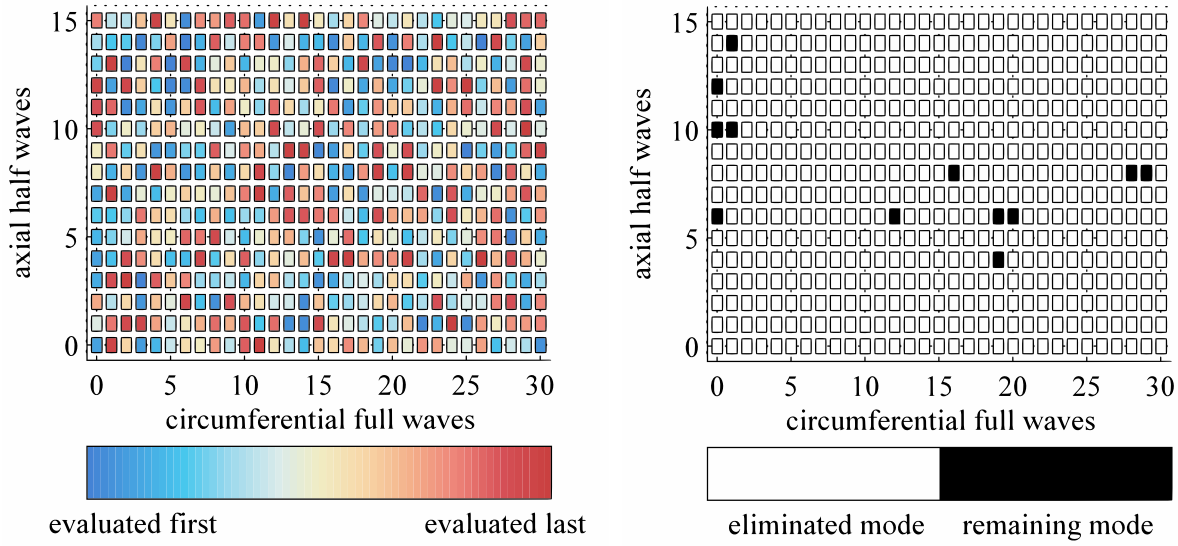

Figure 4-10: SIFM, random order R1: mode evaluation order (left) and remaining modes (right)

To compare the results, a second realization of a random mode order, R2, is established. The according matrices are given in Figure 4-11.

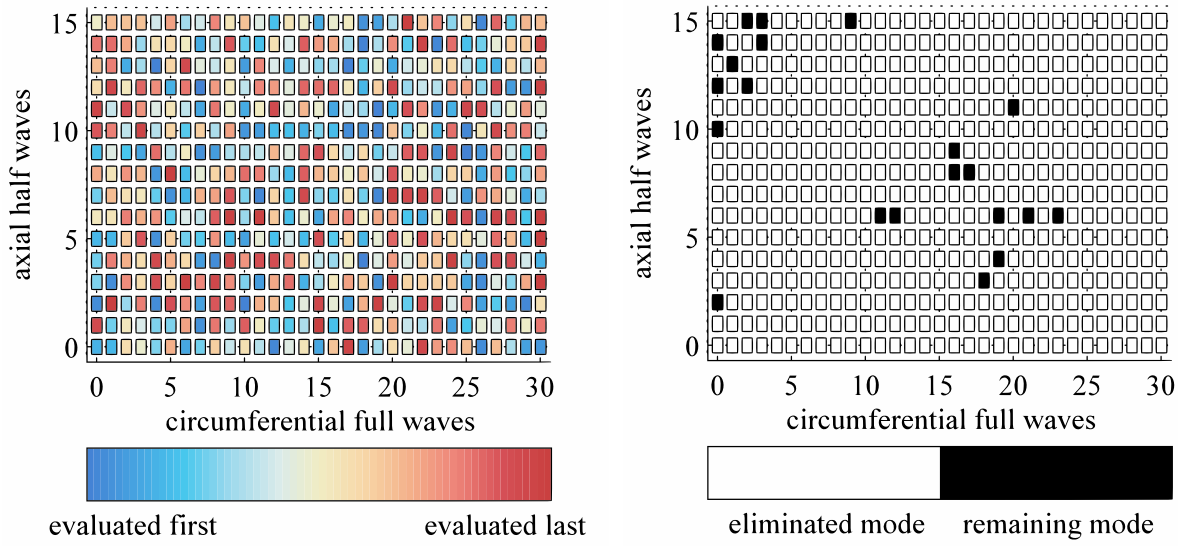

Figure 4-11: SIFM, random order R2: mode evaluation order (left) and remaining modes (right)

Comparing Figure 4-10, right and Figure 4-11, right, two common clusters of essential modes are identified in the regime of low circumferential wave numbers and high axial wave numbers as

well as in the regime of medium to high axial and circumferential wave numbers. It is worth noting that both groups of critical modes are outside of the regime of modes generally treated in literature (around 10 axial half waves and 15 circumferential full waves, compare chapter 4.1.3).

However, despite the general accordance of remaining mode clusters, the two sets include a different amount of different particular modes. Thus, it is noticed that different mode evaluation orders heavily impact the set of remaining modes obtained by the SIFM.

Figure 4-12 gives the imperfection patterns composed from the two reduced sets.

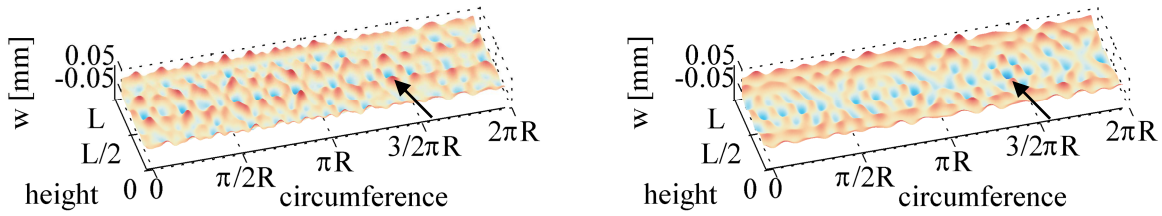

Figure 4-12: SIFM results for mode evaluation order R1 (left) and R2 (right)

While the reduced imperfection patterns are certainly not identical (due to being composed from different sets of modes), they still show similar amplitudes, similar general wavelengths, common buckling loads and, most importantly, the same characteristics at the same position of the respective initial dimples (compare Figure 4-12, arrows). As shown in chapter 3.2.3, the latter is determined by visually evaluating the radial deflection field right before and during buckling.

As all features comply with the main standards and outcomes of the SIFM, it can be assumed that the choice of the mode evaluation order may play a subordinate role.

As discussed earlier, different modes feature different impacts on the buckling load. The SIFM ends once no further modes can be eliminated in one filtration round. Therefore, it seems favorable for the numerical efficiency of the SIFM method to firstly evaluate the modes which will be eliminated most probably and afterwards check the modes which, based on a certain experience, will most probably remain in the spectrum.

As the reduced patterns, like the one exemplarily discussed in chapter 4.2.2, show significantly smaller amplitudes than the original imperfection patterns, it seems that higher amplitude modes tend to be eliminated. Figure 4-13 shows the results of the SIFM for a mode evaluation order based on descending mode amplitudes.

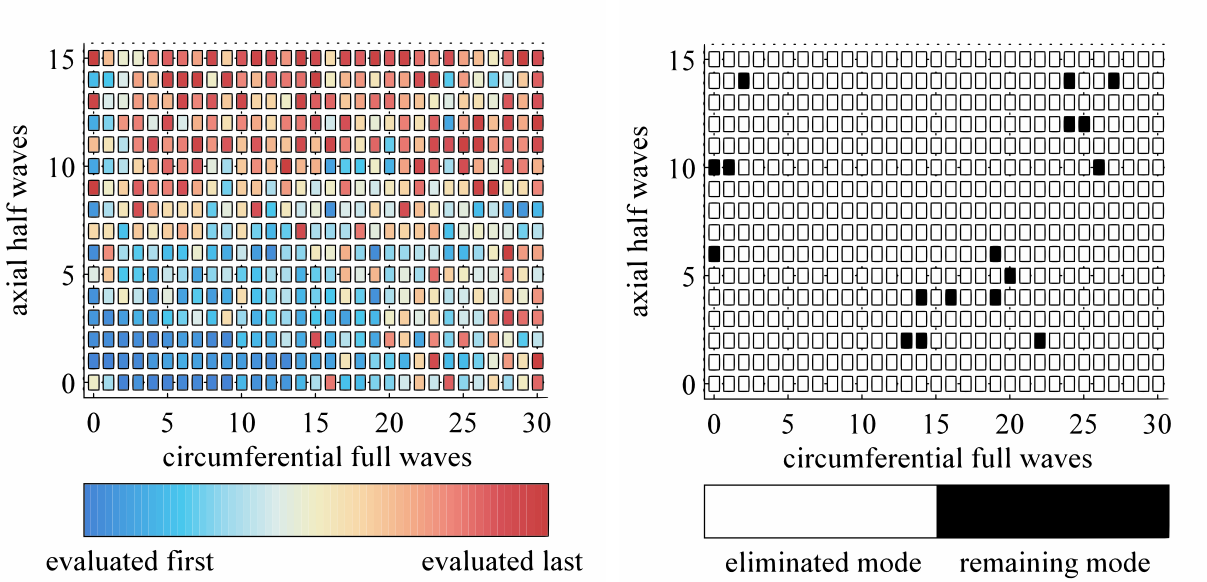

Figure 4-13: SIFM, mode evaluation by descending amplitude: mode evaluation order (left) and remaining modes (right)

Again, a different set of remaining modes is noticed. However, the pattern composed from the set of remaining modes again shows the same commonalities in features described above (compare Figure 4-15, left). It has to be noted that in the case discussed here, the initial dimple of the essential pattern obtained by a descending amplitude mode order does not comply with the initial dimple of the original pattern. This behavior is occasionally noticed when applying the SIFM to measured imperfection patterns and will be discussed in chapter 4.4.

The results shown above, namely the similarities in mode clusters, indicate that not necessarily the mode amplitudes themselves but the wavelength of the respective shapes are crucial for establishing a critical degradation of the shell's load carrying capacity. While in general long-waved modes do not seem to contribute to the buckling load degradation, the essential imperfection shapes are more short-waved. Thus, following the same idea to increase numerical efficiency, as a final variant for the mode evaluation order, the modes are sorted by their ascending wave numbers.

This is achieved by multiplying the wave numbers in axial and circumferential direction to gain a weighting value G_{kl} for every mode. As G_{kl} would be zero for all modes with zero axial waves or zero circumferential waves, the somewhat arbitrary parameters a and b are added to the multiplication:

$$G_{kl} = (k + a)(l + b) \text{ with } a = 1 \text{ and } b = 5 \tag{4-11}$$

The modes are then evaluated in an order based on ascending G_{kl}. Figure 4-14 again gives a visualization of the mode evaluation order and the remaining modes. The corresponding imperfection pattern is the one which was already given above in Figure 4-8 and, for the sake of better comparability, is depicted again in Figure 4-15, right.

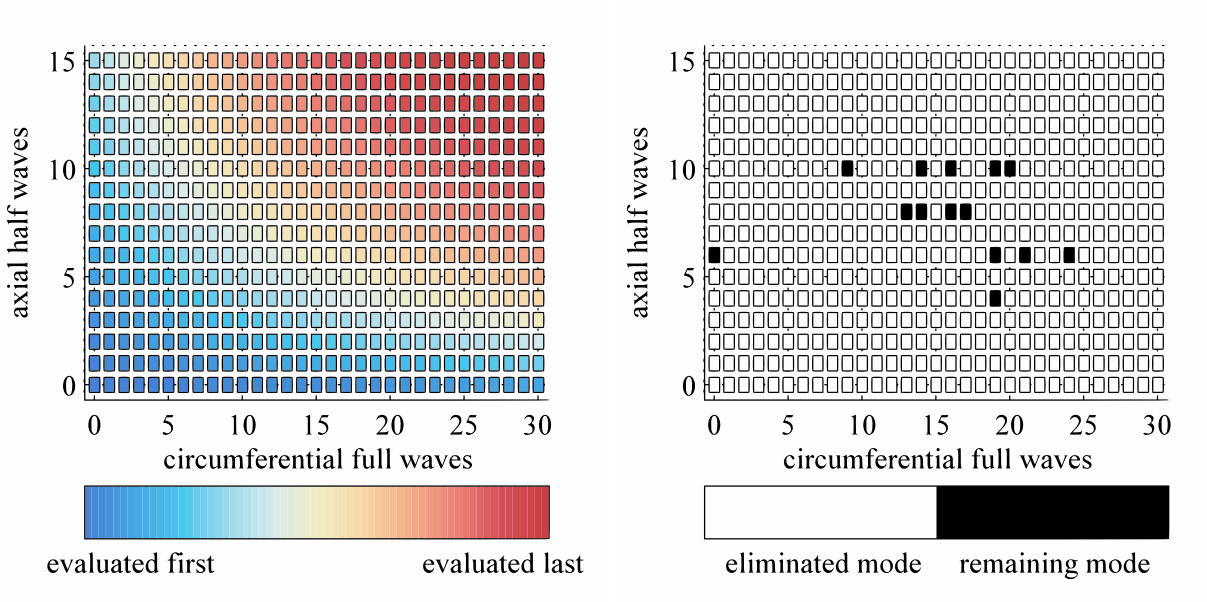

Figure 4-14: SIFM, mode evaluation by ascending wave numbers: mode evaluation order (left) and remaining modes (right)

When looking at Figure 4-14, it is noticed that the set of remaining modes is again different from the other three examples. However, the pattern composed from the set of remaining modes again shows the same commonalities in features described above (compare Figure 4-15, right).

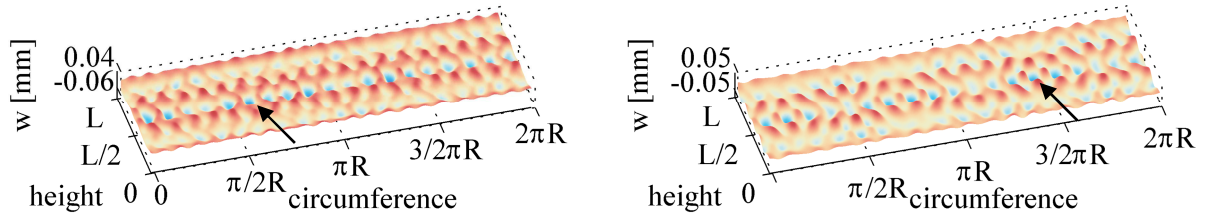

Figure 4-15: SIFM results for different mode evaluation orders: descending amplitude (left) and descending wavelength (right)

All in all it is stated that based on the chosen order of mode evaluation within the SIFM, the sets of particular essential modes differ. However, the corresponding imperfection patterns show distinct commonalities in the main criteria addressed by the SIFM. This is because their amplitudes, their general wavelengths, their buckling loads and their characteristic shapes around the initial dimples closely match. As further discussed in later chapters 4.4.3 to 4.4.6, primarily these local imperfection fields are crucial for destabilizing the shell and triggering the snap in of the initial dimple.

Due to the fact that evaluating the modes in an order based on the modes' wavelengths offers the highest potential to increase numerical efficiency, this variant is chosen for all studies within this thesis.

4.2.4 Variation of the threshold value

When discussing the basic scheme of the stepwise imperfection filtering method (SIFM) in chapter 4.2.1, a threshold value η_t was introduced. By using a reference load level $\lambda_{ref} = \eta_t \lambda_{orig}$ within the SIFM, a certain tolerance for the characterization of Fourier modes as essential or negligible is introduced.

The general aim of the SIFM is to determine the specific parts of a given imperfection pattern that primarily contribute to establishing its buckling load. The threshold value λ_t is used to specify "primarily". To actually identify and interpret the shapes which are essential for buckling, it is necessary to filter the imperfection pattern not only by removing possibly stabilizing modes but also eliminating modes of generally buckling load reducing but practically minor influence.

The smaller the threshold value is chosen, the closer the buckling load of the reduced pattern will be to the buckling load of the original pattern. While at first glance this seems desirable, the main aim of the SIFM, which is to make the essential imperfection shapes visible, might be missed. As explained in the following, this is because in order to establish lower and lower buckling loads, also modes which only cause comparatively small reductions in buckling loads are needed in the remaining pattern. While these modes may still marginally contribute to the low buckling load, they act as impurities or pollution when visibly inspecting and identifying essential modes shapes.

On the other hand, choosing higher threshold values leads to higher buckling loads λ, or, in this context, losses in buckling load reduction $\Delta\lambda$. Thus, while the reduced pattern contains modes which may be judged as extraordinarily critical, the fundamental claim of the SIFM, which is establishing closely comparable buckling loads with only fractions of the original pattern, will be lost.

Table 4-1 gives the results of SIFM calculations with threshold values from $\eta_t = 1.00$ to $\eta_t = 1.10$, thus allowing buckling load tolerances of 0% to 10%. Shell Z25 again exemplarily serves as basis for the calculations. The imperfection shapes resulting from the SIFM are given on the right.

threshold value	buckling load	number of modes	imperfection shape
original pattern	$\lambda_{orig} = 32.95\ kN$	496	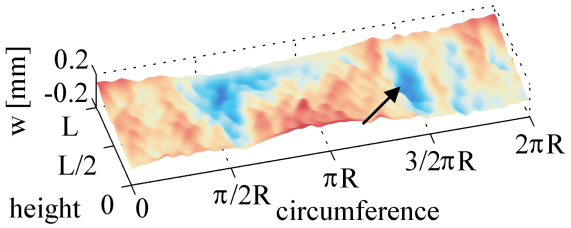
$\eta_t = 1.0$	$\lambda_{red} = 32.95\ kN$	19	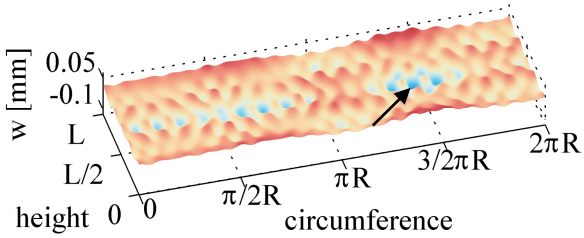
$\eta_t = 1.005$	$\lambda_{red} = 33.12\ kN$	26	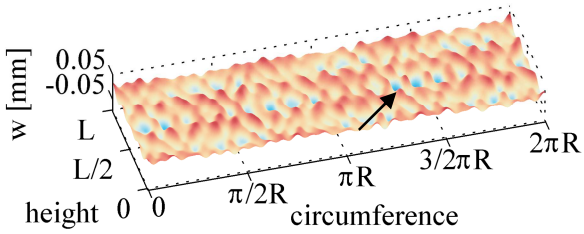
$\eta_t = 1.01$	$\lambda_{red} = 33.27\ kN$	14	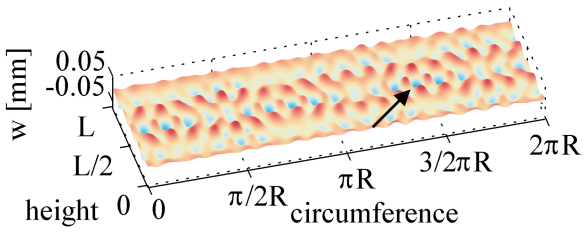
$\eta_t = 1.05$	$\lambda_{red} = 34.60\ kN$	23	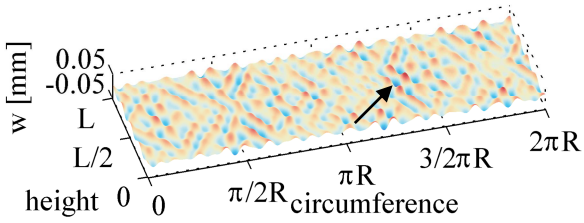
$\eta_t = 1.1$	$\lambda_{red} = 36.26\ kN$	31	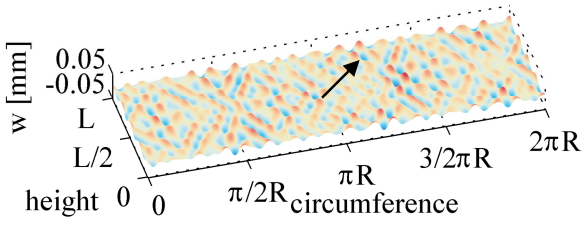

Table 4-1: SIFM applied to shell Z25, results for different threshold values η_t, positions of the initial dimples indicated by arrows

When looking at the results, ascending buckling loads with increasing η_t are noticed. These originate from the definition of the procedure, giving a buckling load tolerance from the reduced pattern to the original pattern. Thus, for example, the buckling load of the reduced pattern obtained with $\eta_t = 1.01$, $\lambda_{red,1.01} = 33.27\ kN$ is close to but still below $\lambda_{ref,1.01} = \eta_t\ \lambda_{orig} = 1.01 * 32.95 = 33.28\ kN$.

In the case of a chosen minimum threshold value of $\eta_t = 1.0$, the SIFM is restricted to maintain the same buckling load level as the original pattern of $\lambda_{orig} = \lambda_{red,1.0} = 32.95\ kN$. Still, a significant amount of modes can be eliminated as they apparently do not contribute to establishing the original pattern's buckling load. These are modes that have a (marginal but still) stabilizing influence on the stability behavior or sets of modes which, in superposition, cancel out each other's destabilizing influence (compare also Figure 4-16, downward slopes). Thus, in this example, a set of 19 specific modes of the original spectrum leads to an imperfection shape which causes the same buckling load as the whole original spectrum (compare Table 4-1, $\eta_t = 1.0$).

The number of modes which form the reduced pattern does not directly correlate to the threshold value.

The general appearance of all reduced patterns is comparable. Especially for $\eta_t = 1.0$ to $\eta_t = 1.01$, the pattern's recognizable characteristics of a local checker board style dimple accumulation generally match. However, when it comes to high threshold values, changes are noticed. While still being composed out of comparable amounts of modes, the reduced patterns of $\eta_t = 1.05$ and $\eta_t = 1.1$ have a much more short waved and uniform appearance with discrete zones of dimples.

Once loaded, all reduced patterns cause a snap-in of the initial dimple at the same position (compare Figure 4-9, right), except for the pattern with $\eta_t = 1.1$, where the initial dimple occurs near the shell's edge.

All in all, it is concluded that with increasing threshold value η_t, the buckling loads and positions of the initial dimples of the reduced pattern diverge from the ones of the original pattern. For small η_t, the reduced pattern's characteristic shapes are well comparable.

To better investigate the influence of the threshold value on the filtration process itself, Figure 4-16 gives the current load levels over the course of the filtration process for different threshold values. While the results for $\eta_t = 1.005$ were beneficial for the investigations given above, for reasons of clarity, they are omitted in Figure 4-16. In line with prior investigations, the original imperfection pattern is again the one of shell Z25.

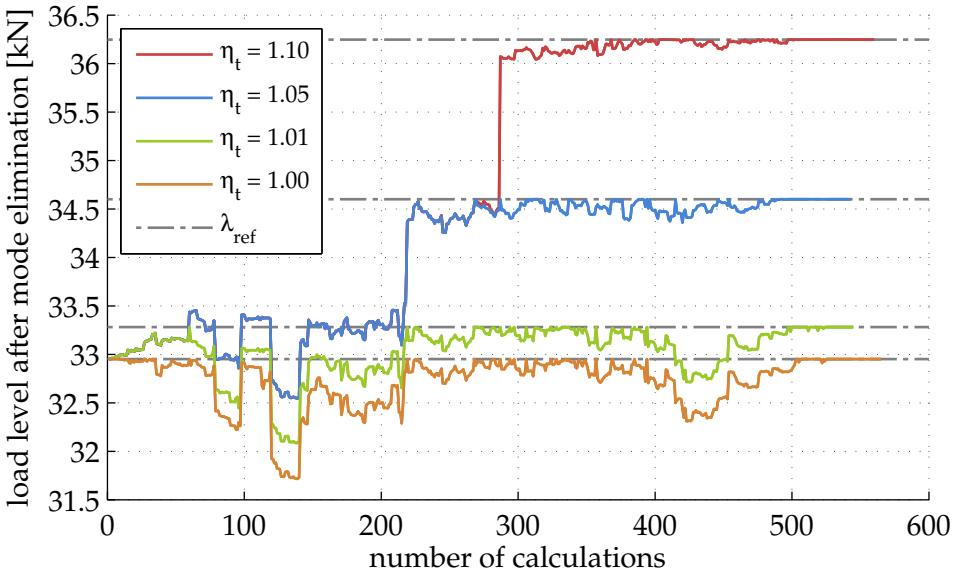

Figure 4-16: Load levels over the course of the SIFM filtration for different threshold values

Every given data point in Figure 4-16 depicts the buckling load of the shell which is obtained by removing one particular mode from the current set of modes. Thus, sudden decreases in load levels indicate the removal of stabilizing modes while sudden increases in load level indicate the removal of modes with detrimental influence on the buckling load. As explained above, this does not only confer to the influence of the single mode shape on the buckling load but also to its geometrical interaction with any or all other modes in the current set.

The different reference load levels $\lambda_{ref} = \eta_t \, \lambda_{orig}$ are indicated with dashed lines. If the removal of a mode leads to a buckling load above the respective dashed line, that particular mode is judged as critical and thus restored to the remaining set of modes. It should be noted that for reasons of clarity, the load levels in Figure 4-16 are limited to the respective reference loads. Thus, if the removal of a particular mode leads to an increase of the load level above the reference load, the actual load level without this mode is not depicted. This is due to the fact that after a mode is judged as essential, it is restored to the spectrum and the load level decreases to its prior state. As it does not contribute to a better understanding of the threshold value, this temporary buckling load is not depicted.

It is worth noting that the curves of all threshold values coincide until the reference load is first exceeded. Consequently, the curves of for example $\eta_t = 1.05$ and $\eta_t = 1.10$ (blue and red, respectively) coincide until the reference load is reached for $\eta_t = 1.05$ at around 270 calculations.

When looking at the load levels, it is noticed that in later stages of the filtration process, the buckling load levels approach the threshold value. This is due to the fact that the buckling load level is continually raised in the earlier stages. When, at the beginning of the process, a mode is eliminated and only a slight increase in buckling loads is noticed, this mode is still judged as negligible as its removal did not cause a crossing of the dashed line (compare for example Figure 4-16, $\eta_t = 1.01$, from 0 to 35 calculations, reprinted excerpt in Figure 4-17). In this way, the buckling load level accumulates and approaches the dashed line, lowering the individual tolerance for all subsequently examined modes.

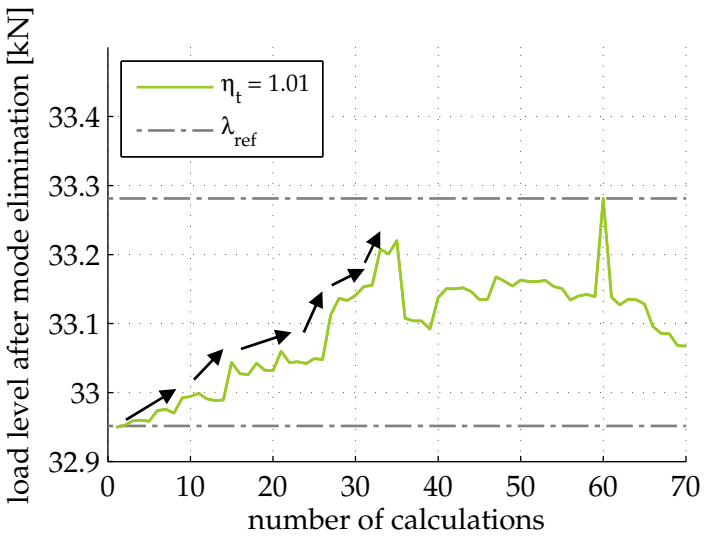

Figure 4-17: Load levels over the SIFM filtration for a threshold values of $\eta_t = 1.01$, general load level accumulation indicated by arrows, excerpt from Figure 4-16

The higher the reference load is chosen, the higher the buckling load level is allowed to accumulate. This can lead to situations where modes, despite showing a comparatively high detrimental influence on the buckling load, are still judged as negligible and thus are removed from the spectrum (compare Figure 4-16, $\eta_t = 1.10$, at around 220 and 290 calculations, reprinted excerpt in Figure 4-18).

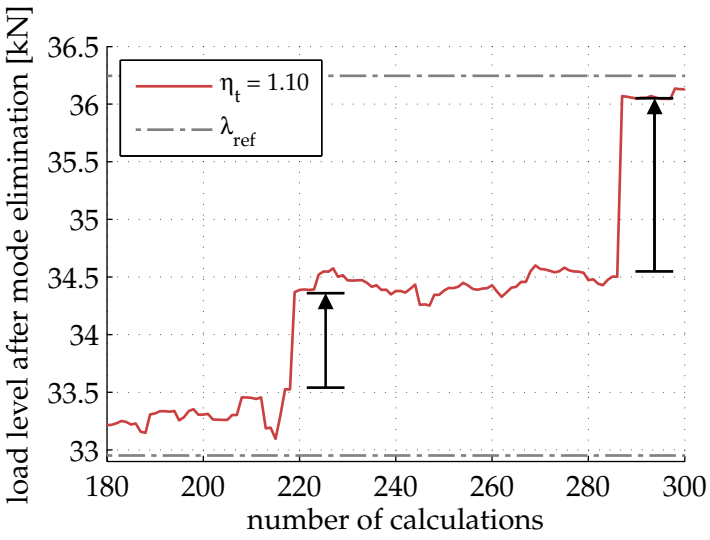

Figure 4-18: Load levels over the SIFM filtration for a threshold values of $\eta_t = 1.10$, eliminated modes with high detrimental influence on the buckling load indicated by arrows, excerpt from Figure 4-16

Despite the comparatively high jump in load levels, the buckling load of the current spectrum without these particular modes is still below the respective reference load and therefore the mode is eliminated. This effect is undesired as it obviously does not comply with the general aim of the SIFM to filter an original pattern to its inherent parts driving the buckling process.

Based on these observations it can be stated that the threshold value η_t does not represent a universal minimum for the buckling load reduction of a particular mode to be judged as critical. It can rather be interpreted as a measure for the tolerance of how similar the final reduced imperfection shape is compared to the original one with respect to its behavior before and during buckling.

These findings lead to a concrete guideline of the influence of the threshold value on the SIFM filtration process:

The higher the threshold value is chosen, the longer the buckling load level can accumulate over the course of the filtration process. This leads to the possibility that medium or highly critical modes are eliminated, as their removal did indeed significantly increase the buckling load level but not above the reference load.

Once load levels reach the vicinity of the reference load, the requirements for a particular mode to be judged as critical, or in other words the tolerance for a particular mode to be judged as negligible, decrease (as the base load level of the filtration is closer to the reference value). This in turn means that the higher η_t is chosen, the more imbalanced the effect of the evaluation criterion is within the whole spectrum, as modes which are checked earlier are judged with higher tolerance than modes which are evaluated later in the process.

However, higher threshold values lead to an increased filtration of the pattern, as a certain freedom for load accumulation leads to numerous modes with comparatively small detrimental influence on the buckling load being eliminated. This confers with the aim of the SIFM to filter out the majority of the original spectrum which only marginally contributes to initiating buckling.

The lower the threshold value is chosen, the less freedom for load accumulation in the early stages of filtration is allowed. Then, the drops in load levels noticed when removing stabilizing modes have a more important impact on the results as they offer the sole option for filtering out modes with smaller detrimental influence on the buckling load (compare Figure 4-16, $\eta_t = 1.00$, at around 130 calculations). Therefore, for low threshold values, tendentially more modes are judged as critical earlier in the process. This however does not mean that the final reduced spectrum would contain more modes in total. By including numerous modes with small detrimental influence early, modes with comparable influence which are evaluated later in the process are more likely to be eliminated (compare Figure 4-16, $\eta_t = 1.0$ and $\eta_t = 1.05$, at around 430 calculations). This makes the procedure itself tendentially more balanced and independent from the mode evaluation order.

In certain cases, this effect can cause a practical problem in the case of mode evaluation orders based on the modes' wavelengths or amplitudes (compare chapter 4.2.3). With these evaluation orders, long waved modes of expectedly higher amplitude are evaluated first. As described above, when choosing a low threshold value, despite these modes' marginal influence on the buckling load, their probability to remain in the spectrum is higher. Thus, when visually inspecting the final reduced pattern, single long waved modes may overlay the rest of the imperfection shape, making the interpretation of essential imperfection shapes difficult. In these cases, a manual elimination of the particular long waved or high amplitude mode may lead to very well comparable buckling loads with much better visibility of the underlying essential imperfection pattern (compare chapter 4.3.1, SIFM application to shell Z17).

In this thesis, the main aim of the development and application of the SIFM is to identify the essential part of a given imperfection pattern to be able to better inspect and interpret the influence of geometric imperfections on the buckling load. Thus, it is desired to prevent spurious modes with high amplitude but low influence on the buckling load from being contained in the reduced imperfection shape. Therefore, a higher value of η_t seems desirable. However, no modes of considerable detrimental influence on the buckling load should be neglected, locking very high values for η_t. When aiming for identifying the essential part of a measured imperfection pattern, it is of vital interest to closely match the buckling load of the original pattern. As $\lambda_{red} \approx^{!} \lambda_{orig}$, a lower threshold value seems mandatory. Furthermore, lower threshold values tendentially lead to higher robustness of the procedure regarding the mode evaluation order.

Therefore, in all subsequent studies, a threshold value of $\eta_t = 1.01$ is chosen. In numerous simulations with all shell measurement available to the author, this has been proven to be best suited to identify the essential parts of measured imperfection patterns and their relations during buckling (compare the following chapters). When applying the SIFM to shells of other characteristic geometry, this choice should be carefully reevaluated.

All investigations given above might lead to the impression that η_t vitally influences the applicability of the SIFM. While from a mathematical or academic point of view the mechanisms depicted above certainly effect the outcome of the procedure, the SIFM's dependence on η_t is certainly damped from an engineering point of view. On the one hand, the effect of most mechanisms even out by constantly reevaluating the remaining spectrum until no further modes can be eliminated (compare chapter 4.1.1). On the other hand, the aim of the procedure is not to identify the particular set of particular modes of the most severe influence on the buckling load but to find an essential imperfection shape, regardless of the particular modes included (compare Table 4-1, $\eta_t = 1.00$ to $\eta_t = 1.01$).

Thus, the scientific progress of this thesis is mainly achieved by, for the first time, revealing the concealed part of a given measured imperfection shape which is responsible for the precise buckling phenomena of this original imperfection shape.

4.2.5 Dynamic adaptation of the reference load level

Within the SIFM, a mode is identified as stabilizing by noticing a decrease in load level when removing that particular mode (compare chapter 4.2.4). Regardless of how the threshold value is chosen, this decrease in load level allows for a subsequent load level accumulation equivalent to that decrease in load level. As discussed above, in certain cases this can lead to a potentially detrimental mode being judged as negligible (compare for example Figure 4-16, at around 140 calculations).

To prevent missing detrimental modes in the reduced spectrum, a modification to the original SIFM procedure given in chapter 4.2.1 can be made. For this purpose, the original reference load level $\lambda_{ref} = \eta_t \, \lambda_{orig}$ is altered in a way that it is derived using the current load level of the filtration state λ_{cur}:

$$\lambda_{ref,mod} = \eta_t \, \lambda_{cur} \tag{4-12}$$

In doing so, the buckling load obtained by removing a particular mode will not be compared to a fixed value around the original pattern's buckling load but to the load level present prior to removing that particular mode. This in turn means that the threshold value η_t now actually is a measure for the minimum detrimental influence of a particular mode on the buckling load.

Figure 4-19 shows the application of the SIFM in this modified version to shell Z25 with a threshold value of $\eta_t = 1.0$, giving the matrix of remaining modes on the left and the corresponding reduced pattern on the right. This again means that the buckling load of the reduced pattern is forced to equal the buckling load of the original pattern (for a detailed discussion on the threshold value η_t confer chapter 4.2.4).

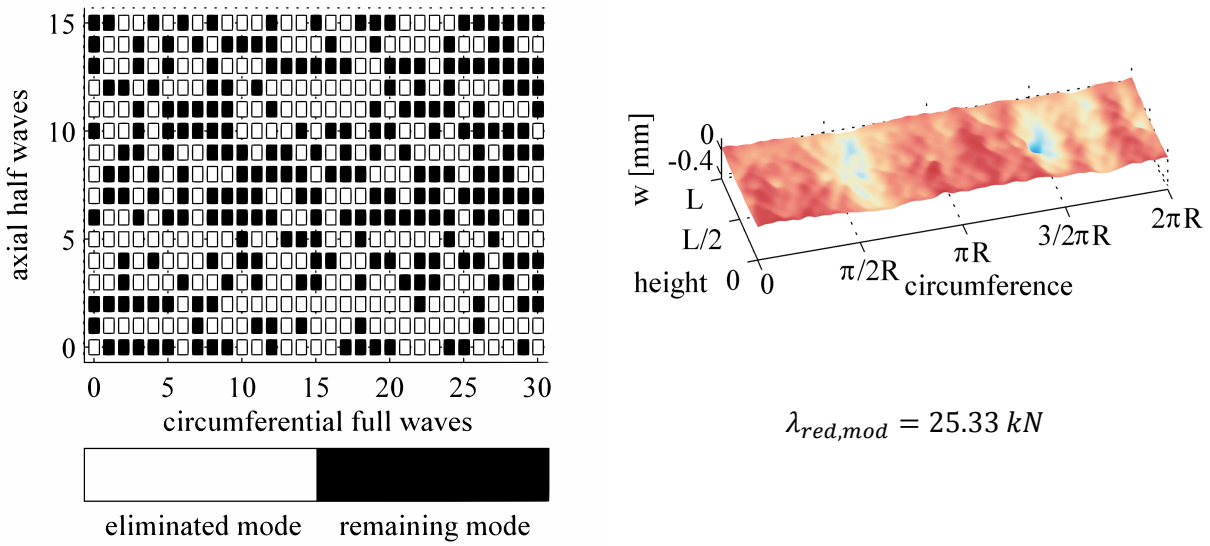

Figure 4-19: SIFM results, shell Z25, modified reference load level $\lambda_{red,mod}$, threshold value $\eta_t = 1.0$, remaining modes (left) and corresponding reduced pattern (right)

When looking at the matrix of remaining modes it is noticed that the reduced spectrum contains a comparatively high number of modes. While all investigations above yielded reduced spectra of

around $n_{red} \approx 20$ to 30 modes, the given spectrum contains $n_{red,mod} = 239$ modes which roughly corresponds to half of the original spectrum. When investigating the corresponding imperfection shape, similarities with the original pattern can be noticed (compare Figure 4-7 to Figure 4-19, right). The amplitude of the reduced pattern is in the regime of the original pattern's amplitude and thus is significantly higher than in the reduced patterns of the before mentioned analyses. The buckling load of the reduced pattern $\lambda_{red,mod} = 25.33\ kN$ shows to be significantly smaller than the one of the original pattern $\lambda_{orig} = 32.95\ kN$.

In a second analysis, the threshold value is raised to $\eta_t = 1.01$, in line with the insights given in chapter 4.2.4. Figure 4-20 shows the application of the SIFM in the modified version to shell Z25 with a threshold value of $\eta_t = 1.01$, giving the matrix of remaining modes on the left and the corresponding reduced pattern on the right.

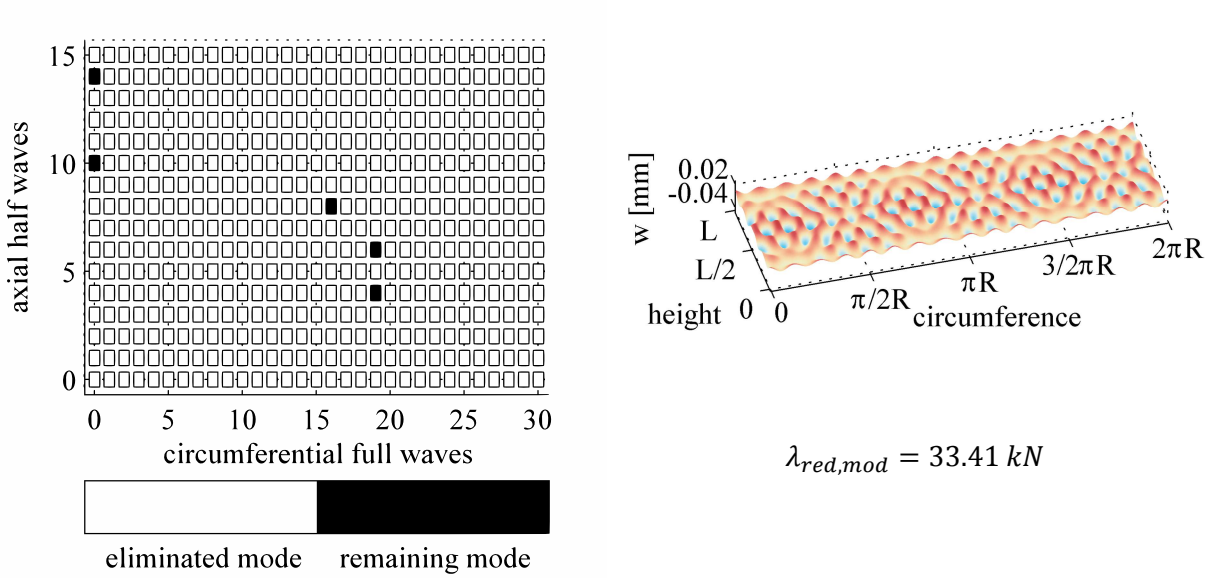

Figure 4-20: SIFM results, shell Z25, modified reference load level $\lambda_{red,mod}$, threshold value $\eta_t = 1.01$, remaining modes (left) and corresponding reduced pattern (right)

It is noticed that the increase of the threshold value from $\eta_t = 1.0$ to $\eta_t = 1.01$ leads to a drastic reduction in remaining mode numbers. Instead of $n_{red,mod} = 239$ for $\eta_t = 1.0$, only $n_{red,mod} = 5$ modes are included in the reduced spectrum for $\eta_t = 1.01$. Accordingly, the corresponding imperfection shape shows a much more homogeneous and undisturbed checker board pattern with comparatively low amplitude. The buckling load of the reduced pattern $\lambda_{red,mod} = 33.41\ kN$ is now higher than the one of the original pattern $\lambda_{orig} = 32.95\ kN$.

The explanation for the results shown above is found in the redefinition of the reference load. When, during the filtration process, the removal of a particular mode leads to an increase in load levels, the magnitude of this increase is compared to the load level λ_{cur} prior to removing the mode, multiplied by η_t (compare (4-12)). The mode is judged as critical if its corresponding increase in load levels is above this threshold. It has to be noted that this again applies to the particular modes' influence on the buckling load as well as its interaction with any or all of the other modes in the reduced spectrum.

Therefore, for $\eta_t = 1.0$, a reduced pattern containing all modes with any detrimental influence on the buckling load, no matter how small, is obtained while all stabilizing modes are filtered out. In other words, conducting the SIFM with the modified reference load and a threshold value of $\eta_t = 1.0$ leads to the most critical set of modes drawn from a given original spectrum.

Conducting the SIFM with the modified reference load and a threshold value of $\eta_t > 1.0$ leads to a reduced pattern containing all modes with a minimum detrimental influence on the buckling load given by the respective value for η_t. Thus, η_t can in this way be used to actively filter a given pattern with respect to the individual modes' criticality. It has to be noted that this does not necessarily lead to a corresponding reduced pattern with a particularly low buckling load as the higher the threshold value η_t is chosen, the more detrimental the remaining modes may be but the smaller their number most certainly is.

Moreover, performing the SIFM in the modified way described above also decouples the reduced pattern's buckling characteristics from the original pattern's buckling load. The modified method can be interpreted as a controllable worst-case approach to obtain the most severe imperfection shapes from a given set of modes, without preserving a mechanical connection to the original pattern. This can be interesting in the pursuit of lower-bound approaches, having in mind the robust design of shell structures.

In contrast to that, the original SIFM described in chapter 4.2.1 filters out imperfection shapes which are unnecessary for establishing the buckling behavior caused by the original pattern. Thus, as the focus of this thesis lies in identifying the crucial parts of a given imperfection pattern which cause its precise buckling phenomena, the modified method will neither be applied nor discussed any further herein.

4.2.6 On the numerical costs

Besides the influence of certain parameters on the outcome of the SIFM, also the methods' numerical costs shall be discussed.

Obviously, the numerical costs of the SIFM are mainly dependent on the profundity of the buckling load evaluations as well as on their required amount.

All buckling load calculations within the SIFM have to be performed geometrically nonlinear to properly depict the decisive highly nonlinear prebuckling behavior (compare chapter 3.2). However, the time to obtain the nonlinear limit point load of a shell with a certain imperfection shape can be influenced by altering the applied FE discretization. Besides using reduced integration schemes and linear element formulations, the physical element size can be increased to lower computational time. Here, usually criteria like for example convergence of a specific target value, in this case the buckling load of the shell, are applied to find the optimal balance between precision of the results and computational effort. In the case of closely investigating on the influence of geometric imperfection wave shapes on the buckling behavior, the mesh fidelity is also directly related to the fidelity of the wave shapes included in an original pattern. This is because when modes of short wavelengths are included in the Fourier series describing the pattern, the element size must comply with the minimum wavelength included to properly geometrically express that wave shape. Here, a general rule of thumb is to use at least six nodes to define the geometry of a single half wave (compare Figure 4-21 and Marburg [109]).

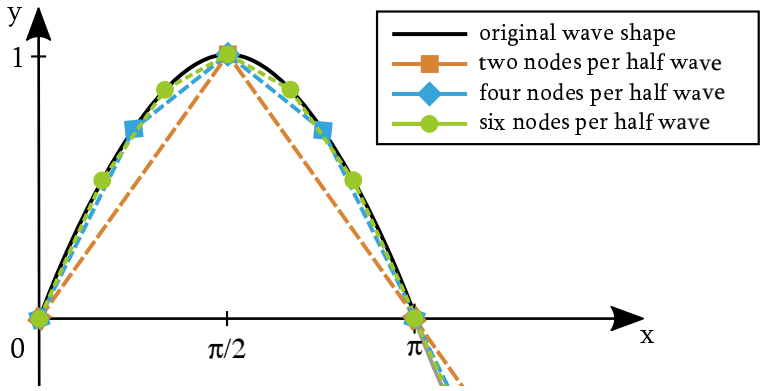

Figure 4-21: Approximation of a given wave shape with different amounts of FE nodes

In addition to optimizing the FE discretization, the computational time of the buckling load evaluations can further be reduced by purposefully canceling the calculation once the axial load level of a given current realization exceeds the reference load level λ_{ref}. This is because if the removal of a mode yields a shell with a prebuckling equilibrium solution at a load level higher than λ_{ref}, this shell will in turn have a buckling load which is at least of this load level. Therefore, this particular mode is characterized as essential in any case and remains in the spectrum. When using the commercial FE solver ABAQUS (compare chapter 6.1.2), the deliberate cancelation of running calculations can be achieved by applying an according user subroutine.

In the context of numerically expensive calculations, the parallelization of computational threads is an often applied tool. In the context of the SIFM, parallelization can only be utilized on the

level of a given particular simulation, not on the level of the method itself. This is due to the fact that the preprocessing of one given simulation, namely the Fourier spectrum applied in that particular calculation, is directly dependent on the results of the preceding simulation, namely the removal or the retention of modes from the Fourier spectrum.

Besides the configuration of the specific FE buckling load calculations, the numerical costs of the SIFM are mainly dependent on the mere amount of these calculations. Here, the fidelity of the Fourier series is the main leverage point to reduce the total time needed to obtain the essential imperfection pattern. This is because the less modes are included in the Fourier representation which defines the original pattern, the less modes have to be evaluated regarding their influence on the buckling load and thus the lower the total numerical costs of the SIFM are. For example, performing the SIFM with a Fourier fidelity of $n_{total} = n_1 x\, n_2 = 11\, x\, 21 = 231$ modes would require $c_{total} = 231 + c_+$ calculations, where c_+ is the unknown number of necessary mode reevaluations towards the end of the procedure (compare chapter 4.2.1). The SIFM results presented in this thesis where performed with a Fourier fidelity of $n_{total} = n_1 x\, n_2 = 16\, x\, 31 = 496$ and thus required a total amount of $c_{total} \approx 520$ buckling load evaluations. When comparing these numbers, the high potential for significant reductions in computational time by reducing the fidelity of the Fourier representation becomes obvious. However, while in this context a low number of modes seems desirable, the fidelity of the Fourier decomposition of a given pattern is decisively dictated by the necessity to properly cover all inherent influential wave shapes. As shown in chapter 4.1.3, the representation of a measured pattern by a Fourier series which is too coarse can significantly alter the obtained buckling loads and lead to false prebuckling phenomena.

In addition to the amount of modes included in the Fourier series, also the order in which the modes are evaluated influences the numerical costs. As shown above, in the exemplary case of shell Z15 to Z26, the final essential patterns are composed of mostly short waved modes, while long waved modes are mostly eliminated. Thus, to reduce computational time, these long waved modes can be evaluated, and thus probably eliminated, first. In this way, the chance of a reevaluation of these modes decreases which in turn lowers the total computational costs (compare chapters 4.2.3 and 4.2.4).

To conclude, performing the SIFM to obtain the essential part of a given imperfection pattern is taxed by high numerical costs. Still, when investigating the physical meaning and influence of geometric imperfections on the buckling load, this effort seems highly worthwhile. This is because numerous spurious wave shapes can be filtered out, the imperfection amplitudes are significantly reduced and the imperfection shape characteristics can be more directly compared to the characteristics of the nonlinear prebuckling deflections. This opens the way to progress into the direction of actually understanding why and which imperfection shapes are responsible for the detrimental buckling load reductions observed.

4.3 Application of the SIFM to multiple shell specimen

4.3.1 Application to shells with coinciding geometry and laminate setup

The SIFM filters given imperfection patterns down to their characteristic parts which are essential for establishing the buckling load of the particular given imperfection pattern. Consequently, in the case of two nominally identical shells with similar original patterns with comparable buckling loads, the SIFM should yield reduced patterns which are not only comparable in corresponding buckling loads but also similar in their characteristic shape. Here, in all subsequent studies, the SIFM is applied in its original definition as given in chapters 4.2.1 to 4.2.4. The modified version discussed in chapter 4.2.5 is neither applied nor discussed any further.

4.3.1.1 Shells Z20 and Z26

The coherences between similar original patterns and their reduced shapes can well be illustrated by exemplarily looking at the SIFM results of shells Z20 and Z26. All shells of the Z2x set feature the same nominal shell geometry. They were made with the same manufacturing technique and thus share similar manufacturing signatures, similar geometric imperfection shapes and comparable maximum imperfection magnitudes [110]. Table 4-2 gives the original measured imperfection shapes on the left and the corresponding reduced patterns on the right. The results for shell Z25, which were thoroughly discussed above, are given again for reasons of comparability. The SIFM results for all shells with available imperfection measurements are given in appendix A.

	original imperfection shape	reduced imperfection shape
Z20	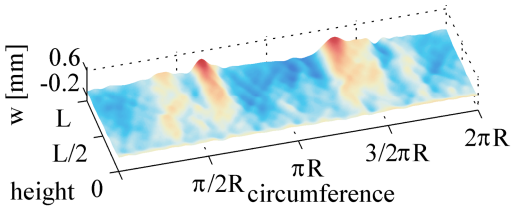 $\lambda_{orig} = 30.48\ kN$	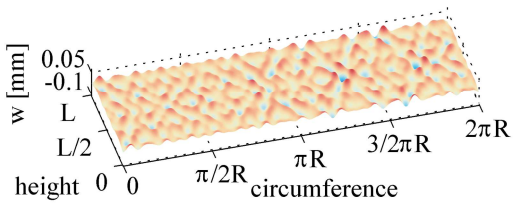 $\lambda_{red} = 30.77\ kN$
Z25	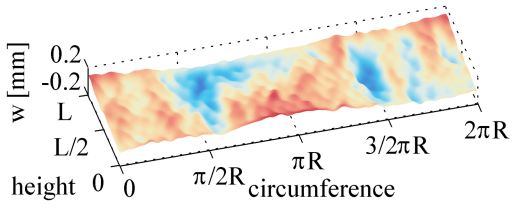 $\lambda_{orig} = 32.95\ kN$	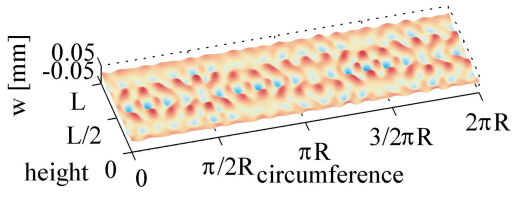 $\lambda_{red} = 33.27\ kN$
Z26	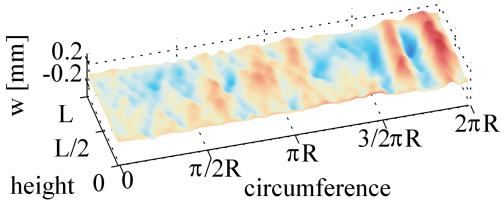 $\lambda_{orig} = 31.46\ kN$	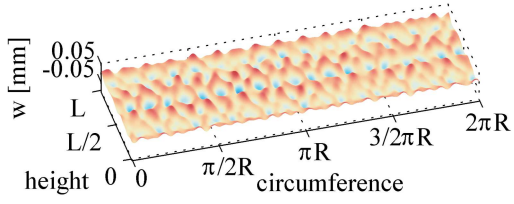 $\lambda_{red} = 31.77\ kN$

Table 4-2: SIFM applied to shells Z20, Z25 and Z26, measured imperfection patterns (left) and reduced patterns (right)

Despite the common manufacturing technique, when comparing the measured imperfection shapes, the different general appearances are noticed. While shell Z20 shows two distinct imperfection maxima at the shell's upper edge, shell Z25 appears more homogeneous in shape. Shell Z26 is comparatively homogeneous but shows a singular folding-like distortion with high amplitudes on the right of the depicted unwrapped surface.

When investigating on the reduced shapes, the commonalities are more apparent. The depicted reduced patterns feature common prevailing wave length, imperfection magnitudes as well as the characteristic checker-board shape of changing local minima and maxima. While the reduced shape of shell Z20 shows a more singular concentration of this characteristic local area, in the case of shell Z25 and Z26 the checker-board pattern is repeated around the shells' circumference. The buckling loads of the reduced patterns cannot be directly correlated to the imperfection shapes.

As no measured imperfection shape looks like another, also the Fourier coefficients the patterns are decomposed into cannot be identical. Therefore, the reduced patterns obtained by applying the SIFM to different measured imperfection shapes will always differ and can never be entirely identical.

While in the previous chapters the wave length of different modes were the main focus of argumentations, it has to be stated that also the different modes' amplitudes and circumferential phase shifts decisively influence their detected impact on the buckling load. Thus, in one particular measured spectrum, a particular mode may have an amplitude high enough or a fitting phase shift to cause a detrimental interaction with other modes. This would cause the particular mode to heavily impact the buckling load. However, in another measured spectrum this may very well no longer be the case and the same particular mode may even be judged as negligible.

This is the reason why for different measured patterns and thus different original Fourier spectra, different modes are judged as critical or filtered out by the SIFM. Still, as shown above, the general appearance of the imperfection patterns corresponding to the reduced spectra show distinct commonalities. This again emphasizes the general understanding of SIFM results: Performing the SIFM does not lead to a concrete set of particular modes which are most critical for the buckling load. The SIFM rather yields a thinned out geometric imperfection shape which causes the same buckling behavior as the original imperfection pattern, regardless of which modes of which amplitudes or phase shifts represent that reduced imperfection shape.

4.3.1.2 Shell Z17: Spurious modes impeding the evaluation of the essential imperfection shape

While the measured imperfection patterns of shells Z20, Z25 and Z26 show certain differences in appearance, their characteristic wavelength and imperfection magnitudes are similar. Thus, to broaden the field of application cases, the SIFM is applied to shell Z17. Table 4-3 again gives the original measured imperfection shape on the left and the corresponding reduced pattern on the right.

	original imperfection shape	reduced imperfection shape
Z17	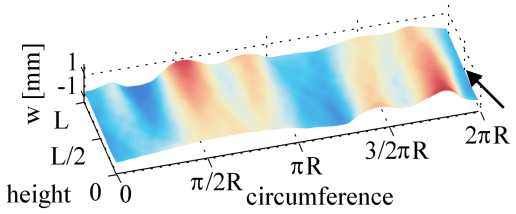	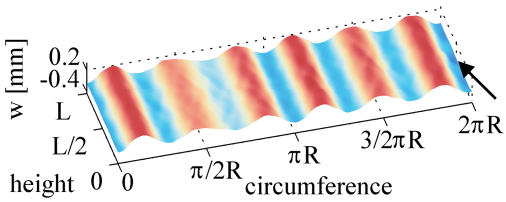
	$\lambda_{orig} = 30.01\ kN$	$\lambda_{red} = 30.35\ kN$

Table 4-3: SIFM applied to shell Z17, measured imperfection pattern (left) and reduced pattern (right), positions of the initial dimples indicated by arrow

When looking at the original imperfection shape, its general appearance is much more long-waved compared to shells Z20 to Z26. In addition to that, the maximum imperfection amplitudes are significantly higher. Similarly, the investigation of the reduced pattern reveals significant differences to the previously discussed reduced patterns. A distinct predominant wave shape with zero axial waves and around six circumferential full waves is clearly visible. Figure 4-22 gives the matrix of modes active in the reduced spectrum on the left.

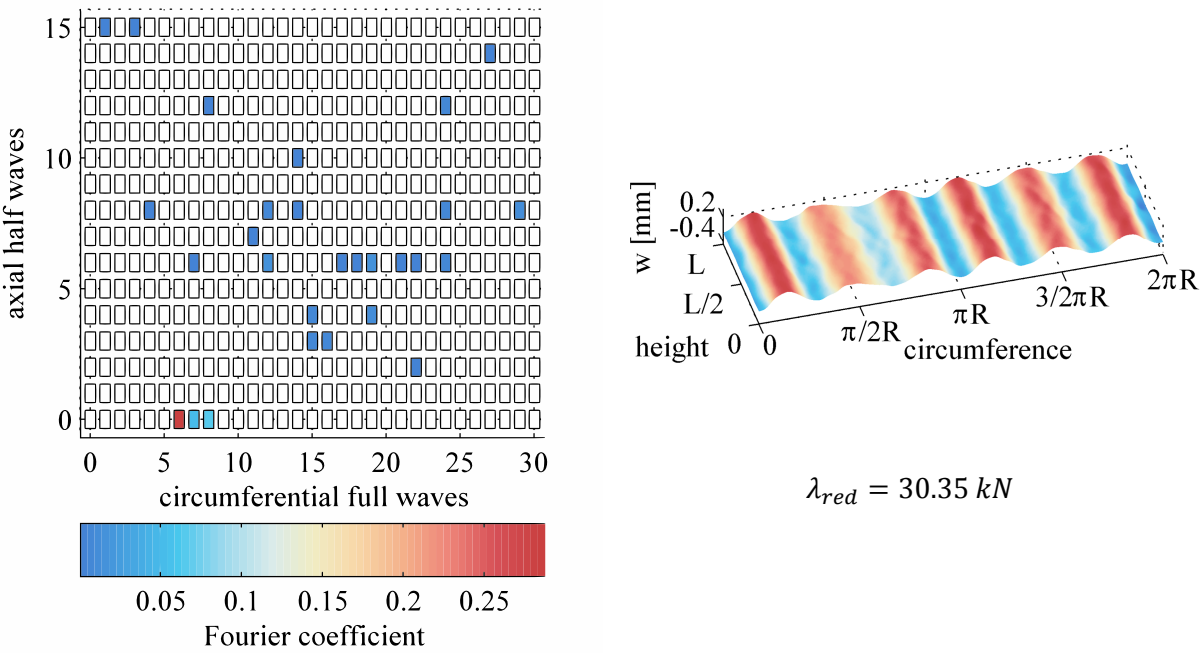

Figure 4-22: SIFM applied to shell Z17, modes in the reduced spectrum (left) and reduced pattern (right)

When looking at the matrix of modes, the predominant wave shape found in the reduced imperfection pattern on the right can easily be identified. It is noticed that three modes of zero

axial half waves and six, seven and eight circumferential full waves with comparatively high amplitudes are clustered and lie isolated from the field of the other remaining modes.

When performing the SIFM with comparatively low threshold values η_t, long waved modes of high amplitude may in certain cases, depending on the mode evaluation order, remain in the reduced spectrum despite having a marginal influence on the buckling load (compare chapter 4.2.4).

It is assumed that the particular wave shape noticed in the reduced pattern of shell Z17 represents one of those cases, where a spurious long waved mode of high amplitude overlays the rest of the imperfection shape, hampering proper evaluation of the essential imperfection pattern.

Figure 4-23, left gives the matrix of remaining modes where the distinct cluster of modes at zero axial half waves and around six to eight circumferential full waves is artificially removed. Figure 4-23, right gives the imperfection shape corresponding to this modified spectrum.

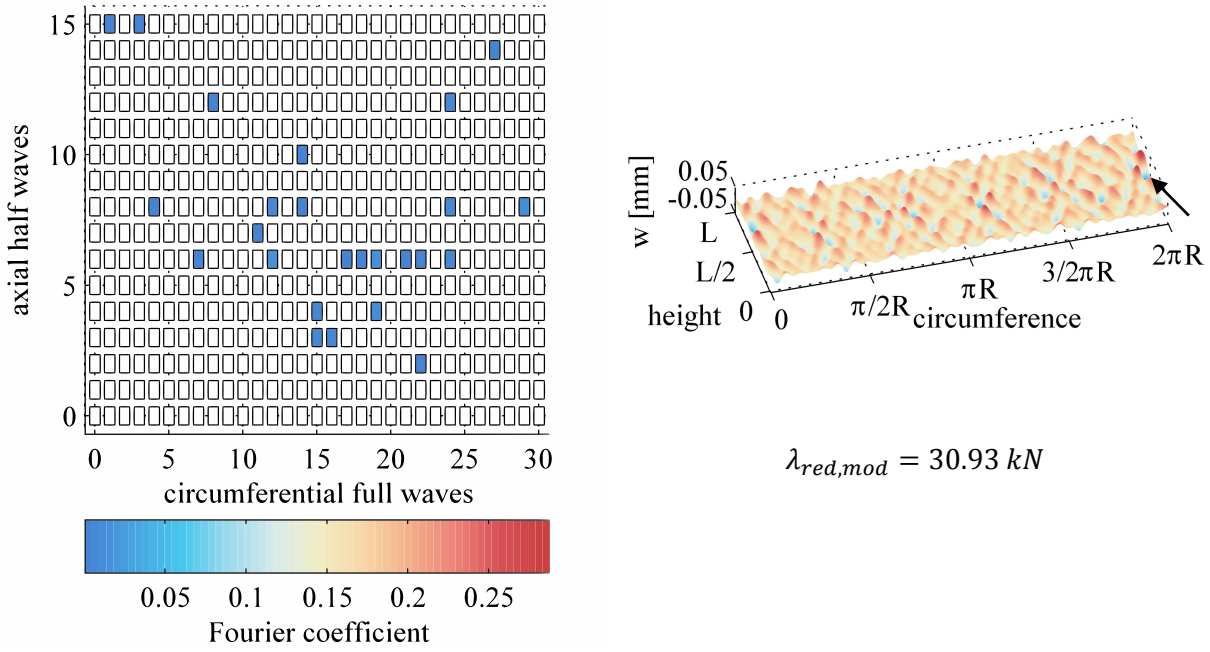

Figure 4-23: SIFM results, shell Z17 with modified reduced spectrum, remaining modes (left) and corresponding reduced pattern (right), position of the initial dimple indicated by arrow

By removing the cluster of long-waved modes discussed above, a modified imperfection pattern is obtained. The maximum imperfection amplitude is reduced to $\frac{w_{max,red,mod}}{w_{max,red}} = \frac{0.046}{0.229} \approx 20\%$ of the unmodified reduced pattern. The positions of the initial dimples of both reduced patterns concur with the one of the original measured imperfection pattern. In contrast to the significant reduction in maximum amplitudes, the buckling load reduction of the modified pattern $\Delta\lambda_{red,mod} = \lambda_{perf} - \lambda_{red,mod} = 37.62 - 30.93 = 6.69\ kN$ is still in the same regime as the buckling load reduction of the unmodified reduced pattern $\Delta\lambda_{red} = 37.62 - 30.35 = 7.27\ kN$.

This increase in buckling loads is attributed to the removal of the local minimum the long-waved mode shapes enforce at the position of the initial dimple. Figure 4-24 schematically depicts the reallocation of the locally critical imperfection shape by a long waved dominant mode shape.

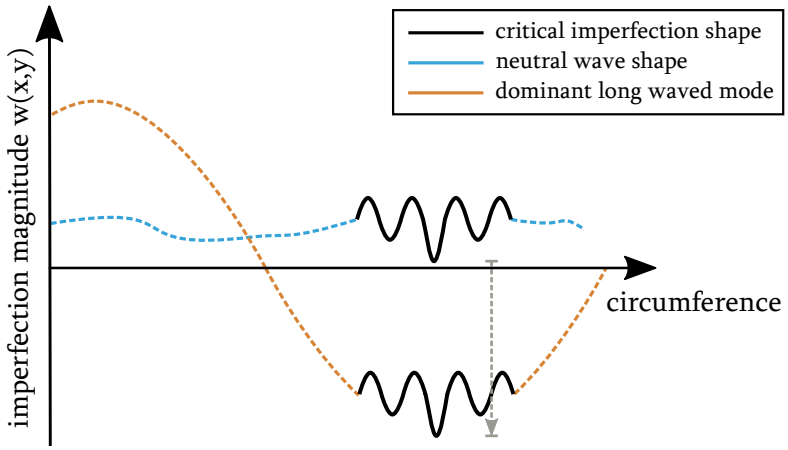

Figure 4-24: Schematic of dominant modes enforcing a radial relocation of the locally critical imperfection shape

When investigating closely on the unmodified reduced pattern given in Table 4-3, right at the position of the initial dimple, the distinct short-waved pattern of the modified reduced pattern given in Figure 4-23, right can be noticed by eye.

It is assumed that while the local checker-board characteristic visible in the modified reduced shape again represents the essential imperfection shape, its influence on the buckling load is slightly further enhanced by being relocated further inwards by the long-waved mode shape's high amplitude (compare Table 4-3 and Figure 4-23, area around the position of the initial dimple).

Therefore, it is concluded that while the long-waved mode shape of around six circumferential full waves may have a certain influence on the buckling load, the imperfection shape which is essential for establishing the majority of the shell's buckling load reduction is the modified and short-waved pattern shown in Figure 4-23, right.

Thus, when the main aim of investigations is to identify the essential part of a given imperfection pattern from an engineering point of view, it is advised to artificially remove spurious modes hampering proper inspection and interpretation of the influence of geometric imperfections on the buckling load. However, when doing so, especially in the case of limited experience with the nominal shell geometry and laminate setup, the corresponding buckling loads have to be carefully evaluated to prevent crucial misjudgments. Furthermore, a re-assessment of the chosen threshold value η_t might be necessary to precisely identify remaining but negligible modes (compare chapter 4.2.4).

4.3.2 Application to shells with varying geometry and laminate setup

The laminate setup of a composite shell decisively influences its mechanical response under loading. Thus, a change in fiber angles not only influences the in-plane strain and bending stiffnesses but also the mechanical coupling of both, represented by the B-matrix in laminate theory. These terms can have a significant impact on the shell's behavior under axial loading when perturbed by lateral loads or geometric imperfections [98]. In turn, it is expected that the characteristic imperfection shape which are essential for the buckling behavior caused by a measured pattern also depend on the shell geometry and laminate setup.

Therefore, after the thorough discussion of the application of the SIFM to different shells of identical nominal geometry and laminate setup (shells Z15-Z26), the SIFM is applied to measurements of shells of heavily diverse geometries and laminate setups. For an overview of all measured imperfection patterns and their reduced shapes, it is again referred to appendix A.

In a first step, the SIFM is applied to shell Z11. It features the same set of ply angles as shell Z25, which was thoroughly discussed above, and shell Z07, which shall now serve as a basis of comparison since it shares the same free length of $L = 510\ mm$ with shell Z11 (compare chapter 6.1.1). However, in the case of shell Z11, one of the axially stiff layers is shifted to the outside of the shell, resulting in a laminate setup of $[+24, \pm 41, -24]$. Table 4-6 gives an overview of the buckling loads of the shells Z07 and Z11 with perfect geometry and with their measured geometric imperfections.

buckling loads λ [kN]	Z07	Z11
perfect shell	33.67	23.67
geometric imperfections	27.13	19.75
buckling load reduction $\Delta\lambda$	6.54	3.92
	19.4 %	*16.6 %*

Table 4-4: Buckling loads for shells Z07 and Z11, perfect shell buckling loads, buckling loads with only geometric imperfections, buckling load reductions Δλ

When comparing the calculation results, a drop in both load levels from shell Z07 to shell Z11 is noticed. At the same time, the discrepancy between the perfect shell's buckling load and the one of the geometrically imperfect shell substantially decreases. While the particular imperfection shapes may influence the particular values of the imperfect shells' buckling loads, it seems agreeable to describe the observed buckling load reduction of shell Z11 as generally lower than the one of shell Z07. Thus, by shifting one axially stiff layer to the inside, the shell becomes less resistant to buckling but at the same time also less imperfection sensitive.

Table 4-5 shows the results of applying the SIFM to shell Z11. It has to be noted that in order to obtain a clear essential pattern, the spurious mode (1,2) had to be removed manually. Very similar to the case of shell Z17 shown in chapter 4.3.1.2, this mode has a negligible influence on the buckling load ($\lambda_{red} = 19.95\ kN$, $\lambda_{red,mod} = 20.04\ kN$) but hampers proper visual investigation of the essential imperfection shapes.

	original imperfection shape	reduced imperfection shape
Z11	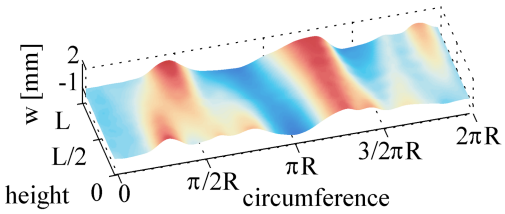	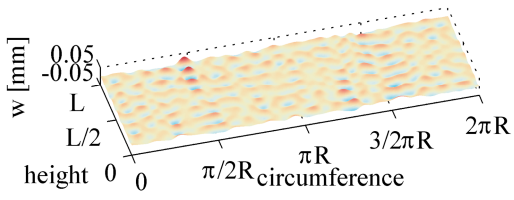
	$\lambda_{orig} = 19.75\ kN$	$\lambda_{red,without\ (1,2)} = 20.04\ kN$

Table 4-5: SIFM applied to shell Z11, measured imperfection pattern (left) and modified reduced pattern (right) with mode (1,2) manually removed

Despite the long waved characteristics of the original pattern, when investigating on the reduced imperfection shape, a generally short waved appearance is noticed. In contrast to the results obtained for the laminate setup of shells Z2x, no checker board pattern can be seen. However, the characteristic oscillation in axial direction from local maxima to local minima is again noticed. In addition to that, the maximum pattern amplitude is also significantly reduced, showing values in the same regime as the reduced patterns of shells Z2x.

In a next step, the SIFM is applied to shell Z09. It again consists of the same nominal geometry, laminate layers and ply angles as shells Z07 and Z11, with the only difference that now both axially stiff $[\pm 24]$ layers are shifted to the outside of the shell. In this way, a laminate setup of $[\pm 41, \pm 24]$ is obtained for shell Z09 (compare chapter 6.1.1). Table 4-6 gives an overview of the buckling loads of shells Z07 and Z09 with perfect geometry and with their geometric imperfections.

buckling loads λ [kN]	Z07	Z09
perfect shell	33.67	17.70
geometric imperfections	27.13	17.63
buckling load reduction $\Delta\lambda$	6.54	0.07
	19.4 %	*0.4 %*

Table 4-6: Buckling loads for shells Z07 and Z09, perfect shell buckling loads, buckling loads with only geometric imperfections, buckling load reductions $\Delta\lambda$

When comparing the calculation results, an even more significant drop in load levels from shell Z07 to shell Z09 is noticed. The discrepancy between the perfect shell's buckling load and the one of the geometrically imperfect shell is again substantially decreased, even more than in the case of shell Z11. Thus, by shifting both axially stiff layers to the outside, the shell became even less resistant to buckling but at the same time also even less imperfection sensitive. The characteristics of this behavior and its influence on shell design procedures were recently discussed by KRIEGESMANN et al. [98].

In the context of applying the SIFM, the very low imperfection sensitivity of shell Z09 poses a problem when choosing an appropriate threshold value η_t. As the geometric imperfections only marginally influence the buckling load of the shell, the threshold value would have to be chosen comparatively small to be able to separate faintly detrimental modes from irrelevant modes. Therefore, in case of shell Z09 the SIFM would eliminate all modes from the spectrum not until the threshold value was lowered to $\eta_t = 1.001$. Table 4-7 again gives the corresponding original and reduced imperfection shape.

	original imperfection shape	reduced imperfection shape
Z09	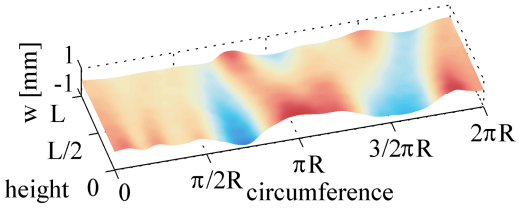	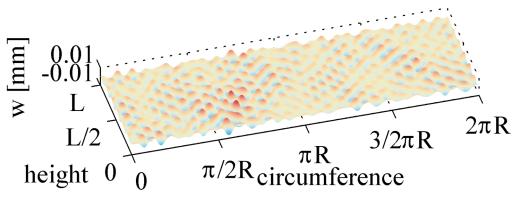
	$\lambda_{orig} = 17.63\ kN$	$\lambda_{red} = 17.65\ kN$

Table 4-7: SIFM applied to shell Z09, measured imperfection pattern (left) and reduced pattern (right)

The reduced pattern only consists of short waved modes with very low amplitudes. However, when looking at the total buckling load reduction of the reduced pattern of $\Delta\lambda_{red} = 0.05\ kN \approx 0.3\ \%$, it seems debatable whether or not the numerically expensive process of filtering the original imperfection pattern is worthwhile. Thus, determining the essential imperfection pattern for a shell which does not show to be sensitive to geometric imperfections at all has to be judged as unreasonable. In shells where the laminate setup causes such a low imperfection sensitivity, other stability aspects like for example the liability to axisymmetric bending shapes during prebuckling dominate.

Similar to the mirroring of laminate stacking sequences of the shell Z09 and Z07, two further shell specimens with opposing stacking sequences were manufactured and tested at DLR, Braunschweig (compare GEIER et al. [32] and ZIMMERMANN [31]). Similar to Z09 and Z07, Z32 was designed to feature a low general buckling load level with low imperfection sensitivity, while reversing the ply order lead to Z33 showing higher general buckling loads and higher imperfection sensitivity. However, in contrast to the more recent shells discussed by HÜHNE et al. [57], the shells Z32 and Z33 are significantly thicker, featuring ten ply layers. They share a ratio of $R/t = 250/1.25 = 200$ and thus represent comparatively thick cylinders. As solely the imperfection pattern of shell Z33 is available to the author, the SIFM cannot be applied to shell Z32 in this context.

Table 4-8 gives the SIFM results for shell Z33.

	original imperfection shape	reduced imperfection shape
Z33	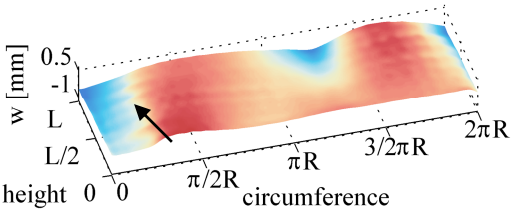	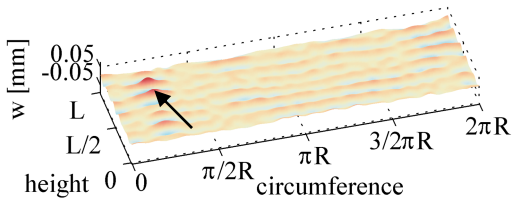
	$\lambda_{orig} = 179.85\ kN$	$\lambda_{red} = 181.60\ kN$

Table 4-8: SIFM applied to shell Z33, measured imperfection pattern (left) and reduced pattern (right), positions of the initial dimples indicated by arrows

The position of the initial dimple of the reduced pattern concurs with the position of the initial dimple of the original pattern. When looking at the reduced imperfection shape, the pattern appears more long-waved in circumferential direction. While an oscillation from local maximum to local minimum to local maximum in axial direction is again noticed around the position of the

initial dimple, the distinct checker-board style noticed in the case of shells Z2x is no longer noticeable. However, it should be noted that the prevalent mode of short axial and long circumferential that can be seen in the reduced pattern is also visible in the original shape.

As a last example, the SIFM is applied to shell specimen Z36. This shell was fabricated, measured and tested within the EU 7th framework project DESICOS. While featuring a R/t ratio similar to the Z2x shells, with a length of $L = 800\ mm$ and a radius of $R = 400\ mm$, it is generally bigger in size than the usual shell specimen. Details on the geometry and laminate setup of shell Z36 are again given in chapter 6.1.1.

Table 4-8 gives the results for shell Z36, showing the original imperfection pattern on the left and the reduced imperfection shape on the right. It should be noted that for reasons of visibility, both patterns are given with inverse height direction.

	original imperfection shape	reduced imperfection shape
Z36	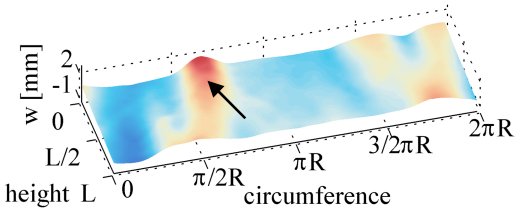	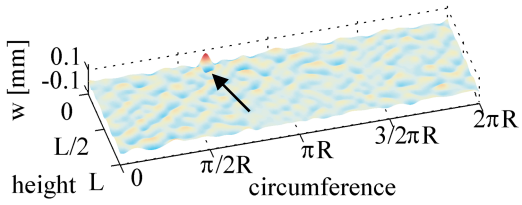
	$\lambda_{orig} = 82.14\ kN$	$\lambda_{red} = 82.96\ kN$

Table 4-9: SIFM applied to shell Z36, measured imperfection pattern (left) and reduced pattern (right), positions of the initial dimples indicated by arrow

The position of the initial dimple of the reduced pattern concurs with the position of the initial dimple of the original pattern. When looking at the reduced imperfection shape, the pattern shows a distinct single maximum near the shell's edge followed by a single minimum. Similar to the case of shell Z33, no striking checker-board pattern is visible.

To conclude, applying the SIFM to shells of varying laminate setup in turn leads to essential imperfection shapes with varying characteristics. This is in agreement with the expectedly different physical behavior of shells of different laminate setup. As the laminate setup not only decisively influences the in-plane and bending stiffnesses themselves but also the coupling of both, it is expected that in turn different wave shapes critically stimulate the shells' physical behavior. However, it is noted that in all investigated cases short waved modes of comparatively low amplitude constitute the essential pattern.

4.3.3 Application to conical shells

In a last application case, the SIFM is applied to conical shells. Here, the semi-vertex angle necessitates a more complex manufacturing as ply tapes have to be cut into optimized trapezoidal shapes to avoid ply overlays (for details confer chapter 6.1.3).

Due to the inclination angle of conical shells, the global nonlinear bending deformations are much more pronounced. Therefore, conical shells are more prone to initial dimples near the shell's edge as the superposition of the degrading influence of bending and geometric imperfections tends to be more severe than geometric imperfections in the center of the shell.

As a second effect, the higher impact of global nonlinear prebuckling deformations leads to a general decrease in imperfection sensitivity of conical shells. This can very well be observed by comparing geometrically imperfect shells to the corresponding perfect shell's buckling load. The measured geometric imperfections of for example conical shell K08 (for details confer chapter 6.1.1) lead to a numerically determined buckling load of $\lambda_{K08,imperf} = 37.92\ kN$ while the buckling load of the perfect shell is calculated to $\lambda_{K08,perf} = 39.10\ kN$. This equals a comparatively low buckling load reduction of $\Delta\lambda = 1.18kN\ (3.3\%)$. While this certainly can be partly attributed to the laminate setup, results obtained by KHAKIMOVA et al. [111] show that the low imperfection sensitivity can be observed for numerous laminate setups and ply topology designs.

As it is the only imperfection pattern of conical shells available to the author, Table 4-8 gives the results for conical shell K08, showing the original imperfection pattern on the left and the reduced imperfection shape on the right.

	original imperfection shape	reduced imperfection shape
K08	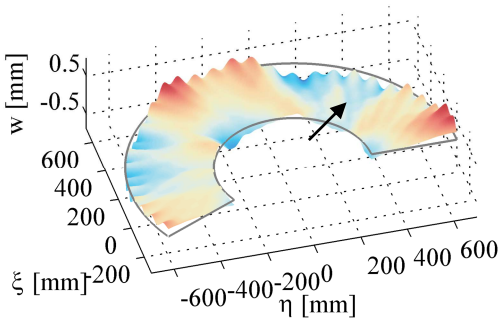	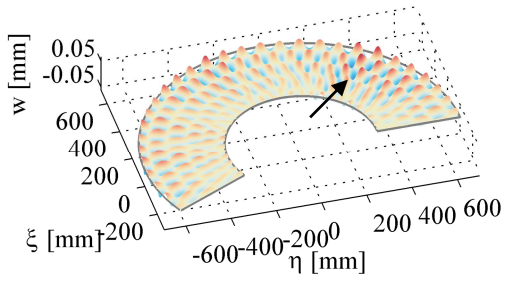
	$\lambda_{orig} = 37.92\ kN$	$\lambda_{red} = 38.30\ kN$

Table 4-10: SIFM applied to shell K08, measured imperfection pattern (left) and reduced pattern (right), positions of the initial dimples indicated by arrow

When looking at the reduced pattern, short waved shapes composed from comparatively few modes are noticed. This is similar to the case of shell Z09 shown before. The reason for the scarce reduced spectrum lies in applying the SIFM with a threshold value of $\eta = 1.01$ to a relatively imperfection insensitive shell. Here, the hurdle to reach a load level of $\lambda_{ref} = 1.01\ \lambda_{orig}$ is comparatively high, resulting in only few modes being judged as critical.

As discussed before in the case of shell Z09, it is debatable whether the SIFM is worth applying to a shell that is more or less insensitive to geometric imperfections.

4.3.4 Interpretation of the reduced imperfection shapes

In chapter 4.2.3 it was shown that the reduced imperfection patterns obtained by the SIFM for shell Z25 show distinct commonalities, independent from the mode evaluation order chosen within the method. While the variation of the threshold value η_t given in chapter 4.2.4 did have a notable influence on the reduced pattern, the general characteristics remained well observable and unchanged. The fact that applying the SIFM in slightly altered ways leads to very similar results ascribes a certain level of robustness to the procedure. It is concluded that the SIFM's results are not entirely and crucially dependent on the choice of the inherent parameters.

In a subsequent step, the SIFM was applied to all measured imperfection patterns available to the author (compare appendix A).

When investigating on the reduced patterns of shells with the same nominal geometry and laminate setups (Z15-Z26), distinct commonalities over all reduced imperfections shapes were noticed (compare chapters 4.2.2, 4.3.1 and appendix A). This indicates that the characteristic imperfection shape shown in Figure 4-8 may not only be the essential part of the imperfection pattern of shell Z25 but much more a generally stimulating imperfection shape for that specific shell geometry and laminate setup. As all measured imperfection patterns of this geometry and laminate setup are reduced to coinciding imperfection shapes with coinciding buckling loads, it seems that the worst realistically expectable part of a real measured imperfection pattern may be found. However, this assumption cannot be proven or confounded without further detailed knowledge about the concrete effect of geometric imperfection shapes on the prebuckling phase of the shell.

The reduced patterns of shells with different nominal geometry and laminate setups show different characteristics in their general shapes. While the general picture of comparatively short waved reduced patterns still applies, the surface around the position of the initial dimple can differ, pulling away from the distinct checker-board pattern of shells Z15-Z26. However, a direct link between the design parameters (for example the laminate setup) of a shell and its essential imperfection shapes cannot be derived at this point.

Until now, the reduced patterns can only be interpreted in comparison to each other as no direct connection between the buckling load of a given imperfection pattern and its shape can be made. The following chapter 4.4 aims at giving insights and guidelines for establishing this knowledge and provides an explanation for the different buckling loads caused by different original and reduced imperfection patterns.

4.4 What makes the essential imperfection shapes essential?

4.4.1 On the exclusivity of the reduced pattern within the original imperfection shape

In chapters 4.2 and 4.3 it was shown that performing the SIFM leads to a reduced geometric imperfection pattern which represents the parts of an original geometric imperfection pattern that cause the same buckling loads as the original pattern. While numerous investigations on these reduced sets of modes and the corresponding patterns are given above and below, the role of the disregarded sets of eliminated modes shall now be in the focus of investigation.

If the buckling load reduction of a shell is attributed to a specific part of its inherent imperfection pattern, it could be assumed that all other parts of that imperfection pattern hardly have any influence on the buckling load. Thus, it could be argued that a pattern composed out of the set of eliminated modes should yield buckling loads close to the buckling load of a perfect shell.

Figure 4-25 gives the measured imperfection pattern of shell Z25 at the top (compare Figure 4-7). On the bottom left, the reduced imperfection shape obtained by performing the SIFM is given (compare Figure 4-8) while the contrasting imperfection pattern composed out of all eliminated modes is given on the bottom right.

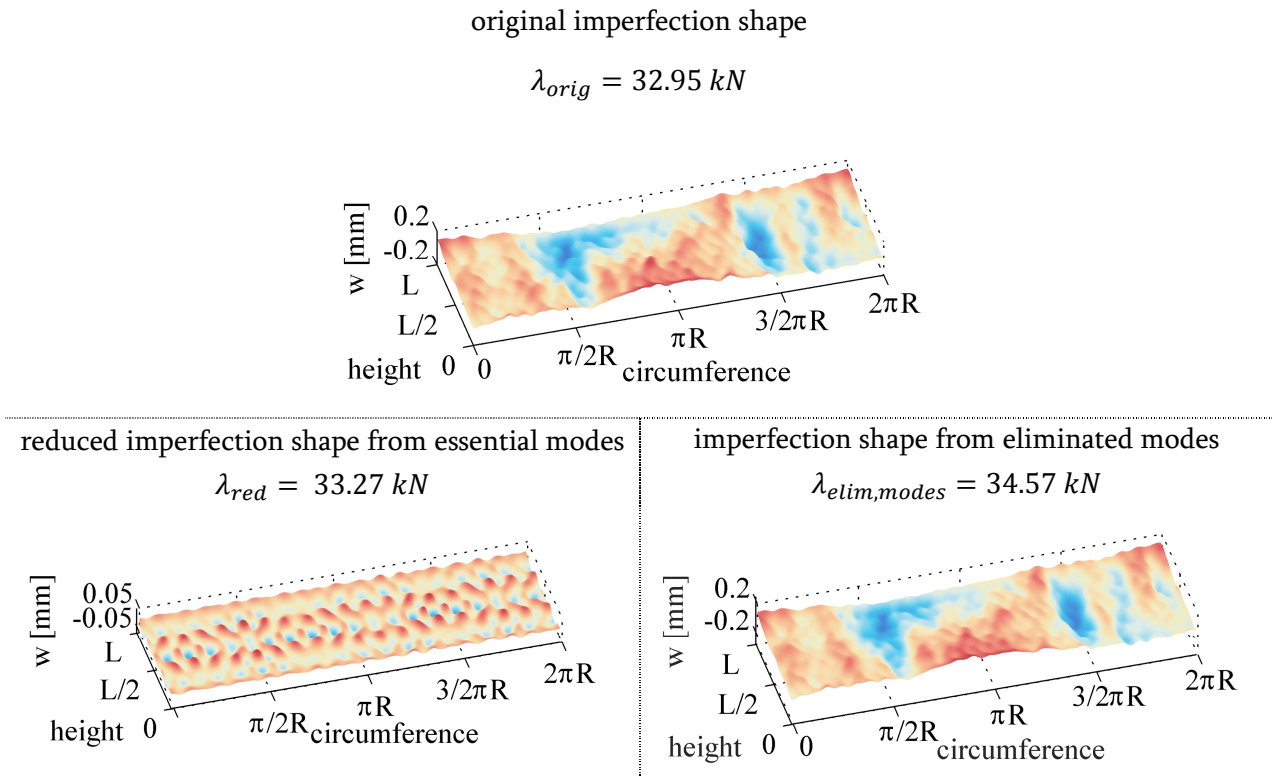

Figure 4-25: SIFM applied to shell Z25, measured imperfection pattern (top) and reduced pattern of essential modes (bottom, left), imperfection shape composed out of all eliminated modes (bottom, right)

As already discussed above, the reduced imperfection shape only resembles a small fraction of the original Fourier spectrum, containing modes of comparatively low amplitude. Thus, removing this imperfection shape from the original imperfection shape hardly changes the visual appearance of the pattern, making the imperfection shape composed out of the eliminated modes appear very similar to the original one. Table 4-11 gives an overview of the different patterns' buckling loads

and their effective buckling load reductions with respect to the perfect shell geometry, λ and $\Delta\lambda$, respectively.

[kN]	λ	$\Delta\lambda$	$\Delta\lambda$ [%]
perfect shell	37.62	-	-
original imperfection shape	32.95	4.67	*100 %*
reduced imperfection shape	33.27	4.35	*93.1 %*
imperfection shape from eliminated modes	34.57	3.05	*65.3 %*

Table 4-11: SIFM applied to shell Z25, buckling loads of perfect shell, original imperfection shape, reduced imperfection shape and imperfection shape from eliminated modes

While including exclusively modes that were judged as negligible by the SIFM, the corresponding pattern still causes a comparatively low buckling load of $\lambda_{elim.modes} = 34.57\ kN$, which corresponds to no less than 65.3 % of the buckling load reduction of the original measured imperfection shape. Or, putting it into the opposite perspective, while the original pattern and the pattern of the eliminated modes are visually hardly distinguishable, the latter one causes a buckling load reduction which is 34.7 % lower than that of the former one.

This finding emphasizes the heavy coupling of different modes and their influences on the buckling load (compare chapter 4.1.4). Contrary to intuitional assumptions, the buckling load reduction of the imperfection shape from essential modes (4.35 kN) and the buckling load reduction of the imperfection shape from eliminated modes (3.05 kN) do not add up to the one of the original imperfection shape ($4.35\ kN + 3.05\ kN \gg 4.67\ kN$).

Based on prior experience with geometric imperfections influencing the buckling load, it again has to be assumed that not the whole imperfection shape shown in Figure 4-25, bottom right but only certain parts of it cause the observed buckling load reduction. Thus, to be able to better understand the phenomenon of a set of assumingly negligible modes having a significant impact on the buckling load, the part of that imperfection shape which mainly drives the buckling load reduction has again to be revealed. This is achieved by reapplying the SIFM to the imperfection shape composed from previously eliminated modes.

Table 4-12 gives the imperfection shape from the initially eliminated modes on the left and the corresponding reduced pattern on the right.

	original imperfection shape	reduced imperfection shape
Z25	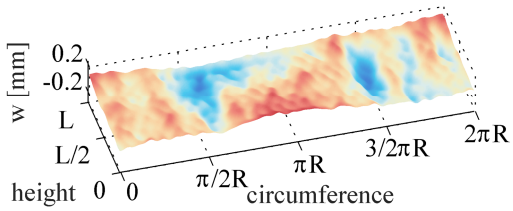	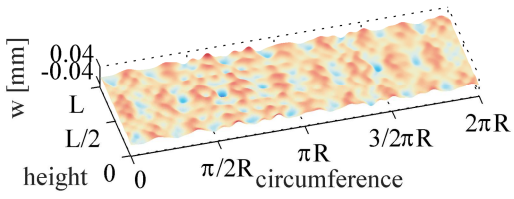
	$\lambda_{elim.modes} = 34.57\ kN$	$\lambda_{elim.modes,red} = 34.90\ kN$

Table 4-12: SIFM reapplied to shell Z25, imperfection shape from initially eliminated modes (left) and reduced pattern (right)

When investigating on the results, it is noticed that the reduced pattern shows significantly lower amplitudes and general wavelengths than the original pattern of eliminated modes shown in Figure 4-25, bottom left. While a single mode of two axial half waves and nine circumferential full waves dominates the pattern, a localized checker-board pattern of shorter wavelengths is still noticeable. This characteristic mode shape is different but still comparable to the essential pattern obtained in the first application of the SIFM to the measured pattern of shell Z25.

As stated above, the SIFM does not give a specific set of particularly critical modes but a specific geometric imperfection shape, regardless of which particular modes are required to establish that shape (compare for example chapter 4.3.1). When the set of specific essential modes is removed from the original spectrum to obtain the pattern discussed above, the mechanical sensitivity of the shell to the corresponding imperfection shape of course is not. Now, due to the fact that given two sets of entirely different modes, still two similar imperfection shapes can be composed, the SIFM is again able to filter the pattern down to an imperfections shape which again stimulates the (unchanged) mechanical sensitivity of the shell and therefore has to be of similar shape.

Based on this, the increase in buckling loads from the visually nearly identical measured imperfection pattern and the pattern composed out of eliminated modes can be explained. The essential pattern obtained by performing the SIFM represents the imperfection shape which – given a fixed original set of Fourier modes with fixed amplitudes and phase shifts – is the closest possible expression of an unknown theoretical worst possible imperfection shape. The grade of similarity between the inherent imperfection shapes of the measured pattern and this unknown worst possible imperfection defines the value of buckling load reduction of a given measured pattern. Thus, once the essential pattern is removed from the original shape of shell Z25, the buckling load rises as the grade of similarity between the now closest possible expression and the unknown worst possible imperfection decreases. It however does only increase by a certain margin, as the remaining pattern of eliminated modes still inherits shapes which are not as close but still similar to the unknown worst possible imperfection.

4.4.2 Putting the essential patterns into context: comparison to other characteristic imperfection shapes

The main goal of the SIFM is to deliver a tool for scientific investigation on the effect of specific geometric imperfection shapes on the buckling behavior. However, in addition to that, it is worthwhile to utilize the special features of the reduced imperfection shapes within innovative design procedures.

To ensure a safe design, it is of great importance that the imperfection shapes applied within a design procedure always show to be robust. This means that the buckling load obtained with a given geometric design imperfection should always be lower than the ones obtained by real imperfection patterns obtained from measurements. Besides the shape of the design pattern, the choice of its maximum amplitude significantly contributes to its associated buckling load. Almost every geometric imperfection pattern shows decreasing buckling loads for increasing maximum amplitudes. Thus, the maximum amplitude has to be chosen high enough so that the effect of

geometric imperfections on the buckling load is robustly accounted for. However, the economic necessity of reducing overly-conservativeness in modern design procedures counteracts low buckling loads and thus limits the maximum practical imperfection amplitude.

Therefore, in the following, the severity of a given imperfection shape will not be evaluated based on its original buckling load but by investigating its influence on the buckling load dependent on its chosen maximum amplitude w, normalized by the shell's thickness t.

4.4.2.1 Linear buckling modes as geometric imperfections

The most prevalent geometric imperfection shapes used in numerical stability analysis in literature as well as engineering practice are Eigenmodes or linear buckling modes (compare chapter 2.2). Eigenmodes are comparatively simple and cheap to obtain (see chapter 3.1.2). Figure 4-26 exemplarily shows the first linear buckling mode of the nominally perfect shell Z25.

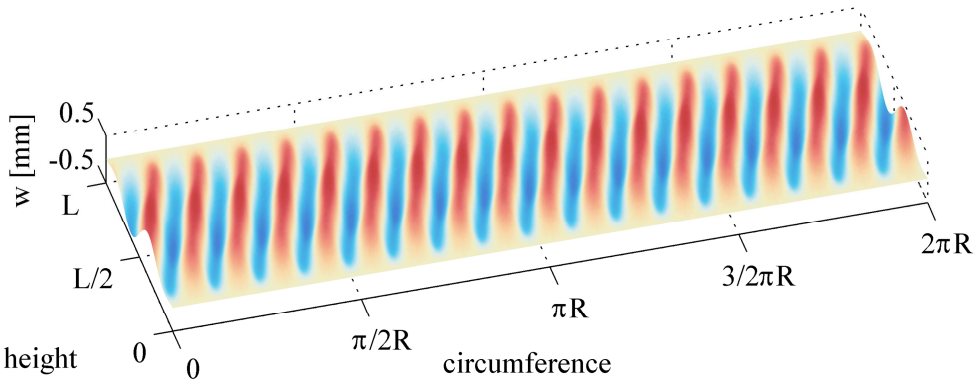

Figure 4-26: First linear buckling mode of shell Z25 with a maximum aplitude of $w/t = 1$

Linear Eigenmodes certainly play an important role in shell analysis, as their evaluation can provide insight on the properties and behavior of a given shell. When assuming a linear prebuckling behavior, Eigenmodes give the stable buckling shape of the shell. Thus, when applying this exact shape as an initial imperfection in a nonlinear analysis, the amount of required external energy to reach a similar postbuckling equilibrium state is comparatively low and so is the buckling load. However, it should be noted that the prebuckling pattern observed right before stability failure of such a shell is fundamentally different from what is observed in experiments. In contrast to a single initial dimple initiating local stability failure, the uniform Eigenmode shapes cause numerous dimples which snap in simultaneously. Furthermore, as HAYNIE et al. [52] show, Eigenmode imperfections can lead to a reduction in effective axial stiffness over the course of loading, which is generally not witnessed in experiments with real shells and thus should be observed with caution.

Despite them being easily obtainable and their inherent significant influence on the buckling load, the major drawback of applying Eigenmodes as geometric imperfections is that they are obtained normalized to a maximum amplitude of $w_{EM} = 1$. Thus, a meaningful choice for the amplitude has to be somewhat arbitrarily chosen since Eigenmodes represent a purely mathematical construct and therefore no physical connection to real measurement data exists as.

4.4.2.2 Axisymmetric imperfection shapes

Other somewhat more mathematical and less realistic geometric imperfections are axisymmetric imperfection shapes. As numerous authors showed, axisymmetric imperfection shapes have significant effects on the load carrying capacity of a cylindrical shell (compare for example FRIEDRICH et al. [100]). Even with comparatively low chosen amplitudes, the maximum bearable loads are heavily reduced compared to the perfect shell. Figure 4-27 exemplarily shows an axisymmetric imperfection with eight axial full waves applied to the nominal geometry of shell Z25.

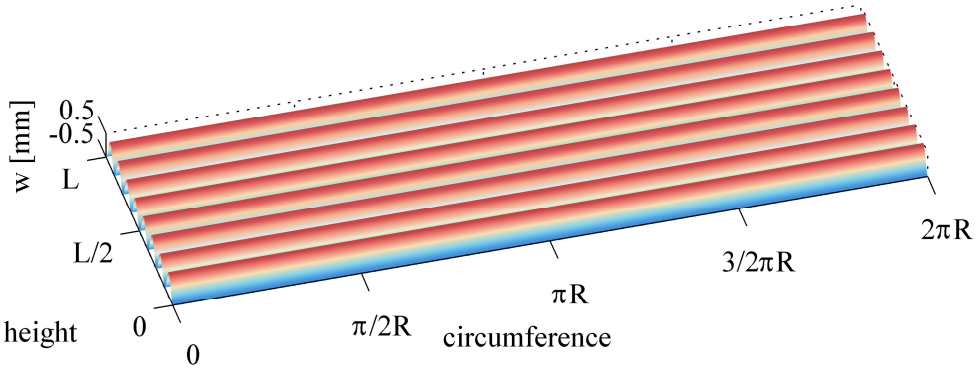

Figure 4-27: Axisymmetric imperfection shape with 8 axial full waves and a maximum aplitude of $w/t = 1$

When investigating the nonlinear prebuckling behavior of shells with such geometric imperfection, a distinctive phenomenon becomes visible. Very similar to the initial imperfection shape, the prebuckling deformations are also heavily dominated by a single axisymmetric wave shape (compare Figure 4-28, right). This deformation shape drastically reduces the nonlinear effective axial stiffness of the shell, much more than what is possible in the case of Eigenmode imperfections. When looking at the load deflection curve given in Figure 4-28, left, a decrease in axial stiffness to almost zero over the curse of the prebuckling phase is noticed.

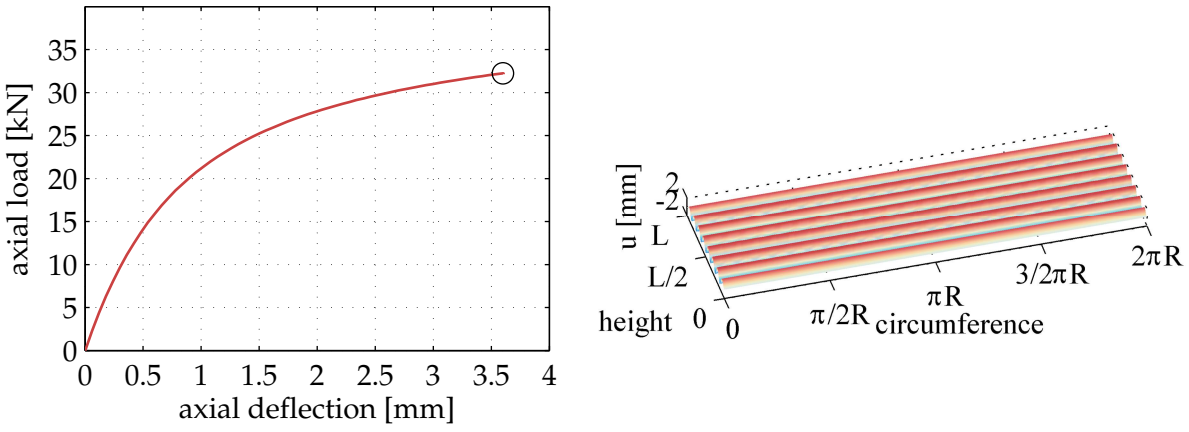

Figure 4-28: Axisymmetric imperfection shape: load deflection curve (left) and radial deformations right before limit point (right), associated equilibrium state indicated by circle in load deflection curve

The predominant bending deformation which accumulates under increased axial loading causes the behavior of the shell to more and more shift from a stability problem to a pure bending problem. In addition to that, neither the fundamental loss of stiffness nor the predominant axisymmetric bending distortion can be seen in experiments with real shell specimen. Thus,

axisymmetric imperfections are judged as inappropriate for use in design procedures which aim at reliably accounting for buckling and thus are not further investigated upon.

4.4.2.3 Single dimple imperfection

As discussed in chapters 2.2 and 3.3.4, the surface distortion caused by a lateral load is suspected to robustly account for the possible influence of geometric imperfections on the buckling load, at least in all investigated cases in this thesis. Similar to the calculation of linear buckling modes, the SPLA is comparatively easy to conduct numerically. Using sophisticated reduction techniques like the one proposed in chapter 3.3.3 it is also comparatively cheap to obtain the desired buckling load levels. When evaluating the deflection state of the shell before axial loading and after lateral loading, a distinct dimple is noticed (compare Figure 4-29). It is noticed that the single dimple is not an isolated local minimum. The wave shape rather oscillates but quickly decays in circumferential direction.

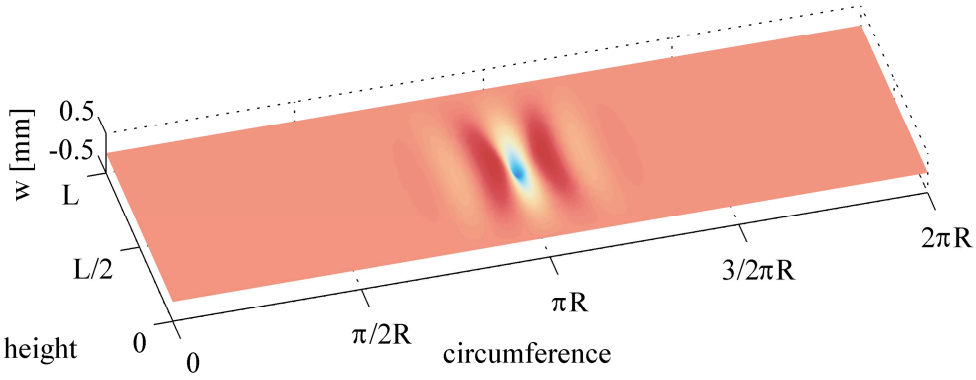

Figure 4-29: Dimple imperfection caused by lateral load with a maximum aplitude of $w/t = 1$

Numerous authors like WANG et al. [61] showed that it only marginally influences the resulting buckling load levels whether the equilibrium stress state caused by a lateral load is taken as the initial condition before axial loading or an equivalent stress free imperfection shape which corresponds to that equilibrium state. Thus, to enhance the comparability of imperfection amplitudes, in the following the deflection state after applying a perturbation load of value $P > P_1$ (compare chapter 3.3, shown in Figure 4-29) is transferred to a corresponding geometric imperfection shape.

4.4.2.4 Comparison to the essential imperfections shapes obtained by SIFM

As a basis for judging on the criticality of different characteristic geometric patterns, the buckling loads associated to the essential imperfection shapes obtained by the SIFM are compared to the ones of the commonly applied imperfection shapes described above. Due to the aforementioned reasons, the imperfection patterns will be varied in amplitude and compared based on the w/t ratio.

Figure 4-30 gives the buckling load corresponding to the perfect shell geometry, Eigenmode imperfection, single dimple imperfection, the original pattern of shell Z25 and the essential pattern obtained by applying the SIFM to shell Z25.

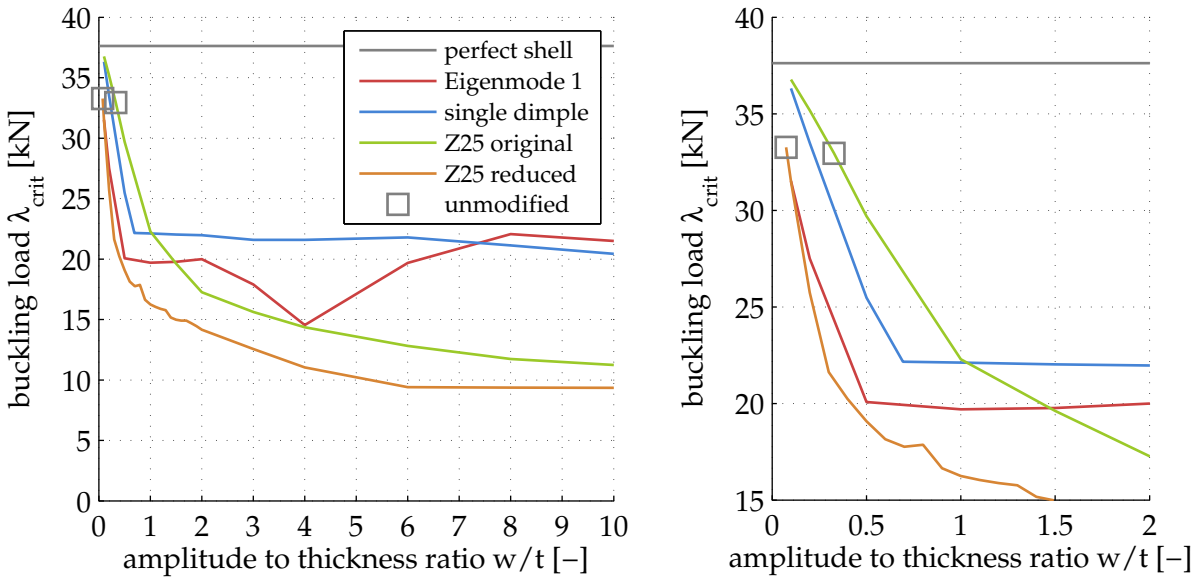

Figure 4-30: Buckling loads based on w/t ratio, corresponding to the perfect shell geometry, Eigenmode imperfection, single dimple imperfection, the original pattern of shell Z25 and the essential pattern obtained by applying the SIFM to shell Z25, unmodified amplitudes for the latter ones given by gray squares (left), zoom on regime of low to medium amplitudes (right)

When comparing all depicted imperfections, a high dependency of buckling loads on the respective imperfection amplitude is noticed in the regime of comparatively low amplitudes.

While for low amplitudes, the Eigenmode imperfections significantly reduce the shell's buckling load from $\lambda_{perf} = 36.2\ kN$ to around $20\ kN$, the curve quickly passes over to a nearly horizontal tangent. In the regime of $w/t = 4$, a significant dent in the curve is noticed, followed by a subsequent increase in buckling loads for increasing amplitudes. This somewhat unanticipated behavior was also observed by HAYNIE and HILBURGER [97], who found an explanation in the significant decrease in axial stiffness, accompanying Eigenmode imperfections of high amplitude.

When investigating on the single dimple imperfection, the characteristic lower bound behavior can easily be noticed, giving the lower bound load $N_1 \approx 22\ kN$ (compare Table 3-1). It is interesting to note that the lateral deflection required to achieve the characteristic lower bound load $w_{P1}/t \approx 0.7$ is well comparable to the regime of real imperfection measurements $w_{meas}/t \approx [0.3 \ldots 2.0]$.

As described in chapter 3.3.2, the lower bound behavior can be traced back to the prebuckling deformations the shell undergoes right before buckling. Here, the local radial deformations at the position of the single dimple are so severe that they effectively act as cut-out in the shell. In turn, due to load redistribution, the initial dimple snaps in next to this area.

When increasing the amplitude of the single dimple imperfection, the areal size of the prebuckling deformations does not change (in case of applying a lateral load instead of a stress free dimple, they marginally grow). Therefore, given an imperfection amplitude high enough to cause a virtual cut-out, the load distribution conditions do not change with higher imperfection amplitudes, nor does the position of the initial dimple. Therefore, the buckling load cannot decrease any further for imperfection amplitudes larger than w_{P1}/t.

The original imperfection pattern of shell Z25 also shows asymptotic tendencies, albeit not as harsh as in the case of the SPLA. Especially in the regime of (for the given manufacturing process) realistic imperfection amplitudes of $w_{meas}/t \approx [0.3 \dots 2.0]$, no lower bound can be defined. When increasing the amplitude of the pattern, the disturbance of local stability consequently increases in severity and thus the shell buckles at a decreasing axial load state.

When looking at the reduced pattern obtained by applying the SIFM to the measured pattern of shell Z25 it is noticed that the corresponding buckling loads show to be lower than all other considered patterns for all considered w/t ratios. As defined, the reduced pattern and the original pattern share a common buckling load value (at different amplitudes) (compare Figure 4-30, right, grey rectangles). Like in the case of the original imperfection pattern, again a steady but converging decrease in buckling loads is noticed.

However, it is noticed that the buckling load of the reduced pattern decreases faster and down to a much lower convergent level than the buckling load of the original pattern, especially in the regime of comparatively low amplitudes. This can be traced back to the differences in both patterns when being scaled to a given w/t ratio. When scaling the original pattern to a particular amplitude, all included shapes are proportionally scaled, essential and negligible wave forms. However, in contrast to the original pattern, the reduced pattern contains only the essential wave forms. Thus, when scaled to the same particular amplitude, the essential wave shapes have a much higher absolute amplitude value than in the case of the original shape. When the absolute amplitude value of the essential wave shapes at given w/t ratio is higher in case of the reduced pattern, the corresponding buckling load in turn has to be (considerably) lower.

To conclude, it is stated that the reduced pattern obtained by applying the SIFM yields buckling loads which are lower than all of the other frequently used and discussed imperfection patterns considered in this study for all considered w/t ratios. Therefore, it seems predestinated for use within a design framework, as a robust representation of the influence of geometric imperfections on the buckling load seems very feasible. However, in order to avoid overly-conservativeness, the high sensitivity of the buckling load to the amplitude of the reduced pattern necessitates careful thoughts on its numerical choice.

4.4.3 From essential parts of meaured patterns to a single perturbation load

In chapter 4.4.2, a steady decrease of buckling loads of the reduced pattern with increasing amplitude has been noticed. In the following, a closer look on this behavior shall be taken to better understand the influence of the amplitude on the essential pattern's impact on the buckling load.

Figure 4-31 again gives the buckling loads based on w/t ratio, corresponding to the reduced pattern of shell Z25, indicating the particular points a) to d) which will be discussed in the following.

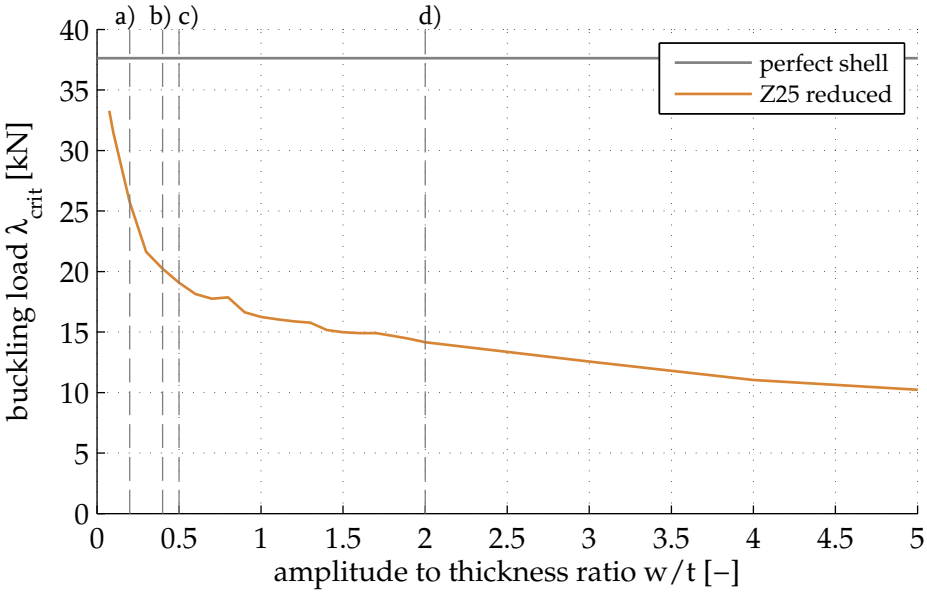

Figure 4-31: Buckling loads based on w/t ratio, corresponding to the reduced pattern of shell Z25, labels a) to d) for cross reference with the subsequent tables

Despite a small singularity at an amplitude of $w/t = 0.8$, the curve follows a monotonously decreasing trend. In the regime of comparatively low amplitudes, high gradients are noticed while in the regime of higher amplitudes, buckling load levels show slower declines and arguably start to converge. By investigating on the radial prebuckling and buckling deflection states at the imperfection amplitudes a) to d), an explanation for this behavior is found.

Table 4-13 and Table 4-14 give the load deflection curves as well as characteristic radial displacement fields for the w/t ratios a) to d). The underlying imperfection pattern is again the essential pattern of shell Z25, as shown in Figure 4-8.

reduced imperfection pattern (unloaded)

Z25

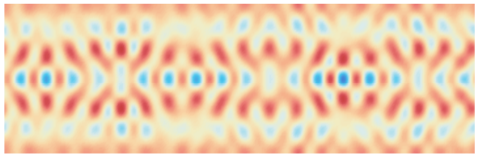

w/t	load-deflection curve	radial displacements under load
a) $w/t = 0.2$	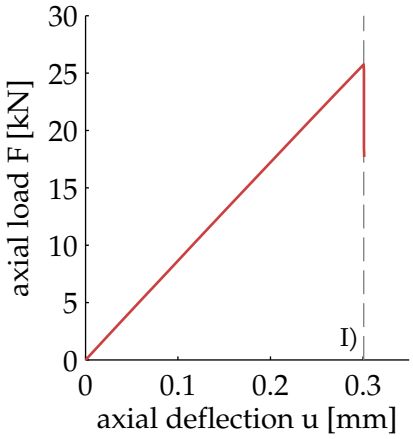	I) 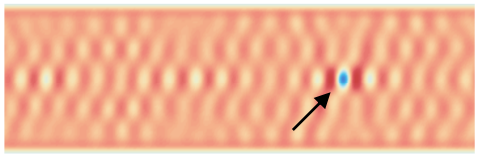
b) $w/t = 0.4$	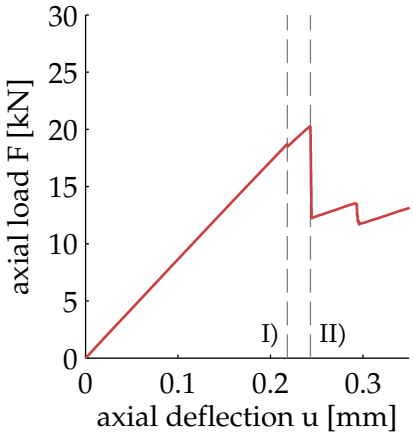	I)  local snap through II) 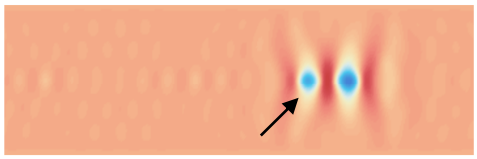 initial dimple

Table 4-13: Load-deflection curves and characteristic radial displacement field for the w/t ratios a) and b), as indicated in Figure 4-31, the underlying imperfection pattern is the essential pattern of shell Z25, local snap-throughs indicated by white arrows, initial dimples indicated by black arrows

		reduced imperfection pattern (unloaded)
	Z25	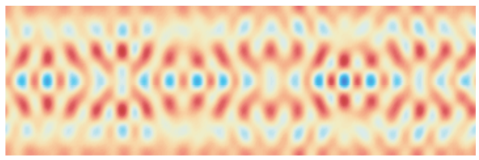

w/t	load-deflection curve	radial displacements under load
c) $w/t = 0.5$	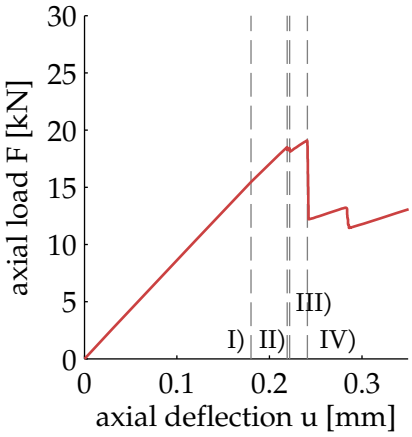	I)  II)  III) 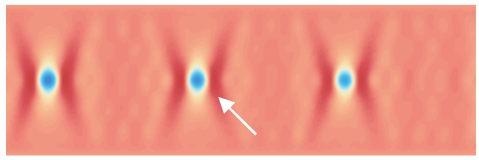 IV) 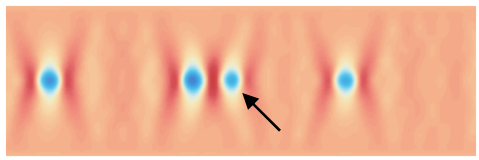
d) $w/t = 2.0$	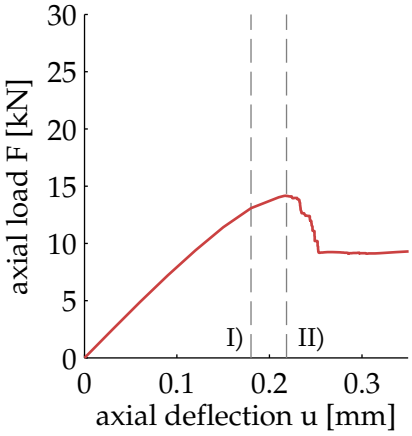	I) 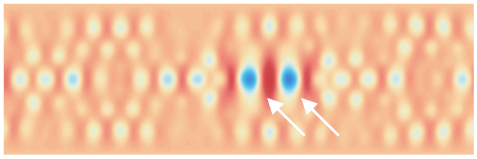 II) 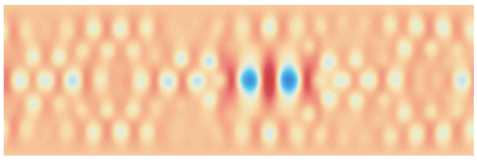

Table 4-14: Load-deflection curves and characteristic radial displacement field for the w/t ratios c) and d), as indicated in Figure 4-31, the underlying imperfection pattern is the essential pattern of shell Z25, local snap-throughs indicated by white arrows, initial dimples indicated by black arrows

When looking at the load-deflection curve of $w/t = 0.2$, the usual abrupt buckling curve is noticed. The corresponding radial deflection pattern right before buckling consequently shows the local nonlinear prebuckling deformations as well as the snap-in of the initial dimple (compare Table 4-13, a) I)). The position of the initial dimple concurs with the local accumulation of checker-board patterns with comparatively high imperfection amplitudes in the unloaded reduced imperfection pattern.

After increasing the imperfection amplitude to $w/t = 0.4$, the behavior fundamentally changes. The load-deflection curves shows a small local maximum before the buckling load is reached, similar to the load deflection curves observed when applying a perturbation load of sufficiently high magnitude (compare Figure 3-16, right). Accordingly, a local snap-through at the position of worst local imperfection is witnessed (Table 4-13, b) I)). Global buckling occurs when the actual initial dimples snaps in next to the position of local snap-through, again in line with the behavior observed in case of the SPLA (compare Table 4-13, b) II) and Figure 3-16, left).

At an imperfection amplitude of $w/t = 0.5$, multiple local snap-throughs are noticed, occurring at the positions where the imperfection pattern show local checker-board accumulations (Table 4-14, c) I) to III)). When the global buckling load is reached, the initial dimple snaps in next to the position of the third local snap-through accumulations (Table 4-14, c) IV)). This behavior precisely matches the effects observed when applying the SPLA with multiple (three) perturbation loads at once.

For imperfection amplitudes in the very high regime, the visibility of the phenomenon declines. Here, parallel snap-throughs at multiple neighbored positions are noticed. Once the buckling load level is reached, the radial deflections show no distinct initial dimple but a relatively uniform transition to the postbuckling pattern. Together with the stiffness reduction noticed in the load-deflection curve, this indicates a general transition from a buckling to a bending dominated problem.

The observed behavior can be explained as follows. With increasing pattern amplitudes, buckling loads decrease, as usual. However, once a specific amplitude of the pattern is reached (here $w/t = 0.4$), the local disturbance under loading is so high, that it again acts as a virtual cut-out, much like in the case of the single dimple imperfection caused by a lateral perturbation load (compare chapter 3.3.2). However, in contrast to the SPLA, the imperfect shell surface is not flat but inhomogeneous in the remaining regions. Therefore, once the conditions at one specific position on the shell's surfaces are severe enough to act like a cut-out, a second position can be found were the local shape is not as critical as in the first position but, due to the increased imperfection amplitude, now suffices to trigger the snap in of a second snap-through. This equates to performing the SPLA with two perturbation loads, triggering two local snap-throughs at the respective positions.

Especially in the regime of low and medium amplitudes, this effect leads to a steady decrease of buckling loads, as for increasing pattern amplitudes, more and more virtual cut-outs develop and thus the initial dimple relocates. For very high amplitudes, the shell is in such a disturbed state

that the certain structural stiffness to cause general buckling behavior is hardly reached. Thus, the whole radial deflection field is dominated by local effects, obscuring the characteristic perturbation behavior and transferring the response of the shell from a buckling to a bending problem. This in turn poses a practical upper limit for the investigations on the amplitude of geometric imperfections if buckling is in the focus of investigations.

The effects described above can also be noticed for measured imperfection patterns of scaling amplitude (compare Table 4-15).

		original imperfection pattern (unloaded)
Z25		

w/t	load-deflection curve	radial displacements under load
$w/t = 1.4$	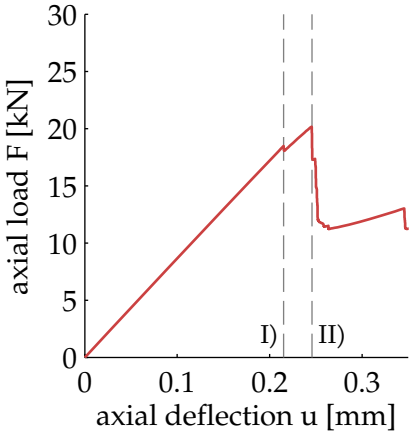	I)  II) 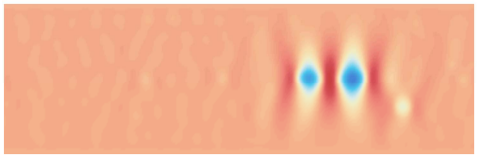

Table 4-15: Load-deflection curve and characteristic radial displacement field for $w/t = 1.4$, the underlying imperfection pattern is the original pattern of shell Z25

As described in chapter 4.4.2, in measured imperfection patterns, multiple modes of high amplitude but low influence on the buckling behavior are equally scaled when choosing a global pattern amplitude. Thus, even though the same phenomena take place (the initial dimple snaps in at the exact same location for low amplitudes, local snap through for higher amplitudes), the required imperfection pattern amplitudes are much higher (compare Figure 4-30). For very high amplitudes, the radial displacement field is again disturbed by multiple irregularities and thus hampers visual recognition of the effects. It is worth noting that this corresponding behavior between the original and the reduced imperfection pattern again emphasizes the latter being the essential part of the former. Consequently, the amplitude to which the original pattern has to be scaled so that the inherent essential shapes cause a local snap-through is much higher than in the case of scaling the plain essential shapes.

The phenomenon of multiple snap-throughs associated with decreasing buckling loads shown above is also observable when performing the SPLA with multiple perturbation loads, frequently referred to as the MPLA (compare for example ARBELO et al. [60]). While for a single perturbation load, a lower bound of buckling loads N_1 can be found, for multiple perturbation loads, this lower bound decreases (compare also chapter 3.3). The differences between multiple perturbation loads and the essential imperfection shape are twofold: Firstly, the essential imperfection shape triggers local snap-throughs at notably lower amplitudes than the required single dimple amplitudes. Secondly, the very same essential imperfection pattern enables the shell to undergo multiple connected physical states (classical initial dimple buckling, single snap-through, multiple snap-throughs) when just increasing the amplitude. This is not attainable with a perturbation approach, as for example the chosen number of perturbation loads predetermines the physical response of the shell.

All in all, it is inferred that in general the worst effect a local imperfection can have on the local stability of the shell may be to trigger a cut-out-like local snap-through. However, the severity of a given global imperfection pattern on the global buckling load directly depends on the imperfection amplitude which is necessary to cause this behavior. Furthermore, not only a single local geometric disturbance but the amount of repetitions of quite regularly distributed local maxima and minima around the shell determines the amount of triggered snap-throughs, diminishing global buckling loads. Here, as shown above, the reduced shape of an original imperfection pattern shows to be of much higher criticality than the single local dimple caused by SPLA.

It has to be noted that the described behavior is clearly observable in case of shell Z25 and other shells of concurring dimensions and laminate setup. Still, certainly supplementary studies are required to confirm the conclusions drawn above and widen the findings to prove general validity.

4.4.4 Comparison of prebuckling equilibrium states

After demonstrating the commonalities between original and reduced patterns, the mechanical reasoning for the reduced pattern being actually the essential part of the original pattern shall be shown and discussed.

As described in chapter 3.2, the prebuckling behavior of cylindrical shells is dominated by nonlinear deflections. This deflection field grows in magnitude until it causes a stress state severe enough to trigger the snap in of the initial dimple. While the applied imperfection pattern obviously predetermine the prebuckling deformations especially in the regime of lower loads, the nonlinear prebuckling stress state is also influenced by the nominal shell geometry and underlying laminate setup.

In chapters 4.2 and 4.3 it was derived that applying the SIFM to a given imperfection pattern yields the essential part of that original imperfection pattern which causes its associated early stability failure. If this holds true, not only the buckling load level but also the complex stress state triggering the snap in of the initial dimple and thus stability failure have to comply.

In the case of composite shells, the evaluation of stress states reaches practical limits as technically the stresses for each individual ply in each coordinate direction would have to be considered. Thus, in the following, the stresses are investigated on in the form of stress resultants, giving the directional stresses σ_{11} and σ_{22} integrated over the laminate's thickness t [112]:

$$(SR_{ax}, SR_{circ}) = \int_{-t/2}^{t/2} (\sigma_{11}, \sigma_{22}) dz \tag{4-13}$$

Stress resultants, which are also commonly referred to as section forces or force intensities, offer a sophisticated way to evaluate the complex stress state from an engineering point of view.

In a first step, the prebuckling state of shell Z20 shall exemplarily be discussed. Figure 4-32, left shows the corresponding unloaded imperfection shape around the position where the initial dimple will snap in once the shell is subjected to axial compression and the buckling load level is reached. Figure 4-32, middle and right depict the stress resultants SR_{ax} and SR_{circ} in axial and circumferential direction, respectively, in the last calculation increment before the highest axial load level is reached.

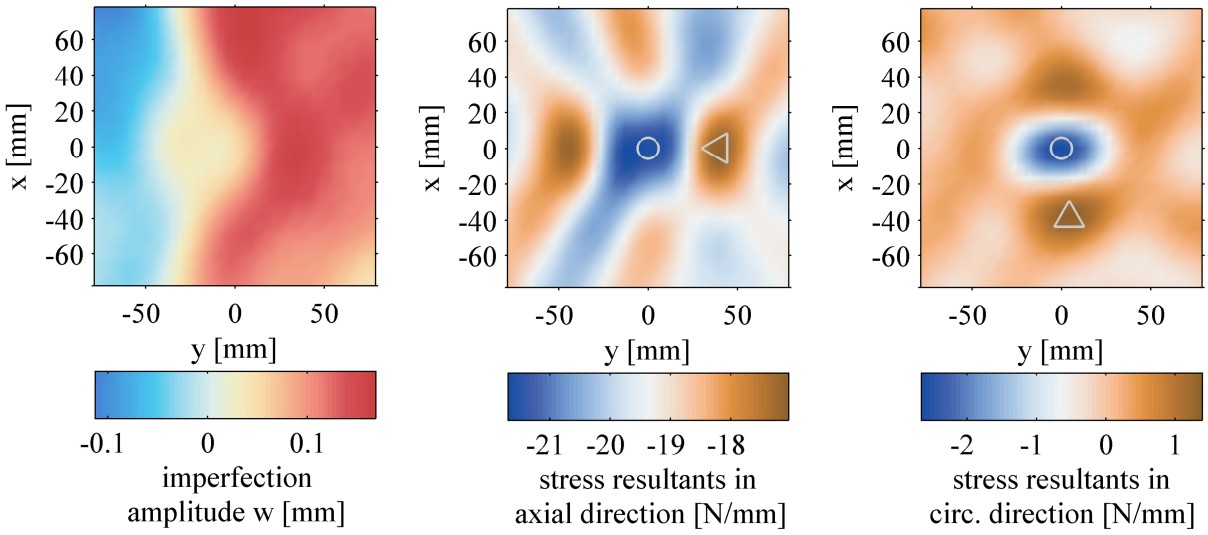

Figure 4-32: Unloaded imperfection shape of shell Z20 around the position of the initial dimple (left), corresponding stress resultants in axial and circumferential direction in the last calculation increment before the buckling load is reached (middle and right, respectively)

When investigating on the distribution of axial forces, a distinct maximum of pressure is noticed at the center of the depicted section where initial dimple snaps in (marked by gray circle). This will be referred to as $SR_{comp,max,ax}$. Neighboring this central maximum to the left and to the right, two locally limited areas of stress relieve are noticed (marked by gray triangle), referred to as $SR_{comp,min,ax}$ in the following.

A different characteristic distribution is noticed in case of the stress resultants in circumferential direction. While the position of the initial dimple again features a local maximum of pressure (marked by gray circle, $SR_{comp,max,circ}$), two neighboring areas above and below are noticed. Here, the compression switches to a tension stress state (marked by gray triangle, $SR_{tens,max,circ}$).

To put these distributions into context, Figure 4-33 again gives the imperfection pattern and stress resultants around the position of the initial dimple, this time for the reduced pattern of shell Z20, received by applying the SIFM.

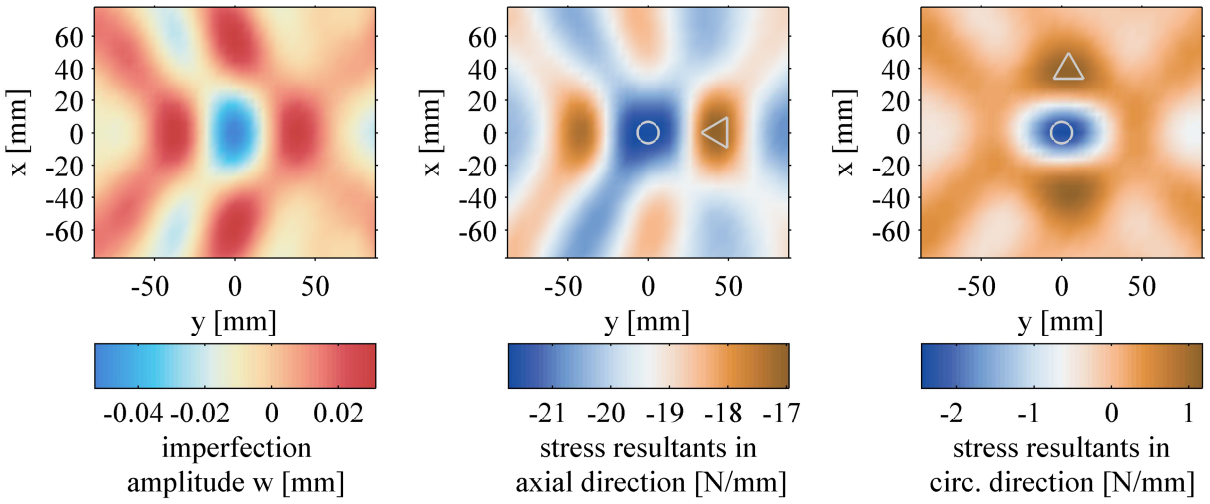

Figure 4-33: Unloaded reduced imperfection shape of shell Z20 around the position of the initial dimple (left), corresponding stress resultants in axial and circumferential direction in the last calculation increment before the buckling load is reached (middle and right, respectively)

When comparing the patterns to the ones shown before, it becomes apparent that not only the buckling load levels comply between the original and reduced patterns (by definition, compare chapter 4.2.1) but also the distribution of stresses triggering the snap in of the initial dimple closely match.

It is interesting to note that a similar behavior is noticed when the position of the initial dimples of the reduced pattern and the original pattern do not comply (compare for example Figure 4-15). In these cases, the axial and circumferential stress resultants at both positions still show to be distinctly similar, leading to buckling at the same axial load level. Therefore, the trustworthiness of a reduced pattern does not suffer if the positions of the initial dimples do no match as long as the corresponding stress states do.

To broaden validity, in a next step the prebuckling stress states of shells Z20 and Z25 are exemplarily compared. Figure 4-34 gives the stress resultants in axial and circumferential direction at the characteristic locations discussed before (minima and maxima left/right and below/above the initial dimple) over the course of axial loading.

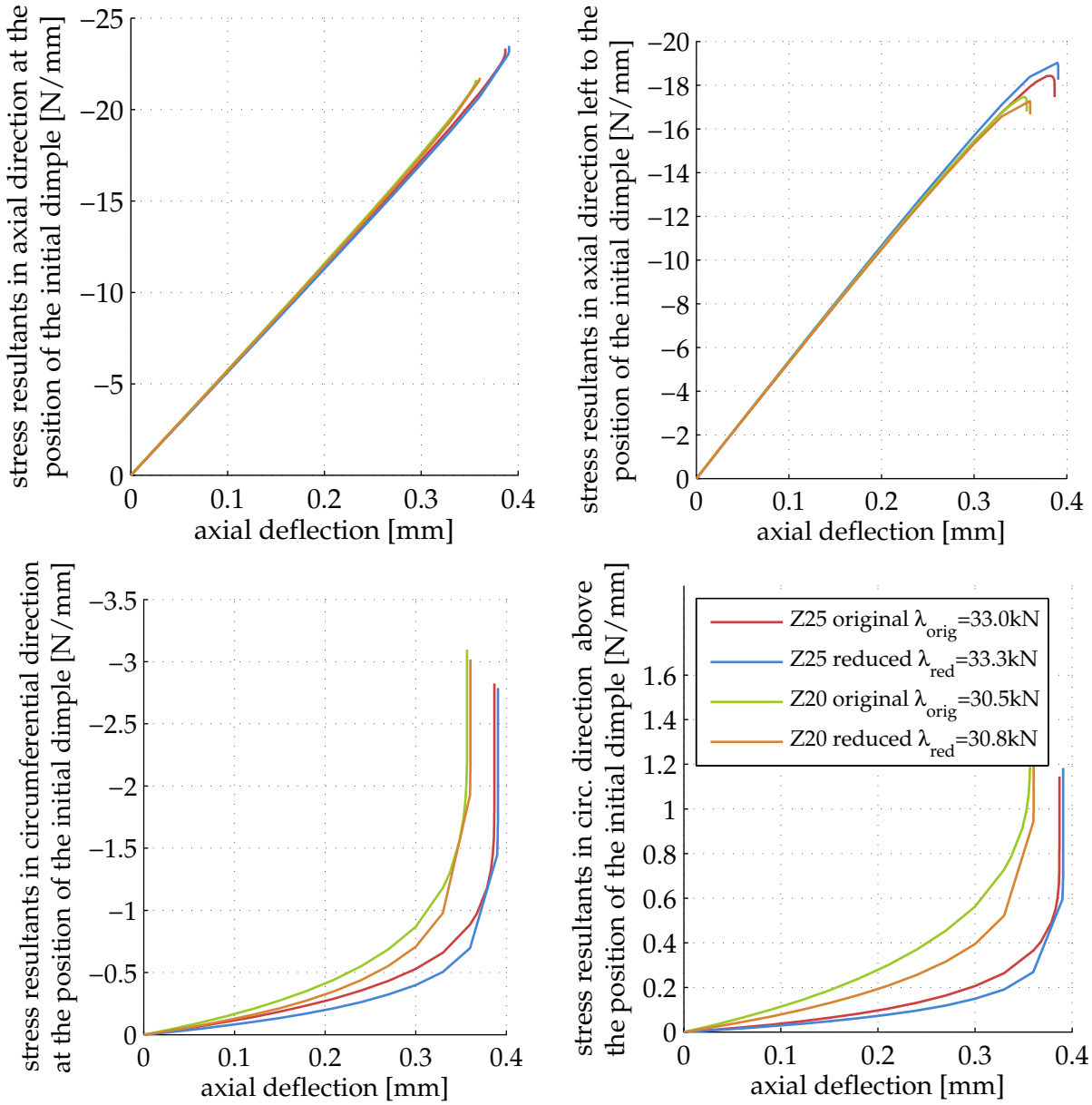

Figure 4-34: Stress resultants of shells Z20 and Z25 over the course of axial loading for original and reduced patterns, evaluated in axial and circumferential direction at the positions marked in Figure 4-32 and Figure 4-33

When comparing the curves corresponding to the axial pressure of both shells (upper diagrams), a general agreement is noticed. This complies with the generally similar buckling load levels of both shells around $\lambda_{orig} \approx 30\,kN$. However, in the regime of higher axial deflections, differences between the curves associated with shells Z20 and Z25 occur. Here, shell Z25 shows higher axial stress resultants at the characteristic positions. This is in agreement with the buckling load of shell Z25 being around 10 % higher than the one of shell Z20.

In the case of the circumferential stress resultants at the characteristic positions (lower diagrams), more significant differences become apparent. Here, shell Z20 shows significantly higher circumferential stresses at lower axial deflection levels. This underlines the findings by for example ARBOCZ [51], who, among others, shows the high disturbing influence on the local stability of the shell caused by inhomogeneous circumferential stress states. Thus, subjected to higher circumferential stresses, shell Z20 fails earlier at lower axial deflections. The distinctly increasing slopes of the stress curves denote the abrupt transition from a prebuckling stress state to

a severe bending deformation during buckling. It should be noted that the highest given values in the regime of vertical tangents are mainly dependent on the numerical stability of the simulation and thus should not be physically interpreted.

When comparing the stress resultants of the respective original and reduced patterns, it is noticed that until very high axial deflection levels, both curves closely match. While deviations can be spotted in the circumferential stress state in the regime of early loading, the peak stress resultants as well as the corresponding axial deflection levels closely match. This holds true both for the circumferential as for the axial stress resultants.

It can be concluded that applying the SIFM to a given imperfection pattern does not only yield a reduced pattern with matching corresponding buckling loads and general prebuckling deformations (compare chapters 4.2 and 4.3). It was shown that also the detailed axial and circumferential prebuckling stress states triggering the initial dimple comply for all cases investigated herein. This again strengthens the interpretation of the reduced pattern to be the essential part of an original pattern which is entirely responsible for its associated buckling load reduction.

4.4.5 Explanation for the buckling load discrepancy of given imperfection patterns

In chapter 4.4.4 it was shown that the stress states right before buckling, which are of vital importance for the localized buckling behavior of the shell, concur for both the original and corresponding reduced patterns. This underlined that the reduced pattern represent the essential parts of the respective original patterns which drive the observed buckling phenomena.

However, when comparing the imperfection patterns of different shell measurements of the same nominal geometry, laminate setup and manufacturing technique, the corresponding buckling loads vary quite significantly, from for example $\lambda_{Z18} = 29.55\ kN$ to $\lambda_{Z25} = 32.95\ kN$. Conversely, the corresponding essential imperfection shapes show to be generally akin (compare Table 4-2).

Still, to explain the considerable differences in calculated buckling loads, it has to be that some imperfection patterns show more critical imperfection features than others when examined in greater detail. In other words, those particular imperfection patterns are more similar to an unknown worst imperfection shape than others (compare chapter 4.4.1). This leads to the general question of shell buckling analysis, which has been investigated on for decades: Which characteristics cause a given imperfection pattern to be a particularly critical and severe imperfection pattern?

According to the findings and conclusions drawn in the previous chapters, the general influence of the imperfection pattern on the buckling load can be narrowed down to two main drivers: firstly, the maximum amplitude of the imperfection pattern and secondly, the detailed geometric characteristics in the area around the position where the initial dimple will snap in once a particular load level is reached. On the one hand, when comparing the buckling loads of two given imperfection patterns, the influence of their respective maximum amplitudes can be eliminated by normalizing both patterns to the same w/t ratio (compare 4.4.2). On the other hand, the proper quantification of the concrete geometric characteristics of the imperfection shape around the position of the initial dimple appears to be comparatively delicate to achieve. Here, the best suited approach most probably is to determine the visually dominating wave lengths in axial and circumferential direction as well as the regularity of the distinctive checker board pattern (compare for example Figure 4-33, left).

To investigate on the connection between imperfection shape and buckling behavior, it seems desirable to concentrate on the influence of one particular parameter, which in the following will be the wave length of the pattern. In this way, by artificially varying the wave length of a single given pattern, various different artificial imperfection shapes and their corresponding buckling behaviors are emulated and can be compared. The resulting observations presented in the following can help to derive concepts to explain why a particular imperfection pattern causes a lower buckling load than another imperfection pattern.

In a first step, the axial wave length of the essential pattern of shell Z25 is artificially varied. This is achieved by mathematically scaling the cylinder's length L when using the Fourier Series to compose the imperfection pattern (compare equations (4-6) and (4-14)).

$$\widetilde{w}_{scaled}(x,y) = 2t \sum_{k=0}^{n_x} \sum_{l=0}^{n_y} \xi_{kl} \cos\left(\frac{k\,\pi\,x}{L_{scaled}} - \rho_{shift}\right) \cos\left(\frac{l\,y}{R} - \varphi_{kl}\right) \tag{4-14}$$

$$\text{with} \quad L_{scaled} = L * \alpha \quad \text{and} \quad \rho_{shift} = k\,\pi \frac{x_{center}}{L}\left(\frac{1}{\alpha} - 1\right)$$

To ensure that the imperfection shape at the position of the critical area where the initial dimple snaps in does not change during axial scaling, a shifting parameter ρ_{shift} is introduced. Due to the fact that the half wave cosine representation is symmetric in axial direction (compare chapter 4.1.1), the imperfection shape beyond the original shell boundaries is symmetrically amended. Figure 4-35 shows the essential pattern of shell Z25 in unmodified state and axially scaled by $\alpha = 150\ \%$ and $\alpha = 250\ \%$.

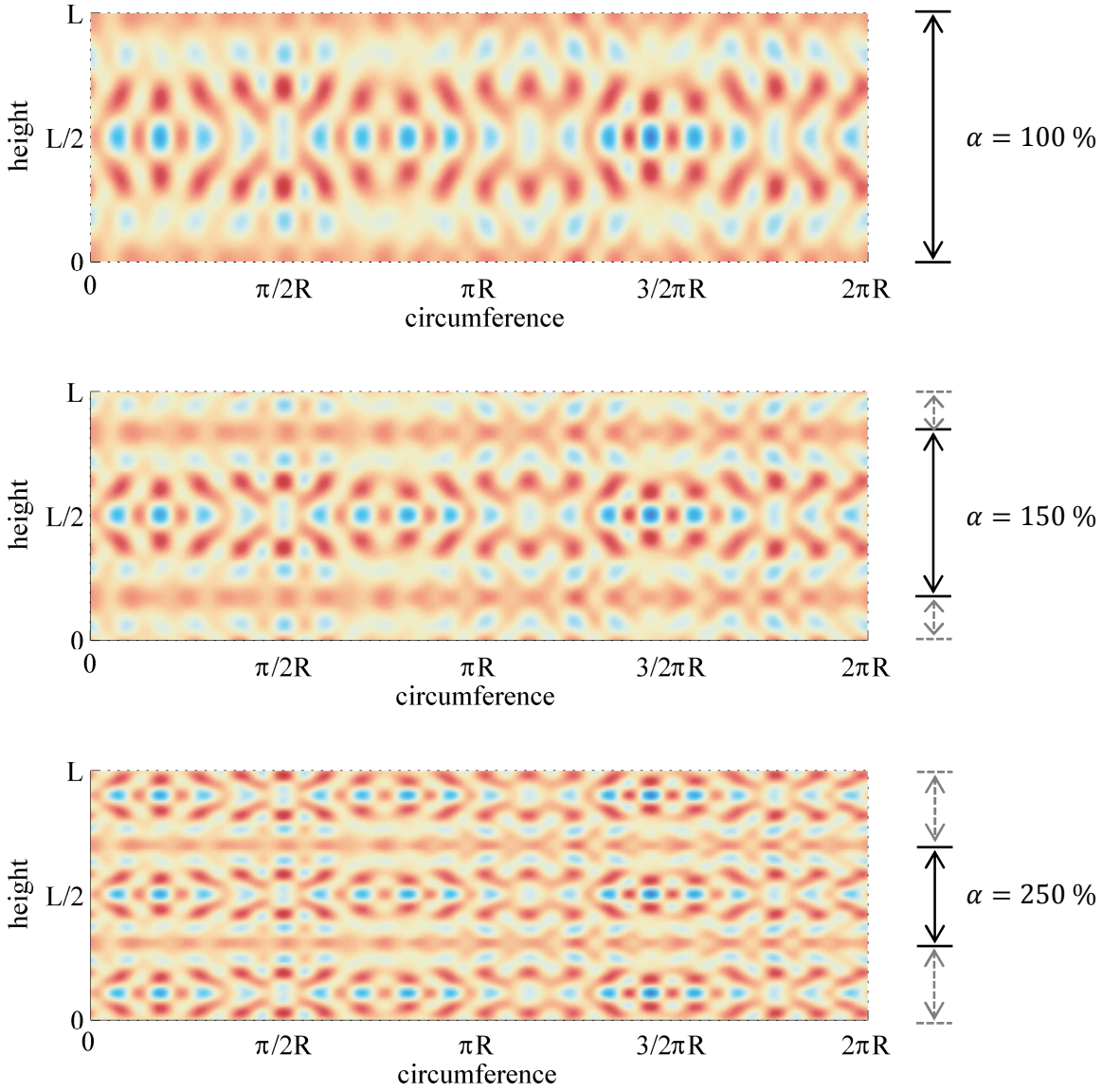

Figure 4-35: Reduced imperfection shape of shell Z25 with the axial length scaled by different scaling factors: 100 %, 150 %, 250 %

For axial scaling factors of 50 % (significant stretching of the pattern) to 400 % (significant compression of the pattern), finite element models are created and the buckling loads are evaluated. Figure 4-36 gives the resulting buckling load distribution.

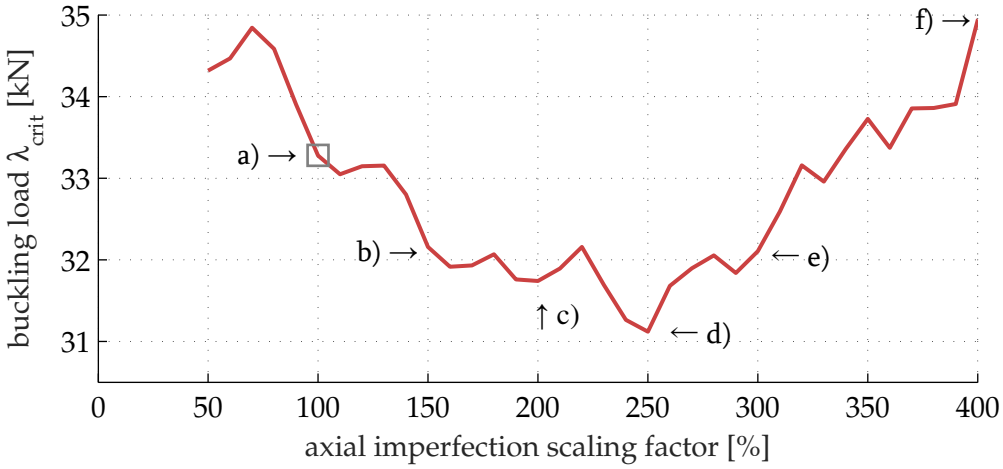

Figure 4-36: Buckling load over the artificial axial scaling of the essential pattern of shell Z25, original pattern indicated by gray rectangle

When looking at the results it is noticed that in the case of stretching the pattern to longer wave lengths than the original one, higher buckling loads are obtained. By compressing the pattern, decreasing buckling loads are observed with a minimum at an axial scaling factor of 250 % (compare also Figure 4-35, bottom). When scaling the pattern beyond 250 %, buckling loads rise again.

To explain this behavior, the stress states of the shells right before buckling shall be investigated on. Therefore, analogous to the study in chapter 4.4.4, the stress resultants in axial and circumferential direction will be evaluated. As reasoned above, the focus will be laid upon the corresponding stress maxima and minima around the position of the initial dimple.

The colored backgrounds of the plots in Figure 4-37 give the unloaded essential imperfection shape for different scaling factors around the (congruent) position where the respective initial dimple will snap in once the shell is loaded.

The gray arrows indicate the positions of the characteristic stress resultants in the calculation increment before the buckling load is reached. Here, circles indicate the local compression maximum in axial direction ($SR_{comp,max,ax}$) and the local compression maximum in circumferential direction ($SR_{comp,max,circ}$) which occur in the position of the initial dimple. Triangles pointing upwards indicate the local tension maximum in circumferential direction ($SR_{tens,max,circ}$) which occurs above or below the position of the initial dimple. Triangles pointing left indicate the local compression minimum in axial direction ($SR_{comp,min,ax}$) which occurs left or right of the position of the initial dimple. As both corresponding stress resultant peaks show nearly congruent values, for the interpretation of results it is irrelevant whether $SR_{tens,max,circ}$ and $SR_{comp,min,ax}$ are indicated above/below or left/right of the initial dimple, respectively. The descriptors a) to f) are given to simplify correlating the patterns to the buckling load curve given in Figure 4-36.

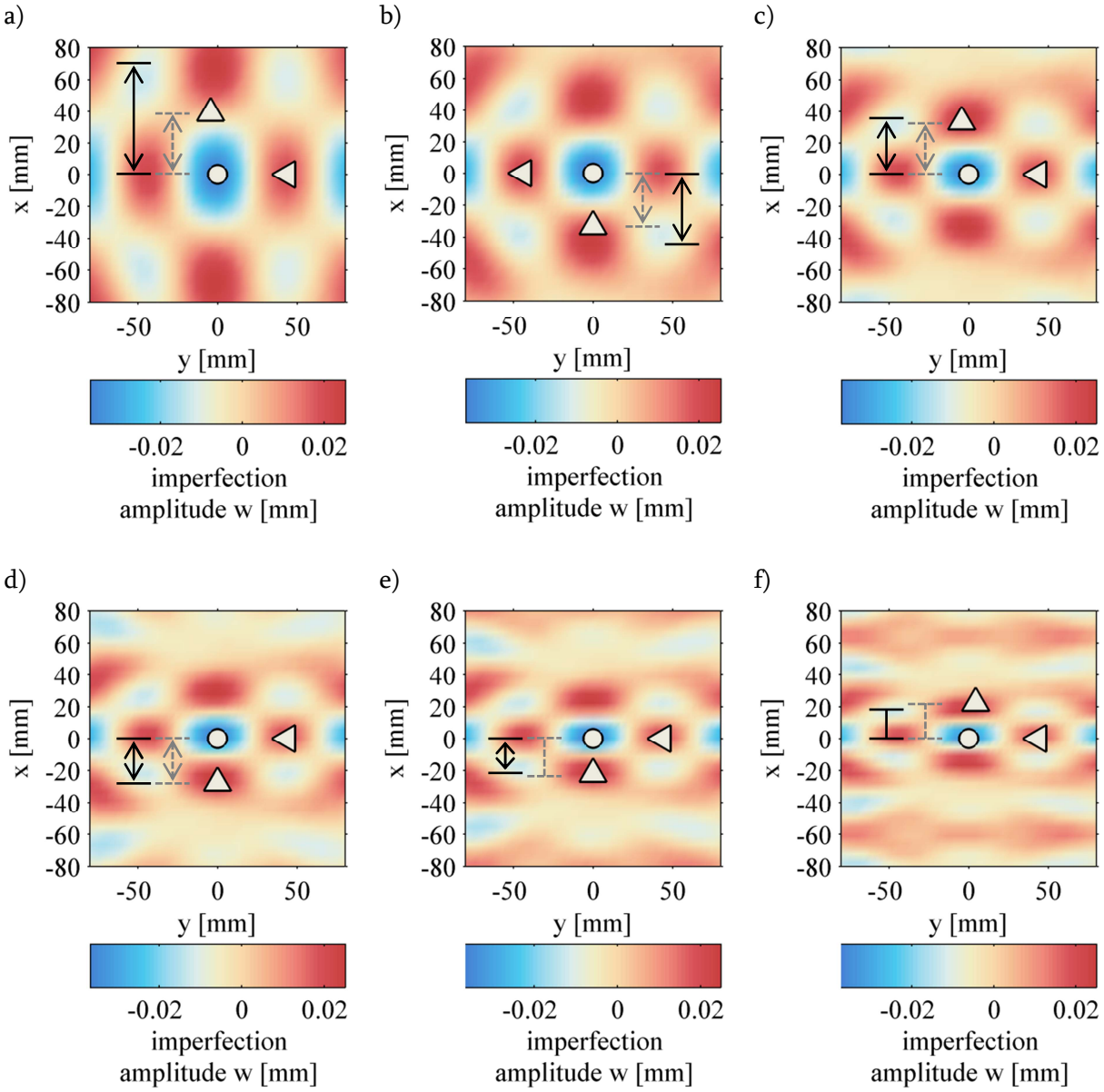

Figure 4-37: Reduced imperfection shape of shell Z25 around the position of the initial dimple for different length scaling factors (compare a) to f) in Figure 4-36), corresponding stress resultant maxima and minima in axial and circumferential direction in the last calculation increment before the buckling load is reached (markers)

When comparing the imperfection shapes and stress resultants peaks, in all cases the imperfection pattern shows a local minimum at the position of $SR_{comp,max,ax}$ and $SR_{comp,max,circ}$ (circle) and a local maximum at the position of $SR_{comp,min,ax}$ (leftward triangle). However, the imperfection maxima above and below the position of the initial dimple do not always coincide with $SR_{tens,max,circ}$ (upward triangle). While for increasing scaling factor from a) to f), $SR_{tens,max,circ}$ slowly moves inward, the local imperfection maxima above and below do also move inward (due to the scaling of the pattern), but faster. Thus, for scaling factors smaller than 250 %, the imperfection maxima lie outwards but approach the stress resultant maximum, for 250 % they coincide and for factors higher than 250 % the imperfection maxima lie slightly inwards and move away from the stress resultant maximum. At the same time, the buckling loads gradually decrease until a minimum is reached at a scaling factor of 250% and then rise again.

A similar behavior can be seen when scaling the imperfection pattern not in axial but in circumferential direction. When looking at Figure 4-38, again a minimum of buckling loads can be noticed at circumferential scaling factors of 90 % to 100 %. Figure 4-38 also gives the imperfection shapes and characteristic stress resultant positions at the bottom.

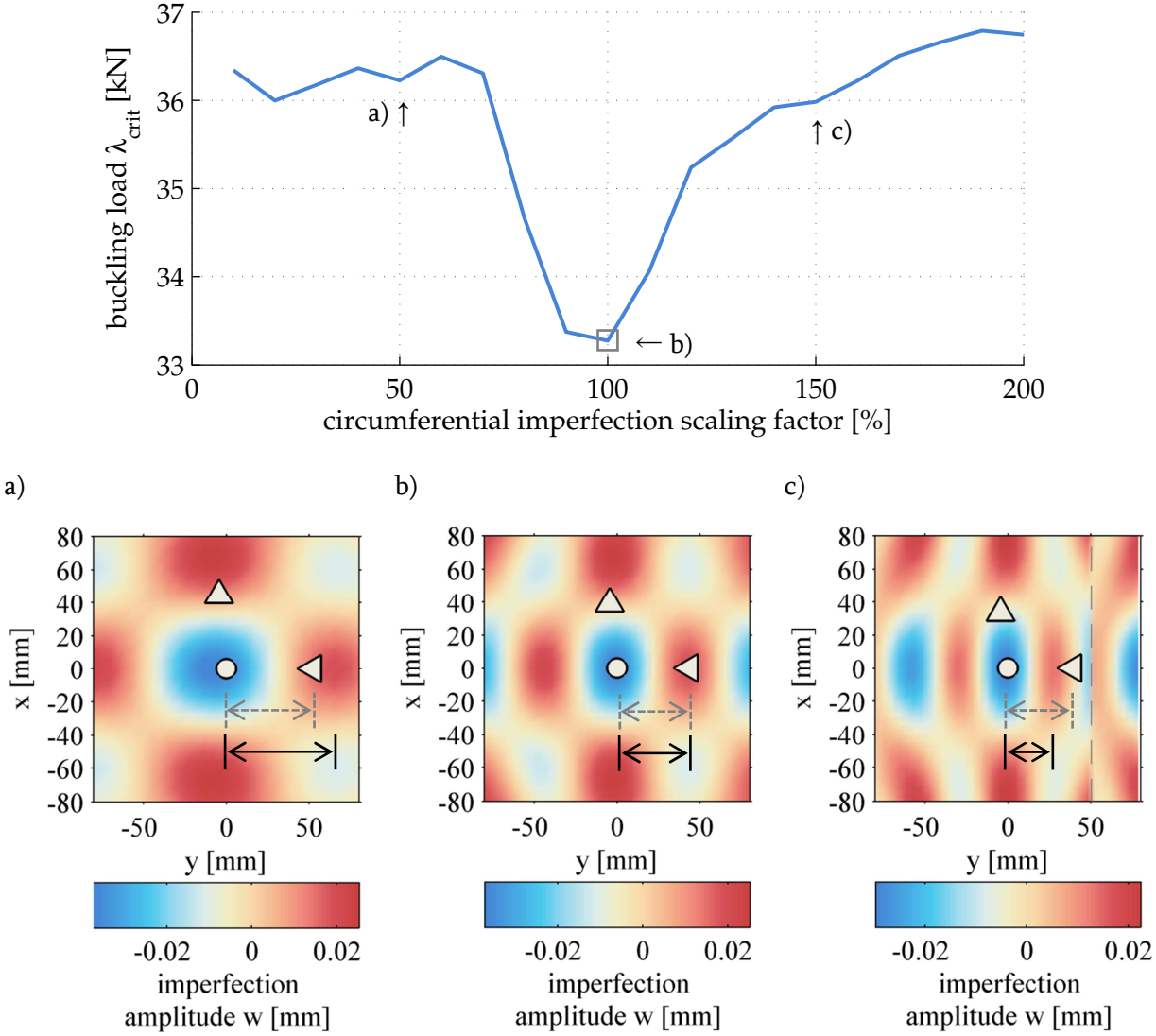

Figure 4-38: Buckling load over the artificial circumferential scaling of the essential pattern of shell Z25 (top), essential imperfection shape of shell Z25 around the position of the initial dimple for different circumferential scaling factors (compare a) to c)) (bottom), corresponding stress resultant maxima and minima in axial and circumferential direction in the last calculation increment before the buckling load is reached (markers)

In the case of circumferential scaling, the distance between the imperfection maxima left and right of the initial dimple and the axial compression minimum $SR_{comp,min,ax}$ varies, while the distance of the other imperfection maxima to $SR_{tens,max,circ}$ remains unchanged. Again, the minimum of buckling loads is reached once the position of the imperfection maximum neighboring the position of the initial dimple coincides with the according stress resultant peak.

It should be noted that in case of a circumferential compression of 150 % (compare Figure 4-38, c)), the location of the initial dimple changes to an area of locally nearly identical imperfection shape which is found near the edge of the commonly used unwrapped surface depiction. When the circumference of the imperfection pattern is artificially scaled and projected onto the original shell geometry, wave shapes are periodically added, similar to the case of axial

scaling. However, when doing so, the circumferential edges of the unwrapped surface do longer match which creates a discontinuous transition (indicated by dashed line in Figure 4-38, c)). This discontinuous transition obviously alters the load transfer and thus has to be handled with special care. As in this case the initial dimple does not snap in at the discontinuous transition but one wavelength apart with the same characteristic behavior concerning the stress resultants, this example is still judged as sufficiently suitable to depict the general mechanisms discussed above.

The same subjection of the buckling load to the geometrical compliance of essential imperfection pattern and stress resultant maxima is noticed for different shell measurements of different laminate setups. Figure 4-39 shows the results of axially scaling the imperfection pattern of shell Z11.

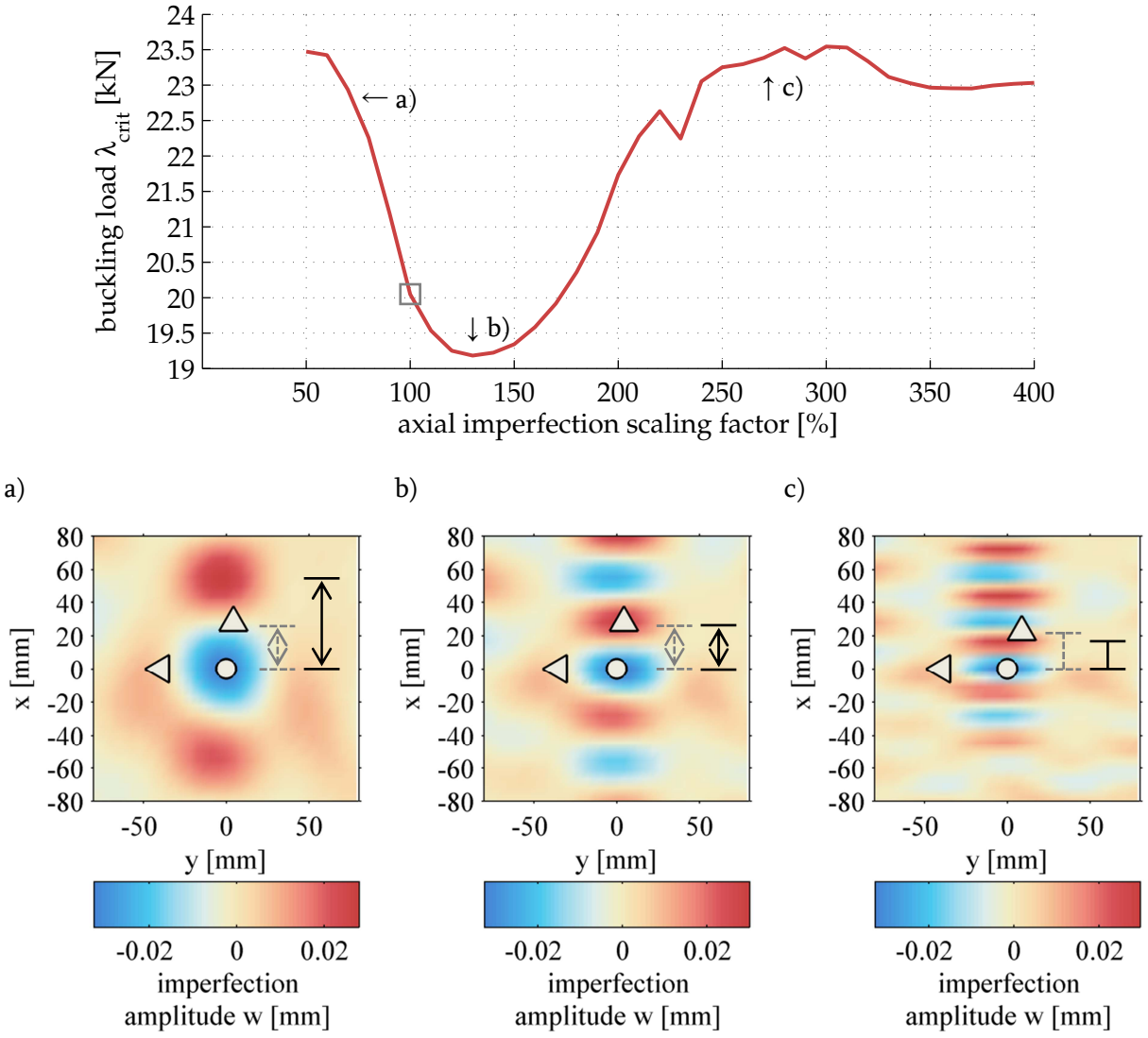

Figure 4-39: Buckling load over the artificial axial scaling of the essential pattern of shell Z11 (top), essential imperfection shape of shell Z11 around the position of the initial dimple for different circumferential scaling factors (compare a) to c)) (bottom), corresponding stress resultant maxima and minima in axial and circumferential direction in the last calculation increment before the buckling load is reached (markers)

While the essential pattern of shell Z11 shows to be generally less distinctively checker board shaped but more dominated by axial oscillation (compare Table 4-5), the connection between buckling loads, local imperfection maxima and stress resultant maxima can again be noticed. The closer the imperfection maximum above the position of the initial dimple is to $SR_{tens,max,circ}$

(upward triangle), the lower is the buckling load. When both coincide, the buckling load minimum is reached. Is the imperfection maximum located inside $SR_{tens,max,circ}$, the buckling loads rise again.

This behavior can be interpreted as follows. The geometric imperfection pattern of a given shell as well as its measurements and material properties constitute the prebuckling stress state which will evolve once the shell is subjected to axial loading (compare chapter 3.2.2). Thus, while the general picture of stress maxima and minima around the initial dimple is witnessed for every investigated shell, the concrete distance of for example the circumferential stress peaks varies, depending on the underlying imperfection pattern (compare for example Figure 4-37, a) to f), upward triangles) as well as the shell's design parameters. However, the closer the geometry of the respective underlying essential imperfection pattern is to the geometry of the corresponding stress state before buckling, the lesser elastic energy (and thus external loading) has to be added to reach that particular stress state. If now the geometry of the imperfection pattern exactly matches the geometry of the stress state before buckling (which itself is strongly influenced by but not equal to the imperfection pattern), a minimum of required external energy is reached and thus the buckling load is at its minimum.

As mentioned above, the question why a particular imperfection pattern causes a higher buckling load reduction than another imperfection pattern is discussed and pondered about for a long time. While certainly numerous insights where gained for artificial patterns of a limited amount of modes in analytical and semi-analytical frameworks, the connection between measured imperfection shapes and the geometry of the prebuckling stress state described herein could not be established before.

In measured imperfection patterns, multiple visually dominant but negligible wave shapes hamper proper evaluation of the geometric properties which are essential for buckling. Therefore, the comparison of geometric imperfection shapes and stress states was moribund and no conclusions could be drawn. However, if in a first step a given measured imperfection shape is filtered to its very parts which are essential for the nonlinear buckling behavior, the coherences between those essential shapes and the prebuckling behavior of the original shell become visible.

It should be noted that the described coherences were observed in all investigated cases. However, bolstering the validity by investigating further specimen is certainly an important part of future work on this matter.

4.4.6 Practical examples: patterns with divergent and matching buckling loads

After deriving first hints of the explanation why a given imperfection pattern leads to a lower buckling load than another given pattern, a brief overview of some sample cases shall be given. It will be shown that the different buckling load levels of different imperfection patterns are directly related to the differences between the positions of the imperfection maxima in the essential patterns and the positions of the corresponding maxima and minima of stress resultants right before buckling.

Figure 4-40 shows the reduced patterns of shells Z25 and Z21 as well as the reduced pattern of an artificially created random imperfection shape (see appendix B) around the positions of the corresponding initial dimples. The positions of the stress resultant maxima are again given by circles and triangles (compare chapter 4.4.4). To eliminate the influence of varying pattern amplitudes on the buckling loads, all reduced patterns are normalized to w/t = 0.1. This is in good agreement to the realistic regime of the reduced patterns of measured imperfection patterns.

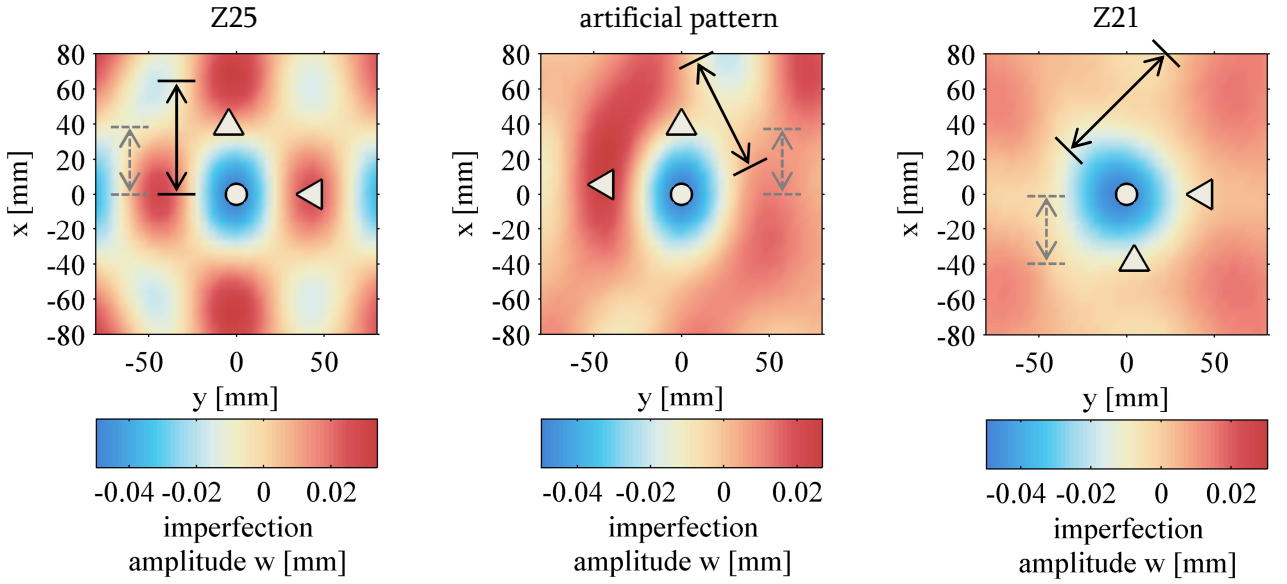

$\lambda_{Z25,red,w/t=0.1} = 31.50\ kN$ $\lambda_{Zart,red,w/t=0.1} = 32.59\ kN$ $\lambda_{Z21,red,w/t=0.1} = 34.39\ kN$

Figure 4-40: Reduced patterns of shells Z25 and Z21 as well as the reduced pattern of an artificially created random imperfection shape around the positions of the corresponding initial dimples (all normalized to $w/t = 0.1$), corresponding stress resultant maxima and minima in axial and circumferential direction in the last calculation increment before the buckling load is reached (markers)

It is again noticed that the buckling loads of the depicted patterns are significantly higher when the imperfection maxima do not concur with the positions of characteristic stress resultants. In the case of the artificial shell, a certain counter-clockwise shift of the upper and lower imperfection maximum is noticed. This trend is even stronger in the case of shell Z21, where the imperfection maxima are not vertically and horizontally aligned to the initial dimple but diagonally. The higher buckling loads of both shells can again be explained by the higher amount of deformation energy which has to be added to the structure to achieve the prebuckling state indicated by the characteristic stress resultants. Likewise, the reduced pattern of Z25 features the lowest of the three buckling loads while appearing most similar to the stress distribution.

Figure 4-41 shows the reduced patterns of shells Z18, Z20 and Z25 with the positions of the characteristic stress resultants, again normalized to a maximum pattern amplitude of $w/t = 0.1$.

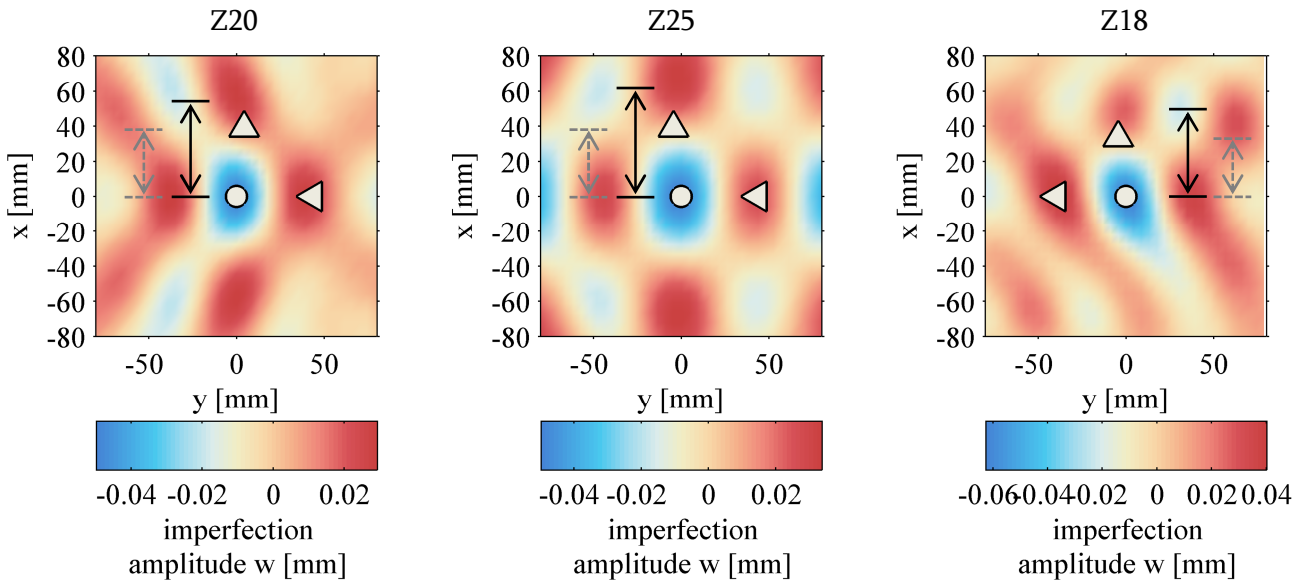

$\lambda_{Z20,red,w/t=0.1} = 31.22\ kN$ $\lambda_{Z25,red,w/t=0.1} = 31.50\ kN$ $\lambda_{Z18,red,w/t=0.1} = 31.52\ kN$

Figure 4-41: Reduced patterns of shells Z18, Z20 and Z25 around the positions of the corresponding initial dimples (all normalized to $w/t = 0.1$), corresponding stress resultant maxima and minima in axial and circumferential direction in the last calculation increment before the buckling load is reached (markers)

Despite all three patterns featuring a slightly different general imperfection shape, the local imperfection maxima and their distances to the characteristic stress resultants are almost identical. As a result, the buckling loads show to be nearly identical.

It is interesting to note that the three reduced patterns depicted above were filtered out from three original imperfection patterns of fundamentally different imperfection characteristics (amplitudes and wave shapes, see appendix A) but still show the exact same structural response in their essential parts.

4.5 Summarizing gain of knowledge

In the following, the main scientific progress ascribed to developing and applying the SIFM shall be briefly summarized.

1. *Revelation of the imperfection shapes which trigger local buckling*
   Using the SIFM, any given imperfection pattern can be filtered down to a reduced pattern with much lower amplitude (as it is only a fraction of the original pattern). While accounting for all nominal parameters like shell geometry and laminate setup, these reduced patterns lead to the same prebuckling stress distributions and buckling loads as the corresponding original patterns. Therefore, the reduced shapes are considered to represent the essential part of a particular imperfection pattern which causes its specific buckling behavior.
2. *Explanation for the buckling load level caused by a particular imperfection pattern*
   Besides first general claims (high amplitudes lead to low buckling loads), over the years detailed insights were gained on how certain mode interactions affect the stability behavior of a shell. Here, predominantly artificial patterns composed from a comparatively small number of modes were applied within analytical and semi-analytical frameworks. Still, the answer to the question about why exactly a particular measured imperfection pattern leads to a lower buckling load than another pattern remains unclear.
   In this thesis, a connection between detailed measured imperfection patterns and the corresponding nonlinear prebuckling states has been established.
   When comparing two imperfection patterns which were normalized to the same amplitude, one pattern leads to a lower buckling load than another pattern if the characteristic geometry of the essential pattern of the former is closer to the emerging distribution of prebuckling stresses.
   However, the effect a given local imperfection shape can have on the local stability seems to be limited by the occurrence of a local snap-through. This puts an upper bound to the severity conditions described above for increasing amplitudes of the respective patterns. Here, supplementary studies are required to further analyze the behavior and confirm the conclusions.
3. *Dependency of the essential imperfection shapes on the shell geometry and laminate setup*
   When applying the SIFM to measured cylindrical and conical shells of different lengths, radii and laminate setups, different essential patterns are obtained. Still, when comparing the essential patterns of specimens with the same design parameters, distinct commonalities are noticed. Therefore, it has to be assumed that the laminate setup and geometry influences the imperfection shape which turns out to be essential for the buckling of a particular specimen. This matches the fact that different laminate setups cause different membrane and bending stiffnesses which might then induce different sensitivities to different geometric imperfection shapes.
   However, while the reduced patterns generally show to be rather short-waved with comparatively low amplitudes, no direct connection of these supposedly critically stimulating patterns to the design parameters or manufacturing process can be formulated at this point.

5 New design method for thin-walled composite shells

Besides the detailed investigations on the complex buckling behavior of cylindrical shells performed in academia, in practice, the main motivation of analysis is the design and certification of structures. However, the application of analysis procedures for design comes with the fundamental transition from analyzing a known structure to analyzing a yet unknown structure.

As shown in chapter 2, over the past decades numerous ways were derived to obtain more or less safe predictions of the load bearing capacity of a structure before its fabrication. However, with the development of new analysis and manufacturing techniques, these design procedures show to be overly conservative in most cases. Therefore, an innovative design approach is proposed in this thesis that aims at delivering safe and at the same time economical design loads.

Thus, after a discussion of the general necessities and demands for shell design procedures in chapter 5.1, the new design approach, namely the probabilistic perturbation load approach (PPLA) is presented in chapter 5.2.

5.1 Necessities and demands for shell design methods

As indicated above, when it comes to designing shell specimens for tests or real launcher structures, a profound prediction or robust estimate has to be made for the load level a given specimen is going to be able to bear once manufactured. This correct estimation of the target value of the future structure, which in the context of this thesis is the buckling load, is the very basis for every design concept.

Only after this is achieved, further methods like optimization schemes can be applied to for example minimize structural weight.

In the case of designing cylindrical and conical shells with regards to buckling, their hypersensitivity to traditional and non-traditional imperfections shows to be the main obstacle of buckling load predictions. While sophisticated numerical methods for the correct prediction of the buckling process have been developed over the last decades, the question of how to assume the initial state of those numerical models, namely their inherent imperfections, is still not answered satisfyingly.

5.1.1 Shortcomings of currently prevailing design methods

As discussed in chapter 2, over the years numerous different methods have been developed to cope with the unpredictability of imperfections the manufactured specimens feature. Still, all of the prevalent methods to circumvent the problem come with noteworthy disadvantages, no matter if they are geared towards establishing certain worst case buckling load levels or focus on extrapolating existing knowledge to a future case. Table 5-1 sums up the procedures prevalent in academia and industry, their main ideas as well as their advantages and drawbacks (compare also chapters 2, 3.3 and 3.4).

Category	Procedure	Main idea	Advantages	Drawbacks
Knock-Down-Factors	NASA-SP 8007	lower bound curve based on slenderness	- based on experiments with real structures	- in most cases overly conservative - only partly applicable to composites
	Eurocode 3, ECCS 56	lower bound curve based on manufacturing quality		
Deterministic Design	Eigenmode imperfections	assumption of a worst case imperfection shape	- no imperfection information necessary	- not representative for real imperfection shapes - not always robust
	SPLA	application of a lateral load leading to a worst case imperfection shape		
Probabilistic Design	Monte-Carlo schemes	prediction of safe load levels by interpretation of numerous realizations	- known level of design reliability	- can be computationally costly - information about anticipated imperfections necessary
	SAP	determination of stochastic moments of the assumed buckling load function		

Table 5-1: Existing methods for design of imperfection sensitive cylindrical shells, main ideas, advantages and drawbacks

5.1.2 What are the features of an ideal design procedure?

All common design procedures listed in Table 5-1 entail disadvantages that make their application difficult. In a situation where the economic desire to decrease weight is only surpassed by the certifications procedures' demand of safe and reliable structures, a thorough assessment of inherent trade-offs is indispensable.

First and foremost, an auspicious new design procedure must deliver design loads which are always robust. This means that the values obtained by applying the procedure (before manufacturing) have to be always lower than the buckling loads of the corresponding real specimen (after manufacturing).

Secondly, in contrast to the cold war situation fueling the space race in the 1960s, current and future launcher designs are and will be evaluated mainly based on their operational costs. Therefore, it is crucial to overcome the inherent overly-conservativeness of the ageing guidelines and design philosophies.

As discussed above, real shell structures always feature numerous deviations from the nominal design. These deviations are generally categorized as traditional and non-traditional imperfections (compare chapter 2). As a third feature of an ideal design procedure, the influence of all those various imperfection types on the buckling load should be incorporated, whether in the way of direct stochastic treatment or by establishing surrogate models.

However, when trying to incorporate the effect of various imperfection types in a design procedure, sufficient knowledge about their stochastic scatter (in the case of probabilistic approaches) or their particular influence on the structural behavior (in the case of deterministic

approaches) has to be available. For non-traditional imperfections, like for example deviations of the composite material properties, this knowledge is comparably cheap to obtain by performing test series on coupons. In contrast to that, when it comes to geometric imperfections, laser measurements of full scale shell structures are very complex endeavors and thus costly. Therefore, an ideal design procedure for cylindrical shells obviously has to properly account for the influence of geometric imperfections on the buckling load but at the same time should requiring preferably as little information on their shape as possible.

In summary, an ideal design procedure should:

1. be always robust,
2. deliver ambitious design load levels,
3. be well applicable with low required time expenses,
4. include the effect of traditional and non-traditional imperfections and
5. require as little information on geometric imperfections as possible.

In this thesis, a new design procedure is proposed which aims at accomplishing these goals (see chapter 5.2). The basic concept is to apply sophisticated deterministic approaches to capture the influence of geometric imperfections on the buckling load. Then, these methods are integrated into an embracing probabilistic framework which captures the nonlinear interaction of a geometrically imperfect shell surface with freely chosen types of non-traditional imperfections.

It should be noted that, as indicated in chapter 3.1.3 and in addition to the uncertainties discussed above, the real structural response of a launcher structure is also characterized by heavy vibrations. However, experimental setups as well as established design procedures account for those dynamic effects by splitting the analysis into a translation of dynamic loads into equivalent static loading conditions and the quasi-static analysis of the structure itself subjected to these equivalent static loading conditions. While recent efforts were made to directly include for example structural damping in aircraft design (EU 7th framework research project DAEDALOS [113]), the strategy of applying equivalent static loading conditions is still well received in multiple fields of aerospace engineering and structural engineering in general. Accordingly, the design procedures proposed herein will be performed on a quasi-static basis and neglect any dynamic influences.

5.1.3 Classification of design procedures regarding their required amount of information about anticipated imperfections

As indicated above, when it comes to the discussion about sculpting an innovative design procedure, a fundamental conflict of interests arises.

On the one hand, the influence of imperfections on the buckling behavior should be accounted for as mechanically and stochastically exact as possible. In the case of deterministic approaches, only the detailed consideration of the phenomena crucial for buckling can lead to worst-case buckling loads that actually stand up to the ones measured in reality. This can either be achieved by precise modeling of actual imperfection shapes or by understanding the physical phenomena to derive surrogate models. In the case of probabilistic approaches, not only the correct modeling but also

the precise assessment of the scatter of the input parameters themselves has a vital influence on the applicability of the procedure itself. For example, KRIEGESMANN recently showed that the design loads obtained with the SAP for the very specimen studied in this thesis are highly dependent on the sample size considered to obtain the scatter of input parameters ([86], [89]).

On the other hand, basically contrary to the preferably precise modeling of imperfections, an ideal design procedure should require as little information about the imperfections as possible, for practical reasons. This is due to the fact that for example geometric imperfections are very expensive to obtain via measurements as well as highly dependent on the manufacturing process. Therefore, appropriate predictions about imperfections are difficult in a situation, were for example the laminate setup of a design is not yet fixed. Thus, for a procedure applied in the design phase, it is of vital interest to require as little reliable information about the manufactured structure as possible.

This conflict of precise modeling and independence from information is characteristic for every discussion about possible new design procedures.

To better locate a particular approach in the area between these poles, a new scheme for classification of design procedures is proposed. Table 5-2 introduces three grades to categorize a given design method based on the required grade of knowledge about imperfections for application of that particular procedure.

	Level of required knowledge	Example
Grade 1	independent from knowledge about imperfections	SPLA, Eigenmode imperfect-tions
Grade 2	basic experience about imperfections required, for example one measured specimen of comparable design	Eurocode 3, ECCS 56
Grade 3	extensive information required, for example by a measurement series with sufficiently high sample size for probabilistic treatment	SAP and other probabilistic approaches

Table 5-2: Classification of design procedures by their required knowledge about anticipated imperfections

The presented grading can generally be applied for every type of traditional and non-traditional imperfections. In the case of cylindrical and conical shells, of all types of imperfections, detailed geometric imperfection patterns are the most expensive to measure and difficult to obtain. Consequently, in the following, design procedures will be graded solely based on their requirements of knowledge about anticipated geometric imperfections.

When exclusively considering Table 5-2, obviously a lower grade would seem beneficial for the applicability of a given design approach. However, as discussed above, with less applied knowledge about the anticipated imperfections, also the potential for safe, precise and thus less conservative outcomes might very well decrease.

It should be noted that the NASA-SP 8007 at first sight does not properly fit into the grades introduced above. An extensive study of most experiments available at the time was used to establish the well-known lower bound curve (compare chapter 2), commanding a grade 3 categorization. Nevertheless, it is at the same time considered as the prime example of overly conservative design procedures, raising an important point: What actually is overly conservativeness? The only valid definition can be that a design procedure is overly conservative when the buckling loads of manufactured specimen greatly and gratuitously exceed the design values used to plan these specimens. The reason can be that the inherent assumptions are too cautious or that the current manufacturing and testing quality greatly surpasses the one present when formulating the design procedure. This is the case for the NASA-SP 8007 and is considered to be the cardinal reason for the strife to develop new, effective and safe design procedures.

5.2 Probabilistic Perturbation Load Approach (PPLA)

The main idea of the probabilistic perturbation load approach (PPLA) is to combine the deterministic lower-bound character of the SPLA with the advantages of a probabilistic analysis framework.

Probabilistic procedures like the SAP (compare chapter 3.4) have the significant advantage to capture the stochastic scatter of various input parameters, which is generally noticed in sets of manufactured specimens. However, adequately determining the scatter of especially geometric imperfections in practice is very costly and thus rarely accomplished.

In contrast to that, a lower bound approach for the influence of geometric imperfections could eliminate the need for costly measurement campaigns. Here, the SPLA leads to a load level which is lower than numerically obtained buckling loads of shells with all geometric imperfection patterns investigated in this thesis. It is therefore assumed to robustly account for the influence of geometric imperfections on the buckling load. A detailed discussion and numerical evaluation on this matter is given in Table 3-1 in chapter 3.3.4. Combined with the findings discussed in chapter 4.4.3, it therefore seems well suited to serve as a surrogate imperfection which represents a lower bound for the influence of geometric imperfections.

5.2.1 Basic scheme

As mentioned above, it is proposed to substitute the stochastically scattering geometric imperfections in the probabilistic analysis by the characteristic single dimple induced by a lateral perturbation load of sufficient magnitude.

Thus, instead of incorporating geometric imperfections within the probabilistic framework (which among others can be the SAP described in chapter 3.4), the objective function of the probabilistic procedure is altered. Instead of calculating the buckling load λ_c depending on the scattering traditional and non-traditional imperfections, the objective function is defined as the lower bound load N_1 obtained by the SPLA, based on solely the scattering non-traditional input parameters. By performing the SPLA for every given realization of non-traditional imperfections, a stochastic distribution of the lower bound load N_1 given by the SPLA is obtained. When using the SAP in the PPLA framework, the final design load $N_{1,d}$ is obtained after assuming a type of distribution and choosing a desired level of reliability.

Figure 5-1 gives a schematic overview of the PPLA using the SAP as the applied probabilistic framework. For enhanced perceivability, the SAP elements which are omitted are dashed and grayed out while the new PPLA elements are highlighted in darker color (compare Figure 5-1 to Figure 3-18).

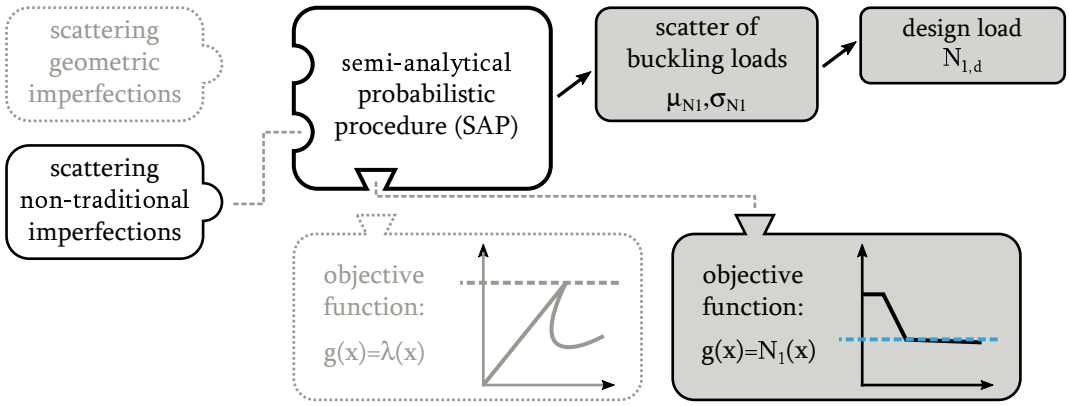

Figure 5-1: The probabilistic perturbation load approach (PPLA): schematic overview, omitted SAP elements dashed and grayed out (compare chapter 3.4)

On the one hand, due to the probabilistic framework, the PPLA accounts for the influence of scattering non-traditional imperfections on the buckling load. On the other hand, by performing the SPLA for every given realization, the PPLA also incorporates the detrimental influence of geometric imperfections on the buckling load. By transforming the usual probabilistic framework to the PPLA-scheme, the required evaluations of the objective function are heavily reduced as the geometric imperfections, described by a comparatively high number of scattering input parameters, are left out. Conversely, the evaluation of the objective function itself is costlier within the PPLA framework, based on which approach is chosen to determine the lower bound load N_1 (compare chapter 3.3).

As described above, the PPLA covers the influence of geometric imperfections by integrating the SPLA. However, evaluating lower bound loads is obviously only legitimate if the application of a lateral perturbation load to the specific shell configuration actually leads to the general characteristic lower bound behavior. For certain laminate setups this may not be the case and therefore has to be ascertained prior to application of the procedure.

However, it should be noted that it is not important whether the SPLA applied to a given specimen would deliver lower bound loads that are lower than experimentally obtained loads (which, in literature, is commonly understood as "applicability" of the SPLA). As it only represents a surrogate geometric imperfection, all non-traditional imperfections, which are present in experimental specimens, can be treated within the probabilistic framework.

5.2.2 Interpreting reliability of design loads

Due to the alteration of the objective function from the shell's buckling load to the lower bound load N_1, the level of reliability which has to be chosen in the last step of semi-analytical probabilistic framework has to be interpreted differently.

In the case of the classical SAP including traditional and non-traditional imperfections, the chosen reliability R is connected to a buckling load level λ_R which is expected to be exceeded by for example $R = 99\%$ of all possible shell realizations (compare Figure 5-2, left, dashed line). This load level is then used as a design load λ_d. Consequently, this means that if the scattering input parameters are appropriately characterized, the chosen level of reliability in the calculation is directly connected to the shell design's real life failure load.

In contrast to that, when it comes to the PPLA, the obtained design load $N_{1,d}$ does not describe a buckling load level which is exceeded in experiments or real applications. It rather has to be interpreted as a lower bound level $N_{1,R}$ which is exceeded by for example $R = 90\%$ of all possible SPLA-evaluations with various kinds of scattering non-traditional imperfections (compare Figure 5-2, left, dashed line).

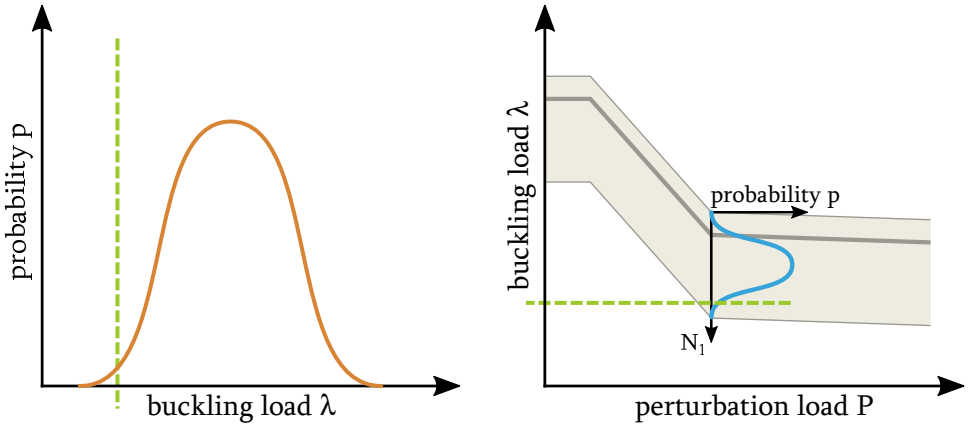

Figure 5-2: Interpreting design loads and reliability levels: the different safety concepts of SAP (left) and PPLA (right)

This vital characteristic is caused by the SPLA delivering a supposedly robust lower bound load of unknown safety (compare chapter 3.3.4). As in the case of all lower bound approaches, it obviously is of great importance for the designer or authorities to account for these characteristics when defining a concrete level of reliability R.

When deriving design values for a shell's buckling load based on scattering traditional and non-traditional imperfections, a chosen level of reliability of $R = 99\%$ seems to be reasonable and is assumed in the following chapters (compare [102] and [89]). This corresponds to the demands in aircraft certification on the material properties of parts which are crucial for the structural integrity of the component, given in CS 25.613 [114].

When deriving design values with the PPLA, a numerical level of reliability of $R = 90\%$ is chosen. This is to avoid overly-conservativeness by redundancy of the integrated lower-bound behavior of the SPLA with a high safety level on top and corresponds well with the reliability level of redundant structures demanded in aircraft certification [114].

It should be noted that the chosen value for the reliability to obtain $N_{1,d}$ can be converted into an actual level of reliability of the shell design by comparison to the buckling load distribution obtained by full probabilistic approaches. In doing so, it is noticed that the actual level of reliability of the PPLA designs of cylindrical shells (with chosen $R = 90\%$) are always higher than 99%. This is because for cylindrical shells, the design loads $N_{1,d}$ always show to be lower that the design loads by SAP $\lambda_{d,R=99\%}$ (compare chapter 6).

5.2.3 Application guideline

In the following, a detailed step-by-step guide for performing the PPLA within the numerically efficient SAP framework is given. For details and further background on the employed SAP equations, it is referred to chapter 3.4 and [89].

1. Allocation of $2n + 1$ parameter sets S_i, where n is the number of random input parameters describing the scattering non-traditional imperfections and Δz_i is the chosen step size for calculation of the numerical derivatives (in this thesis $\Delta z_i = 1.5\,\sigma_i$, compare chapter 3.4.2):

$$S_1 = [\mu_{z1}, \mu_{z2}, \dots, \mu_{zn}]$$

$$S_2 = [\mu_{z1} + \Delta \boldsymbol{z_1}, \mu_{z2}, \dots, \mu_{zn}]$$

$$S_3 = [\mu_{z1}, \mu_{z2} + \Delta \boldsymbol{z_2}, \dots, \mu_{zn}]$$

$$[\dots]$$

$$S_{n+1} = [\mu_{z1}, \mu_{z2}, \dots, \mu_{zn} + \Delta \boldsymbol{z_n}]$$

$$S_{n+2} = [\mu_{z1} - \Delta \boldsymbol{z_1}, \mu_{z2}, \dots, \mu_{zn}]$$

$$S_{n+3} = [\mu_{z1}, \mu_{z2} - \Delta \boldsymbol{z_2}, \dots, \mu_{zn}]$$

$$[\dots]$$

$$S_{2n+1} = [\mu_{z1}, \mu_{z2}, \dots, \mu_{zn} - \Delta \boldsymbol{z_n}]$$

2. Generation of a finite element model FEM_i for each parameter set
3. Calculation of the lower bound loads $N_{1,i}$ for all finite element models FEM_i based on one of the different approaches given in chapter 3.4.2.
4. Determination of the first and second derivatives of the objective function at the mean vector of input parameters $\frac{\partial N_1(\boldsymbol{\mu})}{\partial z_i}$ and $\frac{\partial^2 N_1(\boldsymbol{\mu})}{\partial z_i^2}$, respectively. The corresponding equations are given in chapter 3.4.2 and [89]. Here, in the context of the PPLA the objective function g is the lower bound load N_1 obtained by performing the SPLA.
5. Choice of a complexity of the probabilistic approximation. In this thesis the incomplete second order approach (ISOA) is applied. Subsequently, the equations given in chapter 3.4.2 and [89] are used to determine the stochastic moments of the lower bound load μ_{N1}, σ_{N1} and ν_{N1}, where in the context of the PPLA the objective function g is the lower bound load N_1 obtained by performing the SPLA.
6. Determination of the design load by choice of a type of distribution (in this thesis: normal distribution) and a desired level of reliability R (equations given in chapter 3.4.2 and [89]).

6 Application examples for the new design procedures

Before describing the numerical treatment of the scattering input parameters of the subsequent probabilistic analyses, a more general overview of the calculation software and shell models is given in the following.

With the scatter of input parameters as a basis, the new design procedures proposed in chapter 5 are then applied to various cylindrical and conical composite shells. A comparison to the results of well established procedures is presented to demonstrate the new procedure's potential to significantly decrease structural weight while maintaining levels of reliability.

6.1 Numerical modelling of cylindrical and conical shells

6.1.1 Nominal geometries and laminate setups of considered shells

For all investigations in this thesis, different sets of composite shells manufactured at DLR, Braunschweig were taken as a basis.

With regards to cylindrical structures, shells Z09 to Z12 were produced in the same series and tested by HÜHNE et al. [57] while shells Z15 to Z26 were produced in a different series and tested by DEGENHARDT et al. [110]. It is worthwhile to note that the former show mainly long waved imperfection shapes, the latter feature more short waved imperfection shapes with lower amplitudes. When it comes to shells Z36 and Z37 as well as all conical shells, the specimens were produced and tested by KHAKIMOVA et al. [115], [101] (compare also the technical reports of the EU 7th framework research project DESICOS).

Table 6-1, Table 6-2 and Table 6-3 give an overview of the different shell geometries and laminate setups treated in this thesis.

	Z07-Z08	Z09	Z10-Z11	Z12
length L [mm]	510	510	510	510
radius R [mm]	250	250	250	250
nominal wall thickness t [mm]	0.5	0.5	0.5	0.5
laminate setup	[±24,±41]	[±41,±24]	[+24,+41,-41,-24]	[±45,0,-79]

Table 6-1: Shell geometries and laminate setups of shells Z07-Z12 [57]

	Z15-Z26	Z36-Z37
length L [mm]	500	800
radius R [mm]	250	400
nominal wall thickness t [mm]	0.5	0.75
laminate setup	[±24,±41]	[±34,0,0,±53]

Table 6-2: Shell geometries and laminate setups of shells Z15-Z26 [110] and Z36-Z37 [101]

	K01	K06	K08
height H [mm]	300	300	300
top radius r [mm]	190	190	190
bottom radius R [mm]	400	400	400
semi-vertex angle δ [°]	35	35	35
nominal wall thickness t [mm]	0.75	0.75	0.75
laminate setup	[30,-30,0,0,30,-30]	[30,-30,0,0,30,-30]	[30,0,-30,-30,0,30]
ply topology design	D1	D3	D3

Table 6-3: Shell geometries and laminate setups of K06-K08, detailed ply piece parameters given in [111]

6.1.2 Numerical models for buckling analysis

For all buckling load calculations in this thesis, the widespread finite element software package ABAQUS by SIMULIA was used. For the calculation of shells with perfect geometry, linear buckling analyses were applied (compare chapter 3.1.2). All other simulations were performed geometrically nonlinear and quasi-static to properly capture the nonlinear influence of various imperfection types on the prebuckling and buckling behavior (compare chapter 3.1.3). Here, the Newton-Raphson scheme was applied.

When using ABAQUS to perform geometrically nonlinear simulations, a built-in stabilization function can be used. Doing so adds a constant artificial damping component to the solver in the form an internally created artificial set of nodal forces which act opposed to the nodal displacements. When handling stability problems, in practice it is necessary to add a certain stabilization to ensure that the solver is able to find equilibrium states until the anticipated instability point is reached. However, the stabilization parameter has to be chosen as low as possible to forestall false results by actually missing the instability point. Based on a convergence study, the stabilization parameter was chosen to $\tau_{stab} = 5e - 7$. This value lead to satisfactory results in all investigated cases and is in agreement with the findings of CASTRO et al. [63].

All finite element meshes were realized with 90 elements in axial direction and 360 elements in circumferential direction. While other authors showed that for the given shell structures, mesh finenesses of around $60\ x\ 240$ are sufficient to achieve buckling load convergence (compare [42] and [89]), in the context of this thesis an additional criterion for mesh fineness has to be considered. This is due to the fact that when it comes to the application of the SIFM, the wavelengths of different imperfection modes and their particular influence on the buckling behavior play an important role. Here, as reasoned in chapter 4.2.6, the amount of nodes should be equal to six times the amount of half waves of the shortest wavelength included in the Fourier series. Therefore, in axial direction, 15 axial half waves lead to $15 * 6 = 90$ nodes. In circumferential direction, 30 circumferential full waves lead to $30 * 2 * 6 = 360$ nodes. In addition to this rule of thumb, the convergence of the general appearance of the patterns obtained by application of the SIFM was checked for coarser and finer meshes to assure convergent behavior.

In the corresponding experiments, the shell specimens never showed plastic behavior. As it is common for very thin walled shells, the buckling and postbuckling deflection patterns usually stay within the elastic regime, providing constant buckling load levels over numerous load cycles (compare [57]). Thus, a linear elastic material model was applied in all simulations. As from a point of view of element formulation, the elastic buckling of cylindrical and conical shells has to be considered as a rather modest challenge, common standard “S4R” elements were applied. These elements come with three translational and three rotational degrees of freedom for each of the four nodes and use reduced integration. The FE software includes an automatic hour glass control for these elements. When it comes to element choice, the utilization of full integration or eight-node elements did not notably alter the results while substantially increasing computational times.

All shell models share the same boundary conditions. As usual in experimental setups, both the upper and lower edge of the cylinders and cones are considered to be clamped, realized by so-called pin constraints. This means that all nodes of a given shell edge are connected to one of two reference nodes. All nodes that are connected to a particular reference node then share the same translational and rotational deflections with that reference node. In this way, all degrees of freedom of the nodes on the lower edge of the shell are constraint to zero. At the upper edge of the shell, all degrees of freedom except the axial displacements are constraint. During the displacement driven calculation, the compression is applied to the upper reference node. As a result, the axial compression is spread evenly on all nodes at the upper edge, aiming at reproducing experimental behavior.

Various simulations discussed in this thesis include the application of radial perturbation loads (SPLA and PPLA). Whenever this is the case, the perturbation load is applied at the shell mid-length. The circumferential position of perturbation loads does not alter the results in the case of perfect shell geometries. Only in the case of simulations with perturbation loads applied to inhomogeneous imperfect surfaces (not the case in this thesis) or in the case of simulations with perturbation loads in combination with local imperfections like for example loading imperfection (PPLA), the circumferential position affects the results. Therefore, in all PPLA simulations, the position of the perturbation load defines the mean value of the scattering horizontal angle of the loading imperfection (compare Figure 6-4). By doing so, a worst case scenario of the coupling between radial loads and bending at the boundary is achieved.

6.1.3 Conical shells: peculiarities in manufacturing and modeling

The general strategy to manufacture or numerically model a cylindrical shell can be considered as comparatively straightforward. While manufacturing certainly includes inevitable uncertainties and requires profound knowledge and experience, the general procedure can be well planned and conducted. When applying for example a single fiber at the lower edge of the mandrel with a fiber angle of for example 30°, continually winding up that fiber around the circumference is possible until the upper shell edge is reached. When properly wound up, the fiber angle constantly remains 30° at all locations on the cylinder (compare Figure 6-1, top left). A subsequent fiber can be placed parallel to the first one, also being in 30° angle at all locations. In practice, composite cylinders are usually manufactured by placing tapes stripes, each containing numerous parallel plies, which are wound up on a rotatable mandrel (compare Figure 6-1, top right).

On the numerical side, the creation of a finite element model of such a cylinder represents a rather modest challenge as the same laminate setup properties are equally attributed to every finite element.

When it comes to conical shells however, manufacturing gets more demanding and so does numerical modeling.

When applying a single fiber at the lower edge of a conical mandrel at 30°, it is possible to again keep the local ply angle constant during wind up. However, due to the inclination angle δ of the cone, the fiber then does not follow a straight line on the cone surface. This poses a limitation in

production, as fiber tapes cannot be laid down in arbitrary curves without wrinkles. Otherwise, if the tape stripes are laid on a straight line on the surface, significant fiber angle deviations occur (compare Figure 6-1, bottom left).

In addition to that, the placement of a second single fiber or tape strip next to the first one poses a second significant problem: As the lower radius of a conical shell R is higher than the radius of the upper shell edge r, continuous tapes cannot be placed in parallel to each other without overlapping at the upper shell edge.

To reduce both effects, composite cones are manufactured by pre-cutting separate trapezoidal pieces of ply tapes. The shapes of these ply pieces as well as their positioning are adjusted to minimize the mean fiber angle deviation within a single piece and to eliminate overlapping at the upper shell edge (compare Figure 6-1, bottom right).

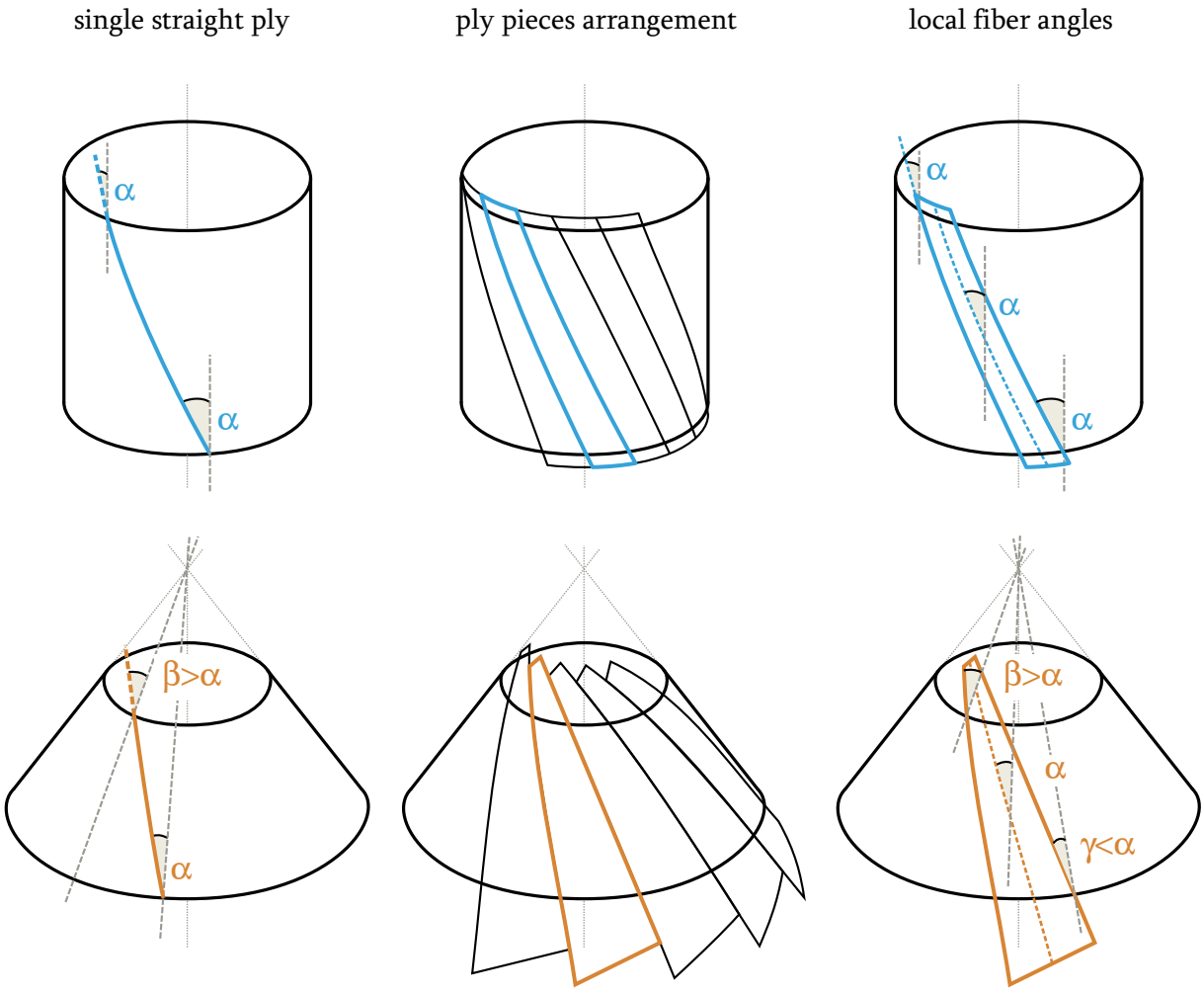

Figure 6-1: Fiber angles and ply piece placement for cylindrical shells (top) and conical shells (bottom)

Likewise, when it comes to establishing a finite element model for a composite cone, attributing a single laminate setup to elements is not sufficient to properly capture the real laminate setup. KHAKIMOVA et al. [111] showed that properly accounting for the local deviations from the nominal ply angle can result in changes of numerically determined buckling loads of up to 9%.

Therefore, the exact ply piece arrangement has to be reproduced. This is realized by calculations of the ply piece positions, followed by an elementwise evaluation of the local fiber angles of all

plies within the preprocessor. For further details and a step-by-step guideline for ply piece arrangement it is referred to the in-depth description by CASTRO et al. [116].

Figure 6-2 exemplarily depicts the as-build ply piece placement of the first laminate layer of shell K06. The local fiber angles are elementwise given in colors, indicating the deviations from the as-planned laminate setup given in Table 6-3.

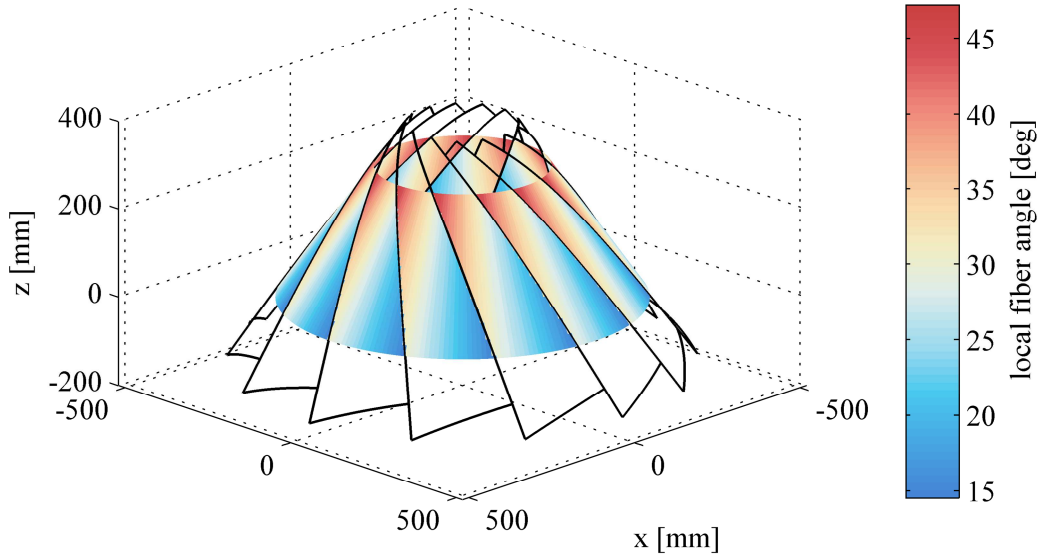

Figure 6-2: Ply piece placement of shell K06, first layer, nominal fiber angle 30°, local fiber angles given in color

It should be noted that numerical models (of cylindrical and conical shells) created in this way still do not represent real manufactured specimens, as fiber angle deviations, inaccuracies and overlaps that happen during manufacturing are not covered. However, it is possible to include these as non-traditional imperfections within design procedures.

6.2 Scatter of input parameters

6.2.1 Application of design procedures in practice: necessities and compromises

Every manufactured cylindrical or conical shell contains numerous types of imperfections. While certainly geometric imperfections or deviating material properties may be the most obvious ones, at the same time various other deviations of nominal properties may be present in the specimen. Examples include, but are certainly not limited to, for example fiber waviness, fiber angle deviations, voids or local delaminations which are most likely part of every real structure and influence its structural behavior.

This fact alone poses a considerable problem for the numerical calculation of shells in general, as all these imperfections have to be measured and modeled correctly to ensure a realistic simulation of the buckling behavior. Here, for every type of imperfection, various authors and researches use different methods. For example thickness imperfections can be modeled as globally smeared thickness deviations [89], as thickness deviations which vary in different areas of the shell [117] or even by mapping high-fidelity ultra-sonic measurements to a very fine FE-mesh [118].

When it comes to probabilistic analyses, the problem deteriorates. On the one hand, the numerical costs tendentially rise due to the repeated evaluation of different realizations of the same specimen. However, first and foremost, representative values for the stochastic scatter of all these input parameters have to be established. This is extremely costly and poses the main obstacle of applying probabilistic design procedures.

Thus, while deterministic procedures may be less demanding regarding the choice and application of imperfections in certain cases, in the area of probabilistic procedure compromises have to be made. These have to take into account:

- the numerical costs due to model fidelity
- the quantitative influence of different imperfection types on the buckling behavior and
- the plain availability of sufficient imperfection measurements

In the work leading to the results shown in this thesis, mainly the third factor was the main driver of decisions. While in an academic surrounding the numerical costs of a procedure may not be the prevailing obstacle, the availability of sufficient imperfection data poses a much more fundamental problem. As numerous measurements of cylinders and cones are necessary to apply the probabilistic procedures, the main difficulty lies in ensuring a sufficiently large sample size of measurements (compare [89] and [86]). Only if that is the case, an adequate application of the methods can be ensured and the resulting design loads can be considered in a professional way.

In other scenarios, for example the pre-design phase of a real launcher structure in industry, other factors may be crucial. Here, to quickly asses multiple regions of the design space, the numerical costs of a procedure may be of higher or even deciding importance, while the demands on the precision of single buckling load predictions may be lower.

The SAP as well as the PPLA are generally capable of including every given type of imperfection. Thus, it is up to the engineer or researcher to decide which model fidelity is necessary, which

imperfections types are crucial to properly describe the structural behavior and which imperfection data is available.

In the following, all imperfection types applied in the simulations in this thesis are discussed, the sources for their stochastic scatter data are given and the way they are treated in the analyses is presented.

6.2.2 Overview of scattering imperfections

In the following, a short overview of the types of imperfections and the sources for their scatter data shall be given. After this, the following chapters provide a more detailed description of the concrete stochastic treatment of the different imperfection types.

As a first step in chapter 6.3, all shell configurations are analyzed using the SAP to establish a basis of comparison to the results obtained by PPLA. While the PPLA is independent from measurements of geometric imperfections, in the framework of the SAP, geometric imperfections are treated stochastically. As a consequence, sufficient knowledge of their anticipated scatter has to be established. For all SAP calculations, the geometric imperfection patterns of shell Z15-Z26 are taken as a basis. This set of ten specimens was manufactured and measured at Deutsches Zentrum für Luft und Raumfahrt (DLR) in Braunschweig, Germany. It represents the biggest set of measurements of nominally identical shells and thus the biggest sample size of geometric imperfections available to the author. For all other shell configurations (Z07-Z12, Z36, Z37, K06-K08), no comparable sample sizes of measurements exist. Thus, in these cases, the measurements of shell Z15-Z26 are again used as a basis to obtain the stochastic scatter. As all other investigated shells also originate from DLR, Braunschweig and show characteristics in their respective measured imperfection patterns similar to the ones of the patterns of shells Z15-Z26, this assumption seems reasonable.

This assessment of the applicability of one given set of measured geometric imperfections to other shell specimen of altering laminate setups and geometries is a prime example for the compromises that have to be made when using probabilistic methods, as reasoned in chapter 6.2.1.

In all calculations in this thesis, thickness deviations are modeled as smeared thickness deviations of the whole skin. DEGENHARDT et al. [110] give the mean measured thicknesses of shells Z15-Z26. From this data, mean value and standard deviations can be estimated for application in the probabilistic approaches. Similar to the case of geometric imperfections, the obtained data is applied to all other shell specimens. However, in the case of shell Z36, Z37 and K06-K08, the shell skin consists of more than four laminate plies. Therefore, a fundamentally different mean thickness of the specimen has to be expected. To account for these differences, the absolute deviations from the mean measured thicknesses to the nominal thickness are calculated for shells Z15-Z26. These deviations are then applied to the nominal thickness of all other specimen in order to obtain a corresponding set of virtual thickness measurement values. Using these, the stochastic moments for the thicknesses of shells Z36, Z37 and K06-K08 are estimated.

When it comes to material properties, the stochastic scatter of E_{11}, E_{22} and G_{12} is considered. Here, the stochastic values for all investigated shells are given in literature. DEGENHARDT et al.

[110] give the mean values and standard deviations for shells Z15-Z26, HÜHNE et al. [57] for Z07-Z12. The scatter of material parameters for Z36, Z37 and K06-K08 are provided by the DLR within the EU 7th framework project DESICOS and published by KHAKIMOVA et al. [111].

The loading imperfections are modeled as a uniform bending of the upper shell edge. Here, the stochastic values for the inclination angles are taken from the reverse-engineering efforts by KRIEGESMANN [89].

Table 6-4 summarizes the sources for the scatter data of all imperfection types and shell specimen considered in this thesis.

imperfection type	Z09 – Z12	Z15 – Z26	Z36 – Z37, K06 – K08
geometric imperfections (for SAP only)	measurements of shells Z15-Z26, provided by DLR		
wall thickness	[Degenhardt et al., 2009] [110]		
material properties (E_{11}, E_{22}, G_{12})	[Hühne et al., 2008] [57]	[Degenhardt et al., 2009] [110]	[Khakimova et al., 2016] [111]
loading imperfections	[Kriegesmann, 2012] [89]		

Table 6-4: Types of imperfections included in the analyses and sources for their stochastic values

6.2.3 Geometric imperfections

As reasoned above, in the case of the SAP, the stochastic scatter of geometric imperfections is included in the finite element models. In accordance to the basis of the reduction techniques presented in this thesis, also the stochastic treatment of geometric imperfections will be based on their decomposition into Fourier series (compare chapter 4.1).

Using the half-wave cosine phase-shift formulation given in equation (4-6), redundancies caused by the circumferential alignment of the shells during measurement can be eliminated (for details compare chapter 4.1.1 and [89]). For all SAP calculations, a fidelity of the Fourier series of $n_1 = 15$ and $n_2 = 30$ is chosen (compare chapter 4.1.3).

To obtain the input data for the scattering geometric imperfections, in a first step, the Fourier coefficients and phase shifts of every decomposed measured pattern are summarized in the vector $\boldsymbol{x}$:

$$\boldsymbol{x} = (\xi_{00}, \phi_{00}, \xi_{10}, \phi_{10}, \dots, \xi_{n1n2}, \phi_{n1n2}) \tag{6-1}$$

Therefore, $2(n_1 + 1)(n_2 + 1) = 2 \cdot 16 \cdot 31 = 992$ random parameters describe the scatter of geometric imperfections. It has to be assumed that these parameters are not stochastically independent. Thus, they have to be decorrelated for use in the semi-analytical framework. This is achieved by applying the Mahalanobis-Transformation, leading to the vector $\boldsymbol{z}$ with only $m - 1 = 10 - 1 = 9$ uncorrelated entries (compare chapter 3.4.3).

As the SAP only serves as a basis for comparison in this thesis, the modeling of the scatter of geometric imperfections is not elaborated on any further. Instead, for more details it is referred to KRIEGESMANN [89].

6.2.4 Wall thickness and material properties

Traditionally, in probabilistic analysis of composite shells, the Young's modulus and the wall thickness are treated as independent random parameters (compare for example [70], [89]).

In reality however, it is certainly possible that a change in local or global thickness comes with a change in fiber volume fraction ϕ, which is defined by

$$\phi = \frac{V_{fiber}}{V_{fiber} + V_{matrix}} = \frac{A_{fp}\, n}{\rho_{fiber}\, t_l} \tag{6-2}$$

Here, A_{fp} is the total area density of the fiber product, n is the number of layers, ρ_{fiber} is the density of the fiber and t_l is the total thickness of the laminate.

If for example too much resign is sucked during the injection process in the autoclave, a change in fiber volume fraction consequently leads to a change in engineering constants:

$$E_{11} = \phi\, E_{l,f} + (1 - \phi) E_m \tag{6-3}$$

Here, $E_{l,f}$ is the longitudinal stiffness of the fibers and E_m is the usually much smaller stiffness of the matrix material.

Figure 6-3, left shows the deviation of the measured thicknesses from the corresponding nominal thicknesses for a set of coupons. The ordinate gives the engineering constant E_{11}, derived by using the nominal thickness $t_l = t_{nom}$ in equations (6-2) and (6-3).

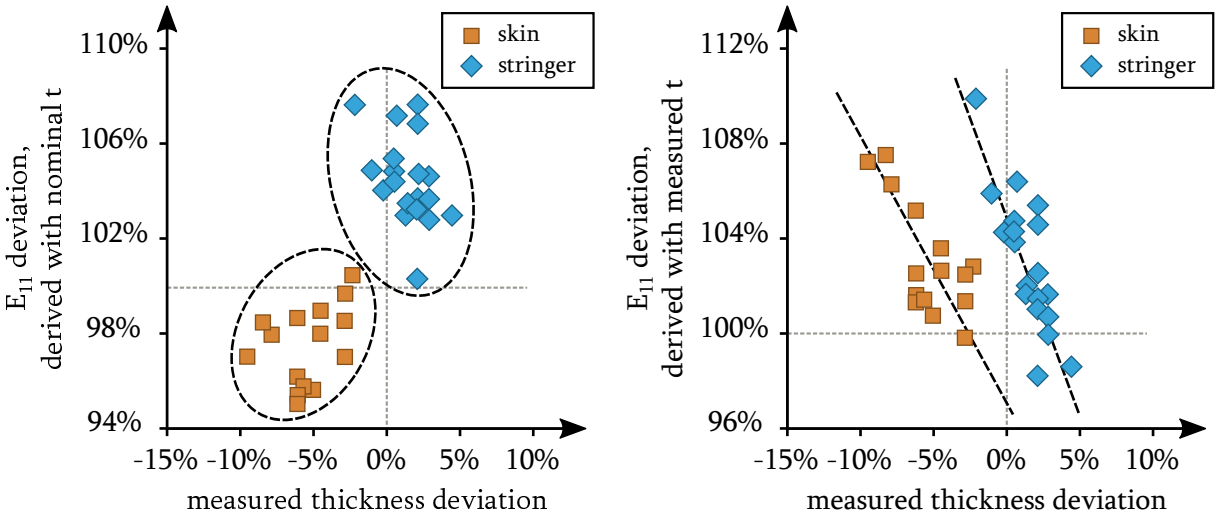

Figure 6-3: Scatter of coupon test results, E_{11} deviation, derived with nominal t (left) and with measured t (right), compare [119]

When looking at the distribution in Figure 6-3, left, no direct correlation of the traditionally derived Young's modulus and the thickness deviation is noticed. However, coupons with for example higher than nominal thickness in general show higher Young's moduli. This can be attributed to an overestimation of the fiber volume fraction when deriving the Young's modulus using the nominal thickness ($t_l = t_{nom}$).

In addition to that, when calculating the Young's modulus using the nominal thickness, the influence of a thickness deviation on the bending stiffness consequently is neglected. Thus, in the case of problems where bending deformations are dominant, it seems important to account for the scatter of thicknesses, their effect on the Young's modulus as well as the correlation of both.

If the Young's modulus is determined using the actual measured thickness of the coupon ($t_l = t_{meas}$), the distribution depicted in Figure 6-3, right is obtained. Here, a strong correlation of measured thickness and E_{11} is noticed. As expected, specimens with higher thickness show a lower fiber volume fraction which in turn leads to lower Young's moduli.

It should be noted that the differences between the values for skin and stringer given in Figure 6-3 are not important in the context of this thesis and thus not further commented upon. Still, it is worthy to note that both sets show the same characteristic of revealing a considerably strong correlation between measured thickness and adjusted engineering constant.

The local loss of stability of cylindrical and conical shells is accompanied by strong bending deformations (compare chapter 3.2). Therefore, the correlation of thickness and material properties is included in all probabilistic analyses in this thesis. It is expected that the reasoning given above does not only apply to E_{11} but also to the other stiffness parameters. However, due to lack of reliable data, only the correlation of t and E_{11} can be accounted for herein.

For the application of the semi-analytical probabilistic framework, uncorrelated input parameters are required. Thus, the input parameters t and E_{11} are decorrelated by application of the Mahalanobis-Transformation, similar to the treatment of geometric imperfections:

$$\left[\begin{pmatrix} t \\ E_{11} \end{pmatrix} - \begin{pmatrix} \mu_t \\ \mu_E \end{pmatrix}\right] \underbrace{\begin{bmatrix} \sigma_t^2 & \sigma_{t,E} \\ \sigma_{t,E} & \sigma_E^2 \end{bmatrix}^{-1}}_{\boldsymbol{\Sigma}} = \begin{pmatrix} \zeta_1 \\ \zeta_2 \end{pmatrix} \tag{6-4}$$

To determine to covariance matrix $\boldsymbol{\Sigma}$, the variance of the thickness σ_t^2, the variance of the Young's modulus σ_E^2 as well as the covariance of both are needed. While the former can be estimated from measurement data (compare chapter 6.2.2), the latter is not available for the shell structures considered herein. However, the covariance $\sigma_{t,E}$ can be computed by:

$$cov(E_{11}, t) = \sigma_{t,E} = \rho_{t,E}\, \sigma_t\, \sigma_E \tag{6-5}$$

Here, the coefficient of correlation $\rho_{t,E} = -0.72$ is taken from [119]. The coefficient of correlation can be interpreted as a measure for the correlation of data. A coefficient near zero indicates no stochastic correlation of given data (the points in Figure 6-3, left lie in a loose cloud) while a coefficient of correlation near $\rho = -1$ or $\rho = 1$ indicates a considerably strong correlation (the points in Figure 6-3, right are centered around the dashed lines).

6.2.5 Loading imperfections

As mentioned in chapter 5.1.3, in the design processes in aerospace industry, the loads applied to a structure are treated separately from its structural resistance and load carrying capability. Consequently, loading imperfections are treated as a separate design factor and are not directly considered in for example buckling analyses, determining the structural resistance. Therefore, for

the development of design methods which are implementation ready in industry, loading imperfections should not be included.

However, before implementing design schemes in industry, they have to be thoroughly validated by comparing design loads to experimental results. This changes the general situation as every experimental facility implicates deviations from an ideal perfect load introduction. Therefore, experimentally obtained buckling loads always include the effect of loading imperfections (to a mostly unknown extent, depending on the particular test facility, see below).

To ensure a meaningful comparison of calculated design loads and experimental buckling loads, it consequently is necessary to account for the influence of loading imperfections on the buckling load within the design methods.

In this work, loading imperfections are modeled as a uniform bending of the shell's upper edge (compare Figure 6-4).

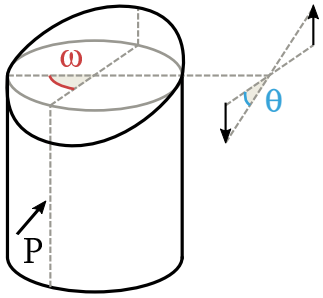

Figure 6-4: Schematic view of uniform bending of the upper shell edge

Here, θ defines the bending angle while ω gives the circumferential alignment of the bending axis.

When it comes to obtaining input values for the analysis, it is comparatively intricate to precisely measure the load inhomogeneities in every buckling test. Thus, in most tests, it is not measured at all. To overcome this lack of data, KRIEGESMANN [89] succeeded to reverse engineer the load asymmetry which was most probably present in the experiments published by HÜHNE et al. [57] and DEGENHARDT et al. [110] for specimens Z07-Z26.

The buckling tests of shells Z36, Z37 and K06-K08 were performed in the very same test facility at DLR, Braunschweig. However, since the experiments by HÜHNE and DEGENHARDT, the load introduction panel was thoroughly reworked and improved significantly. Thus, recent measurements show that the irregularities in load introduction now lie within the measurement tolerance of the displacement transducers (compare Khakimova et al. [111]).

Still, to achieve consistency between the results for all shells considered in this thesis, a conservative assumption is made. Hence, the stochastic values for the bending angle θ determined by KRIEGESMANN for shells Z09-Z26 are accordingly applied to shells Z36, Z37 and K06-K08.

The circumferential alignment angle ω varies uniformly on an interval $[-90°, 90°]$ around the position of the perturbation load (compare Figure 6-4 and [120]).

6.3 Results

In the following, the results of the application of the SAP and the PPLA to the shell specimen introduced in chapter 6.1.1 are given and discussed. By evaluating the objective function for all necessary realizations of input parameters (compare chapter 3.4), the mean values and standard deviations of buckling loads can be estimated. For this, the incomplete second order approach (ISOA) is used for all SAP and PPLA calculations, as reasoned in chapter 3.4.2. By choosing an appropriate type of distribution (here: normal distribution, for reasoning see KRIEGESMANN [89]) as well as a level of reliability, design loads are derived.

As discussed in chapter 5.2.2, for all SAP calculations a level of reliability of $R = 99\%$ is chosen while for all PPLA calculations, the level of reliability is set to $R = 90\%$. It is important to note that the actual level of reliability of the PPLA applied to cylindrical shells is not 90% but indeed well above 99%. This is due to the fact that in the according investigated cases the design loads derived by PPLA lie below the ones derived by SAP and experimental distributions (compare Table 6-6).

The figures given in the following show the cumulative frequency functions and reliability curves for the SAP and PPLA. The design loads obtained from NASA-SP 8007 (chapter 2.2) as well as the buckling loads of the ideal perfect shells (chapter 3.1.2) and the experimental specimens (sources given below) are indicated by vertical lines.

When comparing the results presented below, slight deviations from the ones published by KRIEGESMANN [89] and MEURER et al. [102] can be noticed. These can be explained by mesh refinement from $60x240$ elements to $90x360$ elements (compare chapter 6.1.2), by a finer Fourier series of $n_1 = 15$ and $n_2 = 30$ as well as by the modified stochastic treatment of Young's modulus and wall thickness (compare chapter 6.2.4).

All experimental buckling loads discussed in this thesis were established at DLR, Braunschweig.

6.3.1 Cylindrical Shells

In a first step, SAP and PPLA are applied to shell Z09. Due to its laminate setup, this shell shows a comparatively low sensitivity to geometric imperfections (compare chapters 4.3.2 and 6.1.1). Figure 6-5 shows the cumulative frequency functions on the left and the reliability functions on the right.

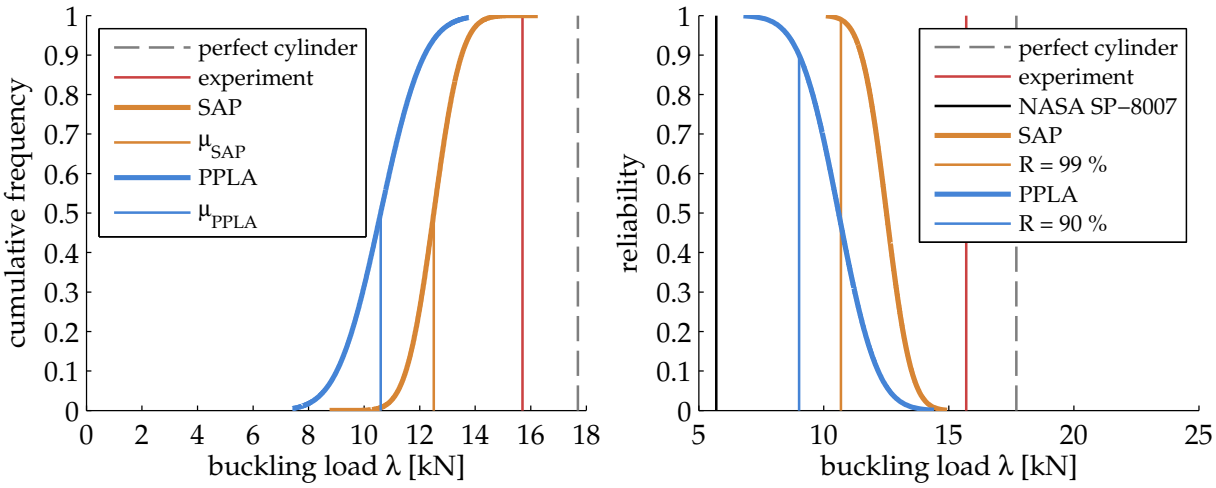

Figure 6-5: Results for shell Z09: cumulative frequency functions (left) and reliability functions (right) of PPLA and SAP, design load by NASA SP-8007 as well as perfect shell and experimental buckling load [42] given by vertical lines

When looking at the distributions, it is observed that the mean values of SAP and PPLA, $\mu_{\lambda_{Z09},SAP} = 12.51\ kN$ and $\mu_{\lambda_{Z09},PPLA} = 10.60\ kN$, respectively, show to be generally similar. As the main difference of SAP and PPLA lie in their treatment of geometric imperfections, it consequently is expected that the corresponding results are closely comparable for a shell configuration with low sensitivity to geometric imperfections.

Still, when investigated in detail, the PPLA results show a notably lower mean value and a higher standard deviation, recognized by the lower gradient of the corresponding curve around its mean value. This might very well lead to the assumption that the interaction of local perturbation loads with load asymmetry poses a more detrimental effect on the structural response than the interaction of global imperfection shapes with load asymmetry. However, first and foremost, a perturbation load equal to or above P_1 (the perturbation load level which is necessary to reach the lower bound regime) in general leads to a much higher imperfection amplitude and lower buckling load than the mean imperfection amplitude of measured imperfection patterns and the corresponding buckling loads (compare chapters 3.3.4 and 4.4.2).

This effect is also noticed when applying SAP and PPLA to all other shell configurations. Figure 6-6 exemplarily depicts the reliability function for shells Z15-Z26 and shells Z36 and Z37.

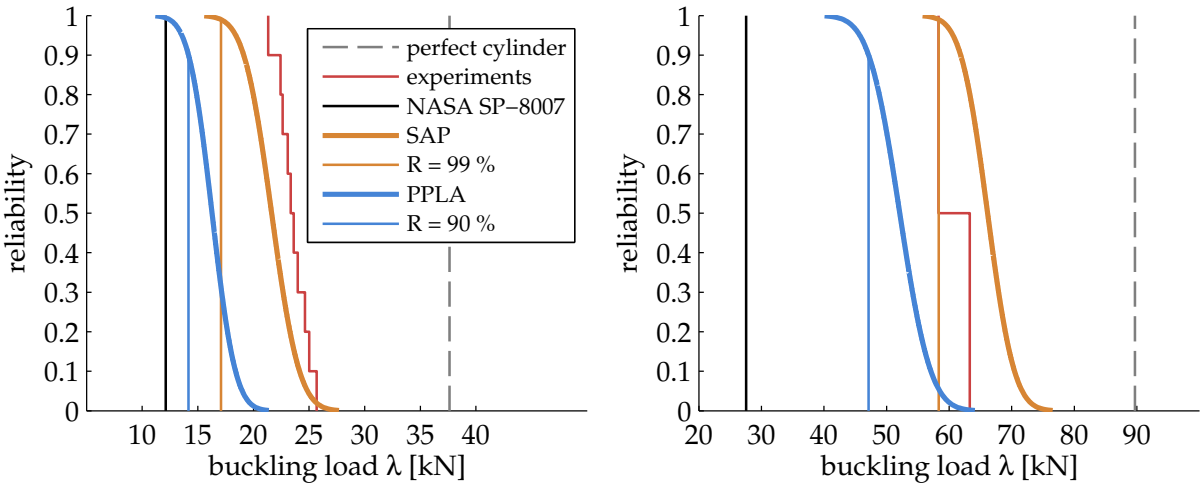

Figure 6-6: Results for shell Z15-Z26 (left) and Z36-Z37 (right): reliability functions of SAP and PPLA, design loads by NASA SP-8007 and buckling loads of the perfect shells as well as experimental buckling loads [110], [101] given by vertical lines

When looking at the results, it is noticed that the SAP delivers mean values that are higher than the ones obtained by PPLA and closer to the distribution of experimental results in all investigated cases. As indicated above, this is attributed to the main difference of SAP and PPLA: While the SAP is tailored to model geometric imperfections as realistically as possible, the PPLA in this aspect follows a worst-case philosophy. This consequently leads to more conservative buckling loads.

Table 6-5 gives an overview of all calculated mean values and standard deviations of buckling loads.

[kN]	Z07-Z08	Z09	Z10-Z11	Z12	Z15-Z26	Z36-Z37
SAP						
mean value μ_λ	20.25	12.51	13.82	17.57	21.64	66.14
standard deviation σ_λ	1.59	0.78	1.41	0.84	1.96	3.36
PPLA						
mean value μ_λ	14.65	10.60	10.85	16.98	16.28	52.11
standard deviation σ_λ	1.22	1.23	1.40	1.19	1.65	3.89

Table 6-5: Stochastic values obtained by SAP and PPLA for all cylindrical shell configurations

With the help of equation (3-26), the stochastic values of buckling loads can be transferred to design loads. Table 6-6 gives the derived design loads of SAP and PPLA, the design loads obtained from NASA-SP 8007 as well as the buckling loads of the ideal perfect shells and the experimental specimens.

[kN]	Z07-Z08	Z09	Z10-Z11	Z12	Z15-Z26	Z36-Z37
perfect cylinder	33.7	17.7	23.7	23.2	37.6	89.7
experiment *(minimum of corresp. set)*	21.8	15.7	15.7	18.6	21.3	58.3
NASA-SP 8007	10.8	5.7	7.5	7.3	12.1	27.6
SAP with R = 99%	16.5	10.7	10.5	15.6	17.1	58.3
PPLA with R = 90%	13.1	9.0	9.0	15.5	14.2	47.1

Table 6-6: Design loads for all cylindrical shell configurations, experimental buckling loads given as minimum of the specific configuration set, experimental buckling load values taken from [42], [110], [101]

The SAP leads to design loads which are less conservative and therefore more economic than the ones by PPLA. However, when applying the SAP to the set of shells Z36 and Z37, a design load is obtained which is very close to the experimentally obtained buckling load of shell Z37, while the mean value shows to be well above the experimental results. As the corresponding measured shape is not available to the author, it has to be assumed that the imperfection pattern of shell Z37 shows significant features that are not adequately represented by the set of measurements of shells Z15-Z26, which was applied as a data basis for all SAP calculations (compare chapter 6.2.3).

The comparison of design loads to the corresponding experimental buckling loads shows that the PPLA is robust in all investigated cases. Still, load levels are obtained which are (21% to 112%, depending on the shell configuration) higher than the ones of the traditionally used NASA-SP 8007. Therefore, the PPLA achieves the goal of no less than a grade 1 design method (compare chapter 5.1.3) which is always robust but at the same time less conservative than established procedures.

It is interesting to note that the PPLA leads to robust load levels even in the particular cases where the original SPLA does not provide safe design loads (compare Table 3-1 and Table 6-6). It seems that the probabilistic interaction of geometric perturbation load imperfections and various kinds of non-traditional imperfections is able to overcome the original lack of robustness discussed in chapter 3.3.4.

6.3.2 Conical Shells

After the application to cylindrical shells, the SAP and PPLA are used to derive design loads for the conical shell specimens K01, K06 and K08.

Figure 6-7 exemplarily shows the cumulative frequency functions on the left and the reliability functions on the right for conical shell K08.

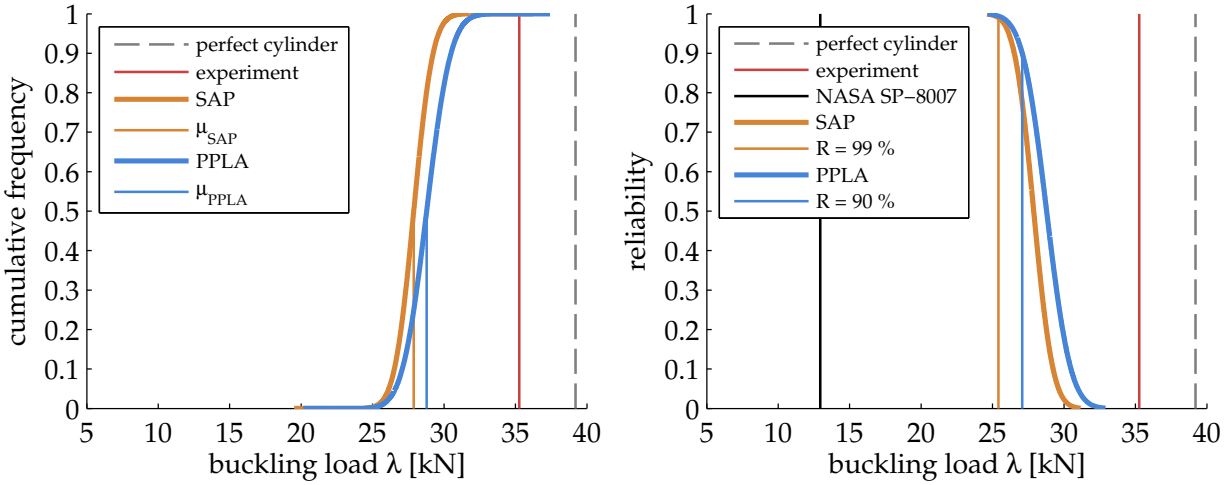

Figure 6-7: Results for shell K08: cumulative frequency functions (left) and reliability functions (right) of SAP and PPLA design load by NASA SP-8019 as well as perfect shell and experimental buckling load [111] given by vertical lines

Table 6-7 gives an overview of all calculated mean values and standard deviations of buckling loads.

[kN]	K01	K06	K08
SAP			
mean value μ_λ	36.29	37.48	27.88
standard deviation σ_λ	1.71	1.53	1.06
PPLA			
mean value μ_λ	34.95	35.68	28.79
standard deviation σ_λ	1.27	1.09	1.33

Table 6-7: Stochastic values obtained by SAP and PPLA for all conical shell configurations

When looking at the distributions, it is noticed that the mean values and standard deviations of SAP and PPLA are comparatively close to each other. As discussed in chapter 4.3.3, conical shells in general seem to be less sensitive to geometric imperfections than cylindrical shells. Due to the bending deformation of the shell's edges being of increased detrimental influence on the buckling load of the shell, differences in geometric disturbance (geometric imperfections or SPLA) play a more subordinate role. This effect is even stronger when including loading imperfections within the probabilistic framework as they narrow down the share of geometric imperfections in buckling load reductions even further. Still, the liability of conical shells to geometric imperfections is also greatly dependent on the laminate setup. Therefore, despite the general trend described above, geometric imperfections certainly have to be included in design procedures for conical shells in general.

When comparing the mean values of SAP and PPLA to the buckling loads obtained in experiment, a distinct conservativeness of both approaches is noticed. Besides the dubiousness of assuming one experimental buckling load as a measure for the expected mean value for that shell configuration, this can first and foremost be attributed to the substantial improvement of the testing facilities at DLR, mentioned above. As when performing the experiments virtually no loading imperfections were present, performing probabilistic with loading imperfections consequently leads to lower buckling loads in general.

Again, the stochastic values of buckling loads are used to derive design loads. Table 6-8 gives the derived design loads of SAP and PPLA, the design loads obtained from NASA-SP 8019 (the equivalent of NASA-SP 8007 for conical shells) as well as the buckling loads of the ideal perfect shells and the experimental specimens.

[kN]	K01	K06	K08
perfect cylinder	46.1	47.0	39.2
experiment	29.1	40.9	35.3
NASA-SP 8019	15.2	15.5	12.9
SAP with R = 99%	32.3	33.9	25.4
PPLA with R = 90%	33.3	34.3	27.1

Table 6-8: Design loads for all conical shell configurations, experimental buckling load values taken from [111]

In the case of K06 and K08 the application of SAP and PPLA gives robust design loads. When it comes to K01 however, the experimentally obtained design load is noticeably low. While K01 and K06 are built with a different ply topology design (compare chapter 6.1.3) but are designed with the same nominal laminate setup, all numerically derived buckling loads are closely comparable. KHAKIMOVA et al. [111] assume that the ply topology design "D1" of K01 leads to a more severe imperfection pattern and thereby might explain the high discrepancy in buckling loads between K01 and K06. Obviously, it would be of high interest to analyze the imperfection pattern of K01. However, as it is not available to the author, the reason for the exceptionally low experimental buckling load cannot be further elaborated upon.

To conclude the analyses of cylindrical and conical shells, it is noted that the PPLA leads to robust design loads in all investigated cases, with the exception of the unresolved case of K01. Furthermore, PPLA design loads show to be higher and thus less conservative than the ones by the commonly applied NASA SP-8007 in all investigated cases. When it comes to the SAP, design loads show to be slightly higher in most cases and thus even more economic than the ones obtained by PPLA. However, it is argued that this is offset by the PPLA's significant advantage of being independent from costly measurements of geometric imperfections.

7 Summary and Conclusions

7.1 Summary

In this work, a procedure to identify the inherent parts of a given imperfection pattern which are essential for the characteristic buckling process has been proposed. By decomposing imperfection patterns into Fourier series and applying the stepwise imperfection filtering method (SIFM), a reduced set of modes is obtained. Once recomposed into an imperfection shape, reduced patterns with comparatively low imperfection amplitudes are obtained which nevertheless lead to nearly the same buckling loads as the original ones.

After the main parameters of the SIFM, their influence on the results as well as recommendations for their choice were discussed, the procedure was applied to various measured imperfection patterns of cylindrical and conical shells with concurring and varying design parameters. While the reduced patterns of shells with the same geometry and laminate setup showed to be closely comparable, the essential shapes deviated when dealing with shells of different length, radii and laminate setup. Still, all reduced patterns calculated in this thesis showed to be of comparatively short wavelength, independent from the underlying nominal shell properties.

After the broad application of the method, the observed behavior could be physically explained. By comparing the stress states and stability failure characteristics, it was shown that shells with reduced imperfection patterns feature the same local stress distributions and stress levels as the original measured shells. Furthermore, the buckling load level caused by a given imperfection pattern directly relates to the similarity between the corresponding essential pattern and the prebuckling stress state.

When normalizing the general pattern amplitudes, it was observed that the reduced patterns caused buckling loads which were lower than numerous usually applied imperfection patterns like measured shapes, eigenmode imperfections and single dimple imperfections. Furthermore, a physical similarity between measured, reduced and single dimple imperfections was identified, as all of those patterns lead to a local snap-through before buckling, given sufficiently high amplitudes. For further increasing imperfection amplitudes, the reduced patterns show the same characteristic of multiple local snap-throughs as perfect shells with multiple perturbation loads of sufficient magnitude.

In the second part of this work, the gained knowledge was transferred to derive a new design procedure for cylindrical and conical shells. The probabilistic perturbation load approach (PPLA) integrates the deterministic lower-bound behavior of the SPLA into a semi-analytical framework to cover the scatter of other types of imperfections like thickness deviations or scattering material properties. In this way, the PPLA is independent from costly measurements of geometric imperfections and at the same time able to depict the impact of traditional and non-traditional imperfections on the buckling load.

7.2 Conclusions

The proposed imperfection filtering method is able to reduce given artificial or measured imperfection pattern to their inherent parts which are driving the buckling initiation of the corresponding shells. By reducing measured patterns to their essential parts, visually dominant but physically negligible shapes can be eliminated. In doing so, a proper evaluation of the geometric properties essential for buckling becomes feasible and a direct connection to the varying buckling load levels can be identified.

When comparing the general shapes of the essential imperfection patterns, they show to be relatively short-waved in all investigated cases, while long-waved imperfection shapes hardly contribute to the buckling load. The amplitudes of the reduced patterns are only a fraction of the ones of the original patterns, again emphasizing that only small fractions of measured imperfection shapes actually contribute to establishing the corresponding buckling load levels.

The findings demonstrate the necessity to increase the commonly applied fidelity of the Fourier series to describe imperfection patterns, which is usually chosen by ensuring only visual resemblance. Only if enough modes of short wavelengths (and mostly very small amplitudes) are included in the decomposition of a measured pattern, the respective essential shapes can be sufficiently well represented, leading to representative buckling load levels.

The prebuckling stress states and buckling loads of shells with reduced and original patterns concur, implying physical equivalence of the original and reduced patterns. By relating the essential imperfection pattern geometry to the corresponding prebuckling stress states, the differences in buckling load reduction of different measured imperfection patterns can now be explained. Here, the imperfection pattern where the characteristic geometry of its essential pattern is closest to the emerging distribution of prebuckling stresses causes the lowest buckling load. When increasing the imperfection amplitudes, the local effect geometric imperfections can have on the local stability of a shell seems to be limited by the occurrence of a prebuckling snap-through, putting an upper limit on the aforementioned relations. However, supplementary studies are certainly required to analyze and confirm this suspicion.

Given the general commonalities and specific differences of the reduced patterns for different shell geometries and laminate setups, a concrete and tangible connection between design parameters and essential shapes could not be formulated yet. If a physical connection between for example shell geometry or laminate setup and the anticipated essential imperfection shapes could be established, a realistically expectable worst case could be identified. This could drastically enhance the capabilities of design procedures which no longer would have to rely on theoretical worst-case or lower bound approaches. To achieve this, investigating possible coherences between B-matrix entries for a given laminate setup and the observed essential imperfection shapes seems promising. As the B-matrix captures the strain-bending coupling of the laminate, it has a fundamental influence on the liability of a shell to local bending deflections and thus imperfections.

By combining deterministic and probabilistic approaches, the PPLA was derived, which is independent from costly measurements of geometric imperfections. The obtained design loads show to be robust with respect to buckling loads obtained in experiments as well as less conservative than the ones by the commonly applied NASA-SP 8007. Still, the PPLA represents a lightweight design tool which is able to deliver robust and at the same time economic design loads.

7.3 Outlook

The main aim of the calculations presented in this thesis is to pave the way to better understand the influence of geometric imperfections on the buckling load, with the ultimate goal to drastically improve or renew established design procedures.

In the context of developing those new design approaches, one of the next steps to utilize the knowledge of essential patterns within design frameworks would be to establish a direct relation between design parameters like for example laminate setup or shell geometry and the essential imperfection shapes. Initially, to obtain an essential imperfection shape, an existing shell specimen has to be measured and the imperfection pattern has to be filtered by applying the SIFM. This poses a problem in the design phase, where the specimen obviously is not manufactured yet. However, it was shown that for concurring design parameters, the essential patterns of different measured original patterns showed very similar characteristics. It was concluded that the essential patterns might not only give the critical parts of a particular original pattern but actually expose the general sensitivity of a given laminate setup to that wave shape. This directly leads to the idea of applying the essential patterns as surrogate imperfections within the design phase.

If now a direct relation between the planned laminate setup and the anticipated essential (and thus critical) pattern could be established, a realistically expectable and at the same time expectably robust surrogate imperfection could be predicted for use in the design phase.

An alternative way would be to directly integrate the SIFM into a design procedure. By determining the essential parts of a representative existing specimen or by assuming an artificial original imperfection spectrum, the essential patterns could be determined, accounting for the currently assumed design parameters.

In both cases, an appropriate value for the amplitude of the surrogate imperfection pattern has to be chosen to calculate buckling loads. While a single perturbation load in most cases conveniently leads to a discrete lower bound, the amplitude variation of reduced patterns showed a) high gradients in the regime of realistically expectable low amplitudes and b) a comparatively slow convergence of buckling loads in the regime of higher amplitudes (similar to an increasing number of applied perturbation loads). This causes a fundamental problem in design, as a) imposes a significant danger of either overly-conservativeness or lack of robustness and b) excludes circumventing the problem by utilizing a lower bound (as in the case of a single perturbation load). Other concepts, like assuming surrogate imperfection amplitudes according to manufacturing tolerances or even inspection criteria, would significantly overestimate the essential patterns and therefore lead to overly conservative designs. The best solution would most probably be to use

a fixed essential imperfection shape and apply a probabilistic scatter to the amplitude of that shape. Here, the stochastic values could be obtained from the reduced patterns of already measured specimens, which unfortunately implicates dependence on costly measurements or profound knowledge of the manufacturing process.

In this regard, the application of the reduction technique can also provide insight which could be used in process planning and enhancement of manufacturing techniques. If not only the connection between design parameters and essential shapes would be known but also the influence of a given manufacturing technique on the anticipated imperfection shape (and its inherent essential parts), potentials for weight saving could be deduced. Here, the shell's sensitivity to the anticipated imperfection shapes could be accounted for not only when designing but also when manufacturing the structures.

A simple example would be the fabrication of an isotropic cylindrical shell composed out of curved panels. If the essential wave shapes for a given shell configuration (dimensions, material, etc.) would be predicted to be dominated by four circumferential waves, building that shell by welding four single panels would have to be considered as rather suboptimal as in turn the imperfection pattern will most likely be dominated by four circumferential waves. By instead composing the shell from six panels, the weld-line induced critical imperfection shape could be avoided. When it comes to monolithic composite structures, the probabilistic simulation of the draping, injection and molding process could help to predict the main expectable characteristics of the anticipated imperfection pattern based on the assumed fabrication parameters and specifications.

Despite both certainly representing rather simple examples, they serve to demonstrate the general idea: By identifying the influence of certain manufacturing process parameters on the wave shapes of the anticipated imperfection patterns, the occurrence of known (since now identifiable) critical shapes could be actively avoided, substantially boosting buckling load levels in general.

In the second part of the thesis, a new design procedure was proposed, comprising the knowledge gained. While the PPLA delivers robust and less conservative design loads, the method certainly has to be extensively validated by further test series. Besides that, the development of an empirical formula to roughly estimate the lower-bound perturbation load level would substantially decrease the computational costs of the method even further.

All in all, it is the sincere hope of the author that the reduction methodology presented in this thesis, the gained insights as well as the pursuit of establishing innovative design procedures contribute to initiating the eagerly awaited shift in aerospace industry from aging worst-case curves to modern design procedures utilizing the technical and scientific advances of the past decades. Hopefully, the SIFM and the presented first hints at the explanation of the physical connection between realistic imperfection patterns and the mechanisms triggering local buckling help paving the way to actually comprehend what ELISHAKOFF [121] called the "twentieth century conundrum in elastic stability", being the "capricious, prima donna type behavior of shells namely, their hyper-sensitivity to imperfections".

List of figures

Figure 1-1: Exploded view of Ariane 5 ECA, compare [1] 1

Figure 2-1: Normalized experimental buckling loads over the slenderness of the shell [8], [9] 4

Figure 2-2: Axial load over lateral deflection caused by a constant perturbation load by RICARDO [55] (left) and critical bending moment over lateral perturbation load by Okubo [56] (right) .. 9

Figure 2-3: Experimental results of axially compressed cylinders with a constant lateral perturbation load P [57] 10

Figure 2-4: Early geometric imperfection measurements by Arbocz et al. [36] (left) and by Singer et al. [28] (right) 11

Figure 2-5: State of the art imperfection measurements by Hühne [57], [64] (left) and imperfection pattern included in the numerical analysis by Kriegesmann [64] (right) 12

Figure 3-1: Schematic overview of stress problems and stability problems, compare [42] and [88] 15

Figure 3-2: Perfect and imperfect shell: buckling load reduction and transition from bifurcation point to limit point 16

Figure 3-3: Schematic overview of Newton-Raphson method (left) and arc length method with Riks constraint (right), compare [94] 21

Figure 3-4: Schematic load deflection curve of an imperfect cylindrical shell: prebuckling, buckling and postbuckling phases 23

Figure 3-5: Schematic load deflection curve of an imperfect cylindrical shell: area of appearance of a) global nonlinear prebuckling deformations, b) local nonlinear prebuckling deformations, c) snap-in of initial dimple, d) postbuckling deformations 24

Figure 3-6: Schematic transformation from three dimensional cylinder and cone to unwrapped shell surfaces 24

Figure 3-7: Global nonlinear radial deformations of shell Z25 with perfect shell geometry (left) and axial cut (right), indicated by black line 25

Figure 3-8: Local nonlinear radial deformations of shell Z25 with imperfect shell geometry (left) and axial cut (right), indicated by black line 26

Figure 3-9: Snap-in of the initial dimple: high speed camera pictures by Esslinger [21] (enhanced in brightness and contrast), late prebuckling state (left) and initial dimple (right) 27

Figure 3-10: Buckling deformations at snap-in of the initial dimple of shell Z25 with imperfect shell geometry (left) and axial cut (right), indicated by black line 28

Figure 3-11: Postbuckling deformations: propagating pattern, high speed camera pictures by Esslinger [21] (enhanced in brightness and contrast) (left) and simulation of shell Z25 (right) 29

Figure 3-12: Postbuckling deformations: stable postbuckling pattern, high speed camera picture by Esslinger [21] (enhanced in brightness and contrast) (left) and simulation of shell Z25 (right) 30

Figure 3-13: The Single Perturbation Load Approach; Schematic overview of the idealized numerical model (left) and buckling load over the applied perturbation load P (right) 31

Figure 3-14: SPLA: shematic shell surface (left) with local snap-through (gray area) and initial dimple (green area) and load-deflection-curve (right) with snap-through load level and global buckling load level 32

Figure 3-15: SPLA: shematic shell surface (left) with local snap-through (gray area) and initial dimple (green area) and load-deflection-curve (right) with snap-through load level and global buckling load level 33

Figure 3-16: SPLA: shematic shell surface (left) with local snap-through (gray area) and initial dimple (green area) and load-deflection-curve (right) with snap-through load level and global buckling load level 33

Figure 3-17: Single Perturbation Load Approach applied to shell Z15; classical scheme (left) and enhanced scheme (right) 35

Figure 3-18: The semi-analytical probabilistic procedure (SAP): schematic overview 40

Figure 4-1: Schematic illustration of the effect of different symmetry conditions of the Fourier series on the aproximated imperfection shape 45

Figure 4-2: Imperfection shapes of shell Z25: Fourier representation with n_1 x n_2 = 496 modes (left) and with 256 modes (right) 48

Figure 4-3: Fourier spectrum of shell Z25 with n_1 x n_2 = 496 modes 49

Figure 4-4: Imperfection shapes of shell Z25: Fourier representation with n_1 x n_2 = 496 modes (left) and with 256 short-waved modes (right) 49

Figure 4-5: Imperfection pattern of shell Z15 (left) and radial prebuckling deformations with the initial dimple (right) 53

Figure 4-6: The stepwise imperfection filtering method (SIFM): schematic overview 55

Figure 4-7: Imperfection shape of shell Z25,Fourier representation fidelity of $ntotal = n1x\ n2 = 16\ x\ 31 = 496$ modes, non-linear buckling load $\lambda orig = 32.95\ kN$ 56

Figure 4-8: Essential imperfection shape of shell Z25, $ntotal = 14$ modes, non-linear buckling load $\lambda red = 33.27\ kN$ 56

Figure 4-9: Pre-buckling deformations of the original shell Z25 (left) and the shell with the reduced imperfection pattern (right) 57

Figure 4-10: SIFM, random order R1: mode evaluation order (left) and remaining modes (right). 58

Figure 4-11: SIFM, random order R2: mode evaluation order (left) and remaining modes (right). 58

Figure 4-12: SIFM results for mode evaluation order R1 (left) and R2 (right) 59

Figure 4-13: SIFM, mode evaluation by descending amplitude: mode evaluation order (left) and remaining modes (right) 60

Figure 4-14: SIFM, mode evaluation by ascending wave numbers: mode evaluation order (left) and remaining modes (right) 61

Figure 4-15: SIFM results for different mode evaluation orders: descending amplitude (left) and descending wavelength (right) 61

Figure 4-16: Load levels over the course of the SIFM filtration for different threshold values 65

Figure 4-17: Load levels over the SIFM filtration for a threshold values of $\eta t = 1.01$, general load level accumulation indicated by arrows, excerpt from Figure 4-16 66

Figure 4-18: Load levels over the SIFM filtration for a threshold values of $\eta t = 1.10$, eliminated modes with high detrimental influence on the buckling load indicated by arrows, excerpt from Figure 4-16 66

Figure 4-19: SIFM results, shell Z25, modified reference load level $\lambda red, mod$, threshold value $\eta t = 1.0$, remaining modes (left) and corresponding reduced pattern (right) 69

Figure 4-20: SIFM results, shell Z25, modified reference load level $\lambda red, mod$, threshold value $\eta t = 1.01$, remaining modes (left) and corresponding reduced pattern (right) 70

Figure 4-21: Approximation of a given wave shape with different amounts of FE nodes 72

Figure 4-22: SIFM applied to shell Z17, modes in the reduced spectrum (left) and reduced pattern (right) 76

Figure 4-23: SIFM results, shell Z17 with modified reduced spectrum, remaining modes (left) and corresponding reduced pattern (right), position of the initial dimple indicated by arrow 77

Figure 4-24: Schematic of dominant modes enforcing a radial relocation of the locally critical imperfection shape 78

Figure 4-25: SIFM applied to shell Z25, measured imperfection pattern (top) and reduced pattern of essential modes (bottom, left), imperfection shape composed out of all eliminated modes (bottom, right) 85

Figure 4-26: First linear buckling mode of shell Z25 with a maximum aplitude of $w/t = 1$ 88

Figure 4-27: Axisymmetric imperfection shape with 8 axial full waves and a maximum aplitude of $wt = 1$ 89

Figure 4-28: Axisymmetric imperfection shape: load deflection curve (left) and radial deformations right before limit point (right), associated equilibrium state indicated by circle in load deflection curve 89

Figure 4-29: Dimple imperfection caused by lateral load with a maximum aplitude of $w/t = 1$ .. 90

Figure 4-30: Buckling loads based on w/t ratio, corresponding to the perfect shell geometry, Eigenmode imperfection, single dimple imperfection, the original pattern of shell Z25 and the essential pattern obtained by applying the SIFM to shell Z25, unmodified amplitudes for the latter ones given by gray squares (left), zoom on regime of low to medium amplitudes (right) 91

Figure 4-31: Buckling loads based on w/t ratio, corresponding to the reduced pattern of shell Z25, labels a) to d) for cross reference with the subsequent tables 93

Figure 4-32: Unloaded imperfection shape of shell Z20 around the position of the initial dimple (left), corresponding stress resultants in axial and circumferential direction in the last calculation increment before the buckling load is reached (middle and right, respectively) .. 99

Figure 4-33: Unloaded reduced imperfection shape of shell Z20 around the position of the initial dimple (left), corresponding stress resultants in axial and circumferential direction in the last calculation increment before the buckling load is reached (middle and right, respectively) 100

Figure 4-34: Stress resultants of shells Z20 and Z25 over the course of axial loading for original and reduced patterns, evaluated in axial and circumferential direction at the positions marked in Figure 4-32 and Figure 4-33 101

Figure 4-35: Reduced imperfection shape of shell Z25 with the axial length scaled by different scaling factors: 100 %, 150 %, 250 % 104

Figure 4-36: Buckling load over the artificial axial scaling of the essential pattern of shell Z25, original pattern indicated by gray rectangle 105

Figure 4-37: Reduced imperfection shape of shell Z25 around the position of the initial dimple for different length scaling factors (compare a) to f) in Figure 4-36), corresponding stress resultant maxima and minima in axial and circumferential direction in the last calculation increment before the buckling load is reached (markers) 106

Figure 4-38: Buckling load over the artificial circumferential scaling of the essential pattern of shell Z25 (top), essential imperfection shape of shell Z25 around the position of the initial dimple for different circumferential scaling factors (compare a) to c)) (bottom), corresponding stress resultant maxima and minima in axial and circumferential direction in the last calculation increment before the buckling load is reached (markers) 107

Figure 4-39: Buckling load over the artificial axial scaling of the essential pattern of shell Z11 (top), essential imperfection shape of shell Z11 around the position of the initial dimple for different circumferential scaling factors (compare a) to c)) (bottom), corresponding stress resultant maxima and minima in axial and circumferential direction in the last calculation increment before the buckling load is reached (markers) 108

Figure 4-40: Reduced patterns of shells Z25 and Z21 as well as the reduced pattern of an artificially created random imperfection shape around the positions of the corresponding initial dimples (all normalized to $w/t = 0.1$), corresponding stress resultant maxima and

minima in axial and circumferential direction in the last calculation increment before the buckling load is reached (markers) 110

Figure 4-41: Reduced patterns of shells Z18, Z20 and Z25 around the positions of the corresponding initial dimples (all normalized to $w/t = 0.1$), corresponding stress resultant maxima and minima in axial and circumferential direction in the last calculation increment before the buckling load is reached (markers) 111

Figure 5-1: The probabilistic perturbation load approach (PPLA): schematic overview, omitted SAP elements dashed and grayed out (compare chapter 3.4) 119

Figure 5-2: Interpreting design loads and reliability levels: the different safety concepts of SAP (left) and PPLA (right) 120

Figure 6-1: Fiber angles and ply piece placement for cylindrical shells (top) and conical shells (bottom) 126

Figure 6-2: Ply piece placement of shell K06, first layer, nominal fiber angle 30°, local fiber angles given in color 127

Figure 6-3: Scatter of coupon test results, E_{11} deviation, derived with nominal t (left) and with measured t (right), compare [119] 131

Figure 6-4: Schematic view of uniform bending of the upper shell edge 133

Figure 6-5: Results for shell Z09: cumulative frequency functions (left) and reliability functions (right) of PPLA and SAP, design load by NASA SP-8007 as well as perfect shell and experimental buckling load [42] given by vertical lines 135

Figure 6-6: Results for shell Z15-Z26 (left) and Z36-Z37 (right): reliability functions of SAP and PPLA, design loads by NASA SP-8007 and buckling loads of the perfect shells as well as experimental buckling loads [110], [101] given by vertical lines 136

Figure 6-7: Results for shell K08: cumulative frequency functions (left) and reliability functions (right) of SAP and PPLA design load by NASA SP-8019 as well as perfect shell and experimental buckling load [111] given by vertical lines 138

List of tables

Table 3-1: SPLA results for different cylindrical shell configurations, experimental buckling loads given as minimum of the specific configuration set, experimental buckling load values taken from [42], [85] and [101] 36

Table 4-1: SIFM applied to shell Z25, results for different threshold values ηt, positions of the initial dimples indicated by arrows 63

Table 4-2: SIFM applied to shells Z20, Z25 and Z26, measured imperfection patterns (left) and reduced patterns (right) 74

Table 4-3: SIFM applied to shell Z17, measured imperfection pattern (left) and reduced pattern (right), positions of the initial dimples indicated by arrow 76

Table 4-4: Buckling loads for shells Z07 and Z11, perfect shell buckling loads, buckling loads with only geometric imperfections, buckling load reductions $\Delta\lambda$ 79

Table 4-5: SIFM applied to shell Z11, measured imperfection pattern (left) and modified reduced pattern (right) with mode (1,2) manually removed 79

Table 4-6: Buckling loads for shells Z07 and Z09, perfect shell buckling loads, buckling loads with only geometric imperfections, buckling load reductions $\Delta\lambda$ 80

Table 4-7: SIFM applied to shell Z09, measured imperfection pattern (left) and reduced pattern (right) 81

Table 4-8: SIFM applied to shell Z33, measured imperfection pattern (left) and reduced pattern (right), positions of the initial dimples indicated by arrows 81

Table 4-9: SIFM applied to shell Z36, measured imperfection pattern (left) and reduced pattern (right), positions of the initial dimples indicated by arrow 82

Table 4-10: SIFM applied to shell K08, measured imperfection pattern (left) and reduced pattern (right), positions of the initial dimples indicated by arrow 83

Table 4-11: SIFM applied to shell Z25, buckling loads of perfect shell, original imperfection shape, reduced imperfection shape and imperfection shape from eliminated modes 86

Table 4-12: SIFM reapplied to shell Z25, imperfection shape from initially eliminated modes (left) and reduced pattern (right) 86

Table 4-13: Load-deflection curves and characteristic radial displacement field for the w/t ratios a) and b), as indicated in Figure 4-31, the underlying imperfection pattern is the essential pattern of shell Z25, local snap-throughs indicated by white arrows, initial dimples indicated by black arrows 94

Table 4-14: Load-deflection curves and characteristic radial displacement field for the w/t ratios c) and d), as indicated in Figure 4-31, the underlying imperfection pattern is the essential

pattern of shell Z25, local snap-throughs indicated by white arrows, initial dimples indicated by black arrows 95

Table 4-15: Load-deflection curve and characteristic radial displacement field for $w/t = 1.4$, the underlying imperfection pattern is the original pattern of shell Z25 97

Table 5-1: Existing methods for design of imperfection sensitive cylindrical shells, main ideas, advantages and drawbacks..... 114

Table 5-2: Classification of design procedures by their required knowledge about anticipated imperfections..... 116

Table 6-1: Shell geometries and laminate setups of shells Z07-Z12 [57] 123

Table 6-2: Shell geometries and laminate setups of shells Z15-Z26 [110] and Z36-Z37 [101] 123

Table 6-3: Shell geometries and laminate setups of K06-K08, detailed ply piece parameters given in [111]..... 123

Table 6-4: Types of imperfections included in the analyses and sources for their stochastic values 130

Table 6-5: Stochastic values obtained by SAP and PPLA for all cylindrical shell configurations. 136

Table 6-6: Design loads for all cylindrical shell configurations, experimental buckling loads given as minimum of the specific configuration set, experimental buckling load values taken from [42], [110], [101]..... 137

Table 6-7: Stochastic values obtained by SAP and PPLA for all conical shell configurations..... 138

Table 6-8: Design loads for all conical shell configurations, experimental buckling load values taken from [111]..... 139

Appendix A

SIFM applied to all available measured imperfection patterns, $\eta_t = 1.01$ *if not noted elsewise.*

SIFM results for shells Z07-Z08, $L = 510mm$, $R = 250mm$, $t = 0.5mm$, $[\pm 24, \pm 41]$:

	original imperfection shape	reduced imperfection shape
Z07	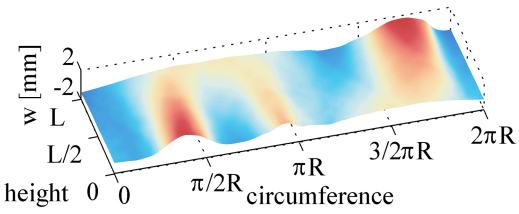 $\lambda_{orig} = 27.13\ kN$	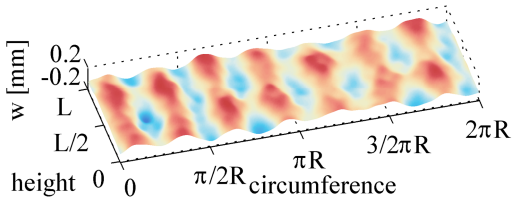 $\lambda_{red} = 27.38\ kN$
Z08	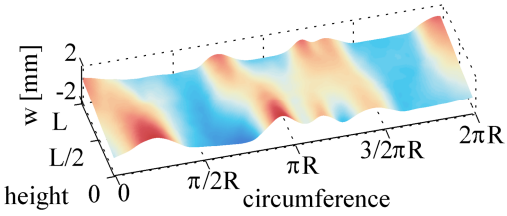 $\lambda_{orig} = 27.83\ kN$	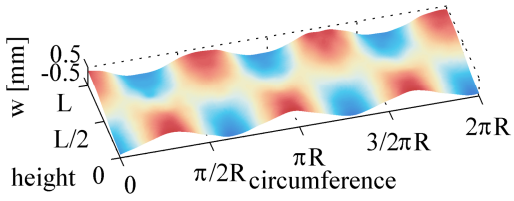 $\lambda_{red} = 28.10\ kN$
		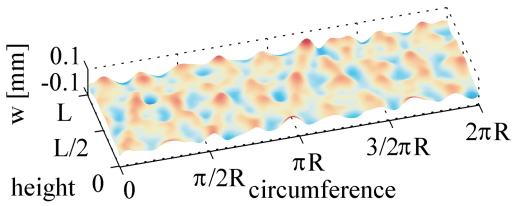 $\lambda_{red,(1,3)removed} = 28.46\ kN$

SIFM results for shell Z09, $L = 510mm$, $R = 250mm$, $t = 0.5mm$, $[\pm 41, \pm 24]$, $\eta_t = 1.001$:

	original imperfection shape	reduced imperfection shape
Z09	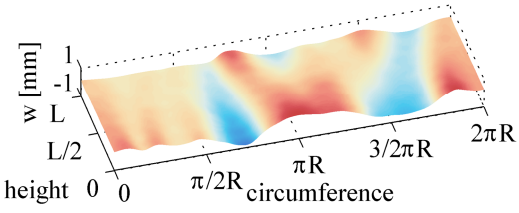 $\lambda_{orig} = 17.63\ kN$	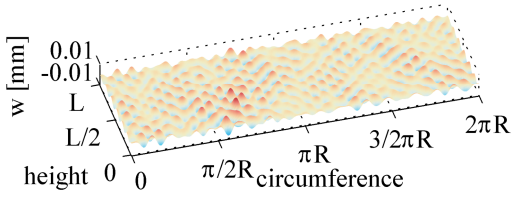 $\lambda_{red} = 17.65\ kN$

SIFM results for shells Z10-Z11, $L = 510mm$, $R = 250mm$, $t = 0.5mm$, $[+24, +41, -41, -24]$:

	original imperfection shape	reduced imperfection shape
Z10	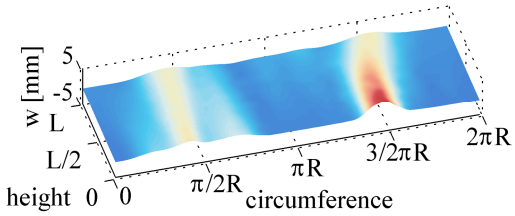 $\lambda_{orig} = 14.21\ kN$	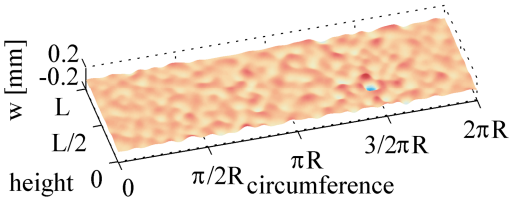 $\lambda_{red} = 14.35\ kN$
Z11	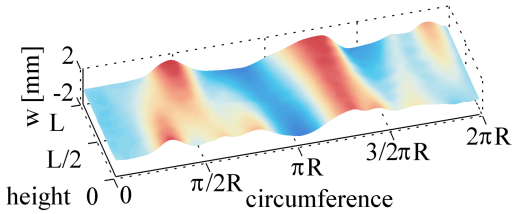 $\lambda_{orig} = 19.75\ kN$	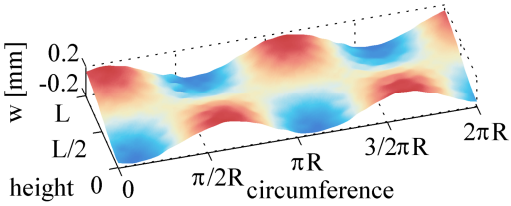 $\lambda_{red} = 19.95\ kN$
		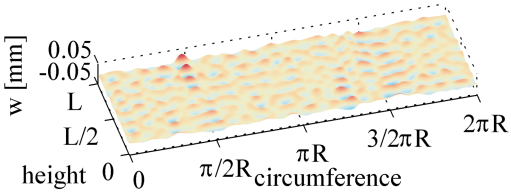 $\lambda_{red,(1,2)removed} = 20.04\ kN$

SIFM results for shell Z12, $L = 510mm$, $R = 250mm$, $t = 0.5mm$, $[\pm 45, 0, -79]$, $\eta_t = 1.005$:

	original imperfection shape	reduced imperfection shape
Z12	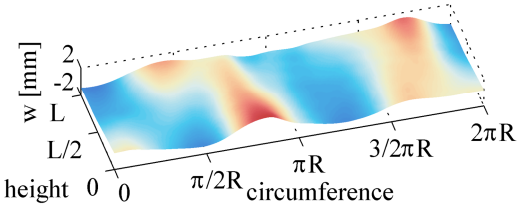 $\lambda_{orig} = 23.10\ kN$	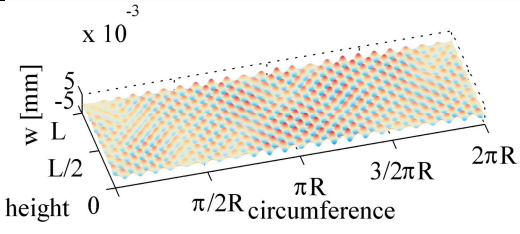 $\lambda_{red} = 23.21\ kN$

SIFM results for shells Z15-Z18, $L = 500mm$, $R = 250mm$, $t = 0.5mm$, $[\pm 24, \pm 41]$:

	original imperfection shape	reduced imperfection shape
Z15	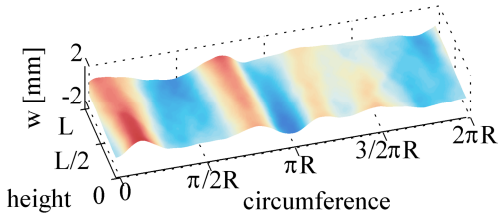 $\lambda_{orig} = 31.06\ kN$	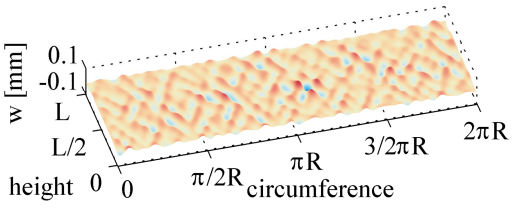 $\lambda_{red} = 31.37\ kN$
Z17	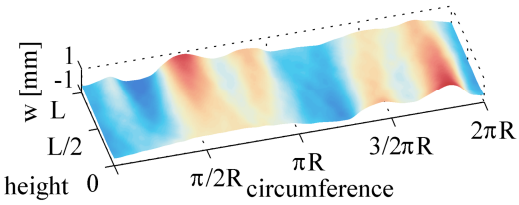 $\lambda_{orig} = 30.01\ kN$	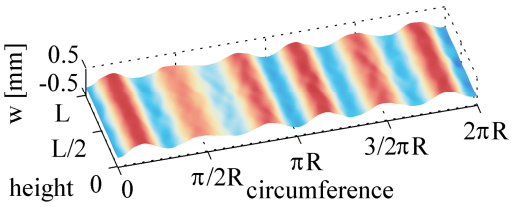 $\lambda_{red} = 30.35\ kN$
		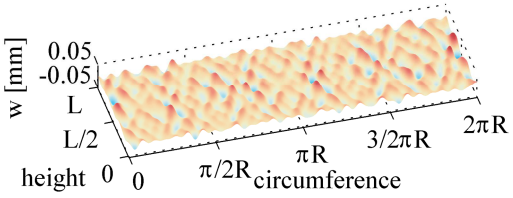 $\lambda_{red,(0,6-8)removed} = 30.93\ kN$
Z18	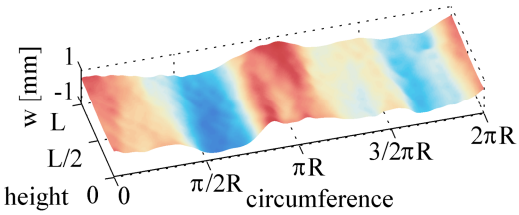 $\lambda_{orig} = 29.55\ kN$	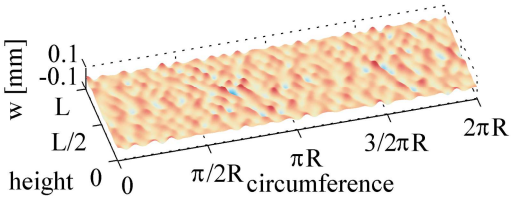 $\lambda_{red} = 29.84\ kN$

SIFM results for shell Z33, $L = 510mm$, $R = 250mm$, $t = 1.25mm$,
$[-51, +51, -45, +45, -37, +37, -19, +19, 0, 0]$:

	original imperfection shape	reduced imperfection shape
Z33	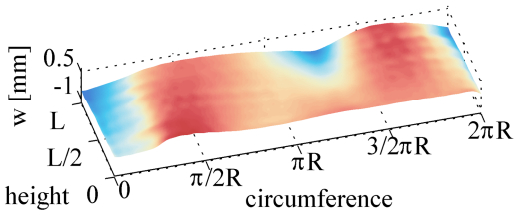 $\lambda_{orig} = 179.85\ kN$	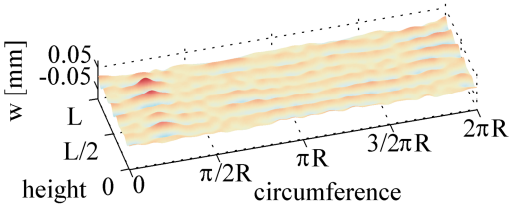 $\lambda_{red} = 181.60\ kN$

SIFM results for shells Z20-Z22, $L = 500mm$, $R = 250mm$, $t = 0.5mm$, $[\pm 24, \pm 41]$:

	original imperfection shape	reduced imperfection shape
Z20	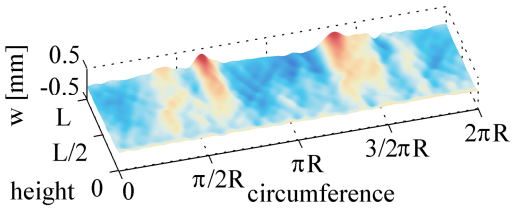 $\lambda_{orig} = 30.48\ kN$	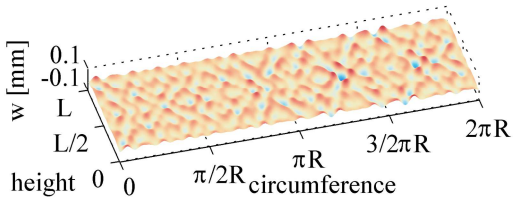 $\lambda_{red} = 30.77\ kN$
Z21	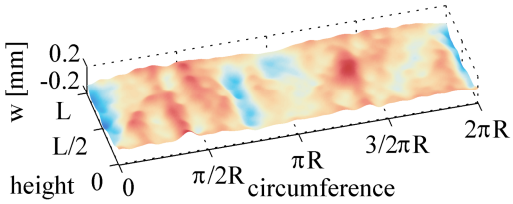 $\lambda_{orig} = 31.27\ kN$	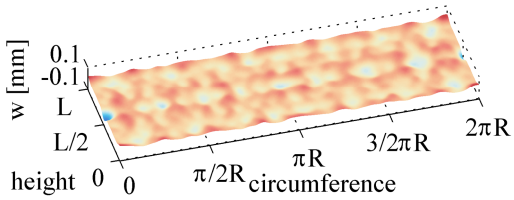 $\lambda_{red} = 31.58\ kN$
Z22	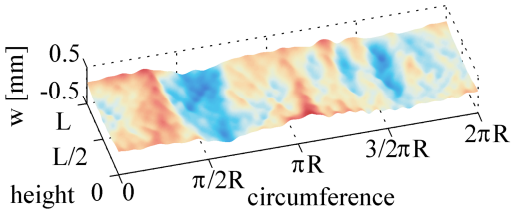 $\lambda_{orig} = 31.33\ kN$	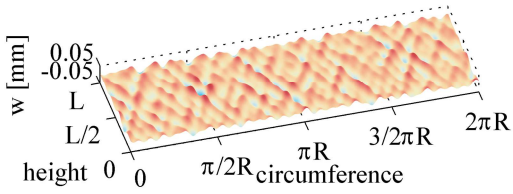 $\lambda_{red} = 31.64\ kN$

SIFM results for K08, $H = 300mm$, $R = 400mm$, $\alpha = 35°$, $t = 0.75mm$, $[30,0,-30,-30,0,30]$:

	original imperfection shape	reduced imperfection shape
K08	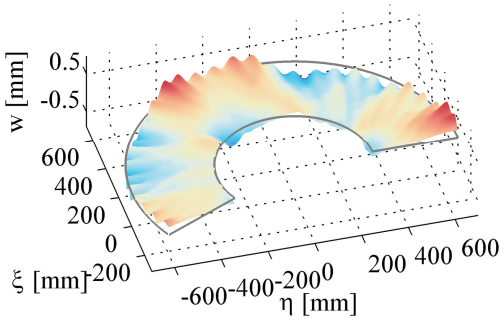 $\lambda_{orig} = 37.92\ kN$	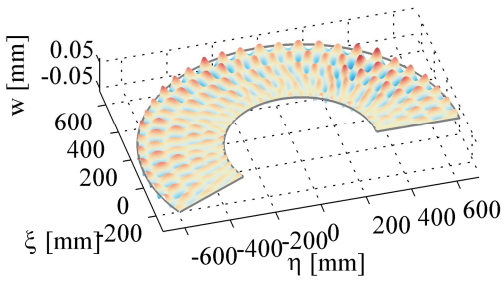 $\lambda_{red} = 38.30\ kN$

SIFM results for shells Z23-Z26, $L = 500mm$, $R = 250mm$, $t = 0.5mm$, $[\pm 24, \pm 41]$:

	original imperfection shape	reduced imperfection shape
Z23	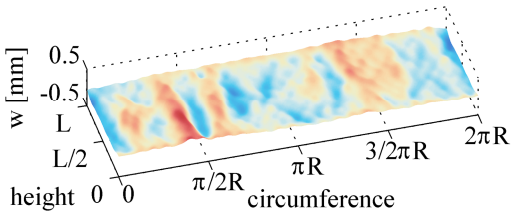 $\lambda_{orig} = 32.19\ kN$	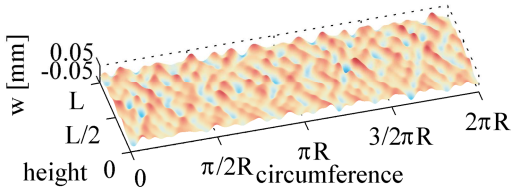 $\lambda_{red} = 32.51\ kN$
Z24	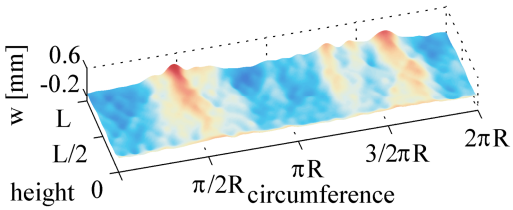 $\lambda_{orig} = 31.34\ kN$	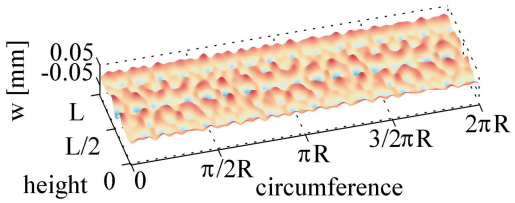 $\lambda_{red} = 31.65\ kN$
Z25	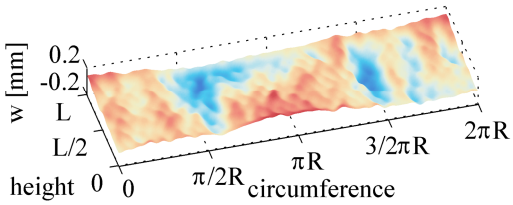 $\lambda_{orig} = 32.95\ kN$	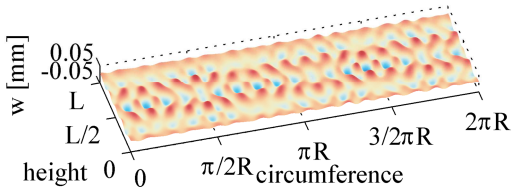 $\lambda_{red} = 33.27\ kN$
Z26	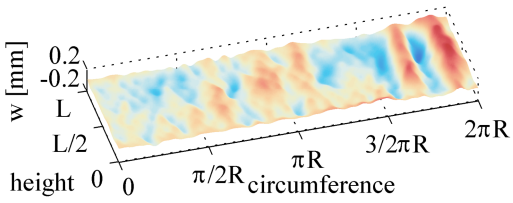 $\lambda_{orig} = 31.46\ kN$	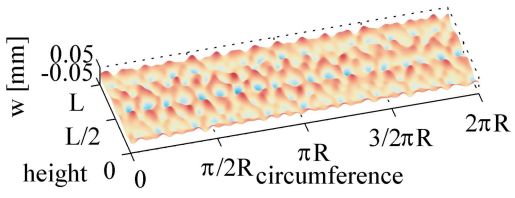 $\lambda_{red} = 31.77\ kN$

SIFM results for shell Z36, $L = 800mm$, $R = 400mm$, $t = 0.75mm$, $[\pm 34,0,0, \pm 53]$:

	original imperfection shape	reduced imperfection shape
Z36	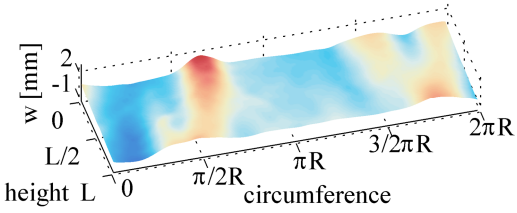 $\lambda_{orig} = 82.14\ kN$	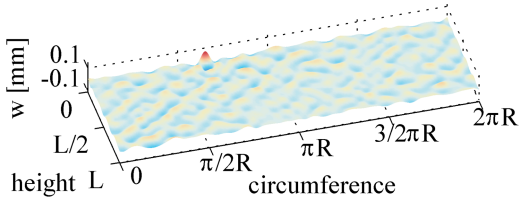 $\lambda_{red} = 82.96\ kN$

Appendix B

SIFM applied to artificially created imperfection patterns, $\eta_t = 1.01$ *if not noted elsewise.*

SIFM results for the artificially created shell discussed in chapter 4.4.6. The imperfection shape contains the Fourier spectrum of shell Z25 with random phase shifts of the Fourier modes, $L = 500mm$, $R = 250mm$, $t = 0.5mm$, $[\pm 24, \pm 41]$:

	original imperfection shape	reduced imperfection shape
$Z_{artificial}$	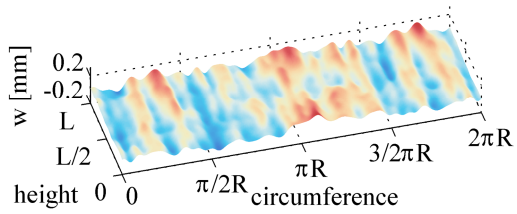 $\lambda_{orig} = 31.06\ kN$	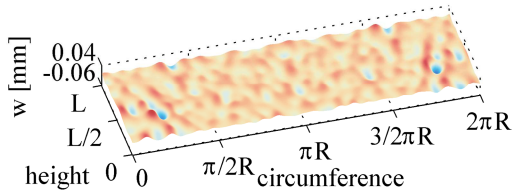 $\lambda_{red} = 31.37\ kN$

References

[1] Arianespace, Service & Solutions, *Ariane 5 - User's Manual*, Issue 5. 2008.

[2] R. Lorenz, "Achsensymmetrische Verzerrungen in dünnwandigen Hohlzylindern," *Zeitschrift Verein Deutscher Ingenieure*, vol. 52, no. 43, pp. 1706–1713, 1908.

[3] S. P. Timoshenko, "Einige Stabilitätsprobleme der Elastizitätstheorie," *Zeitschrift für Mathematik und Physik*, vol. 58, no. 4, pp. 378–385, 1910.

[4] R. V. Southwell, "On the General Theory of Elastic Stability," *Philosophical Transactions of the Royal Society of London. Series A, Containing Papers of a Mathematical or Physical Character*, vol. 213, pp. 187–244, 1914.

[5] E. E. Lundquist, "Strength Tests of Thin-Walled Duralumin Cylinders in Compression," National Advisory Committee for Aeronautics, NACA Report 473, 1934.

[6] L. H. Donnell, "A New Theory for the Buckling of Thin Cylinders Under Axial Compression and Bending," *Trans. ASME*, vol. 56, no. 11, pp. 795–806, 1934.

[7] T. von Kármán and H. S. Tsien, "The Buckling of Thin Cylindrical Shells Under Axial Compression," *Journal of Aeronautical Sciences*, vol. 8, pp. 302–335, 1941.

[8] V. I. Weingarten, E. J. Morgan, and P. Seide, "Elastic Stability of Thin-Walled Cylindrical and Conical Shells Under Axial Compression," *AIAA Journal*, vol. 3, no. 3, pp. 500–505, 1965.

[9] J. Arbocz, "Recent developments in shell stability analysis," *Journal of Theoretical and Applied Mechanics*, vol. 25, no. 4, pp. 523–540, 1987.

[10] P. Seide, *A Survey of Buckling Theory and Experiment for Circular Conical Shells of Constant Thickness*. Defense Technical Information Center, 1962.

[11] N. J. Hoff, T. V. Kármán, and U. S. A. F. O. of S. Research, *The perplexing behavior of thin circular cylindrical shells in axial compression*. Stanford University. Department of Aeronautics and Astronautics, 1966.

[12] B. O. Almroth, "Influence of Edge Conditions on the Stability of Axially Compressed Cylindrical Shells," NASA CR-161, 1965.

[13] W. T. Koiter, C. B. Biezeno, TU Delft: Mechanical Maritime and Materials Engineering, and TU Delft, Delft University of Technology, "Over de stabiliteit van het elastisch evenwicht." 14-Nov-1945.

[14] W. T. Koiter, "On the Stability of Elastic Equilibrium," NASA, NASA-TT-F-10833, 1967.

[15] B. Budiansky and J. W. Hutchinson, "Dynamic buckling of imperfection-sensitive structures," in *Applied Mechanics*, H. Görtler, Ed. Springer Berlin Heidelberg, 1966, pp. 636–651.

[16] R. C. Tennyson and D. B. Muggeridge, "Buckling of axisymmetric imperfect circular cylindrical shells underaxial compression," *AIAA Journal*, vol. 7, no. 11, pp. 2127–2131, 1969.

[17] N. Yamaki, *Elastic Stability of Circular Cylindrical Shells*. 1984.

[18] R. K. Jürcke, *Zur Stabilität und Imperfektionsempfindlichkeit Elastischer Schalentragwerke: Finite-Element-Formulierung Der Anfangs-Nachbeul-Theorie*. Inst. für Konstruktiven Ingenieurbau, 1985.

[19] G. A. Herzlinger, "Localized Diamond-Shaped Buckling Patterns of Axially Compressed Cylindrical Shells," *Aiaa Journal - AIAA J*, vol. 13, no. 6, pp. 837–838, 1975.

[20] M. Eßlinger, "Hochgeschwindigkeitsaufnahmen vom Beulvorgang dünnwandiger, axialbelasteter Zylinder," *Der Stahlbau*, vol. 39, pp. 73–76, 1970.

[21] M. Esslinger, *Beulen und Nachbeulen dünnwandiger Schalen isotroper Kreiszylinder unter Axiallast : Begleitveröffentlichung*. Köln: Deutsche Forschungs- und Versuchsanst. für Luft- und Raumfahrt, 1971.

[22] C. Bisagni, "Composite cylindrical shells under static and dynamic axial loading: An experimental campaign," *Progress in Aerospace Sciences*, vol. 78, pp. 107–115, Oktober 2015.

[23] E. Byskov and J. W. Hutchinson, "Mode Interaction in Axially Stiffened Cylindrical Shells," *AIAA Journal*, vol. 15, no. 7, pp. 941–948, 1977.

[24] B. O. Almroth, *Design of composite material structures for buckling an evaluation*. Flight Dynamics Laboratory; Air Force Wright Aeronautical Laboratories, 1981.

[25] J. W. Hutchinson and J. C. Amazigo, "Imperfection-Sensitivity of Eccentrically Stiffened Cylindrical Shells," *AIAA Journal*, vol. 5, no. 3, pp. 392–401, 1967.

[26] T. Weller and J. Singer, "Experimental Studies on the Buckling Under Axial Compression of Integrally Stringer-Stiffened Circular Cylindrical Shells," *J. Appl. Mech.*, vol. 44, no. 4, pp. 721–730, Dezember 1977.

[27] C. Bisagni and P. Cordisco, "Post-buckling and collapse experiments of stiffened composite cylindrical shells subjected to axial loading and torque," *Composite Structures*, vol. 73, no. 2, pp. 138–149, Mai 2006.

[28] J. Singer, J. Arbocz, and C. D. Babcock Jr., "Buckling of Imperfect Stiffened Cylindrical Shells under Axial Compression," *AIAA Journal*, vol. 9, no. 1, pp. 68–75, Jan. 1971.

[29] J. Arbocz, J. H. Starnes, and M. P. Nemeth, "A Hierarchical Approach to Buckling Load Calculations," presented at the 40th AIAA/ASME/ASCE/AHS/ASC Strcutures, Structural Dynamics and Materials Conference, St. Louis, USA, 1999, p. AIAA-99-1232.

[30] T. Weller, "Combined Stiffening and in-Plane Boundary Conditions Effects on the Buckling of Circular Cylindrical Stiffened-Shells," *Computers & Structures*, vol. 9, no. 1, pp. 1–16, Jul. 1978.

[31] R. Zimmermann, "Optimierung axial gedrückter CFK-Zylinderschalen," VDI Verlag, Fortschritt-Berichte VDI, Reihe 1, Fortschritt-Berichte VDI 207, 1992.

[32] B. Geier, H.-R. Meyer-Piening, and R. Zimmermann, "On the Influence of Laminate Stacking on Buckling of Composite Cylindrical Shells Subjected to Axial Compression," *Composite Structures*, vol. 55, no. 4, pp. 467–474, 2002.

[33] M. W. Hilburger and J. H. Starnes Jr, "Effects of Imperfections on the Buckling Response of Compression-Loaded Composite Shells," *International Journal of Non-Linear Mechanics*, vol. 37, no. 4–5, pp. 623–643, 2002.

[34] M. K. Chryssanthopoulos and C. Poggi, "Probabilistic Imperfection Sensitivity Analyses of Axially Compressed Composite Cylinders," *Engineering Structures*, vol. 17, no. 6, pp. 398–406, 1995.

[35] I. E. Esong, A. Y. Elghazouli, and M. K. Chryssanthopoulos, "Measurement techniques for buckling sensitive composite shells," *Strain*, vol. 34, no. 1, pp. 11–17, Feb. 1998.

[36] J. Arbocz and J. Babcock Charles D., "The Effect of General Imperfections on the Buckling of Cylindrical Shells," *J. Appl. Mech.*, vol. 36, no. 1, pp. 28–38, März 1969.

[37] L. A. Harris, "The Stability of Thin-Walled Unstiffened Circular Cylinders Under Axial Compression Including the Effects of Internal Pressure," *Journal of the Aeronautical Sciences (Institute of the Aeronautical Sciences)*, vol. 24, no. 8, pp. 587–596, 1957.

[38] "Buckling of Thin-Walled Circular Cylinders," NASA, NASA SP-8007, 1968.

[39] "Buckling of Thin-Walled Truncated Cones," NASA, NASA-SP 8019, 1968.

[40] J. de Vries, "The Imperfection Data Bank and its Applications," TU Delft, Delft, 2009.

[41] A. Takano, "Statistical Knockdown Factors of Buckling Anisotropic Cylinders Under Axial Compression," *J. Appl. Mech.*, vol. 79, no. 5, pp. 051004–051004, Jun. 2012.

[42] C. Hühne, "Robuster Entwurf beulgefährdeter, unversteifter Kreiszylinderschalen aus Faserverbundwerkstoff," Dissertation, Leibniz Universität Hannover, Institut für Statik und Dynamik, Mitteilungen des Instituts für Statik und Dynamik der Leibniz Universität Hannover, Hannover, 2006.

[43] J. Arbocz and J. H. Starnes Jr, "Future Directions and Challenges in Shell Stability Analysis," *Thin-Walled Structures*, vol. 40, no. 9, pp. 729–754, 2002.

[44] "Buckling of Steel Shells: European recommendations," Brussels, Belgium, ECCS 56, 1988.

[45] "Stahlbauten – Stabilitätsfälle, Schalenbeulen," Berlin, DIN 18800 Teil 4, 1990.

[46] "General Rules: Strength and Stability of Shell Structures," Brussels, Belgium, Eurocode 3 Part 1.6, 2002.

[47] L. Kollár and E. Dulácska, *Schalenbeulung Theorie und Ergebnisse der Stabilität gekrümmter Flächentragwerke*. 1975.

[48] S. G. P. Castro, R. Zimmermann, M. A. Arbelo, R. Khakimova, M. W. Hilburger, and R. Degenhardt, "Geometric Imperfections and Lower-Bound Methods Used to Calculate Knock-

down Factors for Axially Compressed Composite Cylindrical Shells," *Thin-Walled Structures*, vol. 74, pp. 118–132, Jan. 2014.

[49] J.-F. Imbert, "The effect of imperfections on the buckling of cylindrical shells," engd, California Institute of Technology, 1971.

[50] J. Singer, H. Abramovich, and R. Yaffe, "Initial imperfection measurements of stiffened shells and buckling predictions," *Israel Journal of Technology*, 1979.

[51] J. Arbocz, "Post-buckling behaviour of structures numerical techniques for more complicated structures," in *Buckling and Post-Buckling*, Springer Berlin Heidelberg, 1987, pp. 83–142.

[52] W. Haynie and M. Hilburger, "Comparison of Methods to Predict Lower Bound Buckling Loads of Cylinders Under Axial Compression," in *51st AIAA/ASME/ASCE/AHS/ASC Structures, Structural Dynamics, and Materials Conference*, American Institute of Aeronautics and Astronautics.

[53] B. O. Almroth, A. B. Burns, and E. V. Pittner, "Design criteria for axially loaded cylindrical shells," *Journal of Spacecraft and Rockets*, vol. 7, no. 6, pp. 714–720, 1970.

[54] J. W. Hutchinson, D. B. Muggeridge, and R. C. Tennyson, "Effect of a local axisymmetric imperfection on the buckling behaviorof a circular cylindrical shell under axial compression," *AIAA Journal*, vol. 9, no. 1, pp. 48–52, 1971.

[55] O. G. Ricardo, "A Report on Three Series of Experiments and the Description of a Simplified Model of the Thin Wall Cylinder and Cone Buckling Mechanism." Instituto Tecnologico de Aeronautica, Brasil, 1961.

[56] S. Okubo, P. E. Wilson, and J. S. Whittier, "Influence of concentrated lateral loads on the elastic stability of cylinders in bending," *Experimental Mechanics*, vol. 10, no. 9, pp. 384–389, Jun. 1970.

[57] C. Hühne, R. Rolfes, E. Breitbach, and J. Teßmer, "Robust Design of Composite Cylindrical Shells Under Axial Compression – Simulation and Validation," *Thin-Walled Structures*, vol. 46, no. 7–9, pp. 947–962, 2008.

[58] H. Wang, A. P. Bueschel, R. Degenhardt, K. Rohwer, X. Sun, and W. Wagner, "An empirical formula for the critical perturbation load," presented at the Cocomat Workshop, 2008.

[59] P. Steinmüller, R. Degenhardt, and K. Rohwer, "Investigations of Axially Loaded Unstiffened CFRP Cylindrical Shells Subject to Single Perturbation Loads," presented at the 2nd International Conference on Buckling and Postbuckling Behaviour of Composite Laminated Shell Structures with COCOMAT Workshop, Braunschweig, Germany, 2008.

[60] M. A. Arbelo, R. Degenhardt, S. G. P. Castro, and R. Zimmermann, "Numerical Characterization of Imperfection Sensitive Composite Structures," *Composite Structures*, vol. 108, pp. 295–303, Feb. 2014.

[61] B. Wang, P. Hao, G. Li, Y. Fang, X. Wang, and X. Zhang, "Determination of realistic worst imperfection for cylindrical shells using surrogate model," *Struct Multidisc Optim*, vol. 48, no. 4, pp. 777–794, Oct. 2013.

[62] L. Wullschleger, *Numerical investigation of the buckling behaviour of axially compressed circular cylinders having parametric initial dimple imperfections*. Zürich: ETH, 2006.

[63] S. G. P. Castro, R. Zimmermann, M. A. Arbelo, and R. Degenhardt, "Exploring the Constancy of the Global Buckling Load After a Critical Geometric Imperfection Level in Thin-Walled Cylindrical Shells for Less Conservative Knock-down Factors," *Thin-Walled Structures*, vol. 72, pp. 76–87, Nov. 2013.

[64] B. Kriegesmann, R. Rolfes, C. Hühne, J. Teßmer, and J. Arbocz, "Probabilistic Design of Axially Compressed Composite Cylinders with Geometric and Loading Imperfections," *International Journal of Structural Stability and Dynamics*, vol. 10, no. 4, pp. 623–644, 2010.

[65] J. Arbocz, "The Effect of Initial Imperfections on Shell Stability," *Thin-shell structures: Theory, experiment, and design*, pp. 205–245, 1974.

[66] I. Elishakoff, S. van Manen, P. G. Vermeulen, and J. Arbocz, "First-Order Second-Moment Analysis of the Buckling of Shells with Random Imperfections," *AIAA journal*, vol. 25, no. 8, pp. 1113–1117, 1987.

[67] R. E. Reed, "Remarks on imperfections of axially loaded cylinders," Apr. 1968.

[68] M. Gillie, "Measures of Circularity for Shell Structures," *Journal of Structural Engineering*, vol. 137, no. 10, pp. 1241–1243, 2011.

[69] J. Arbocz and J. M. A. M. Hol, "Collapse of Axially Compressed Cylindrical Shells with Random Imperfections," *AIAA Journal*, vol. 29, no. 12, pp. 2247–2256, 1991.

[70] R. Degenhardt *et al.*, "Probabilistic Approach for Improved Buckling Knock-down Factors of CFRP Cylindrical Shells," in *Proceedings of the 1st European Air and Space Conference (CEAS), Berlin*, 2007.

[71] M. Broggi, A. Calvi, and G. I. Schuëller, "Reliability Assessment of Axially Compressed Composite Cylindrical Shells with Random Imperfections," *Int. J. Str. Stab. Dyn.*, vol. 11, no. 02, p. 215, 2011.

[72] A. A. El Damatty and A. O. Nassef, "A Finite Element Optimization Technique to Determine Critical Imperfection of Shell Structures," *Structural and Multidisciplinary Optimization*, vol. 23, pp. 75–87, 2001.

[73] M. P. Nemeth, R. D. Young, T. J. Collins, and J. H. Starnes Jr, "Effects of Welding-Induced Imperfections on Behavior of Space Shuttle Superlightweight Tank," *Journal of Spacecraft and Rockets*, vol. 36, no. 6, pp. 812–819, Dec. 1999.

[74] T. A. Winterstetter and H. Schmidt, "Stability of Circular Cylindrical Steel Shells Under Combineed Loading," *Thin-Walled Structures*, vol. 40, pp. 893–909, 2002.

[75] V. V. Bolotin, “Statistical Aspects in the Theory of Structural Stability,” in *Dynamic Stability of Structures (G. Herrmann, ed.)*, Oxford: Pergamon Press, 1967, pp. 67–81.

[76] I. Elishakoff, “Simulation of Space-Random Fields for Solution of Stochastic Boundary-Value Problems,” *J. Acoust. Soc. Am.*, vol. 65, no. 2, pp. 399–403, Feb. 1979.

[77] I. Elishakoff and J. Arbocz, “Reliability of Axially Compressed Cylindrical Shells With General Nonsymmetric Imperfections,” *Transactions of the ASME*, vol. 52, pp. 122–128, 1985.

[78] E. Velds, J. Wijker, and M. Klein, “Probabilistic Buckling Analysis Using the Finite Element Method,” *Proceedings of the European Conference on Spacecraft Structures, Materials & Mechanical Testing*, pp. 1–13, 2002.

[79] C. C. Chamis and G. H. Abumeri, “Probabilistic Dynamic Buckling of Composite Shell Structures,” *Composites Part A: Applied Science and Manufacturing*, vol. 36, no. 10, pp. 1368–1380, Oktober 2005.

[80] R. Dancy and D. Jacobs, “The Initial Imperfection Data Bank at the Delft University of Technology: Part II,” Delft University of Technology, Faculty of Aerospace Engineering, LR-559, 1988.

[81] J. Arbocz, J. H. Starnes, and M. P. Nemeth, “On the Accuracy of Probabilistic Buckling Load Predictions,” presented at the 42nd AIAA/ASME/ASCE/AHS/ASC Structures, Structural Dynamics, and Materials Conference, Seattle, WA, 2001, p. AIAA-2000-1236.

[82] M. Chryssanthopoulos, M. Baker, and P. Dowling, “Statistical Analysis of Imperfections in Stiffened Cylinders,” *Journal of Structural Engineering*, vol. 117, no. 7, pp. 1979–1997, 1991.

[83] J. Arbocz and M. W. Hilburger, “Toward a Probabilistic Preliminary Design Criterion for Buckling Critical Composite Shells,” *AIAA Journal*, vol. 43, no. 8, pp. 1823–1827, 2005.

[84] B. Kriegesmann, R. Rolfes, C. Hühne, and A. Kling, “Fast Probabilistic Design Procedure for Axially Compressed Composite Cylinders,” *Composites Structures*, vol. 93, pp. 3140–3149, 2011.

[85] R. Degenhardt *et al.*, “Investigations on Imperfection Sensitivity and Deduction of Improved Knock-down Factors for Unstiffened CFRP Cylindrical Shells,” *Composite Structures*, vol. 92, no. 8, pp. 1939–1946, 2010.

[86] B. Kriegesmann, M. Möhle, and R. Rolfes, “Sample size dependent probabilistic design of axially compressed cylindrical shells,” *Thin-Walled Structures*, vol. 74, pp. 222–231, Jan. 2014.

[87] J. Arbocz and H. Abramovich, “The Initial Imperfection Data Bank at the Delft University of Technology: Part I,” TU Delft, Faculty of Aerospace Engineering, LR-290, 1979.

[88] H. Rothert and V. Gensichen, *Nichtlineare Stabstatik - Baustatische Methoden Grundlagen*. Springer Berlin Heidelberg, 1987.

[89] B. Kriegesmann, “Probabilistic Design of Thin-Walled Fiber Composite Structures,” Dissertation, Mitteilungen des Instituts für Statik und Dynamik der Leibniz Universität Hannover

15/2012, ISSN 1862-4650, Gottfried Wilhelm Leibniz Universität Hannover, Hannover, Germany, 2012.

[90] U. Jäppelt, *Stabilitätsversagen dünnwandiger versteifter Kreiszylinderschalen unter Axiallast im elastisch-plastischen Bereich*. Hannover: Inst. für Statik, 1998.

[91] A. Pflüger, *Stabilitätsprobleme der Elastostatik*. Springer-Verlag, 1975.

[92] P. Wriggers, *Nichtlineare Finite-Element-Methoden*. Springer Berlin Heidelberg, 2001.

[93] M. S. El Naschie, *Stress, stability, and chaos in structural engineering: An energy approach*. McGraw-Hill London, 1990.

[94] L. Nasdala, *Fem-Formelsammlung Statik und Dynamik: Hintergrundinformationen, Tipps und Tricks*. Springer-Verlag, 2010.

[95] E. Riks, "Bifurcation and stability, a numerical approach," Presented at the WAM Symposium on Innovative Methods for Nonlinear Problems, New Orleans, USA, NLR MP 84078 U, Dec. 1984.

[96] R. Khakimova, C. J. Warren, R. Zimmermann, S. G. P. Castro, M. A. Arbelo, and R. Degenhardt, "The single perturbation load approach applied to imperfection sensitive conical composite structures," *Thin-Walled Structures*, vol. 84, pp. 369–377, Nov. 2014.

[97] W. T. Haynie, M. W. Hilburger, M. Bogge, and B. Kriegesmann, "Validation of Lower-Bound Estimates for Compression-Loaded Cylindrical Shells," in *Proceedings 53rd AIAA/ASME/ASCE/AHS/ASC Structures, Structural Dynamics and Materials Conference*, Honolulu, USA, 2012, p. AIAA Paper 2012-1689.

[98] B. Kriegesmann, E. L. Jansen, and R. Rolfes, "Design of cylindrical shells using the Single Perturbation Load Approach – Potentials and application limits," *Thin-Walled Structures*, vol. 108, pp. 369–380, Nov. 2016.

[99] H. N. R. Wagner, C. Hühne, and S. Niemann, "Constant single-buckle imperfection principle to determine a lower bound for the buckling load of unstiffened composite cylinders under axial compression," *Composite Structures*, vol. 139, pp. 120–129, Apr. 2016.

[100] L. Friedrich, T.-A. Schmid-Fuertes, and K.-U. Schröder, "Comparison of theoretical approaches to account for geometrical imperfections of unstiffened isotropic thin walled cylindrical shell structures under axial compression," *Thin-Walled Structures*, vol. 92, pp. 1–9, Jul. 2015.

[101] R. Khakimova, S. G. P. Castro, D. Wilckens, K. Rohwer, and R. Degenhardt, "Buckling of axially compressed CFRP cylinders with and without additional lateral load: experimental and numerical investigation," *Thin-Walled Structures*, Oct. 2017.

[102] A. Meurer, B. Kriegesmann, M. Dannert, and R. Rolfes, "Probabilistic perturbation load approach for designing axially compressed cylindrical shells," *Thin-Walled Structures*, vol. 107, pp. 648–656, Oktober 2016.

[103] A. Haldar and S. Mahadevan, *Probability, Reliability, and Statistical Methods in Engineering Design*. John Wiley & Sons New York/Chichester, UK, 2000.

[104] W. Härdle and L. Simar, *Applied Multivariate Statistical Analysis*. Berlin: Springer Verlag, 2007.

[105] M. K. Chryssanthopoulos, M. J. Baker, and P. J. Dowing, "Imperfection Modeling for Buckling Analysis of Stiffened Cylinders," *Journal of Structural Engineering*, vol. 117, no. 7, pp. 1998–2017, 1991.

[106] M. W. Hilburger, M. P. Nemeth, and J. H. Starnes Jr, "Shell Buckling Design Criteria Based on Manufacturing Imperfection Signatures," *AIAA Journal*, vol. 44, no. 3, pp. 654–663, 2006.

[107] H. Friebe and A. Grube, "Optische 3D Messtechnik zur Materialkennwertermittlung und Deformationsanalyse in der Bauteilprüfung," ZWICK testXpo, 14-Oct-2015.

[108] R. Mendricky, "Determination of measurement accuracy of optical 3D scanners," *MM Science Journal*, Dec. 2016.

[109] S. Marburg, "Six boundary elements per wavelength: is that enough?," *J. Comp. Acous.*, vol. 10, no. 01, pp. 25–51, März 2002.

[110] R. Degenhardt *et al.*, "Investigations on Imperfection Sensitivity and Deduction of Improved Knock-down Factors for Unstiffened CFRP Cylindrical Shells," *Composite Structures*, vol. 92, no. 8, pp. 1939–1946, 2009.

[111] R. Khakimova, D. Wilckens, J. Reichardt, R. Zimmermann, and R. Degenhardt, "Buckling of axially compressed CFRP truncated cones: Experimental and numerical investigation," *Composite Structures*, vol. 146, pp. 232–247, Jun. 2016.

[112] "Abaqus 6.10 Online Documentation." Dassault Systèmes, 2010.

[113] C. Bisagni, "FP7 project DAEDALOS - Dynamics in Aircraft Engineering Design and Analysis for Light Optimized Structures," presented at the Composites 2011, Hannover, Germany, 2011.

[114] European Aviation Safety Agency, "Certification Specifications for Large Aeroplanes CS-25." 06-Jul-2009.

[115] R. Khakimova, R. Zimmermann, D. Wilckens, K. Rohwer, and R. Degenhardt, "Buckling of axially compressed CFRP truncated cones with additional lateral load: Experimental and numerical investigation," *Composite Structures*, vol. 157, pp. 436–447, Dezember 2016.

[116] S. G. P. Castro, P. Schor, J. Reichardt, F. Burau, and E. Lozano, "DESICOS Abaqus plug-in," 2015-2014. [Online]. Available: http://desicos.github.io/desicos/. [Accessed: 01-Oct-2016].

[117] M. Broggi and G. I. Schuëller, "Efficient modeling of imperfections for buckling analysis of composite cylindrical shells," *Engineering Structures*, vol. 33, no. 5, pp. 1796–1806, Mai 2011.

[118] J. Kepple, M. T. Herath, G. Pearce, B. Gangadhara Prusty, R. Thomson, and R. Degenhardt, "Stochastic analysis of imperfection sensitive unstiffened composite cylinders using realistic imperfection models," *Composite Structures*, vol. 126, pp. 159–173, Aug. 2015.

[119] B. Kriegesmann, "On the Correlation of Thickness and Stiffness Properties in Probabilistic Analyses," presented at the ECCOMAS Thematic Conference on the Mechanical Response of Composites, Bristol, UK, 2015.

[120] A. Meurer, M. Dannert, and R. Rolfes, "New Design Approach for Axially Compressed Composite Cylindrical Shells combining the Single Perturbation Load Approach and Probabilistic Analyses," presented at the 3rd International Conference on Buckling and Postbuckling Behaviour of Composite Structures, Braunschweig, Germany, 2015.

[121] I. Elishakoff, "Probabilistic Resolution of the Twentieth Century Conundrum in Elastic Stability," *Thin-Walled Structures*, vol. 59, pp. 35–57, Oct. 2012.